Combined material and process design for the adsorption refrigeration process

A thesis accepted by the Faculty of Energy-, Process- and Bio-Engineering
of the University of Stuttgart to fulfil the requirements
for the degree of Doctor of Engineering Sciences (Dr.-Ing.)

by

Marc Scherle
born in Breisach am Rhein

Main examiner:	Prof. Dr.-Ing. U. Nieken
Co-examiner:	Prof. Dr.-Ing. B. J. M. Etzold
Chairperson of the examination:	Prof. Dr.-Ing. A. Thess
Day of the oral examination:	8th April 2022

Institute of Chemical Process Engineering
of the University of Stuttgart
2022

Acknowledgement

This dissertation was written during my time as a research assistant at the Institute of Chemical Process Engineering at the University of Stuttgart.

I would like to express my sincere thanks to Prof. Ulrich Nieken for the trust placed in me and the freedom to contribute and implement my ideas. The discussions and suggestions have contributed significantly to the success of this work.

I would also like to thank Prof. Etzold for preparing the second opinion and the very good cooperation within the DFG research project (NI 932/10-1 & ET 101/11-1).

An important contribution to the success of this dissertation was also made by the student work of Julian Liedtke and Stefan Welzel, whom I would also like to thank. In particular, I would like to thank my former colleagues at ICVT for the good cooperation, be it on the 2nd floor, in the secretariat, in the workshop or in the technical centre. Because of the support and the constructive atmosphere, I will always have fond memories of my time at ICVT.

A very special thank you goes to my family, especially to my dear mother, who always motivates me with her optimism and support to pursue my goals. Finally, I thank my dear wife Janine from the bottom of my heart for her patience and understanding when the dissertation once again kept me busy for a longer time.

Table of content

Zusammenfassung

Kern dieser Arbeit ist die Optimierung von adsorptiven Wärmepumpen für die Anwendung einer regenerativen Kühlung. Es werden mehrere Ansätze und deren Potential untersucht, um die Effizienz adsorptiver Kältemaschinen zu optimieren. Dabei steht jeweils eine kombinierte Untersuchung der Prozess- und Materialeigenschaften im Fokus. Die kombinierte Material- und Verfahrensentwicklung ist vielversprechend, da beide Faktoren einen erheblichen Einfluss auf die Prozessperformance haben und eine unabhängige Betrachtung lediglich lokale Optima liefert.

Der Adsorptionskälteprozess ist ein zyklisches Verfahren und besteht aus drei Hauptapparaten: Adsorber, Verdampfer und Kondensator, wobei die Kälteproduktion durch Verdampfung eines Kältemittels erfolgt. Zur Verdampfung kommt es infolge eines Druckabfalls in der Gasphase, welcher durch die Anlagerung (Adsorption) von Gasmolekülen an einem hoch porösen Feststoff (Adsorbens) hervorgerufen wird. Das Adsorbens befindet sich im Adsorber, das Herzstück einer Adsorptionskältemaschine. Ist das Adsorbens gesättigt, wird der Adsorber aufgeheizt, das Kältemittel vom Adsorbens desorbiert und im Kondensator verflüssigt. Angetrieben wird eine Adsorptionskältemaschine durch Wärme, welche z.B. aus solarer Einstrahlung oder durch Abwärme aus Industrieprozessen bereitgestellt werden kann. Zur Bewertung des Prozesses werden der thermische Wirkungsgrad (Coefficient of Performance - COP) als Effizienzgröße und die spezifische Leistungsdichte (Specific Cooling Power - SCP) verwendet. Wie viele Prozesse zeichnet sich der Adsorptionskälteprozess durch die Pareto-Optimalität von Effizienz und Leistungsdichte aus. Betriebsbedingungen mit hoher Effizienz weisen eine geringe Leistungsdichte auf und umgekehrt. Das Pareto-optimale Verhalten wird in der vorliegenden Arbeit berücksichtigt, indem für verschiedene Prozess-Material Kombinationen nach dem maximalen COP gesucht wird, welcher sich bei einer gewünschten Leistungsdichte einstellt.

In Adsorptionskälteanlagen kommen unterschiedliche Adsorbenzien zum Einsatz, wobei jeweils ein zum Adsorbens passendes Kältemittel genutzt wird. Die gängigen Stoffpaare sind Silica-Gel mit Wasser, Zeolith mit Wasser oder Aktivkohle mit Methanol. In dieser Arbeit werden exemplarisch Kohlenstoff haltige Adsorbenzien in Form von kompaktierten, quaderförmigen Kompositen und Methanol als Kältemittel untersucht. Aktivkohle ist ein attraktives Adsorbens, da sich der Prozess damit mit Niedertemperaturwärme unter 100 °C betreiben lässt. Die entwickelten Methoden sind jedoch auf beliebige Stoffpaare übertragbar.

Der adsorptive Kälteprozess ist ein attraktives Verfahren, um nicht genutzte Wärmequellen oder solare Wärme zur regenerativen Kälteproduktion zu nutzen. Vor allem der apparative Aufwand sowie die geringe thermische Effizienz und Leistungsdichte stehen jedoch einer weiten Verbreitung von kommerziellen Anlagen im Wege. Ein wesentlicher Grund für die geringe Prozessperformance lässt sich in den konkurrierenden Eigenschaften des Adsorbens identifizieren. Auf der einen Seite wird eine hohe Porosität und innere Oberfläche benötigt, um den Gasmolekülen eine gute Zugänglichkeit zu den Bindungsplätzen sowie eine große Adsorptionskapazität zur Verfügung zu stellen. Durch die hohe Porosität weisen technische Adsorbenzien eine geringe Wärmeleitfähigkeit auf. Aufgrund der Exothermie der Adsorption bzw. Endothermie der Desorption wird jedoch eine gute Wärmeleitfähigkeit benötigt, um das Adsorbens möglichst homogen zu temperieren. Die Anforderungen an ein optimales technisches Adsorbens sind somit vielfältig: Neben einer großen Adsorptionskapazität werden auch gute Wärme- und Stofftransporteigenschaften benötigt.

Die im Zuge dieser Arbeit untersuchte kombinierte Material- und Verfahrensentwicklung zielt im Speziellen darauf hin, optimale Materialeigenschaften für verschiedene Prozessbedingungen zu identifizieren und somit Ansätze zur Verbesserung der thermischen Effizienz des Prozesses zu liefern ohne Einbußen in der Leistungsdichte hinzunehmen und somit zu einer weiteren Verbreitung der Technologie beizutragen. Im Wesentlichen wurden zwei Ansätze identifiziert und in Prozesssimulationen untersucht. Erstens: Heterogene Strukturierung von Adsorbenskompositen mit perkolierenden Wärmeleitstrukturen und Transportkanälen zur Intensivierung der Wärme- und Stofftransporteigenschaften. Zweitens: Interne Rückgewinnung von sensibler sowie latenter Wärme durch Anwendung eines Mehrbettverfahrens.

Experimentelle Charakterisierung von Adsorbenskompositen

In Kapitel 2.4 werden zunächst valide Materialmodelle zur Beschreibung der Adsorbenskomposite abgeleitet, welche mit Hilfe experimenteller Daten parametriert wurden. Hierbei lag das Augenmerk darauf, die Materialeigenschaften, wie Transportparameter, Adsorptionskapazität usw. in Relation zur Kompositzusammensetzung zu setzten. Die Formulierung der Materialmodelle ist durch experimentelle Erkenntnisse motiviert. Die experimentelle Parametrisierung der Materialmodelle wird in Kapitel 4 vorgestellt wobei zunächst Adsorbenspulver und anschließend Adsorbenskomposite mit variierendem Anteil und Typ an Binder und Wärmeleitadditiv untersucht und Material-Wirkungskorrelationen abgeleitet werden. Die Wärmeleitadditive wurden den Kompositen hierbei statistisch zugemischt.

Kombinierte Material- und Prozessauslegung für 2-Bett Adsorptionskältemaschinen

Neben der Zusammensetzung spielt die Schichtdicke der Komposite eine wesentliche Rolle für den Wärme- und Stofftransportwiederstand sowie für die Adsorptionskapazität. Wird eine hohe Leistungsdichten (SCP) angestrebt, sollten möglichst dünne Schichten eingesetzt und der Prozess mit kurzer Zykluszeit betrieben werden. Nachteilig bei dünnen Kompositschichten und kurzen Zykluszeiten ist jedoch, dass ein zunehmender Anteil an Energie für den Temperaturwechsel der inerten Massen anstatt für die Regeneration des Adsorbens aufgewendet werden muss. Derartige Prozessvariationen weisen somit eine geringe thermische Effizienz (COP) auf. Umgekehrt lässt sich die Prozesseffizienz durch dickere Kompositschichten sowie lange Zykluszeiten erhöhen, wobei jedoch nur geringe Leistungsdichten erzielt werden. Um die konkurrierenden Material- und Prozesseigenschaften zu untersuchen, wird in Kapitel 3 ein eindimensionales, dynamisches Prozessmodell des 2-Bett Adsorptionskälteprozesses abgeleitet, wobei der Wärme- und Stofftransport in den Kompositen entlang der Schichtdicke aufgelöst wird. Mit Hilfe effektiver Materialmodelle können damit beliebige Kompositzusammensetzungen unter dynamischen Prozessbedingungen untersucht und optimale Material-Prozesskombinationen identifiziert werden.

Die kombinierte Material- und Verfahrensoptimierung wurde zunächst mit Prozesssimulationen für ausgewählte, experimentell charakterisierte Komposite durchgeführt. Das Vorgehen und die Ergebnisse sind in Kapitel 5 dargestellt. In den Prozesssimulationen wurde für beliebige Leistungsdichten die optimale Kombination aus Schichtdicke und Zykluszeit identifiziert, für welche die Effizienz maximal ist. Mit diesen Untersuchungen konnte festgestellt werden, dass durch die statistische Zugabe von Wärmeleitadditiven zu Adsorbenskompositen keine Verbesserung der Prozesseffizienz erzielt werden kann. Das ist im Wesentlichen darauf zurückzuführen, dass durch die statistische Zugabe zunächst nur lokal isolierte Kluster mit deutlich erhöhter Wärmeleitfähigkeit entstehen, welche jedoch nur in geringem Maße zur effektiven Wärmeleitfähigkeit der Komposite beitragen. Eine signifikante Steigerung der effektiven Wärmeleitfähigkeit lässt sich erst beim Erreichen der Perkolationsschwelle erzielen, wofür ein hoher Anteil an Additiven benötigt wird. Der hohe Anteil der inerten Additive geht zu Lasten der Adsorptionskapazität, deren Verringerung durch die Erhöhung der Wärmeleitfähigkeit nicht überkompensiert werden kann. Diese Erkenntnisse konnten durch weitere Prozesssimulationen bestätigt werden, welche mit einem Materialmodell durchgeführt wurden, welches aus der Theorie effektiver Medien abgeleitet wurde. Durch diese Prozesssimulationen konnte somit eine wichtige Erkenntnis gewonnen werden: Die statistische Zugabe von

Wärmeleitmaterialien zu Adsorbenskompositen verspricht keine Verbesserung der Prozesseffizienz von Adsorptionskältemaschinen.

Da Transportwiederstände in den Adsorbenskompositen jedoch ein wesentlicher Grund für die geringe Prozesseffizienz darstellen, wurden im nächsten Schritt strukturierte Komposite untersucht, wobei perkolierende Wärmeleitstrukturen betrachtet wurden. Bereits mit einem geringen Anteil perkolierender Strukturen kann die effektive Wärmeleitfähigkeit von Kompositen stark erhöht werden, ohne mit einer signifikanten Reduktion der Adsorptionskapazität einherzugehen. In Kapitel 5.3 wurden diese Untersuchungen zunächst mit einem einfach Materialmodell mit perkolierender, linearer Wärmeleitstruktur durchgeführt. Neben Zykluszeit und Schichtdicke wurden in den Prozesssimulationen zusätzlich die Volumenanteile an Adsorbens und Wärmeleitadditiv variiert und im Anschluss die optimalen Parameterkombinationen identifiziert.

3D-Strukturierung von Adsorbenskompositen

Basierend auf diesen Erkenntnissen wurde in Kapitel 6 die gezielte Strukturierung von Adsorbenskompositen untersucht. Hierfür wurde exemplarisch eine Rippengeometrie gewählt, welche die Komposite vollständig durchdringt und somit zu einer deutlichen Erhöhung der effektiven Wärmeleitfähigkeit beiträgt. Zusätzlich wurden makroskopische Transportkanäle in die Komposite eingebracht, die zu einer besseren Verteilung des gasförmigen Kältemittels über der Höhe der Komposite beitragen. Die heterogen strukturierten Geometrien wurden zunächst in Prozesssimulationen optimiert, wodurch nochmals eine deutliche Effizienzsteigerung gegenüber den linear strukturierten Kompositen erzielt werden konnte. Anschließend wurde eine vielversprechende Rippengeometrie ausgewählt und heterogen strukturierte Komposite hergestellt, welche in einer Laboranlage auf ihre Prozessperformance untersucht wurden. Mit den experimentellen Untersuchungen konnten die Simulationsergebnisse bestätigt werden: Durch die heterogene Strukturierung von Adsorbenskompositen können die Stoff- und Wärmetransporteigenschaften verbessert und damit die Schichtdicken deutlich erhöht werden, was zu einer signifikanten Steigerung der Prozessperformance beiträgt.

Wärmeintegriertes Mehrbettverfahren

Neben der Strukturoptimierung der Adsorbenskomposite bietet die Prozessverschaltung großes Potential zur Verbesserung der Effizienz. Hierbei ist die Wärmeintegration zur Rückgewinnung von sensibler Wärme und vor allem latenter Adsorptionswärme ein vielversprechender Ansatz. Um das volle Wärmerückgewinnungspotential auszunutzen, wurde in Kapitel 7 ein

Mehrbettverfahren untersucht, wobei mehrere stofflich getrennte Adsorbensbetten zum Einsatz kommen. Die Verschaltung der einzelnen Adsorber wurde derart gewählt, dass die exotherme Adsorptionswärme teilweise für die endothermen Desorption zur Verfügung steht, wodurch die benötigte Wärme für den Antrieb des Prozesses deutlich reduziert wird und somit die Prozesseffizienz gesteigert werden konnte. Die Verschaltung der Adsorber und die Umschaltung zwischen den einzelnen Prozessschritten erfolgt durch das Umschalten des Wärmeträgerfluids. Somit ergibt sich eine simulierte Bewegung der Adsorber durch den thermodynamischen Kreisprozess, was auch als Simulated-Moving-Bed bekannt ist. Für die effiziente simulative Untersuchung des Mehrbettverfahrens wurde ein stationäres True-Moving-Bed Modell abgeleitet und wiederum eine kombinierte Material- und Verfahrensoptimierung durchgeführt. Zusätzlich zur Kompositschichtdicke und Zykluszeit wurde hierbei die Wärmerückgewinnungszone als Parameter in der Optimierung betrachtet. Durch die Optimierung der Material- und Prozessparameter und vor allem durch die interne Rückgewinnung von sensibler und latenter Wärme konnte die Prozessperformance nochmals deutlich gesteigert werden.

Abschließend lässt sich festhalten, dass durch die kombinierte Material- und Verfahrensoptimierung die Prozessperformance von Adsorptionskältemaschinen gesteigert werden kann. Vor allem die heterogene Strukturierung von Adsorbenskompositen und die interne Wärmerückgewinnung von sensibler und latenter Wärme sind vielversprechende Ansätze. Die Methoden wurden in dieser Arbeit exemplarisch für kohlenstoffhaltige Adsorbenzien in quaderförmiger Kompositform mit Methanol als Kältemittel entwickelt. Die Übertragung auf andere Stoffpaare und Kompositgeometrien ist durch die Anpassung der Material- und Prozessmodelle direkt möglich. Des Weiteren wurden die Untersuchungen exemplarisch für adsorptive Wärmepumpen für die Kälteanwendung durchgeführt. Die Methoden lassen sich auch äquivalent zur Optimierung von Adsorptionswärmepumpen für den Heizzweck übertragen.

Abstract

The core of this work is the optimisation of adsorption heat pumps for the application of regenerative cooling. Several approaches and their potential are investigated to optimise the efficiency of adsorption refrigeration machines. In each case, the focus is on a combined investigation of the process and material properties. The combined material and process development are promising, as both factors have a significant influence on the process performance and an independent consideration only provides local optima.

The adsorption refrigeration process is cyclic and consists of three main apparatuses: Adsorber, Evaporator, and Condenser, where refrigeration is produced by evaporation of a refrigerant. Evaporation is driven by a pressure drop in the gas phase, which is caused by the adsorption of gas molecules on a highly porous solid (adsorbent). The adsorbent is located in the adsorber, the heart of an adsorption refrigeration machine. When the adsorbent is saturated, the adsorber is heated, the refrigerant is desorbed from the adsorbent and liquefied in the condenser. An adsorption chiller is driven by heat, e.g. from solar radiation or waste heat from industrial processes. To evaluate the process, the thermal efficiency (Coefficient of Performance - COP) and the specific power density (SCP) are used. Like many processes, the adsorption refrigeration process is characterised by the Pareto optimality of efficiency and power density. Operating conditions with high efficiency have low power density and vice versa. The Pareto-optimal behaviour is taken into account in this work by searching for the maximum COP that is obtained at a prescribed power density for different process-material combinations.

Different adsorbents are used in adsorption refrigeration systems, whereby a refrigerant is used that matches the adsorbent. Conventional material pairs are silica gel with water, zeolite with water, or activated carbon with methanol. In this work, carbon-containing adsorbents in the form of compacted, cuboidal composites and methanol as a refrigerant are investigated. Activated carbon is an attractive adsorbent, as the process can be operated with low-temperature heat below 100 °C. The methods developed can, however, be applied to any material.

The adsorption refrigeration process is attractive for the utilization of unused heat sources or solar heat for regenerative cold production. However, the complexity of the equipment and the low thermal efficiency and power density are the main obstacles to the widespread use of commercial plants. A major reason for the low process performance can be identified in the

competing properties of the adsorbent. A high porosity and internal surface area are required to provide good accessibility to the adsorption sites and a large adsorption capacity. Due to the high porosity, technical adsorbents have a low thermal conductivity. However, due to the exothermic nature of adsorption or the endothermic nature of desorption, a good thermal conductivity is required to keep the adsorbents as homogeneously tempered as possible. The requirements for an optimal technical adsorbent are therefore manifold: in addition to a large adsorption capacity, good heat and mass transfer properties are also needed.

The combined material and process development applied in the course of this work aims in particular at identifying optimal material properties for different process conditions and thus providing approaches for improving the thermal efficiency of the process without sacrificing power density and thus contributing to further dissemination of the technology. Two main approaches were identified and investigated in process simulations. First: 3D structuring of adsorbent composites with percolating heat conduction ribs and transport channels to intensify the heat and mass transfer properties. Second: Efficient internal recovery of sensible as well as latent heat by applying a multi-bed process.

Experimental characterisation of adsorbent composites

For the combined material and process development, material models for the description of the adsorbent composites are outlined in chapter 2.4, which were parameterised with experimental data. The focus was laid on correlating the material properties, such as transport parameters, adsorption capacity, etc., to the composition of the composite. The formulation of the material models is motivated by experimental findings. The results of the experimental parameterisation of the material models are outlined in chapter 4. Adsorbent composites with varying amounts and types of binder and the thermal additive were investigated and material-property correlations were derived. The heat-conducting additives were statistically mixed with the composites.

Combined material and process design for 2-bed adsorption chillers

In addition to the composite composition, layer thickness plays an important role in the heat and mass transfer resistance. If high power densities are desired, thin layers should be used, and the process should be operated with a short cycle time. The disadvantage of thin composite layers is their low specific storage capacity for the refrigerant. Therefore, such process variations have low thermal efficiency. Conversely, process efficiency can be increased by thicker composite layers and long cycle times, but only low power densities are achieved. To investigate the competing material and process properties, a one-dimensional dynamic process model of the 2-bed

adsorption refrigeration process was derived in Chapter 3, where the heat and mass transfer in the composites is resolved. With the help of effective material models, any composite compositions can be investigated under dynamic process conditions and optimal material-process combinations can be identified.

The combined material and process optimisation was carried out in chapter 5 with process simulations for selected, experimentally characterised composites. Here, the efficiency was optimised in such a way that the optimal combination of layer thickness and cycle time was identified for any power densities. With these investigations, it could be determined that no improvement of the process efficiency can be achieved by the statistical addition of heat conduction additives to adsorbent composites. This is mainly because the statistical addition creates locally isolated clusters with significantly increased thermal conductivity, which, however, only contribute to a small extent to the effective thermal conductivity of the composites. A significant increase in the effective thermal conductivity can only be achieved when the percolation threshold is reached, for which a high proportion of additives is required. The high proportion of inert additives is at the expense of the adsorption capacity, the reduction of which cannot be overcompensated by the increase in thermal conductivity. These findings could be confirmed by further process simulations, which were carried out with a material model derived from effective medium theory. Through these process simulations, an important insight could thus be gained: The statistical addition of heat-conducting materials to adsorbent composites does not promise an improvement of the process performance.

However, since transport resistances in the adsorbent composites are a major reason for the low process efficiency, structured composites were investigated in the next step, whereby percolating heat-conducting additive was considered. Even with a small proportion of percolating additives, the effective thermal conductivity of composites can be greatly increased without being accompanied by a significant reduction in adsorption capacity. In chapter 5.3, these investigations were first carried out with a simple material model with a percolating, linear heat-conducting additive. In addition to cycle time and layer thickness, the volume fractions of adsorbent and heat conduction additive were also varied in the process simulations and the optimal parameter combinations that provided the maximum efficiency for different power densities were subsequently identified.

3D-structuring of adsorbent composites

Based on these investigations, the 3D-structuring of adsorbent composites was examined in detail in chapter 6. For this purpose, a rib geometry was chosen, which completely penetrates the composites and thus contributes to a significant increase in the effective thermal conductivity. In addition, macroscopic transport channels were introduced into the composites, which contribute to a better distribution of the adsorptive over the height of the composites. The 3D-structured geometries were first optimised in process simulations, which resulted in a further significant increase in efficiency compared to the linearly structured composites. Subsequently, a promising rib geometry was selected, and 3D-structured composites were produced, which were tested for their process performance in a laboratory setup. The experimental investigations confirmed the simulation results: The 3D-structuring of adsorbent composites can improve the mass and heat transport properties and thus significantly increase the layer thickness, which contributes to a significant increase in process performance.

Heat-integrated multi-bed process

In addition to the structural optimisation of the adsorbent composites, the process design offers a high potential for improving efficiency. Here, heat integration for the recovery of sensible heat and especially latent heat of adsorption is a promising approach. To exploit the full heat recovery potential, a multi-bed process was investigated in chapter 7, whereby several adsorbent beds separated by material are used. The interconnection of the individual adsorbers was chosen in such a way that the exothermic adsorption heat is partly available for the endothermic desorption, which significantly reduces the heat required to drive the process and thus increases the process efficiency. The interconnection of the adsorbers and the switching between the individual process steps is done by switching the heat transfer fluid. This results in a simulated movement of the adsorbers through the thermodynamic cycle, which is also known as Simulated-Moving-Bed. For the efficient simulative investigation of the multi-bed process, a steady-state True-Moving-Bed model was derived and again a combined material and process optimisation was performed. In addition to the composite layer thickness and cycle time, the heat recovery zone was considered as a parameter in the optimisation. Through the optimisation of the material and process parameters and especially through the internal recovery of sensible and latent heat, the process performance could again be significantly increased.

In conclusion, it can be said that the combined material and process optimisation provides approaches for improving adsorption chillers. Especially the 3D-structuring of adsorbent composites and the internal heat recovery of sensible and latent heat are promising approaches.

In this work, the methods were developed exemplarily for carbon-based adsorbents in cuboidal composite form with methanol as refrigerant. The transfer to other material pairs and composite geometries is directly possible by adapting the material and process models. Furthermore, the investigations were carried out exemplarily for adsorptive heat pumps for refrigeration applications. The methods can also be transferred equivalently to the optimisation of adsorption heat pumps for heating purposes.

List of Symbols and abbreviations

Latin letters:

Symbol	Unit	definition
A	$Jmol^{-1}$	Adsorption potential in Dubinin formalism
A	m^2	Surface area
a^s	m^2g^{-1}	Specific surface area of adsorbent
B_0	m^2	Permeability
B	$ms^{-1}N^{-1}$	Mobility of a species
b	Pa^{-1}	Adsorption equilibrium constant in Langmuir isotherm & BET isotherm
C	$-$	BET-parameter
c	$molm^{-3}$	Concentration
c_p	$Jkg^{-1}K^{-1}$	Specific heat capacity
COP	$-$	Coefficient of Performance
D	m^2s^{-1}	Diffusion/ transport parameter
d	m	Diameter
E_0	$Jmol^{-1}$	Characteristic adsorption energy
G	J	Free energy
g	$Jmol^{-1}$	Specific free energy/ chemical potential
h	$Jmol^{-1}$	Molar enthalpy
$\bar{h}$	$Jmol^{-1}$	Partial molar enthalpy
K'	$mol\,kg^{-1}Pa^{-1}$	Henry constant
k	$Wm^{-2}K^{-1}$	Heat transfer coefficient
k	s^{-1}	Kinetic parameter (Langmuir & LDF)
k_B	JK^{-1}	Boltzmann-constant
L	m	Length
M	kg	Mass

m	kgm^{-2}	Surface specific mass
MW	$kgmol^{-1}$	Molecular mass
N_m^a	mol	BET-parameter, monolayer capacity
N	mol	Moles
N_A	mol^{-1}	Avogadro number
N_L	m^{-3}	Loschmidt constant
n	$-$	Homogeneity parameter in Dubinin formalism
$\dot{N}$	$mols^{-1}$	Molar flow
$\dot{n}$	$molm^{-2}s^{-1}$	Molar flux
n_N	$molecules\, m^{-3}$	Molecular density
$\dot{n}_N$	$molecules\, m^{-2}s^{-1}$	flux of molecules
p	Pa	Pressure
q	$mol\, kg^{-1}$	Adsorbent loading or moles adsorbed
q	Jm^{-2}	Heat density
$\dot{q}$	$Js^{-1}m^{-2}$	Heat flux
R	$Jmol^{-1}K^{-1}$	Gas constant
R	KW^{-1}	Thermal resistance
R, r	m	Radius
r	$-$	Coefficient of regeneration
s	m	Layer thickness
s	$JK^{-1}mol^{-1}$	Molar entropy
$\bar{s}$	$JK^{-1}mol^{-1}$	Partial molar entropy
SCP	Wkg^{-1} or Wm^{-2}	Specific Cooling Power
T	K	Temperature
t	s	Time
u	Jm^{-3}	Internal energy density
u^{bed}/u^{hf}	ms^{-1}	Velocity of moving bed/ heat transfer fluid
V	m^3	Volume
v	$m^3kg^{-1}\ or\ m^3mol^{-1}$	Mass or molar specific volume

v	ms^{-1}	Velocity
$\bar{v}$	m^3mol^{-1}	Partial molar volume
$\bar{v}$	ms^{-1}	Mean molecular velocity
$V_m^{v,ad}$	m^3	Gaseous equivalent monolayer volume
$v_m^{v,ad}$	cm^3g^{-1}	Specific gaseous equivalent monolayer volume, BET-parameter
v_0	m^3mol^{-1}	Molar volume at normal conditions
$\overline{v}$	$m\ s^{-1}$	Mean molecular velocity
w	cm^3g^{-1}	Specific pore volume in Dubinin isotherm model
w	–	Probability factor
w	J	Mechanical energy
w_p	m	Pore width
X	gg^{-1}	Mass specific loading
y_j	mol_jmol^{-1}	Molar fraction
y	–	Spatial coordinate of moving bed (in TMB approach)
y	–	Fraction of heat recovery zone
z	–	Spatial coordinate of composites
z'	–	Regular transport coordinate in a porous medium

Greek letters

Symbol	Einheit	Definition
α	K^{-1}	Thermal expansion coefficient of adsorbate
α	$Wm^{-2}K^{-1}$	Heat transfer coefficient
α	m^2s^{-1}	Thermal diffusivity
β	–	Affinity constant in Dubinin formalism
$\beta_{e,c}$	$kgPa^{-1}s^{-1}m^{-2}$	Mass transfer parameter
ε	m^3m^{-3}	Porosity/ volume fraction
ξ	m	Spatial coordinate of primary particles
η	Pas	Dynamic viscosity

Θ	–	Fractional coverage of adsorbent surface
Θ	–	Contact angle
λ	$Wm^{-1}K^{-1}$	Thermal conductivity
λ_j	m	Mean free path of species j
$\mu = g$	$Jmol^{-1}$	Chemical potential
ξ	–	Dynamic state
ϱ	kgm^{-3}	Density
σ_m	m^2	Cross-sectional area of one adsorbate molecule
σ	m	Collision diameter of a molecule
σ	Nm^{-1}	Surface tension
τ	–	Tortuosity factor
τ	s	Residence time
ϕ	–	Relative pressure

Subscripts

Index	Definition
0	Normal conditions (T=273.15K, p = 1.01325 bar)
0	Maximum values (in Dubinin formalism), e.g., maximum specific pore volume
0	Top layer of adsorbent composites
ads	Adsorption
app	Apparent
$bind$	Binding
$bulk$	Bulk
c	Condenser
$comp$	Consolidated composite (contains adsorbent + binder (+ heat additive))
$cont$	Continuum
$cool$	Cooling/ pre-cooling step
cyc	Cycle

d	Diffusive
des	Desorption
e	Evaporator
env	Envelope
$evap$	Evaporation
exp	Experimental
$heat$	Heating/ pre-heating step
$high$	Highest temperature level
hr	Heat recovery
hrp	Heat recovery potential
i, j	Index for species
$infl$	Inflection point
int	Intrusion
j	SMB modules
K	Kapitza
low	Lowest temperature level
M	Mass
m	Monolayer of adsorbed molecules
mid	Middle-temperature level
mol	Molecular
N	Number of molecules
p	Pore (intraparticle micro- and mesopores in primary particle)
par	Primary particle
sat	Saturation condition
$skel$	Skeleton
$surf$	Surface
sw	Switch
$visc$	Viscous
w	Wall

Superscripts

Index	Definition
ad	Adsorbate
c	Channels
D	Diffusion
eff	Effective
eq	Equilibrium
g	Gas phase
gas	Free gas phase in adsorber
ha	Heat additive
hf	Heat transfer fluid
l	Fictious liquid phase in equilibrium with adsorptive
ma	Macropores/ interparticle voids
mi	Micropores/ intraparticle pores
p	Pores (intraparticle)
pm	Passive mass of heat exchanger
S	Surface
s	Adsorbent
$theo$	Theoretical
v	Adsorptive

Abbreviations

Abbreviation	Definition
AC	Activated carbon
AdHex	Adsorbent - heat exchanger
Ag	Silver
atm	Atmospheric conditions
BN	Boron nitride
C	Graphite powder

CDC	Carbide derived carbon
CMC	Carboxymethylcellulose
CSS	Cyclic steady-state
DAE	Differential algebraic equations
DFG	Deutsche Forschungsgemeinschaft (German Research Foundation)
DGM	Dusty gas model
DSC	Differential scanning calorimetry
EMT	Effective medium theory
HEX	Heat exchanger
HP	Heat pump
Kn	Knudsen number
LDF	Linear driving force
MFM	Mass flow meter
PDE	Partial differential equation
PTFE	Polytetrafluoroethylene
REM	Raster electron microscope
SMB	Simulated-Moving-Bed
Ti-CDC	Titanium carbide derived carbon
TMB	True-Moving-Bed

1. Introduction

The supply of regenerative cooling energy is a central task of the 21st century which is driven by two dominant energy trends: decarbonization of the global energy sector and rapidly growing cooling demand in developed and developing countries due to global warming. The global cooling demand is expected to increase significantly due to rising prosperity and population growth especially in hot regions of the world, as well as global climate change [1]. Especially maintaining a comfortable indoor climate, primarily through cooling, is essential to keep humans comfortable and productive. Forecasts predict that by 2050, two out of three private households could have air conditioning, with India, China, and Indonesia alone accounting for half of all units [2]. The growing demand for cooling requires ever-increasing amounts of electricity, which must be produced by carbon-neutral sources to protect the planet from further warming. With energy demand for space cooling being one of the least considered, yet one of the largest energy consumers today, there are warnings of an impending global "cold crunch" [2]. Air conditioning already accounts for 20 % of total electricity consumption in buildings, with the potential to triple if no countermeasures are taken [2]. In addition, the expected global electricity demand is rising, especially due to electrification of building and industry, transportation, digitalization, and population and prosperity growth. Due to the increasing electricity demand, a near-term conversion of electricity production to climate-neutral technologies is not to be expected [3].

In addition to the production of climate-neutral electricity (by sun, wind, water, etc.), the reduction of electricity consumption and sustainable utilization of industrial and transport heat (waste heat usage, heat transformation, and storage) are the central tasks [4]. Concerning space climatization, advantageous is the locally as well as temporally simultaneously occurring demand for cooling energy and heat input by solar insolation. The regions which are exposed to large solar heat input, have at the same time a large demand for cooling energy. Systems are needed that take advantage of this, such as photovoltaic-powered compression chillers [1] or thermally-driven sorption heat pumps [5]. Joemann compares the solar thermal and solar electrical cooling systems [6]. Solar electrical cooling systems seem to be advantageous if it comes to system efficiency, potential improvement of the efficiency, higher value of excess electricity compared to solar heat excess, and lower investment costs. However, often, the local cooling demand requires more than half of the peak electricity consumption [7] and to overcome this, decentral electricity production with photovoltaic is required [1]. Alternatively, the heat supply can be utilized in solar thermal cooling systems directly taking advantage of the low-quality heat instead of converting

solar insolation to electricity with the help of photovoltaic systems. This technology is very interesting to recover energy with great potential for saving energy [8]. Beyond that, a free choice of heat sources can be applied in sorption heat pumps, such as industrial waste heat or gas burners.

Thus, to reduce the electricity consumption by air conditioning, the usage of low-quality energy sources with low temperatures such as thermal energy, geothermal energy, and waste heat is the key [7]. These low-quality heat sources have significantly lower temperature potential below 100 °C than that achieved by burning fossil fuels and thus giving rise as a potential niche technology and can directly be applied in thermally driven sorption chillers [4]. For that, either adsorption or absorption heat pumps can be applied. In this thesis, the adsorption refrigeration process is investigated, and optimization potentials are identified.

1.1 Adsorption Heat Pumps for cooling purposes

Solid sorption heat pumps are regenerative alternatives for meeting future cooling and heating demands. Thermal energy is required to drive these machines, which can be provided by solar heat or industrial waste heat, thus reducing primary energy consumption. Besides, the commonly used adsorption pairs are environmentally friendly, reducing the direct greenhouse gas emissions [4].

In adsorption heat pumps, no mechanical or electrical energy is produced or used (only for pumping the external heat transfer circuits). Instead of mechanical compression, thermal compression is the key mechanism to overcome the pressure difference between evaporator and condenser. This takes place in the adsorber where gas molecules are adsorbed on the pore walls of a solid medium (adsorbent) under the release of adsorption heat (exothermic), at ambient temperature level (mid), and evaporator pressure. Adsorption from the gas phase is accompanied by a pressure decrease which drives the evaporation of refrigerant on the low-temperature level in the evaporator. If cooling production is the purpose of the adsorption heat pump, evaporation of refrigerant is the benefit of the process, which cools down an external heat transfer circuit. After a certain time, the adsorbent is saturated where the adsorption rate becomes zero, and the evaporation stops. Subsequently, heat at a high-temperature level is supplied in the (endothermic) desorption step to regenerate the adsorbent. By providing the driving energy, the gas molecules are released from the adsorbent at condenser pressure. Depending on the molecular binding-forces between adsorbate and adsorbent, regeneration temperatures as low as 50-70 °C can be used in adsorption heat pumps. Common adsorbent materials are zeolites [9], [10], silica gels

[11]–[16], activated carbons [17]–[22], or metal-organic frameworks (MOFs) [23], [24]. As the refrigerant, mostly water or alcohol (methanol or ethanol) are used.

Technical adsorption processes for energetic or separation purposes are operated cyclic with alternating adsorption and desorption. To ensure quasi-continuous refrigeration, at least two adsorbers are required, one of which is always in the adsorption phase and the other in the desorption phase. In addition to the cooling production and regeneration phases, the process also includes two short steps (pre-cooling and pre-heating), in which the adsorbers are not connected to either the condenser or the evaporator. Schematically, the process set-up with two adsorber beds is shown in Figure 1-1 on the left, with adsorber 2 connected to the condenser via valve V-b being regenerated/ desorbed and adsorber 1 connected to the evaporator via valve V-c. In addition, the thermodynamic changes of states are shown in a Clausius-Clapeyron diagram on the right together with the supplied and removed heat flows at the corresponding temperature levels. Initially, in the thermodynamic cycle, adsorber 1 is located at point 1 where the evaporation step (cooling production) starts with minimally loaded adsorbent, and adsorber 2 is located at point 3 where the condensation step (adsorbent regeneration) starts with maximally loaded adsorbent.

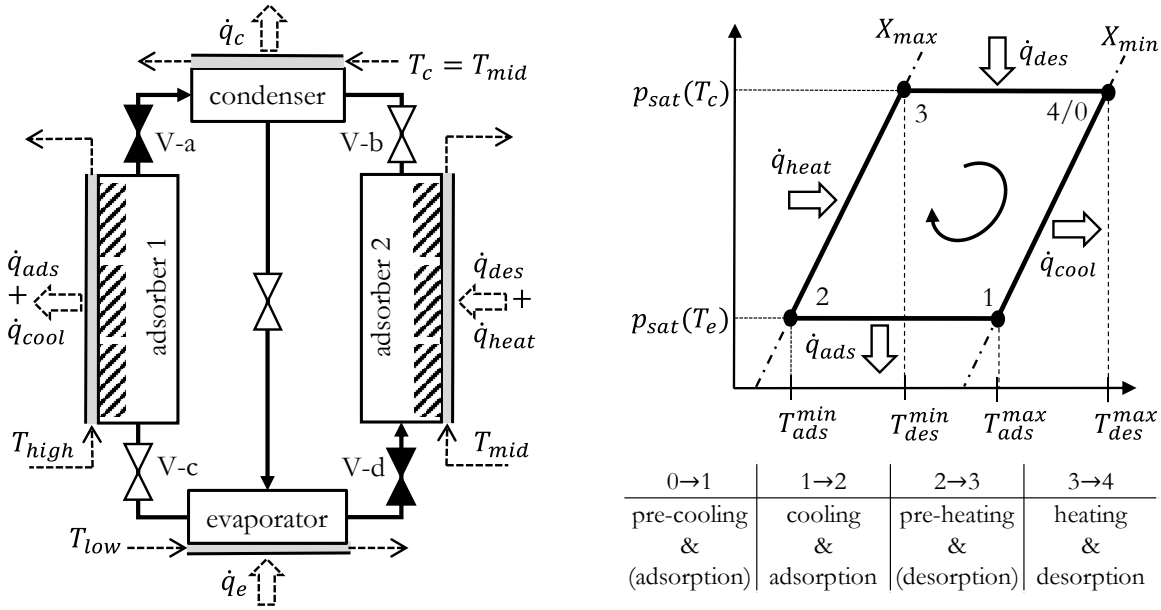

Figure 1-1: On the left: Adsorption chiller with 2 adsorbers, condenser, and evaporator. Heat fluxes transferred via the external system boundaries as well as the corresponding external temperature levels are shown. On the right: States and heat fluxes are shown in a Clausius-Clapeyron diagram.

The cycle starts at point 1 with the evaporation step and the cooling production as soon as the valve V-c between evaporator and adsorber 1 opens. At this point, the adsorbent is already pre-cooled and has the minimum loading X_{min}. For a certain evaporation time (t_e), the adsorber is connected to the evaporator and further cooled, until the adsorption half cycle is terminated and the minimal adsorber temperature T_{ads}^{min} and maximal loading X_{max} are reached at point 2. The heat flux $\dot{q}_{ads}$ leaving adsorber 1 contains sensible heat and latent heat of adsorption. At point 2 valve V-c is closed and the desorption half cycle begins with the pre-heating step by supplying the heat flux $\dot{q}_{heat}$. In this pre-heating step, the sensible masses of the adsorber are heated up along the isostere (constant loading) to T_{des}^{min} for a certain time of t_{heat}. The increase in temperature is accompanied by a decrease in the adsorption potential inducing desorption of refrigerant followed by an increase of the adsorber pressure. As soon as the condenser pressure $p_{sat}(T_c)$ is reached at point 3, the check valve V-a to the condenser opens inducing the isobaric condensation period with a duration t_c, which requires the supply of the heat flux $\dot{q}_{des}$ containing latent and sensible contributions. The desorption step is finished when point 4 is reached and valve V-a is closed. At that point, the adsorption half cycle begins with the pre-cooling step by removing the heat flux $\dot{q}_{cool}$ containing the sensible heat of the passive mass (e.g., heat exchanger, inert additives). The pre-cooling takes place along the isostere with minimal loading and for a duration of t_{cool} until T_{ads}^{max} is reached at point 1. Here, adsorber 1 reaches the initial state as shown in Figure 1-1 and the cycle is completed with a specified cycle time of $t_{cyc} = t_{cool} + t_e + t_{heat} + t_c$. While evaporation and condensation can be specified by the user, the duration of the pre-heating and pre-cooling period depend on the apparatus setup (e.g., gas volume in the adsorber), the mass of adsorbent in the system, the overall kinetics of the system adsorbent – heat exchanger (AdHex) as well as the adjusted evaporation and condensation times. Alternatively, the total adsorption and desorption durations can be user-specified. In this work, the adsorption time t_{ads} is defined as pre-cooling plus evaporation time and the desorption time t_{des} is the pre-heating plus the condensation time. The single process steps and conditions of adsorbers and valves are summarized in Table 1-1.

In technical applications, the adsorbent is temperature-controlled utilizing a heat exchanger (Hex). The interaction of the AdHex is crucial for the performance of adsorption heat pumps. In the simulation studies conducted in this work, stainless steel flat tubes are regarded for the Hex on which adsorbent composites are attached, which is schematically shown in Figure 1-2 on the left. Additionally, the cross-section of a flat tube is shown on the right with adsorbent composites as investigated in this work consisting of primary adsorbent particles.

Table 1-1: Mode of operation and state of components. Regarding the valves, X means closed and O means open.

	adsorber 1	adsorber 2	V-a	V-b	V-c	V-d
Switching	pre-cooling	pre-heating	X	X	X	X
Ads/ Des	cooling	heating	X	O	O	X
Switching	pre-heating	pre-cooling	X	X	X	X
Des/ Ads	heating	cooling	O	X	X	O

The process efficiency and power density of adsorption refrigerators are commonly evaluated with the coefficient of performance (COP) and the (adsorbent mass) specific cooling power (SCP) obtained in one cycle with cycle time t_{cyc}

$$COP = \frac{\int_0^{t_{cyc}} \dot{q}_e dt}{\int_0^{t_{cyc}} (\dot{q}_{heat} + \dot{q}_{des}) dt}, \tag{1-1}$$

$$SCP = \frac{\int_0^{t_{cyc}} \dot{q}_e dt}{m_{comp} t_{cyc}}. \tag{1-2}$$

COP and SCP exhibit a Pareto-optimal behaviour, representing the trade-off between efficiency and power density. If the driving power is available at a low cost (e.g., solar insolation, industrial waste heat), SCP should be preferred as a cost function.

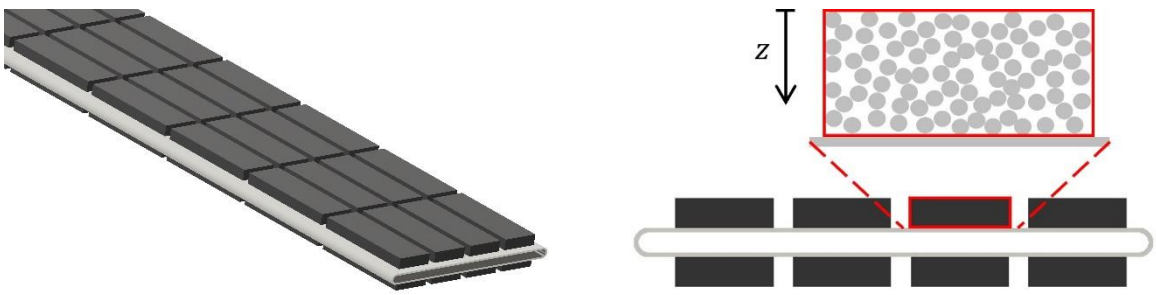

Figure 1-2: Stainless steel flat tube Hex covered with adsorbent composites on both sides.

However, the COP should be maximized if the thermal process efficiency is the decisive parameter. Due to the Pareto optimality, a combined measure of performance is preferable, taking efficiency and power density into account. Concerning the efficiency of adsorption heat pumps, due to the inevitable temperature swing between adsorption and desorption, a high ratio of adsorbent to passive Hex mass is required which can be realized with thick layers of adsorbent. This, however, is accompanied by increased transport paths for heat and mass reducing process kinetics and thus is contradicting the power density. From these considerations, it follows that the heat and mass transfer properties of the adsorbent must be improved without reducing the adsorption capacity to any significant extent. However, these requirements for an optimal adsorbent are contradictory, as the improvement of one parameter is always accompanied by a reduction of another parameter. Therefore, the adsorbent composition, structuring, and layer thickness need to be optimally tailored to the process interconnection, process conditions, and the user specifications requiring a simultaneous investigation of material and process.

A serious disadvantage of solid sorption heat pumps is their low thermal efficiency. Additionally, the low specific power, which leads to large systems, and the comparatively high costs are limiting factors for the further dissemination of this technology [25]. To improve COP and SCP of solid sorption heat pumps, different approaches can be identified which are outlined in the next section.

1.1.1 Potentials for intensification of solid sorption heat pumps

The adsorbent itself, the process interconnection, and heat recovery offer the greatest chances for enhancing adsorption heat pumps. Although these approaches have been known for a long time, they still represent the greatest potential for improvement [25]. The work carried out can be roughly divided into the fields of material development (adsorbents) and process development (optimum parameters, interconnections). The combination of these two efforts is a promising approach for the targeted optimization of solid sorption heat pumps.

In adsorption heat pumps, a high adsorbent mass to passive mass ratio is targeted to reduce the detrimental influence of the thermal swing and therefore to improve the thermal process efficiency. Concerning the flat-tube Hex, this could be achieved with thick layers of adsorbent composites. However, by increasing the layer thickness of composites, the heat and mass transfer resistance increases which lead to low power densities. Therefore, the perfect adsorbent should have a high adsorption capacity, high thermal conductivity as well as high mass transfer capability, enabling thick layers of composites which leads to high thermal efficiencies without

sacrificing power density [4], [26], [27]. However, in technical adsorbents, these requirements are contradicting.

Due to the contradicting nature of the adsorbent characteristics, technical adsorbents are always a compromise, and depending on the structural properties of the porous material, heat and mass transport and capacity are strongly related. Therefore, in recent studies, considerable effort has been devoted to improving the cooling power density by intensifying heat and mass transfer in adsorbents as well as heat transfer resistance between adsorbent and Hex. This can be achieved by using composites of binder, adsorbent, and additives [28], [29], consolidation of the adsorbent [19], [30]–[32], in situ direct synthesis on the Hex, and binder-based coatings [33]. Furthermore, thermal conductivity can be intensified, e.g., by using fin-type heat exchangers, thermally coupled adsorbent beds, foamed adsorbent beds, consolidated adsorbents, and adsorbent coatings [33]. In addition, heat additives can be used to improve the thermal conductivity of consolidated adsorbents [31], [32], [34], [35]. Most recently, homogeneously structured adsorbents (consisting of one material) gain interest, mainly for application in adsorption separation processes [36]–[39]. However, homogeneous structured adsorbents are limited in the free choice of adsorbent materials. Thus, 3D-structured adsorbents (wherein the pure material properties of two or more components are utilized) can overcome this drawback with an almost free choice in the adsorbent material, conductivity structure, and mass transfer paths.

Besides adsorbent-related improvements, novel process interconnections and optimization of process parameters are promising to intensify the performance. Due to the dynamic nature of the sorption heat pumps, the cycle time is a decisive process parameter that needs to be optimized depending on the user requirements. With long cycle times, the adsorbent approaches equilibrium where it is maximally saturated with refrigerant molecules. In equilibrium, the thermal efficiency reaches the maximal value. However, since the uptake kinetic is very slow close to the equilibrium loading, the cooling power decreases with increasing cycle times.

In addition to process parameters, novel process designs are promising aiming to reduce the energy demand and thus to improve the process efficiency. For that, heat and mass recovery can be utilized [40], [41]. For utilizing internal heat recovery, at least two adsorbers or additional heat storage are required. In addition to sensible heat, especially, internal heat regeneration of latent heat of adsorption shows a large potential for improving adsorption heat pumps [42]. Thus, novel designs need to be developed exploiting the full potential of heat recovery concerning sensible as well as latent heat. Multi-bed setups are promising for increasing processes performance by utilizing internal heat regeneration [43]–[45].

1.2 Aim and outline of this work

Over the last decades, numerous studies have focused on the improvement of adsorption cooling machines. However, poor system performance, low efficiency, and comparably high costs are still limiting commercial dissemination [25], [46]. Mostly, the research either focuses on improving the adsorbent material properties, the process parameters, or the process interconnection. By examining material and process separately, identification of an overall optimum is impossible. So far, only a few studies have simultaneously analysed material and process properties, trying to identify optimal structural material properties together with optimal operational parameters and process interconnections to intensify energy efficiency. Therefore, the approach followed in this work is a combined material and process optimization dedicated to the intensification of the thermal efficiency of adsorption refrigerators without sacrificing specific cooling power.

On the material side, for the two-bed process shown in Figure 1-1, the main aim is to achieve the thickest possible composite layers, which is to be achieved by intensifying the heat and mass transfer properties. One approach is an experimental variation of the statistical composite composition (adsorbent, binder, thermal conducting additives) and determination of composition-property correlations. Based on the experimental observations, effective material models are developed. These statistical composites are compared to novel-developed 3D-structured adsorbent composites. The effective material models are the basis for distributed process simulations. In the process simulations, a combined material and process optimization for the classic two-bed process is carried out by varying the material (composition, layer thickness) and process parameters (cycle time). Here, the aim is to identify sets of parameters that optimize the thermal process efficiency regarding prescribed power densities. Additionally, the great potential of 3D-structuring of adsorbent composites is investigated in simulations of the two-bed process. Finally, the internal heat recovery potential is exploited with multi-bed interconnections revealing the high potential of heat regeneration for improving solid sorption heat pumps.

After a literature review of the fundamentals concerning adsorption as well as heat and mass transport in porous media at the beginning of chapter 2, effective material models are developed. In chapter 3, the process models are developed which are parameterized with experiments outlined in chapter 4. Subsequently, the simulations dedicated to the combined optimization of process and material parameters are outlined for the classical two-bed process in chapter 5. Material design is investigated in chapter 6 in experimental and simulation studies. The potential of internal heat recovery is investigated with a novel multi-bed process setup in chapter 7 and chapter 8 summarizes and concludes this thesis.

2. Literature review

Adsorption describes the adhesion of molecules from a fluid phase to a solid surface due to a reduction in the potential energy of the molecule by the existence of a force field at the solid surface [47]. The reverse process is termed desorption. If the adherence takes place by Van der Waals forces, the process is termed physisorption which is reversible, and often multiple layers of molecules are adsorbed. Chemisorption is limited to monolayer coverage, and the forces involved are much stronger than in physisorption. The solid surface is the adsorbent, the fluid phase to be adsorbed is the (ad)sorptive, and the adsorbed phase is termed adsorbate. The ability of technical adsorbents to adsorb molecules to a high amount is based on a large internal surface area due to internal pores. According to the definitions introduced by the International Union of Pure and Applied Chemistry (IUPAC) [48], the pores can be classified into micro-, meso- and macropores as listed in Table 2-1.

Table 2-1: Pore classification based on the IUPAC recommendations [48].

Micropores:	Pore width < 2 nm
Mesopores:	2 nm < Pore width < 50 nm
Macropores:	Pore width > 50 nm

The accessible volume in micropores can be regarded as adsorption space, and, thus, the underlying process is termed micropore (volume) filling compared to surface coverage taking place on the walls of the macro- and mesopores. In microporous solids, the adsorption capacity corresponds to the micropore volume being much larger than the monolayer coverage [47]. During volume or micropore filling, due to the narrow sizes of the micropores, the surface adsorption transitions to volume adsorption due to the overlapping force fields of opposing pore walls. Concerning porous media, defined terminologies are necessary to avoid ambiguity, especially regarding porosities, pores, density, etc. The terminology used in this thesis is taken from the standard literature concerning adsorption [49]. Further informative sources are [50]–[52].

The following section provides a literature review of the relevant physical phenomena for this work concerning adsorption thermodynamic, mass transport as well as heat transport in porous media, and effective parameter models describing adsorbent composites.

2.1 Thermodynamics of Adsorption

2.1.1 Adsorption equilibrium

In the (dynamic) adsorption equilibrium between adsorptive (v) and adsorbed phase (ad), the average molecular flows of the adsorption and desorption process are equal. This state depends on three variables: the partial pressure of the adsorptive in the gas phase, the temperature, and the adsorbed volume (loading of the adsorbent (s)). The loading is defined as the mass ratio of adsorbate to adsorbent in g^{ad}/g^{s}

$$X = \frac{M^{ad}}{M^{s}}, \tag{2-1}$$

or in terms of moles per adsorbent mass in mol^{ad}/kg^{s}

$$q = \frac{N^{ad}}{M^{s}}. \tag{2-2}$$

With temperature, pressure and loading, the equilibrium of adsorption can be described in three ways:

- Adsorption isotherms: constant temperature $T\ (p, X)$
- Adsorption isobars: constant pressure $p\ (T, X)$
- Adsorption isosteres: constant loading $X\ (T, p)$

In equilibrium thermodynamics of pure component adsorption, the adsorbent surface A^{s} is regarded as an inert component assumed to be independent of temperature and pressure. The adsorbate is represented as a separate and single-component phase that is in thermodynamic equilibrium with the adsorptive. According to the condition introduced by Josiah Willard Gibbs (1839 - 1903), the free enthalpy (G) of the total system (here adsorbate + adsorptive phase) must be minimal in equilibrium. Further details of the fundamental thermodynamic relationship between pressure, temperature, and loading can be reviewed in the literature, e.g., in the works of Ruthven [47], [53], Kast [54], Do [55], Rouquerol [49], and [56]. Following, the relevant theory used in this thesis is briefly outlined.

The enthalpy difference of adsorbate and adsorptive is known as the heat of adsorption [53] which is additively composed of the enthalpy of binding ($\Delta_{bind}h$) and the enthalpy of condensation ($-\Delta_{evap}h$)

$$\Delta_{ads}h = h^{ad} - h^{v} = (h^{ad} - h^{l}) - (h^{v} - h^{l}) = \Delta_{bind}h - \Delta_{evap}h. \tag{2-3}$$

Here, the index l denotes a fictitious liquid phase that is in thermodynamic equilibrium with the adsorptive phase. Since this fictitious liquid phase is not affected by the force field of the adsorbent, the enthalpy (h^l) is greater than the adsorbate enthalpy (h^{ad}). The binding enthalpy ($\Delta_{bind}h$) denotes the enthalpy released during the transition from the liquid to the adsorbed state and thus has a negative sign. Since the molecules in the adsorbed state are at a lower energy level than in the gas phase, adsorption is exothermic, and desorption is an endothermic process.

The Clausius-Clapeyron equation for the adsorption equilibrium at constant loading is given by

$$\left(\frac{\partial ln\left(p^v(T,X)\right)}{\partial(-1/T)}\right)_X = -\frac{\Delta_{ads}h(T,X)}{R}. \tag{2-4}$$

With the assumption of a temperature-independent heat of adsorption, integrating equation (2-4) with temperature yields a straight-line equation which states that the isosteres in a Clausius-Clapeyron diagram ($ln(p^v)$ over $-1/T$) are straight lines (see Figure 1-1 on the right)

$$ln\,(p^v) = konst + \frac{\Delta_{ads}h(X)}{RT}. \tag{2-5}$$

The advantage of this graph is that the adsorption enthalpy can be directly determined from the straight-line slope of the respective isostere. Compared to the corresponding vapor pressure curve, the isosteres are steeper because the adsorption enthalpy is greater than the evaporation enthalpy. Another statement can be made about the position of the isosteres. Due to the vapor pressure reduction in the presence of an adsorbent and the resulting lower pressure level than in the imaginary liquid phase, the isosteres are below the vapor pressure curve [56].

The heat of adsorption is a function of the degree of coverage, which is determined by the strong loading dependence of the binding enthalpy. Ruthven [53] gives values of $\Delta_{ads}h \approx 1.5 - 2\Delta_{evap}h$ for a first estimation. While the maximum heat of adsorption is released during the adsorption of the first layers of molecules, adsorption gradually turns into condensation at higher loadings. This provides the basis for the BET theory, which describes multilayer adsorption. Another basic adsorption isotherm is the Langmuir isotherm, which represents the important monomolecular surface coverage. A variety of other statistical, empirical, or physically motivated models are available to describe the thermodynamics of adsorption equilibrium, which will not be discussed in further detail. The adsorption isotherm used in this work was developed by Dubinin based on Polanyi's potential theory, which is presented in the subsequent section.

2.1.2 Adsorption isotherm models

Physisorption isotherm data can classically be assigned to one of the five isotherm types (or an extension of these) shown in Figure 2-1, which are reproduced from [57].

Thommes et al. give a broad explanation of the individual isotherm types. In this work, mainly Type I and Type II isotherms are of interest. Type I(a) isotherms are mainly observed in strictly microporous materials with narrow pore size distribution and Type I(b) isotherms are possible when additionally small mesopores are present. If macropores are also present in the porous media, Type II isotherms can be observed. A sharp change in incline at point B marks the transition from monolayer to multilayer adsorption, whereas an indistinct point B indicates an overlap of monolayer and multilayer adsorption. In all isotherm types, the curves show linear course in the limit of zero loadings at very low relative pressures, which is described by the Henry isotherm.

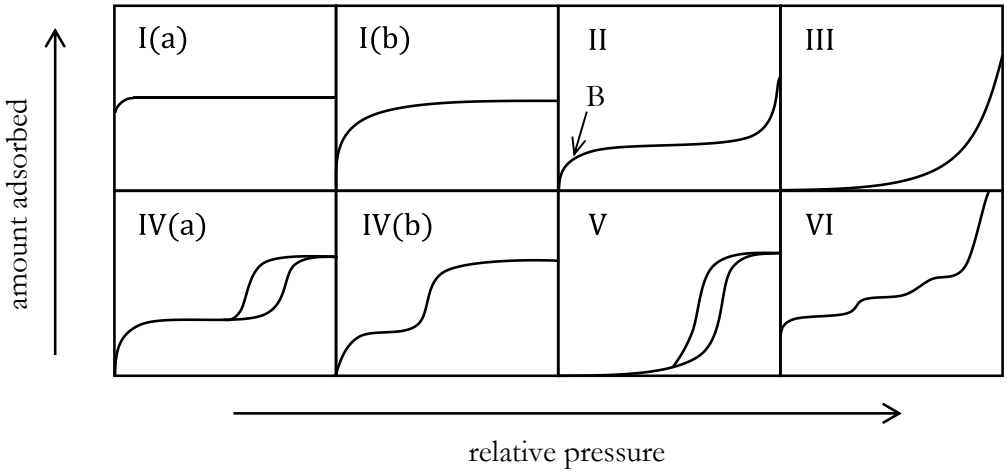

Figure 2-1: Five classic adsorption isotherm types originally presented by Brunauer et al. [58]. An extension of these was given by Thommes et al. [57].

Henry's Law

For physisorption of molecules at very low pressure (no competition for free adsorption sites) on a uniform surface, the surface coverage is sufficiently low that the adsorbed molecules do not interact. This is described by the Henry law which is a simple linear relationship between adsorptive pressure and adsorbent loading [53]

$$q = K'p. \tag{2-6}$$

Therefore, the slope of the isotherm is given by the thermodynamic equilibrium constant for adsorption K' (Henry constant) [59]

$$\lim_{p\to 0}(\partial q/\partial p)_T = K'. \tag{2-7}$$

The temperature dependence of K' follows a van't Hoff expression

$$\frac{dlnK'}{dT} = \frac{\Delta_{ads}h}{RT^2}, \tag{2-8}$$

with the difference in enthalpy $\Delta_{ads}h$ between adsorbate and adsorptive. Integration (and neglecting differences in the heat capacities of the phases [59]) yields

$$K' = K'_\infty e^{-\Delta_{ads}h/(RT)}. \tag{2-9}$$

Due to the exothermic nature of adsorption, K' decreases with temperature. At higher pressures and loadings, interaction of adsorbate molecules occurs, and the equilibrium behaviour deviates from the ideal linear behaviour.

Langmuir isotherm

Langmuir developed his model to describe monolayer adsorption phenomena on a plane, homogeneous surface which was dedicated to describing the adsorption on non-porous surfaces [60]. The main assumptions are: The surface consists of well-defined adsorption sites which can each hold one adsorbed molecule and which are all energetically equivalent; the adsorbed molecules do not interact [61]. The adsorption and desorption rates are given by [53]

$$\begin{aligned}\dot{N}_{ads} &= k_{ads}p(1-\Theta),\\ \dot{N}_{des} &= k_{des}\Theta,\end{aligned} \tag{2-10}$$

with the fractional surface coverage $\Theta = q/q_{sat}$ being the ratio of equilibrium to saturation loading [61]. In the dynamic adsorption equilibrium, the equivalence of adsorption and desorption rates follows to

$$\frac{k_{ads}}{k_{des}}p = \frac{\Theta}{1-\Theta}. \tag{2-11}$$

With the adsorption equilibrium constant $b = k_{ads}/k_{des}$, the Langmuir adsorption isotherm is given

$$\Theta = \frac{q}{q_{sat}} = \frac{bp}{1+bp}. \tag{2-12}$$

q_{sat} and b are the model parameters of the Langmuir isotherm. The saturation capacity represents a fixed number of adsorption sites and is therefore independent of temperature. The equilibrium constant, however, follows a van't Hoff equation [53]

$$b = b_0 e^{-\Delta_{ads}h/(RT)}. \tag{2-13}$$

In the limit of low pressure, the Langmuir isotherm approaches Henry's law with $K' = q_{sat}b$. In the Langmuir model, it is assumed, that the horizontal plateau of Type I isotherms is present due to completed monolayer coverage. However, today it is clear, that the plateau represents the completion of pore filling of micropores instead of monolayer coverage [48] and thus, Langmuir's equations are not applicable on highly microporous adsorbents [62].

Brunauer-Emmet-Teller (BET) method

To describe multilayer adsorption, Brunauer, Emmet, and Teller introduced their BET-isotherm in [63] which is still widely used even though critics raised about the non-physical basis of this isotherm. The BET theory was developed in the 1930s and represents an extension of the Langmuir isotherm to multilayer adsorption [63]. Originally, it was used to describe Type II and IV isotherms, which results in linear BET plots in the suggested range of $\phi = p/p_{sat} = 0.05 - 0.3$ [64]. In a conclusion, the transition from monolayer to multilayer adsorption was localized at the beginning of the middle, linear part of the isotherm (referred to as Point B), where the uptake was in good agreement with the BET monolayer capacity (N_m^{ad} in mol) [62]. N_m^{ad} is the amount needed to cover the adsorbent surface with a monolayer of adsorbate molecules and thus it can be used to identify the specific surface area of a porous material, which is a key parameter to characterize porous materials [53]. The BET method is still standard for the characterization of porous materials based on physisorption measurements [57] and applied in this work in section 4.2. However, especially for microporous adsorbents, its application is questionable since the adsorption mechanism is rather pore-volume filling than multilayer surface adsorption. Then, the surface obtained with the BET method rather represents an apparent or equivalent BET surface area [65]. Sing identifies the difficulties and uncertainties in applying the BET method as follows: Validity of monolayer capacity, heterogeneity of monolayer surface, and failure of assumptions when micropore filling occurs [62]. Despite its limitations, the BET method is widely used and accepted in the characterization of microporous adsorbents (e.g., surface area, micropore volume) [20], [57], when its applicability is checked for. A critical review of the applicability of the BET method on microporous adsorbents and its underlying assumptions is given by Rouquerol et al. [66]. The following assumptions were made in the development of the BET theory [63]:

- Adsorption on an energetically uniform surface of all molecules in the monolayer.

- No steric limitation for the thickness of the adsorption layer.
- One adsorbed molecule provides one adsorption site for a molecule in the next layer.
- Adsorption energy is released when molecules are adsorbed in the first layer whereas liquefaction energy is released when molecules are adsorbed in the upper layers.
- The interaction of molecules in the same layer is negligible.
- The growth of the upper layer begins before the completion of the first layer.

The BET-isotherm in terms of the equivalent adsorbed gas volume $V^{v,ad}$ is given by [53]

$$\frac{V^{v,ad}}{V_m^{v,ad}} = \frac{q}{q_m} = \frac{bp/p_{sat}}{(1-p/p_{sat})(1-p/p_{sat}+bp/p_{sat})}, \tag{2-14}$$

with the equilibrium and saturation pressures p and p_{sat}, respectively, b the BET parameter which is in equivalence to the Langmuir parameter b and $V_m^{v,ad}$ the adsorbed monolayer gas quantity in terms of volume units. The BET parameter b contains information on the shape of the isotherm in the BET range [57]. Most often, the BET isotherm is related to the mass of adsorbent using the specific adsorbed gas volume $v^{v,ad}$ yielding the specific adsorbed monolayer gas quantity $v_m^{v,ad}$ in unit volume per mass. The BET-isotherm can be written in a linear form which gives 'the BET plot'

$$\frac{p/p_{sat}}{v^{v,ad}(1-p/p_{sat})} = \frac{1}{v_m^{v,ad}b} + \frac{b-1}{v_m^{v,ad}b}p/p_{sat}. \tag{2-15}$$

In this form, the two parameters b and $v_m^{v,ad}$ can be obtained from a linear fit, when using relative pressures and adsorbed gas volumes from physisorption experiments. This method is limited to the linear part of the BET plot, which is often in the range of $p/p_{sat} \sim 0.05 - 0.3$ (for Type II and Type IVa isotherms [57]).

From the specific adsorbed monolayer capacity $v_m^{v,ad}$, the specific monolayer surface area (a^s in $m^2 g^{-1}$) can be calculated, when the molecular cross-sectional area occupied by one adsorbate molecule (σ_m in m^2) is known and identical for all adsorbed molecules. Further assumptions are [66]:

- The adsorbed molecules are arranged hexagonal close-packed.
- σ_m can be obtained from the adsorptive density in the bulk liquid state.

Then, with the Avogadro number N_A (in mol^{-1}) or the Loschmidt constant N_L (in m^{-3}), the specific surface area is given by

$$a^s = \frac{v_m^{v,ad} N_A \sigma_m}{v_0} = v_m^{v,ad} N_L \sigma_m. \quad (2\text{-}16)$$

which is an important material parameter in the characterization of porous media. With the mole volume of an ideal gas at norm conditions $v_0 = 0.02241\ m^3 mol^{-1}$. Often, the amount adsorbed to cover the adsorbent with a monolayer of molecules is given in terms of the specific monolayer capacity (n_m^{ad} in $molg^{-1}$)

$$n_m^{ad} = \frac{v_m^{v,ad}}{v_0}. \quad (2\text{-}17)$$

This procedure is commonly applied to evaluate nitrogen physisorption experiments, with $\sigma_{m,N_2} = 0.162nm^2$. It is suited for Type II and IV isotherms even though great caution is needed in the presence of micropores since a distinction of monolayer-multilayer adsorption and micropore volume filling is not possible [57]. Then, the obtained surface area should rather be termed equivalent or apparent BET area [65].

The following recommendations should be considered when applying the BET method on microporous adsorbents, even though they do not necessarily confirm the validity, but still provide reproducible, meaningful, and useful information [57], [66]:

- The BET parameter b should be positive, otherwise, it would be meaningless.
- Selection of appropriate pressure range: The BET method should be used exclusively in the range where the term $V^{v,ad}(1 - p/p_{sat})$ is monotonically increasing with p/p_{sat}.
- The relative pressure $p/p_{sat,m}$ associated with $V_m^{v,ad}$ should be in the selected BET range (the linear range).

Due to the microporous nature of the carbon active materials used in this work, these recommendations are checked for in section 4.2 before applying the BET method on N_2 physisorption experiments.

Polanyi followed another path in his potential theory and introduced the idea of volume filling which is more intuitive than multilayer-surface adsorption concerning micropores with sizes in the range of a few molecule diameters. Based on these ideas, Dubinin and co-workers developed the Dubinin-based adsorption isotherms, which are widely used in characterizing carbon-based adsorbents with predominantly micropores.

Potential theory of Polanyi and Dubinin

Adsorption isotherms considering adsorption as surface layering such as the Langmuir equation or its extensions, consider the adsorbent as inert and its chemical potential as independent of loading. Especially for substances with a high boiling temperature, where the intermolecular forces are in the range of the adsorption forces or when energetically heterogeneous, microporous adsorbents (e.g., activated carbon) are considered, this simplification is no longer valid. Therefore, for microporous adsorbents, where adsorption is rather volume filling than surface adsorption, the adsorbent chemical potential depends on loading, which is considered in Dubinin's isothermal theory [55].

The origins of Dubinin's isothermal theory are based on Polanyi's potential theory [67]. The characteristic variable for adsorption is not the adsorbent inner surface area, but the pore volume available for adsorption. This consideration is particularly useful for very small pores, where it can no longer be assumed that the adsorbent is loaded layer by layer on a surface, and therefore the term micropore volume filling has been introduced [55]. In such pores, the adsorptive molecules are exposed to the superimposed force fields of the adsorbent and thus the forces involved are greater than in the case of surface adsorption. Furthermore, it is assumed that the adsorbate behaves like a liquid. Due to the influence of the adsorbent, the properties of the liquid adsorbate differ from the properties of a theoretical bulk liquid, which is not exposed to the force field of the adsorbent.

Dubinin took a macroscopic approach to illustrate the thermodynamic relationships and defined the adsorption potential A [68]. A describes the potential difference of the free energy between a theoretical bulk liquid and the adsorbate phase. The reference point of the bulk liquid is a liquid that is in equilibrium with the adsorptive phase at the saturation vapor pressure p_{sat} and has the same temperature as the adsorbate

$$A = -\Delta_{bind} g(T,p,X) = \mu^{l}(T,p_{sat}) - \mu^{ad}(T,p,X) = -RTln\left(\frac{p_{sat}}{p}\right). \tag{2-18}$$

The adsorption potential can be interpreted as the isothermal compression work of an ideal adsorbate, which is released during the transition from the saturated vapor pressure $p_{sat}(T)$ of the bulk liquid to the equilibrium pressure p at a given loading and temperature.

The second central quantity in Dubinin's theory is the specific pore volume w in cm^3/g^s describing a volumetric loading

$$w = \frac{V^{ad}}{M} = \frac{X}{\varrho^{ad}(T)}. \tag{2-19}$$

Here, V^{ad} is the adsorbate volume and M the reference mass which can e.g. be the active adsorbent mass or the composite mass. The density of the adsorbate phase $\varrho^{ad}(T)$ can be approximated in the subcritical range with the liquid density [53]. The maximum specific pore volume $w_0 = V_0^{ad}/M$ is assumed to be independent of temperature and is an important parameter in the Dubinin formalism. The maximum loading, however, depends on temperature and can be obtained from the maximum specific pore volume and the adsorbate density

$$X_0(T) = w_0 \varrho^{ad}(T). \tag{2-20}$$

The adsorption equilibrium is thus given by the interaction of the three quantities $w, A,$ and T.

A central assumption in Dubinin's theory is the temperature invariance of the specific pore volume at constant adsorption potential. Thus, it is assumed that the filled pore volume does not explicitly change with temperature

$$\left(\frac{\partial w}{\partial T}\right)_A = 0. \tag{2-21}$$

This assumption is justified with experimental observations, which could be confirmed for a large number of substance pairs (among others [69], [70]), although thermodynamic consistency is not fully present [71]. Ruthven explains why the experimental data can nevertheless be represented very well with the help of a characteristic curve [53] for non-polar systems with the fact that the adsorption energy is applied solely by temperature-independent Van der Waals forces. Furthermore, the entropy fraction of the adsorption potential is negligible. Consequently, there is only an implicit temperature dependence of the pore volume w via the adsorption potential $A(T)$, and the adsorption equilibrium is reduced to a two-dimensional dependence of w and A. This relationship is called the characteristic curve and contains the essential thermodynamic information of the adsorptive – adsorbent pair. For activated carbon adsorbents, the characterization of the adsorption equilibrium by the Dubinin method works well. The equation of the characteristic curve is given as follows [68]

$$w = w_0 exp\left[-\left(\frac{A}{\beta E_0}\right)^2\right]. \tag{2-22}$$

This is the commonly known Dubinin-Radushkevich equation. E_0 has the unit of specific energy and is termed the characteristic adsorption energy. This value depends solely on the properties of the adsorbent and should not be interpreted as the interaction energy between adsorbate and adsorbent. $\beta = E/E_0$ represents an adsorptive-specific constant value, which Dubinin describes as an affinity coefficient [72]. Since Dubinin performed his experiments on the substance pair

activated carbon - benzene, he chose benzene as the reference gas with $\beta(C_6H_6) = 1$. For other gases, β deviates from 1.

A generalization of the Dubinin-Radushkevich approach is the Dubinin-Astakhov approach, in which the quadratic exponent is replaced by an arbitrary exponent n [72]

$$w = w_0 exp\left[-\left(\frac{A}{\beta E_0}\right)^n\right]. \tag{2-23}$$

n take values between 1.5 and 3 for activated carbon and gives information about the homogeneity of the adsorbent. The higher the value of n to characterize the experimental data of an adsorbent, the greater its homogeneity. Replacing the adsorbed pore volume with the loading according to equation (2-19) and the adsorption potential with equation (2-18), the adsorption isotherm can be formulated in a loading-specific manner

$$X(p,T) = w_0 \varrho^{ad}(T) exp\left[-\left(\frac{RTln\left(\frac{p_{sat}}{p}\right)}{E}\right)^n\right]. \tag{2-24}$$

This equation represents the adsorption isotherm used in the present work for describing methanol uptake on carbon active adsorbents.

In the Dubinin formalism, the heat of adsorption follows with the adsorption potential (equations (2-3) and (2-18)) [71]

$$\begin{aligned} \Delta_{ads}h &= \Delta_{bind}h - \Delta_{evap}h = \Delta_{bind}g + T\Delta_{bind}s - \Delta_{evap}h \\ &= -A + T\frac{\partial A}{\partial T}\Big|_X - \Delta_{evap}h = -A + T\alpha\frac{\partial A}{\partial ln(w)}\Big|_T - \Delta_{evap}h, \end{aligned} \tag{2-25}$$

with the thermal expansion coefficient of the adsorbate

$$\alpha = -\frac{1}{\varrho^{ad}}\frac{\partial \varrho^{ad}}{\partial T}. \tag{2-26}$$

The thermal expansion coefficient is small and often neglectable and thus saturation capacity is constant and not affected by temperature [73]. This is the case if the adsorbate density is approximated with the fluid density [74]. If the thermal expansion of the adsorbate is neglected, the heat of adsorption follows to

$$\Delta_{ads}h = -A - \Delta_{evap}h, \tag{2-27}$$

which is the formulation used in this work.

Due to its non-physical asymptotic behaviour and inherent weakness in describing adsorption data in the Henry law region in the limit of low relative pressures, the Dubinin-based adsorption isotherms are of limited value for the application in fundamental studies [47]. However, despite the lack of theoretical validity, the Dubinin-based isotherms are useful semi-empirical correlations of adsorption equilibrium and represent adsorption equilibrium data of alcohols on activated carbons well [69].

2.2 Mass transport in porous media

To model mass transport in packed beds of porous adsorbents viscous and diffusive fluxes need to be considered, depending on the underlying transport regime. The mass transport in the pore system can be divided into different processes, some of which occur in succession and some in parallel [75]:

- Viscous flow (adsorptive phase)
- Knudsen diffusion (adsorptive phase)
- Continuum and free-molecular pore diffusion (adsorptive and adsorbate phase)
- Surface diffusion in the adsorbed monolayer (adsorbate phase)
- Hydrodynamic flow in the adsorbate layers above mono-layer coverage (adsorbate phase)
- Capillary condensate flow

Surface diffusion, hydrodynamic flow, and capillary condensate flow are present in the adsorbate and condensate phase predominantly in the micropores of the adsorbent, and the greater the loading, the greater their contribution to the total transport. However, since adsorption predominantly takes place in the micropores of the primary particles, a contribution to the total flux in consolidated adsorbents or packed adsorbent beds by adsorbate or condensate transport would require mass transport between adjacent particles. Therefore, in highly dynamic, technical gas-phase adsorption processes, the transport processes in the adsorbate and condensate phases are often neglected [76]. Furthermore, in pure-substance systems, no free diffusion occurs and thus, the total mass transfer occurs in the adsorptive phase.

To model mass transport in the adsorptive phase, the Dusty gas model (DGM) can be used, containing viscous flow, the Knudsen diffusion, and free pore diffusion [77]. The different transport phenomena are treated individually and summarized to an effective transport parameter which can be used to model the spatially distributed mass transport in porous media (at least one-dimensional). Mason et al. [77] interpreted the combined modes of transport with an electrical analogy, which should just be a “mnemonic device” for interpreting the combined fluxes in the

DGM. Diffusive fluxes combine in series to an effective diffusion flux, in analogy to resistors. The total diffusive flux then combines in parallel with other fluxes (viscous flux, surface flux), in analogy to electrical current as shown in Figure 2-2.

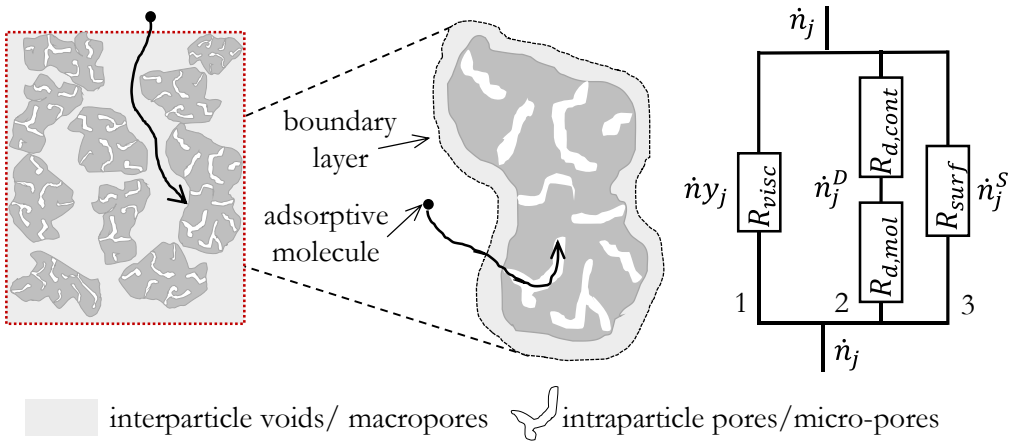

Figure 2-2: Macroporous adsorbent bed with interparticle voids and microporous primary particles as well as electrical analogue resistant circuit combining different mass transport phenomena. Adsorptive molecules are transported by a combination of viscous flux (1) and diffusive flux (2, continuum, free-molecule, and Knudsen) in the voids and by diffusive as well as surface flux (3) in the primary particles. The diffusive fluxes add up in series to the total diffusive flux which itself adds up in parallel with viscous and surface flux.

In contrast to spatially resolved models, in a lumped parameter approach the entire transport resistance is transferred to a fictitious boundary layer, which is assigned a fictitious resistance parameter. In such models, the entire mass transport resistance of a porous medium is described using effective driving force approaches where the overall coefficient for the transport resistance scales with the driving force. Most often, the loading or concentration difference between equilibrium and actual conditions is used as the driving force. The model parameters are obtained by fitting the simulations to experimental data or by using a model approach, e.g., an LDF approach (Linear Driving Force).

In this work, a spatially distributed and lumped parameter approach are combined to model the mass transport in consolidated adsorbent composites as shown in Figure 2-3. In detail, the transport of adsorptive molecules in the interparticle voids is spatially resolved and takes place by a superposition of viscous flow and Knudsen-diffusion. The overall intraparticle transport resistance in the micropores of the primary adsorbent particles is transferred in the particle's boundary layer using the LDF approach. Thus, the intraparticle transport is not resolved spatially.

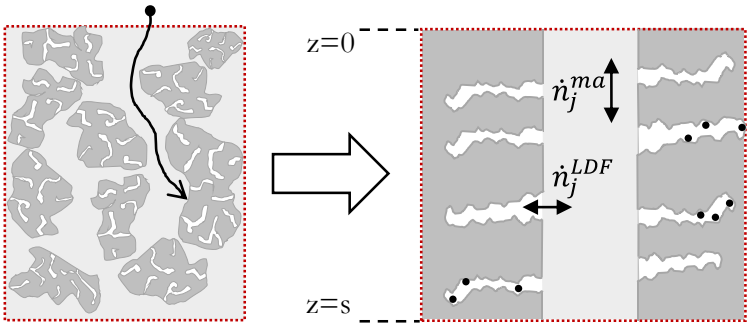

Figure 2-3: Modelling approach for mass transfer in the consolidated adsorbent composites. Transport in the interparticle voids is spatially resolved and modelled with the Dusty-Gas-Model. The transport resistance in the intraparticle adsorbent pores is summarized in the LDF approach.

The total flux of a component j in $mol_j/m^2/s$ is given by a superimposition of the individual transport phenomena

$$\dot{n}_j = \underbrace{\dot{n}y_j}_{viscous\ flow} + \underbrace{\dot{n}_j^D}_{diffusive\ transport} + \underbrace{\dot{n}_j^S}_{surface-diffusion}. \tag{2-28}$$

Due to the bimodal pore size distribution of the investigated consolidated composites (macro- and micropores), different transport phenomena need to be considered. Viscous flow and Knudsen diffusion contribute to the interparticle void transport

$$\dot{n}_j^{ma} = \dot{n}y_j + \dot{n}_j^{Kn,ma}, \tag{2-29}$$

and in the micropores of the adsorbent particles, the pore width is narrow, so that transport is either dominated by adsorptive molecule – pore wall interactions or by transport in the adsorbed phase, which is summarized in the LDF approach

$$\dot{n}_j^{LDF} = \dot{n}_j^{mi} = \dot{n}_j^{Kn,mi} + \dot{n}_j^S. \tag{2-30}$$

Subsequently, the different transport phenomena are briefly introduced and discussed, concerning transport in porous media.

2.2.1 Continuum, viscous flow in porous media

Viscous flow occurs in the continuum regime where the molecule-molecule interactions predominate and thus the flow is driven by a pressure gradient [77]. In pressure-driven, laminar flow of a fluid in a pore or a porous media, the pressure drop due to fluid friction with the

surrounding solid matrix is predominant and dominates all other forces in the Navier-Stokes equations. This flow can be described with Darcy's law, which was empirically motivated and originally published in 1856 [78]. Even though Darcy originally studied the flow of water in a bed of sand, it is equally valid for gas flows. Formally, it can be derived by volume averaging of the Navier-Stokes equation [79], [80]. Neglecting gravity, the viscous flux of the gas phase in a porous media driven by the pressure gradient ∇p^g can be described according to Darcy's law [81], [82]

$$\dot{n} = -\frac{B_0}{\eta}\frac{p^g}{RT}\nabla p^g, \tag{2-31}$$

where $\eta(T)$ is the dynamic viscosity. The structural parameter B_0 is termed permeability. For laminar flow through a circular capillary with a diameter d_p the permeability is [83]

$$B_0 = \frac{d_p^2}{32}, \tag{2-32}$$

known as Hagen-Poiseuille law. (Remark: The gradient ∇ in equation (2-31) is related to the inner dimension of the transport pores which are not straight but rather tortuous. To relate it to the outer dimension of the consolidated adsorbent composite, it needs to be scaled with the tortuosity-factor; see equation (A-36)).

2.2.2 Knudsen flow in porous media

Knudsen diffusion occurs in the transition flow regime when the mean free path λ_j of a molecule is significantly larger than the width of the corresponding transport pore d_p, which is quantified by the Knudsen number

$$Kn = \lambda_j/d_p >> 1. \tag{2-33}$$

The mean free path is the average distance a molecule travels between two impacts and can be calculated from the kinetic theory of gases

$$\lambda_j = \frac{MW/N_A}{\sqrt{2}\pi\sigma^2\varrho} = \frac{M}{\sqrt{2}\pi\sigma^2\varrho}, \tag{2-34}$$

with σ the collision diameter, MW the molecular mass, N_A the Avogadro number, ϱ the mass density, and M the mass of the molecule [84], [85]. The Knudsen number is generally used to categorize the flow regime as shown in Table 2-2.

Table 2-2: Regimes of gas flow in porous media categorized with the Knudsen number [85].

Continuum regime	0	$< Kn <$	10^{-2}
Slip flow	10^{-2}	$< Kn <$	10^{-1}
Transition regime	10^{-1}	$< Kn <$	10
Free-molecule flow	10	$< Kn <$	∞

Mason et al. [77] provided a fundamental work concerning flow regimes in porous media. The following abstract is reproduced from their publication.

Knudsen diffusion occurs when molecules move entirely independently of each other. This has intensively been studied by Knudsen considering a very thin plate with a small hole. The number of molecules passing through the hole in one second in $[molecules/cm^2/s]$ can be described as follows

$$\dot{n}_N^{Kn} = w n_N \overline{v}, \tag{2-35}$$

with the gas number density n_N in $molecules/cm^3$, and w a dimensionless probability factor. For an infinitesimal thin plate with a very small hole, $w = 1/4$. For a long straight circular tube of radius r and length L, w gets $(2/3)(r/L)$. $\overline{v}$ is the mean molecular velocity

$$\overline{v} = \left(8 k_B \frac{T}{\pi MW}\right)^{1/2}, \tag{2-36}$$

with k_B the Boltzmann constant and T the absolute temperature. If gas is present at both sides of the hole, the flux of molecules is proportional to the gradient of the gas number density ∇n_N between both sides and the Knudsen-diffusion coefficient D^{Kn} in cm^2/s

$$\dot{n}_N^{Kn} = -D^{Kn} \nabla n_N. \tag{2-37}$$

By comparing equations (2-37) and (2-35), the proportionality of D^{Kn} to $\overline{v}$ becomes apparent. This proportionality can be made explicit for a long, straight, cylindrical pore of radius r and with equation (2-36), the Knudsen-diffusion coefficient follows

$$D^{Kn} = \frac{4}{3}\frac{r}{2}\overline{v} = \frac{4}{3}\frac{r}{2}\left(8 k_B \frac{T}{\pi MW}\right)^{1/2}. \tag{2-38}$$

With the Avogadro-constant N_A, the gas number density in equation (2-37) can be expressed as mole density or concentration in mol/cm^3

$$c = \frac{n_N}{N_A}. \tag{2-39}$$

In terms of $mol_j/cm^2/s$, the Knudsen-diffusion flux of a molecule species j can be expressed with the concentration

$$\dot{n}_j^{Kn} = -D_j^{Kn} \nabla c_j \tag{2-40}$$

and the Knudsen-diffusion coefficient with the universal gas-constant $R = N_A k_B$

$$D_j^{Kn} = \frac{d_p}{3}\left(8R\frac{T}{\pi MW_j}\right)^{1/2}. \tag{2-41}$$

It is noteworthy, that the Knudsen-diffusion coefficient proportionally scales with $T^{1/2}$, which can be used to verify gas flow measurements of a single component gas through a porous medium. In addition, Graham's law [86]–[88] can be derived when assuming isothermal, isobaric conditions on both sides of the hole with two different gases with different molecular masses. Then, equations (2-41) and (2-40) result in the correlations

$$-\frac{\dot{n}_1^{Kn}}{\dot{n}_2^{Kn}} = \frac{D_1^{Kn}}{D_2^{Kn}} = \left(\frac{MW_2}{MW_1}\right)^{1/2}, \tag{2-42}$$

which can also be used to compare Knudsen-diffusion coefficients obtained with gas flow measurements of single-component gases through the same porous medium.

2.2.3 Surface diffusion

The transport of molecules in the monolayer of the adsorbed phase is called surface diffusion and combines additively with the viscous flow and gas-phase diffusion. It mainly occurs in the micropores of adsorbent particles, where all molecules are exposed to the force field of the adsorbent, and it is negligible in macropores. The surface diffusion flux of a single species can be formulated in form of a Fickian equation [77], [83], [89]

$$\dot{n}^S = -D^S \nabla c^{ad}, \tag{2-43}$$

with $\dot{n}^S$ the surface flux in mol per cross-sectional area adsorbate, D^S the surface diffusion coefficient in m^2/s related to the concentration of the adsorbed species c^{ad}. D^S is often termed corrected diffusivity, composed of surface diffusivity at zero coverage D_0^S multiplied with a thermodynamic correction factor (Darken factor) containing the intraparticle adsorptive concentration c^v and adsorbate concentration c^{ad} in mol/m_p^3 [90], [91]

$$D^S = D_0^S \underbrace{\frac{c^{ad}/c^v}{\left(\frac{\partial c^{ad}}{\partial c^v}\right)_T}}_{Darken-factor}. \tag{2-44}$$

The Darken expression describes the dependence of adsorbed amount on the surface diffusivity and states, that the surface diffusivity at any loading is equal to the value at zero loading D_0^S multiplied by a thermodynamic factor [55]. Application of the corrected diffusivity requires knowledge of the adsorption isotherm. Mostly, the Darken-factor is given in terms of the derivative of the logarithms [75], [89], [91]

$$\left(\frac{\partial lnc^v}{\partial lnc^{ad}}\right)_T = \left(\frac{\partial c^v}{\partial c^{ad}}\right)_T \frac{c^{ad}}{c^v}. \tag{2-45}$$

For almost all isotherms (except Henry isotherm), the thermodynamic factor increases with loading, and thus D^S increases with loading (if D_0^S is constant). This model is widely used, even though it overestimates the surface flux and underestimates the gas flux due to a neglection of the path: desorption – gas diffusion – adsorption [92].

2.2.4 Linear-driving force approach

The linear driving force (LDF) model introduced by Glueckauf in 1955 [93] is a frequently used approach to model the effective mass transport in porous media. The overall transport resistance is transferred into a theoretical boundary layer with an effective transport coefficient k_{LDF} [94], which results in a significant reduction in simulation time due to dimensional reduction of the transport equation [95]. For the driving force often the difference between averaged loading and the equilibrium loading at bulk conditions is used. Even though strong simplifications are made in the derivation, the LDF approach is well suited to describe the kinetics in adsorption processes [96]. Formally, it can be derived from the mole balance of the pores (in mol/m_p^3) of a spherical adsorbent particle with radius R_{par} with the intraparticle adsorptive concentration c^v and adsorbate concentration c^{ad} [97], [98]

$$\nabla \cdot \dot{n}^{mi} = -\frac{\partial (c^v + c^{ad})}{\partial t}. \tag{2-46}$$

A detailed derivation of the LDF approach and the application on the DA-adsorption isotherm is outlined in Appendix A.1.

In the classic LDF approach for a spherical particle with a parabolic loading profile presented by Glueckauf, the loading difference between equilibrium loading at bulk conditions and average loading in the adsorbent is used as driving force

$$\frac{\partial \bar{X}}{\partial t} = \frac{15 D^{eff,mi}}{R_{par}^2} \left(X^{eq}\left(c^{v,bulk}, T\right) - \bar{X}\right), \tag{2-47}$$

with the LDF-factor

$$k_{ldf} = \frac{15 D^{eff,mi}}{R_{par}^2}. \tag{2-48}$$

The effective micropore diffusion coefficient $D^{eff,mi}$ is a superposition of adsorptive and adsorbate diffusivity and depends on the spatial loading distribution in the adsorbent particles. However, since the determination of micropore diffusion coefficients is not the aim of this work, for simplification the intraparticle transport is supposed to be of a solely gaseous diffusive nature. For a single-component gas, the transport in the adsorptive phase can thus be formulated with the Knudsen-diffusion coefficient

$$D^{eff,mi} \approx D^{v} = D^{Kn,mi}, \tag{2-49}$$

with the Knudsen diffusion coefficient defined in equation (2-41).

2.2.5 Generalized Maxwell-Stefan Diffusion and Dusty-Gas Model

In the following the Dusty-Gas Model (DGM) for a single-component gas is introduced based on the work of Krishna and Wesselingh [83] beginning with the generalized Stefan-Maxwell multi-component transport approach. The DGM was developed by Evans, Mason, and co-workers in the early 1960s [77], [81], [99] and serves as a formalization of the coupling of convection and diffusion mechanisms. Besides continuum diffusion and viscous flow, it also considers the molecule-pore wall interactions where the solid particles are treated as a fixed component of the gas mixture (Knudsen diffusion). In a single-component gas, the solid particles are treated as the second component. The DGM is well suited to describe the effective mass transport of adsorptive in packed beds of adsorbent particles, adsorbent composites, and adsorbent primary particles. In the DGM, the question of pore geometries is avoided until it can be handled separately, which is a huge advantage and underlines the generality of the DGM. The mass flux $\dot{m}$ of a single-component gas in a porous medium can be written according to the DGM as follows

$$\dot{m} = -\frac{MW\,\varepsilon^{ma}}{RT}\left(\frac{D^{Kn}}{\tau} + \frac{B_0 p}{\tau\eta}\right)\frac{dp}{dz}. \tag{2-50}$$

A derivation of the DGM is outlined in Appendix A.2.

In addition to mass transport, the energy transport in porous media plays a decisive role in describing technical adsorption processes. Besides convectively transported energy, the effective thermal conductivity of an adsorbent bed or composite is crucial for energy transport.

2.3 Thermal conductivity in porous media

In thermal swing adsorption processes, the overall heat transfer resistance in the adsorber is crucial. In recent years, many studies have emphasized the resistances between the heat transfer medium and the adsorbent as well as the effective thermal conductivity of the adsorbent bed as limiting variables in adsorption refrigeration [100]. The first resistance is not investigated in this work but can be reduced e.g., by direct crystallization of the adsorbent onto the heat exchanger [33], coating the heat exchanger with adsorbent utilizing a binder, or by direct adsorbent deposition over metallic foams [101]. However, the focus in this work lies in the description and reduction of the second resistance, the resistance due to the poor effective thermal conductivity of adsorbent composites.

The effective conductive heat flux in Watt per cross-sectional area of composite is modelled with Fourier's law with the temperature gradient as the driving force [102]

$$\dot{q}^{\,eff} = -\lambda^{eff}\nabla T. \tag{2-51}$$

The description of the effective thermal conductivity of a porous medium λ^{eff} consisting of two or more phases requires sufficient models including the thermal conductivities of the pure components, their volume concentrations (porosities) and shapes as well as the distribution of the phases in the composite. Five basic structural models are existent on which most analytical models for describing effective thermal conductivities are based; the Parallel, Series, Maxwell-Eucken 1&2, and the Effective Medium Theory (EMT) models [103], [104].

Due to the high porosity of technical adsorbents, the cross-sectional area for heat flux is limited resulting in low thermal conductivities, especially for beds of loose grains. The main contribution of heat conduction in porous media is along the solid adsorbent paths. Besides, at sufficiently high rates of loading, the contribution of the adsorbate phase can be of relevant order of magnitude requiring a combined formulation. Furthermore, heat is transferred via thermal conduction in the adsorptive phase. However, when the process pressure regime is low, thermal

conductivity in the adsorptive may be negligible low [55]. For the determination of the effective transport properties of heterogeneous systems containing multiple constituents, sufficient model approaches are required. Subsequently, a short literature overview of common approaches applied in adsorption heat transformation technology is given followed by the introduction of a very simple model containing parallel and serial phases. Subsequently, the idea of effective medium approximations is discussed.

Loose beds of spherical silica-gel adsorbents were investigated [12], [105], where the adsorbent particles effective thermal conductivity $\tilde{\lambda}^{s+ad}$ was formulated by additively summing up the single contributions of adsorbent and adsorbate

$$\tilde{\lambda}^{s+ad} = \tilde{\lambda}^{s} + X\lambda^{ad}(T). \tag{2-52}$$

In this formulation, the thermal conductivity of the adsorptive in the interparticle voids is supposed to be negligibly small, $\tilde{\lambda}^{s}$ is the apparent thermal conductivity of the adsorbent particles (intraparticle porosity included) at zero loadings, and λ^{ad} is the adsorbate thermal conductivity. Cacciola et al. [28] assumed a parallel, percolating adsorbent phase and used intraparticle- ($\varepsilon^{mi} \equiv \varepsilon_{p,comp}$) and void- ($\varepsilon^{ma}$) porosities to corelate the individual thermal conductivities with the effective thermal conductivity of composite carbon bricks. Dawoud et al. [9] studied the effective thermal conductivities of wetted zeolite (4A zeolite with water) and came up with a validated, theoretical model which uses an extended formulation of equation (2-52). In that formulation, the temperature dependency of the adsorbent and the thermal conductivity of the adsorptive (λ^{v}) are considered.

Woodside and Messmer [106] used a model containing parallel and serially aligned phases to the heat flux direction to describe the effective thermal conductivity of a porous medium saturated with a fluid phase. Applying this model concept to composite adsorbents consisting of micro-porous adsorbent particles, heat conductive additive, adsorbate, and adsorptive, the model sketch in Figure 2-4 (left) can be developed. This model sketch is simplified and is only applicable if the heat conductive additive phase is percolating. For a non-percolating, randomly distributed heat additive, the description of the effective thermal conductivity gets more complicated [32], and the application of effective medium approximations is required. In the simplified model sketch in Figure 2-4 (left), heat conductive additive, solid adsorbent, and intraparticle macropores (void adsorptive) are considered as parallel aligned phases, while adsorbate and fractions of adsorbent and adsorptive are oriented in series to the heat flux direction. In analogy to the mass transport in porous media, a resistance circuit diagram for the thermal conductivity can be developed as shown in Figure 2-4 on the right.

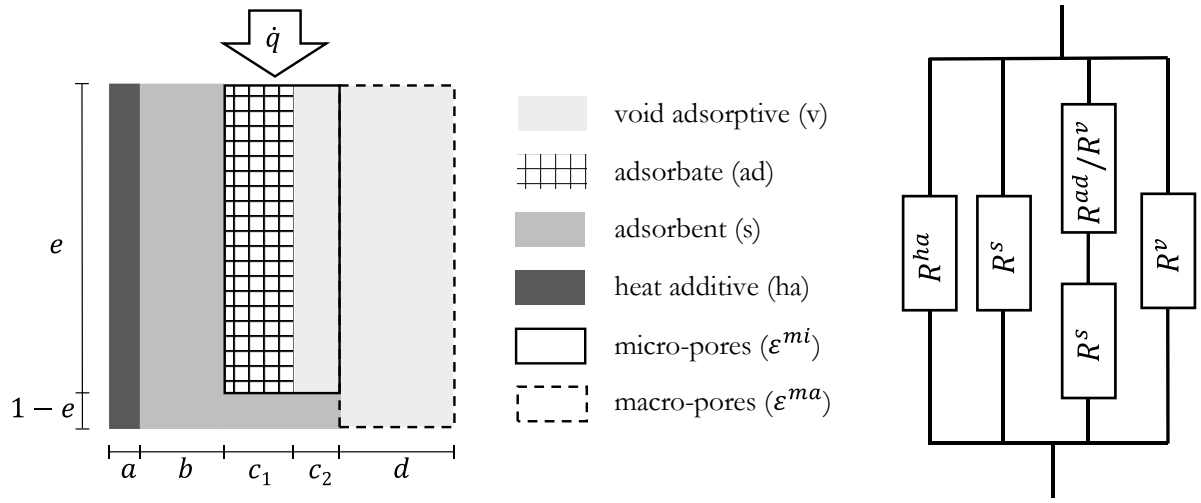

Figure 2-4: Model sketch with phases aligned in series or parallel to the heat flux direction and contributing with arithmetic or harmonic mean to the effective thermal conductivity (left) as well as electric analog resistance circuit diagram (right). The lengths specifications are given in relative values: $1 = a + b + c_1 + c_2 + d$.

The serially arranged phases are described with a weighted harmonic mean of the individual thermal conductivities involved, whereas the phases arranged in parallel are described with the weighted arithmetic mean. Therefore, the effective thermal conductivity can be formulated as

$$\lambda^{eff} = \underbrace{a\lambda^{ha} + b\lambda^{s} + d\lambda^{v}}_{parallel\ contributions} + \underbrace{c_1 \frac{\lambda^{s}\lambda^{ad}}{e\lambda^{s} + (1-e)\lambda^{ad}} + c_2 \frac{\lambda^{s}\lambda^{v}}{e\lambda^{s} + (1-e)\lambda^{v}}}_{contributions\ in\ series}. \tag{2-53}$$

Since the thermal conductivity of the gas phase is often significantly lower than the other contributions, in literature the terms concerning adsorptive are often neglected. This is a valid assumption for the adsorptive (low-pressure methanol vapour) regarded in this work (e.g., $\lambda^{v}_{CH_3OH}(T = 298K) = 0{,}0157\ W/m/K$ [107]). Therefore, equation (2-53) can be reduced to

$$\lambda^{eff} = a\lambda^{ha} + b\lambda^{s} + c_1 \frac{\lambda^{s}\lambda^{ad}}{e\lambda^{s} + (1-e)\lambda^{ad}}. \tag{2-54}$$

While the relative lengths perpendicular to the heat flux (a, b) can be correlated to geometrical parameters which are experimentally accessible, this is not applicable for the length e being a measure of the serial contributions. Instead of geometrically weighting the serial fraction of adsorbate, the mass loading X can be used as a weighting factor [9], [12], [105], which is physically plausible. The more micropores are filled with adsorbate, the higher the loading X and

thus, the contribution to thermal conductivity by the adsorbed phase. Applying this simplification, equation (2-54) reduces to

$$\lambda^{eff} = a\lambda^{ha} + b\lambda^{s} + X\lambda^{ad}. \tag{2-55}$$

If a three-dimensional composite with a constant cross-sectional area is considered, volume fractions instead of relative lengths can be used

$$1 = a + b + c_1 + c_2 + d \equiv \varepsilon^{ha} + \underbrace{\varepsilon^{s} + \varepsilon^{mi}}_{\tilde{\varepsilon}^{s}} + \varepsilon^{ma}, \tag{2-56}$$

with the volume fractions of heat additive ε^{ha}, solid adsorbent skeleton ε^{s}, micropores ε^{mi} and macropores ε^{ma}, respectively. Instead of λ^{s}, the thermal conductivity of the dry adsorbent particle $\tilde{\lambda}^{s}$ (interparticle porosity included) can be used corresponding to the particles apparent volume fraction $\tilde{\varepsilon}^{s}$. With these considerations, equation (2-55) follows to

$$\lambda^{eff} = \varepsilon^{ha}\lambda^{ha} + \varepsilon^{s}\lambda^{s} + X\lambda^{ad} \equiv \varepsilon^{ha}\lambda^{ha} + \tilde{\varepsilon}^{s}\tilde{\lambda}^{s} + X\lambda^{ad}. \tag{2-57}$$

The method of serial and parallel aligned phases can also be applied to a sub-system of the composites. Therefore, without taking the macropores into account, the combined thermal conductivity of adsorbate, adsorbent, and heat additive can be formulated to

$$\tilde{\lambda}^{ad+s+ha} = \frac{\varepsilon^{ha}}{\tilde{\varepsilon}^{s} + \varepsilon^{ha}}\lambda^{ha} + \frac{\tilde{\varepsilon}^{s}}{\tilde{\varepsilon}^{s} + \varepsilon^{ha}}\left(\tilde{\lambda}^{s} + \frac{X\lambda^{ad}}{\tilde{\varepsilon}^{s}}\right). \tag{2-58}$$

By combining equations (2-56) and (2-58) and comparing this with equation (2-57), the following relation can be identified

$$\lambda^{eff} = (1 - \varepsilon^{ma})\tilde{\lambda}^{s+ad+ha}. \tag{2-59}$$

The model concept of treating thermal conductivity of parallel phases weighted by their volume fraction in analogy to parallel resistors, has been widely used and experimentally validated. This approach is adapted to formulate a model for effective thermal conductivity used in this work, based on equation (2-57). However, this formulation is only valid for linear, percolating phases. For composites with statistically distributed particles of heat additive as regarded in this work, this model is not appropriate which requires more complex approaches from effective medium theory. Independent of the model used, increasing the thermal conductivity of adsorbents and adsorbent composites is crucial to improving the process performance of adsorption heat pumps.

The effective thermal conductivity of a loose bed of adsorbent particles can be increased by compaction [19], [108]–[110], however, with a detrimental effect on permeability. Furthermore,

heat-conducting additives can be added to the adsorbent grains. For different adsorbents, effective thermal conductivity was increased by using graphite flakes [19], [32], [108], metallic additive [100], or boron nitride [34]. Regarding this method, three related problems can be identified. First, the adsorption capacity of the composites is reduced by the addition of inert additives. Second, the additives are usually mixed in such a way that they are statistically distributed in the composite. By that, the effective thermal conductivity is only slightly increased as long as the volume fractions of the additives are too small to reach the percolation threshold. Third, if the additives are smaller than the adsorbent particles, the interparticle voids are filled increasing the bulk density and reducing the permeability. Aiming to describe and optimize the composition of consolidated composites containing adsorbent particles and additives, more sophisticated approaches are required.

2.3.1 Effective medium theory

In addition to mass transport, energy transport in porous media is elementary and, however, incomparably more difficult to describe for heterogeneous, anisotropic media. Especially for multi constituent materials with different pure material heat conductivities, random distribution and volume fractions of the single phases, a complete description of heat conduction through such a network is very complicated [102]. Regarding a system with multiple constituent phases as quasi-homogeneous and determination of an averaged or rather effective thermal conductivity is thus simplifying the system. Numerous approaches have been developed to describe effective transport properties of heterogeneous media by assuming the medium to be macroscopically homogeneous. A comprehensive review of models from the effective medium theory (EMT) is given by Pietrak et al. [103]. Often, these EMT approximations are unable to correctly predict properties of heterogeneous material beyond the percolation threshold. In a quasi-homogeneous or effective medium, temperature and heat flux can be interpreted as averaged values over the system volume. Heterogeneities need to be small compared to the size of the quasi-homogeneous system, which itself needs to be small compared to the overall dimension of the conducting system.

This section gives a brief overview of the simplest and most common effective medium models for the determination of effective thermal conductivity of heterogeneous media. The general idea behind the effective medium theory is to consider multiphase systems as quasi-homogeneous with effective transport characteristics, e.g., effective thermal conductivity λ^{eff}. Among other things, these transport characteristics depend on the volume concentrations and shapes as well as transport properties of the pure-component phases. Major attempts describing the effective

electrical conductivity of heterogeneous systems were conducted by Maxwell in the 19th century[1]. Mathematically, thermal conductivity can be treated in analogy to electrical conductivity [103]. The same dependencies are present when determining electrical conductivities, diffusion coefficients, or permeabilities [106]. For small volume fractions ε_b (below about 25% [103]) of non-percolating, non-interacting solid spheres with conductivity λ_b embedded in a second continuous solid phase with conductivity λ_a, Maxwell provided the following relation

$$\frac{\lambda^{eff}}{\lambda_a} = 1 + \frac{3\varepsilon_b}{\left(\frac{\lambda_b + 2\lambda_a}{\lambda_b - \lambda_a}\right) - \varepsilon_b}. \tag{2-60}$$

Equation (2-60) is a simple correlation for the determination of the effective thermal conductivity of a heterogeneous two-component system, where the volume fraction of the diluted phase is far beyond the percolation threshold. However, Maxwell's approach neglects any interfacial resistance between the two phases. In composite materials, the interfacial transport resistance can arise from poor chemical or mechanical adhesion at the interface and different physical properties of the constituents (different thermal expansion parameters). The latter one is known as Kapitza resistance R_K, discovered by Kapitza who investigating temperature discontinuities at the interface between constituent phases [111]. The interfacial thermal resistance is dramatically influencing the effective thermal conductivity of composites [112], especially with decreasing particle sizes and thus increasing the area of interfacial contact related to the volume of the composite [103]. In the presence of interfacial resistance to heat transfer, the temperature profile experiences a discontinuity across the interface between the two phases proportional to the heat flux. Taking the dimensionless Kapitza resistance N_{Ka} into account, Oettinger obtained a modified Maxwell equation [113]

$$\frac{\lambda^{eff}}{\lambda_a} = 1 + \frac{3\left(\frac{\lambda_b}{\lambda_a} - 1\right)\varepsilon_b}{2 + \frac{\lambda_b}{\lambda_a}(1 + 2N_{Ka})}. \tag{2-61}$$

In the limit of $N_{Ka} = 0$, equation (2-61) converges to equation (2-60). An extension of the Maxwell model is the Maxwell-Eucken formulation [104], [114] considering one phase dispersed

[1] J. C. Maxwell, *A Treatise on Electricity and Magnetism*, Oxford University Press, 3rd edition (1891, reprinted 1998), Vol. 1

(index b) in a continuous phase (index a). In that formulation, the effective thermal conductivity is given as follows

$$\lambda^{eff} = \frac{\lambda_a \varepsilon_a + \lambda_b \varepsilon_b \frac{3\lambda_a}{2\lambda_a + \lambda_b}}{\varepsilon_a + \varepsilon_b \frac{3\lambda_a}{2\lambda_a + \lambda_b}}. \tag{2-62}$$

Finally, in the EMT model, a random distribution of the two components is assumed. In the EMT model, the effective thermal conductivity is given as follows [104]

$$0 = \varepsilon_a \frac{\lambda_a - \lambda^{eff}}{\lambda_a + 2\lambda^{eff}} + \varepsilon_b \frac{\lambda_b - \lambda^{eff}}{\lambda_b + 2\lambda^{eff}}. \tag{2-63}$$

In adsorption heat transformation technology, often consolidated composite types are used consisting of adsorbent particles, binder, and heat conducting additives. The components form a complex heterogenous network with interparticle voids required for mass transport. The description of effective thermal conductivities of such multi-component composites is very complex and often not possible since an exact distribution of the components is not known. However, the previously introduced model approaches can be applied to develop models for the determination of effective thermal conductivities of composites. Nevertheless, for exact determination, visualization techniques and/ or experimental investigations are necessary.

As shown and pointed out by Wang et al. [104], a combination of each of the beforementioned model approaches can be used to describe the effective thermal conductivity of composite materials. Therefore, a composite containing a dispersed heat additive phase in a continuous phase of adsorbent primary particles and void space can be described in a two-step approach. In the first step, an effective thermal conductivity of the parallel phases is calculated with the parallel model approach. In the second step, the value obtained in the first step is combined with the Maxwell-Eucken model to describe the dispersed heat additive phase. This procedure will be applied in the next section.

2.4 Effective material models of consolidated composites

To reduce the dimensions and thus complexity of a model, a heterogeneous system can be approximated as quasi-homogeneous described with effective parameters. Subsequently, three different effective material models are derived based on the basic structural models introduced in section 2.3.

2.4.1 Material model of (quasi-) homogenous materials

In this section, an effective material model of consolidated adsorbent composites is developed based on the basic parallel model. This model describes the adsorbent composites as quasi-homogeneous mediums with the material parameters being a function of the volume fractions of adsorbent particles and interparticle voids. The volume fractions add up to 1 as follows

$$1 = \underbrace{\varepsilon^s + \varepsilon^{mi}}_{\tilde{\varepsilon}^s} + \varepsilon^{ma}. \tag{2-64}$$

In this effective model, it is assumed, that primary adsorbent particles, as well as voids, form percolating, parallel phases, which is simplified in a linearized model sketch shown in Figure 2-5. The composite consists of primary adsorbent particles, the interparticle voids, and a negligible volumetric contribution of binder (CMC, <2 weight % with a density of $1.6\ gcm^{-3}$).

The derivation of the model is driven by the idea of correlating experimentally accessible transport and material parameters with the local volume fractions. The apparent porosity $\tilde{\varepsilon}^s$ describes the apparent volume fraction of adsorbent particles (micropores included) which is experimentally more easily accessible than ε^s. Equation (2-64) can be reformulated to obtain the skeleton adsorbent volume fraction ε^s in m_s^3/m_{comp}^3

$$\varepsilon^s = \tilde{\varepsilon}^s\left(1 - \frac{\varepsilon^{mi}}{\tilde{\varepsilon}^s}\right) = \tilde{\varepsilon}^s\left(1 - \frac{\varepsilon^{mi}}{1-\varepsilon^{ma}}\right) = \tilde{\varepsilon}^s\left(1 - \frac{\varepsilon_{exp}^{mi}}{1-\varepsilon_{exp}^{ma}}\right), \tag{2-65}$$

with $\varepsilon^{mi}/\tilde{\varepsilon}^s$ describing the ratio of micropore volume to primary particle volume. This ratio is a constant and depends on the grade of porosity of the primary particles which can be determined experimentally. Independent of the volume fractions of voids, primary particles, and heat-conducting additive, it remains constant. Therefore, by specifying ε^{ma}, the values of $\tilde{\varepsilon}^s$ and ε^s can be calculated with equations (2-66) and (2-65).

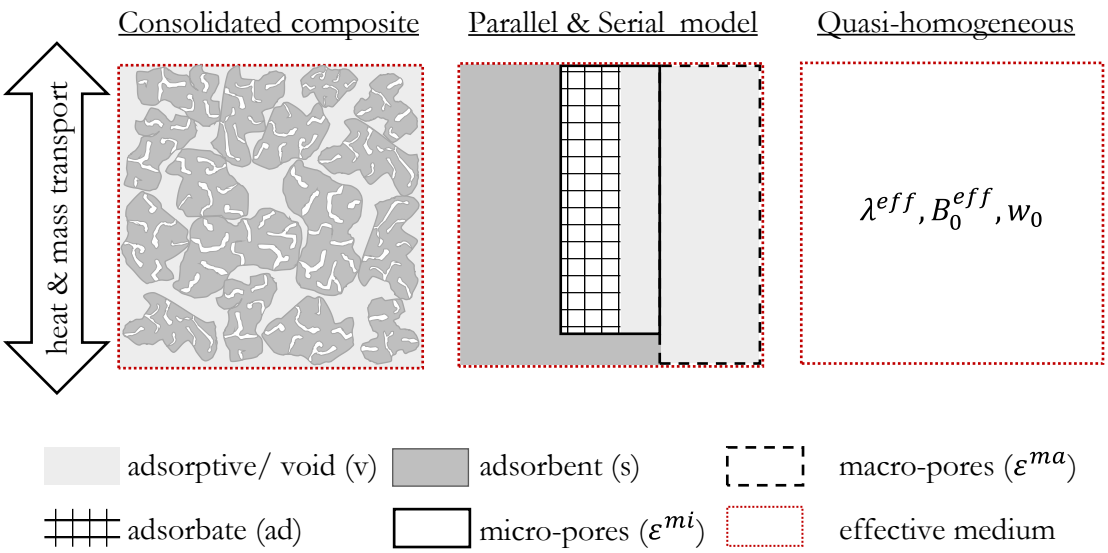

Figure 2-5: Schematic representation of the composite consisting of microporous adsorbent particles and interparticle voids (macropores) (left). A linearized material model assuming percolation of adsorbent and macropores (middle) and the quasi-homogeneous medium with effective material parameters (right).

The bulk density in units kg_{comp}/m^3_{comp} can either be calculated with the adsorbent skeleton density ϱ_{skel} or the apparent density of the primary particles $\varrho_{app,par}$ and is given by

$$\varrho^{bulk} = \varepsilon^s \varrho^s \equiv \varepsilon^s \varrho_{skel} = \tilde{\varepsilon}^s \varrho_{app,par}. \tag{2-66}$$

For loose composites with high void porosity and primary particles with high porosity, the bulk density is low.

In this work, the Dubinin-Astakhov adsorption isotherm introduced in section 2.1.2 is used to describe the material pair methanol – carbonaceous adsorbent. The adsorption capacity is related to the mass of composites and is given in units $cm^3 kg^{-1}_{comp}$. The maximum adsorption capacity of a consolidated composite is correlated with the maximum specific micro- and mesopore volume w_0 of the carbon active porous material. A variation in void porosity and according to equation (2-64) in the volume fraction of primary particles is not influencing the maximum specific micropore volume and thus

$$w_0 = w_0^{exp}. \tag{2-67}$$

This correlation is valid if no inert additive (e.g., heat-conducting additive) with a significant mass fraction is added to the consolidated composite. The contribution of the binder is considered by

taking the maximum specific micropore volume w_0^{exp} into account which is experimentally obtained for consolidated samples containing the binder.

The mass transport of adsorptive molecules depends on the void geometries and sizes. However, in the effective model approach, it is modelled with the Dusty-Gas model introduced in section 2.2.5. The effective permeability and the Knudsen-diffusion coefficient linearly scales with the void porosity which will be discussed in detail in section 4.4.1. Using these correlations, the mass transport parameters can be formulated as follows

$$B_0^{eff} = \frac{\varepsilon^{ma} B_{0,exp}^{eff}}{\varepsilon_{exp}^{ma}}, \tag{2-68}$$

$$D^{Kn,const} = \frac{\varepsilon^{ma} D_{exp}^{Kn,const}}{\varepsilon_{exp}^{ma}}. \tag{2-69}$$

Finally, the effective thermal conductivity is formulated assuming percolating phases of adsorbent particles and void space using the parallel model as introduced in section 2.3

$$\lambda^{eff} = \varepsilon^s \lambda^s + X\lambda^{ad} \equiv \tilde{\varepsilon}^s \tilde{\lambda}^s + X\lambda^{ad}, \tag{2-70}$$

which is applied to calculate the effective heat flux per cross-sectional area of consolidated composites using equation (2-51). Alternatively, the combined heat flux per apparent adsorbent cross-sectional area can be formulated by utilizing equation (2-59)

$$\dot{q}^{ad+s} = -\lambda^{ad+s} \nabla T = \frac{\dot{q}^{eff}}{1 - \varepsilon^{ma}}, \tag{2-71}$$

with the combined thermal conductivity

$$\lambda^{ad+s} = \frac{\varepsilon^s}{\varepsilon^{mi} + \varepsilon^s} \left(\lambda^s + \frac{X\lambda^{ad}}{\varepsilon^s} \right) = \frac{\lambda^{eff}}{1 - \varepsilon^{ma}}. \tag{2-72}$$

λ^s is the thermal conductivity of the solid, skeleton adsorbent which is not accessible experimentally. Therefore, the apparent porosity $\tilde{\varepsilon}^s$ and apparent thermal conductivity $\tilde{\lambda}^s$ are used to formulate the thermal conductivity (with $\varepsilon^{ha} = 0$ in equation (2-58))

$$\lambda^{ad+s} \equiv \tilde{\lambda}^{ad+s} = \tilde{\lambda}^s + \frac{X\lambda^{ad}}{\tilde{\varepsilon}^s}. \tag{2-73}$$

By locally varying the composition of the composite in the effective material model, different kinetic and equilibrium parameters are obtained to be used in process simulations. In the context

of material design, the determination of the optimal spatial distribution of additives in the composite requires sufficient optimization techniques.

So far, the contribution of heat additive is not included in the effective material model. This part will be covered in the next section for a percolating and a non-percolating heat additive phase.

2.4.2 Effective material models of composite materials

Previously, a material model describing quasi-homogeneous adsorbent composites was outlined. By adding heat additive to the composites, besides thermal conductivity, further quantities such as adsorption capacity are influenced which requires effective material models.

Taking the inert heat additive phase with volume fraction ε^{ha} and density ϱ^{ha} into account, the apparent porosity of the primary particles is given by

$$\tilde{\varepsilon}^{s} = 1 - \varepsilon^{ma} - \varepsilon^{ha} = \varepsilon^{s} + \varepsilon^{mi}, \tag{2-74}$$

and the bulk density extended by the heat additive term can be written as follows

$$\varrho^{bulk} = \varepsilon^{s}\varrho^{s} + \varepsilon^{ha}\varrho^{ha} = \tilde{\varepsilon}^{s}\varrho_{app,par} + \varepsilon^{ha}\varrho^{ha}. \tag{2-75}$$

The specific adsorption capacity related to the composite mass scales with the active adsorbent mass and is thus reduced by the inert heat additive according to

$$w_0 = w_0^{exp}\frac{\varepsilon^{s}\varrho^{s}}{\varepsilon^{s}\varrho^{s} + \varepsilon^{ha}\varrho^{ha}}. \tag{2-76}$$

It is assumed, that mass transport is independent of the heat additive and only depends on the void porosity. Therefore, equations (2-68) and (2-69) can equally be applied to describe the effective mass transport in composites with heat additives.

Heat conducting additive is added to improve the effective thermal conductivity of consolidated composites. However, according to percolation theory, the desired effect is only achieved when the heat additive phase reaches the percolation threshold [115]. In the following sections, two effective medium models are formulated, one assuming statistically distributed, non-interacting heat additive particles and the other a percolating heat additive phase.

2.4.2.1 Statistical materials without percolating heat conducting additive

If the heat additive particles are statistically distributed within the consolidated composites as schematically shown in Figure 2-6, the effective thermal conductivity needs to be formulated with approaches from the effective medium theory outlined in section 2.3.1.

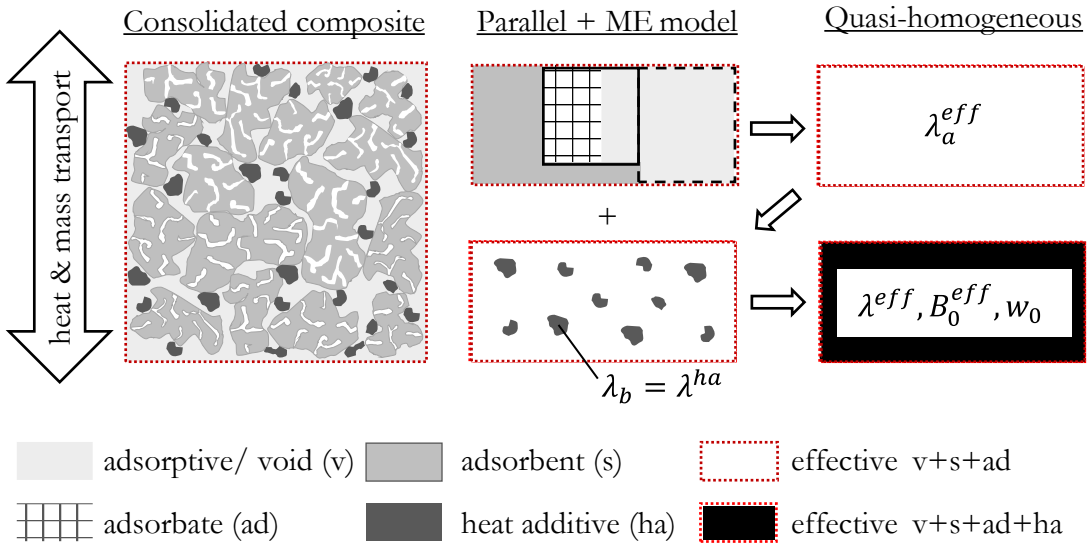

Figure 2-6: Consolidated composite with statistically distributed inert heat additive (left), parallel and Maxwell-Eucken model (middle), and quasi-homogeneous models (right).

Assuming non-percolating, non-interacting spheres of heat additive with low volume fraction, and neglecting interfacial transport resistances, the Maxwell-Eucken formulation can be applied. Therefore, the heat conducting additive with λ_b is treated as the diluted phase randomly distributed in a quasi-continuous phase consisting of adsorbent primary particles and interparticle voids with effective thermal conductivity λ_a^{eff}. In a first step, the effective thermal conductivity of the continuous phase is obtained with the parallel model approach

$$\lambda_a^{eff} = \frac{\tilde{\varepsilon}^s}{\tilde{\varepsilon}^s + \varepsilon^{ma}} \left(\tilde{\lambda}^s + \frac{X \lambda^{ad}}{\tilde{\varepsilon}^s} \right). \tag{2-77}$$

In the second step, the Maxwell-Eucken model (equation (2-62)) is applied to obtain the effective thermal conductivity of the composite with $\lambda_a = \lambda_a^{eff}$, $\lambda_b = \lambda^{ha}$, $\varepsilon_a = \tilde{\varepsilon}^s + \varepsilon^{ma}$, and $\varepsilon_b = \varepsilon^{ha}$

$$\lambda^{eff} = \frac{\lambda_a^{eff}(\tilde{\varepsilon}^s + \varepsilon^{ma}) + \lambda^{ha}\varepsilon^{ha}\dfrac{3\lambda_a^{eff}}{2\lambda_a^{eff} + \lambda^{ha}}}{(\tilde{\varepsilon}^s + \varepsilon^{ma}) + \varepsilon^{ha}\dfrac{3\lambda_a^{eff}}{2\lambda_a^{eff} + \lambda^{ha}}}. \tag{2-78}$$

For the description of the mass transport, the bulk density, and the adsorption capacity, equations (2-68), (2-69), (2-75), and (2-76) are equally valid as described in the previous sections.

With the effective material model with a statistically distributed heat additive, the contradicting trends of adsorption capacity and thermal conductivity can be visualized. To show this, experimentally obtained material parameters of composites without heat additive (termed Exp_{CDC}), which are outlined in Table B-6, are used to evaluate the model equations. The effective thermal conductivity is calculated at 330K and with an aluminium alloy (AlSi10Mg) as heat conducting additive with $\lambda^{ha} = 140 W m^{-1} K^{-1}$ and $\varrho^{ha} = 2680 kg m^{-3}$ [116]. Due to the insulation of the individual heat additive particles, they contribute only slightly to the effective thermal conductivity as can be seen in Figure 2-7. Even with a heat additive volume fraction of up to 20 vol%, the effective thermal conductivity does not exceed 1.2 W/m/K.

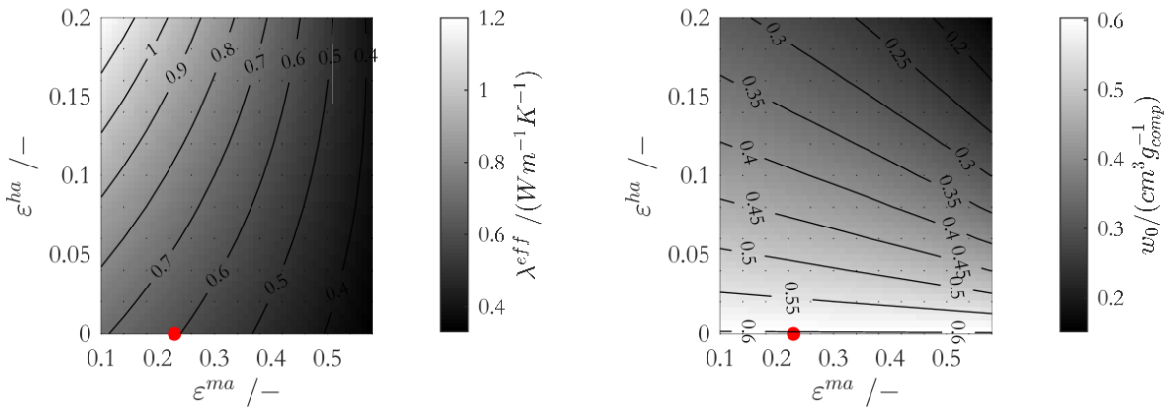

Figure 2-7: Effective thermal conductivity and adsorption capacity as a function of the volume fractions of heat additive ε^{ha} and voids ε^{ma} obtained with the combined parallel and Maxwell-Eucken model (equations (2-77) and (2-78)). The dot shows experimental material parameters evaluated at 330K which are the base of the effective material model (experimental parameters are outlined in Table B-6). Aluminium was chosen for the heat conducting additive with $\lambda^{ha} = 140 W m^{-1} K^{-1}$ and $\varrho^{ha} = 2680 kg m^{-3}$.

2.4.2.2 Materials with percolating heat additive phase

Optimally, the heat additive percolates and contributes in parallel to the effective thermal conductivity of an adsorbent composite. The extension of the material model presented in section 2.4.1 by a linear, percolating heat additive phase is straightforward and shown in Figure 2-8.

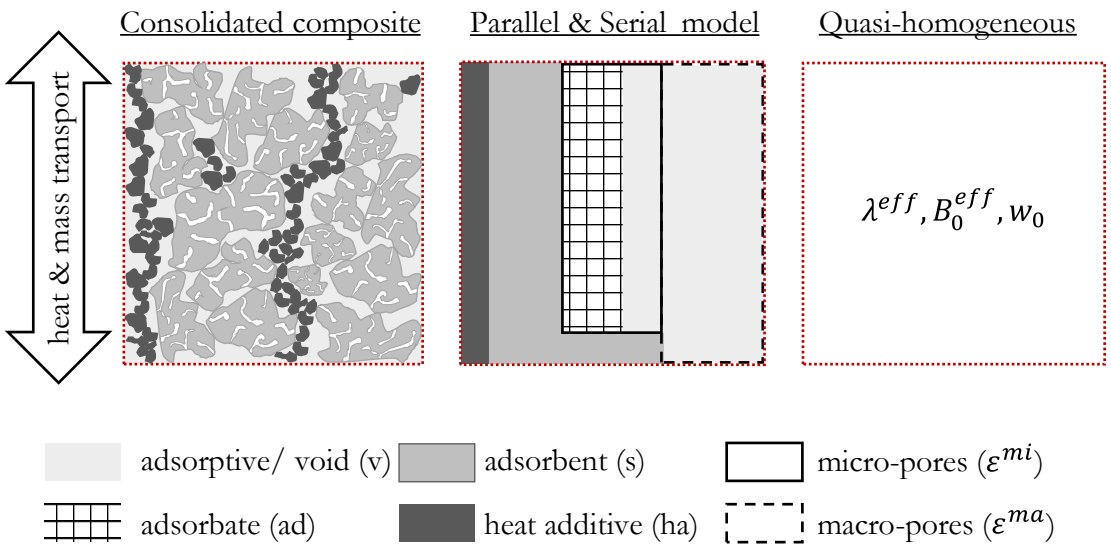

Figure 2-8: Consolidated composite with percolating inert heat additive, a simplified material model containing parallel and serial contributions, and quasi-homogeneous medium.

This model is very simplified and not developed to correctly reproduce the experimentally determined thermal conductivities of consolidated composites. It should rather be used in process simulations to investigate the maximal benefit of percolating, heat-conducting structures aiming to conduct a virtual material design.

The thermal conductivities are extended by the term of the heat conducting additive and follow to (also see equations (2-57) and (2-58))

$$\lambda^{eff} = \varepsilon^{ha}\lambda^{ha} + \tilde{\varepsilon}^{s}\tilde{\lambda}^{s} + X\lambda^{ad}, \tag{2-79}$$

$$\tilde{\lambda}^{ad+s+ha} = \frac{\varepsilon^{ha}}{\tilde{\varepsilon}^{s} + \varepsilon^{ha}}\lambda^{ha} + \frac{\tilde{\varepsilon}^{s}}{\tilde{\varepsilon}^{s} + \varepsilon^{ha}}\left(\tilde{\lambda}^{s} + \frac{X\lambda^{ad}}{\tilde{\varepsilon}^{s}}\right). \tag{2-80}$$

This effective model is applied to investigate the benefit of percolating, linear heat conducting structures on the overall process performance of adsorption chillers.

Figure 2-9 shows surface plots of the effective thermal conductivity and the adsorption capacity as functions of the void and heat additive volume fractions. While the addition of heat conducting additive has a dramatic effect on the effective thermal conductivity, the influence of the volume fractions of voids, as well as adsorbent particles, are negligible. For the mass-specific adsorption capacity, however, the volume fractions of heat additive, as well as adsorbent particles, are decisive. The higher the amount of heat conducting additive, the greater the

influence of the void fraction which results in increasing gradients of the straight lines with constant adsorption capacity.

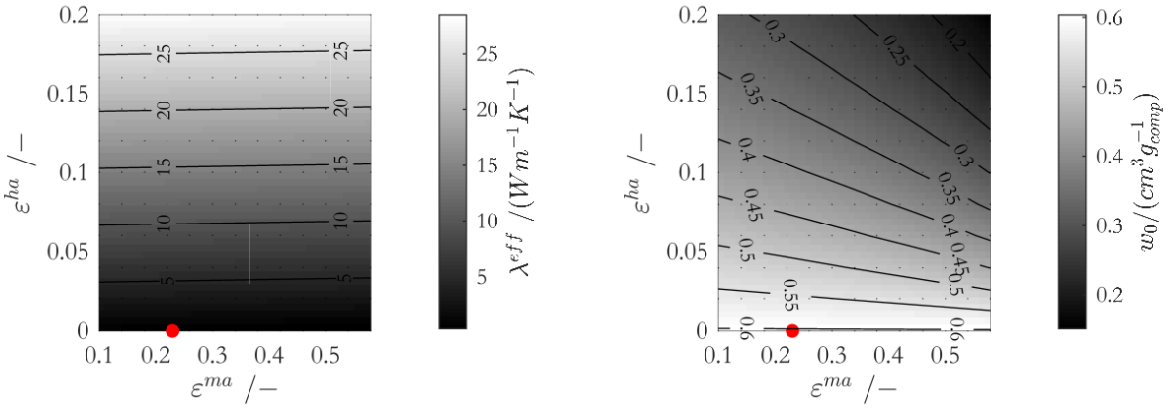

Figure 2-9: Effective thermal conductivity (left) and adsorption capacity (right) as functions of the volume fractions of heat conducting additive ε^{ha} and voids ε^{ma} obtained with the effective material model with percolating heat additive phase (equations (2-76) and (2-79)). The dots show experimentally obtained parameters evaluated at 330K which are the base of the effective material model, and which are summarized in Table B-6 (Exp_{CDC}). Here, an aluminium alloy was chosen for the heat additive with $\lambda^{ha} = 140 Wm^{-1}K^{-1}$ and $\varrho^{ha} = 2680 kgm^{-3}$ (see Table 5-1).

Due to the improved effective thermal conductivity, the transport resistance for heat conduction is reduced and thicker composite layers can be realised. As thermal conductivity increases, the likelihood that mass transport will limit the overall kinetics increases. Hence, a further enhancement of thermal conductivity does no longer contributes to process improvement. If this is the case, an enhancement of the mass transfer is required by e.g., increasing the void porosity or introducing macroscopical mass transfer channels in the composites. However, both, thermal conducting structures and macroscopical mass transfer channels introduced in a defined manner reduce the volume fraction of the active adsorbent phase. The local composition of such structured adsorber composites thus represents an optimization problem, the solution of which promises to improve the process performance of adsorption chillers.

In summary, the presented material models are obtained by treating the individual phases by the serial, parallel, or Maxwell-Eucken models introduced in section 2.3. Each of the models is based on assumptions and none of the presented models can describe the effective thermal conductivity near the percolation threshold, let alone the transition of non-percolating to percolating heat additive phase. Nevertheless, applying the presented effective models in process

simulations is helpful to get an idea of how important percolation and thus structuring of the thermal conducting phase is. With this understanding, in chapter 6 another effective material model is derived describing structured composites with triangular prism-shaped heat-conducting ribs as well as macroscopic mass transfer channels.

3. Adsorption refrigeration process – Modelling

Adsorption cooling machines are environmentally friendly apparatus, which are driven by thermal energy supplied by an external heat source as described in section 1.1. In the application, the adsorbent needs to be heated and cooled using a heat transfer fluid. Therefore, heat exchangers (Hex) are required with a minimum thermal resistance as well as passive mass. The ratio of active adsorbent to passive Hex mass is crucial for the efficiency of adsorption heat pumps due to the inevitable temperature swing between adsorption and desorption. In this work, stainless steel flat tubes are used as Hex as schematically shown in Figure 1-2, with a wall thickness of 0.5 mm and a mass density of $\varrho^{pm} = 8000 kg/m^3$. From that, the specific mass of the Hex results to 4 kg/m^2. In addition, the three ambient temperature levels are crucial parameters for thermal heat pump performance. For the sake of comparison, the simulation studies in this work were conducted with constant boundary temperature levels which are listed in Table 3-1 in addition to the Hex parameters.

Table 3-1: Temperature boundary conditions of the adsorption refrigeration process and parameters of the heat exchanger passive mass.

$T_{des}^{max}\ /K$	353.15
$T_{ads}^{min} = T_c\ /K$	303.15
T_e/K	288.15
$c_p^{pm}/(Jkg^{-1}K^{-1})$	500
$m^{pm}/(kgm^{-2})$	4

3.1 Evaluation of adsorption chiller process performance

The maximum thermal efficiency a heat engine can achieve is known as Carnot efficiency. For processes with non-isothermal heat transfer with variable temperature levels, the classical formulation of the Carnot efficiency is insufficient and leads to a significant overestimation [71]. Therefore, the varying temperature levels needs to be considered by introducing energy conservation equations for the four steps presented in the Clausius-Clapeyron diagram in Figure 1-1. This diagram shows the idealized, thermodynamic changes of states of the adsorbent. In each step, the adsorbent is exposed to varying pressure and temperature conditions since the

adsorber is heated or cooled and connected to the condenser or evaporator. The thermodynamic cycle consists of four separate steps, during which the heat transfer occurs at varying temperature levels. The adsorption period includes pre-cooling and adsorption. The desorption period includes pre-heating and regeneration of the adsorbent. In an ideal thermodynamic cycle with an ideal change of thermodynamic states (pressure, loading, and temperature), these four steps can be separated into isobaric and isosteric changes of state. During pre-cooling and pre-heating, the loading of the adsorbent is almost constant, whereas the ideal adsorption and desorption steps are isobaric.

For the evaluation of the thermal efficiency of adsorption chillers, the Coefficient of Performance (COP) is commonly used which was introduced in equation (1-1). The thermodynamic ideal COP can be calculated as follows

$$COP^{theo} = \frac{\int_0^{t_{cyc}} \dot{q}_e^{ideal} dt}{\int_0^{t_{cyc}} \left(\dot{q}_{heat}^{ideal} + \dot{q}_{des}^{ideal}\right) dt}. \tag{3-1}$$

The real process efficiency deviates from the thermodynamic efficiency which is caused by inefficiencies, e.g., due to mass and heat transport resistances in the adsorbent composites. In the limiting case of infinite cycle time, the process COP (equation (1-1)) reaches the theoretical COP^{theo}. The idealized cooling heat flux ($\dot{q}_e^{ideal}$) is calculated with the equilibrium adsorption rate ($\frac{\partial X_{eq}}{\partial t}$), heat of evaporation ($\Delta_{evap}h$) and the mass density of the dry adsorbent (m^s), reduced by the recycle of liquid methanol from the condenser to evaporator. (Note: if the mass of binder in the composites is negligible and no further additive is used, $m^s \approx m_{comp}$. Otherwise, m_{comp} needs to be used or the adsorption isotherm needs to be referred to the dry mass of the adsorbent.)

$$\dot{q}_e^{ideal} = m^s \frac{\partial X_{eq}}{\partial t}\left(\Delta_{evap}h - c_{p,c}^{l}(T_c - T_e)\right). \tag{3-2}$$

The denominator of COP^{theo} is separated into two terms resulting from the lumped-parameter model which is discussed subsequently in section 3.2.1

$$\dot{q}_{heat}^{ideal} = \left(X_{max} m^s c_p^{ad} + m^s c_p^s + m^{pm} c_p^{pm}\right)\frac{\partial T}{\partial t}, \tag{3-3}$$

$$\dot{q}_{des}^{ideal} = \left(X_{eq} m^s c_p^{ad} + m^s c_p^s + m^{pm} c_p^{pm}\right)\frac{\partial T}{\partial t} - m^s \frac{\partial X_{eq}}{\partial t}\Delta_{ads}h. \tag{3-4}$$

Equation (3-3) describes the sensible heat flux provided to the adsorber for heating the Hex, adsorbent composite as well as adsorbate from T_{ads}^{min} to T_{des}^{min}. Equation (3-4) contains sensible and latent heat contributions and describes the heat flux required for further heating up the Hex and dry adsorbent with constant mass as well as adsorbate with variable mass due to desorption. Additionally, the heat of desorption is considered. At this point, the importance of taking the passive mass of the heat exchanger into account for a correct evaluation of the thermal efficiency of the process must be emphasized. If the passive masses were not considered, an optimization would always result in an adsorbent composite with maximum transport parameters and minimum transport paths, since the adsorption capacity is no longer of importance. In the limit of long cycle times, the identical COP would result regardless of the adsorbent mass used, which does not correspond to the real adsorption refrigeration process.

In addition, by using the idealized heat flux provided to the evaporator $\dot{q}_e^{ideal}$, a theoretical (mass) specific cooling power can be calculated

$$SCP^{theo} = \frac{\int_0^{t_{cyc}} \dot{q}_e^{ideal} dt}{m_{comp} t_{cyc}}. \tag{3-5}$$

The thermodynamic evaluation criteria are useful to quickly estimate the maximum expected performance for an adsorber design and adsorbent – adsorbate pair. However, the true performance deviates due to transport limitations in the system. Therefore, the equations (1-1) and (1-2) need to be used and evaluated with the true heat fluxes obtained from process simulations or experiments.

3.2 Model development

Physical processes can be modelled at different time and size scales with varying levels of detail. Models on the molecular scale offer the highest level of detail yet are not suitable for describing macroscopic technical processes. In opposite, models on the macroscopic scale do not include microscopic or molecular interactions. Bird, Steward, and Lightfoot [102] distinguish three different model approaches with increasing level of detail, without defining sharp boundaries between the scales: macroscopic level, microscopic level, and molecular level. Figure 3-1 shows the three levels exemplified for a fixed bed containing microporous adsorbent primary particles.

The macroscopic models are typically in the size range of technical devices, e.g., fixed bed adsorbers with several meters of length. The more detailed microscopic level typically includes all size ranges from µm to centimetres and sometimes meters, depending on the length of the

investigated fixed bed. The microscopic level also contains a spatial resolution of the system or parts of the system, e.g., primary particles, if continuum equations apply to the underlying transport processes. On the molecular scale, interaction forces between the individual molecules are investigated. In this thesis, only models of the first two types are used since molecular level simulations for complete technical processes are numerically not feasible.

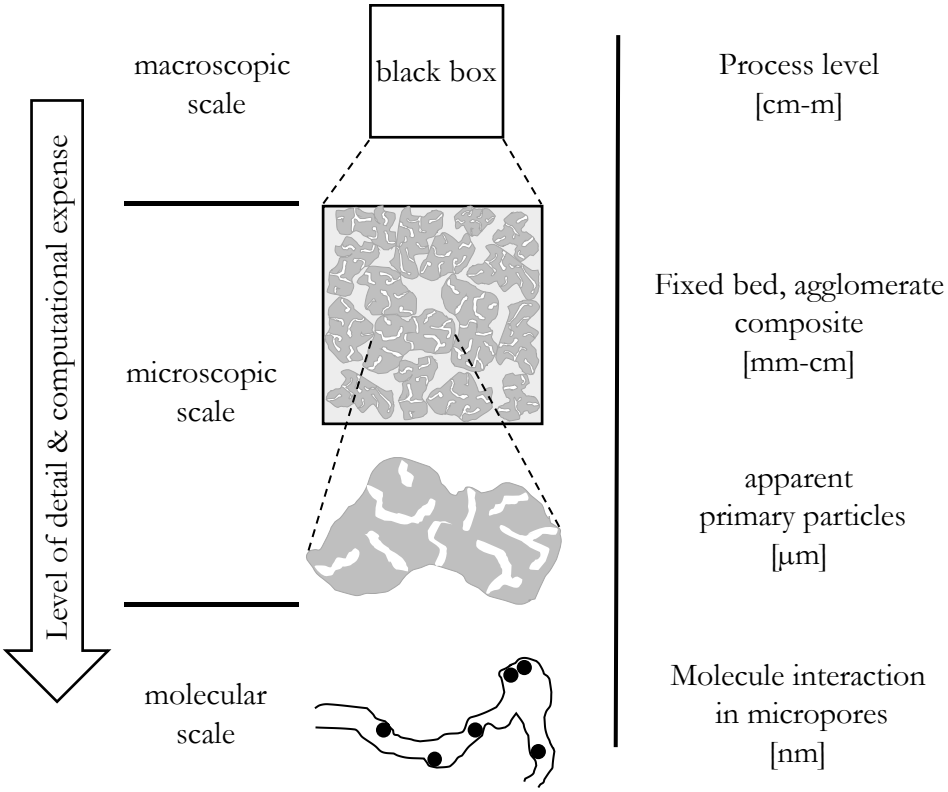

Figure 3-1: Three classical levels of detail for modelling physical processes following the nomenclature of Bird, Steward, Lightfoot [102]: Macroscopic scale, microscopic scale, and molecular scale.

In the case of negligible kinetic transport resistance (with large transfer parameters between the individual systems), only the equilibrium is important, which depends on state variables such as pressure and temperature. If this is the case, so-called thermodynamic models are obtained [117], which are a useful tool for evaluating limiting thermal efficiencies.

The determination of suitable system boundaries is of decisive importance in modelling engineering processes. In the following sections, a macroscopic level lumped-parameter model of adsorption refrigeration machines is outlined. It contains macroscopic balances of mass and energy of adsorber, evaporator, and condenser. In addition, a thermodynamic model is derived from the lumped-parameter model. With the aim of the structural design of adsorbent

composites, subsequently, spatially distributed equations of change for mass and energy of the consolidated adsorbent composites are derived (microscopic level model), which represent the heart of the process models applied in this work.

3.2.1 Macroscopic level – lumped-parameter model of adsorption chillers

In lumped-parameter models, conservation equations of momentum, mass, and energy are used on a macroscopic level. The conservation quantities change by the introduction or removal of these quantities via entering or leaving streams and other inputs and outputs via the system boundaries. The modelling of exchange flows in macroscopic models is often motivated by the properties of connecting armatures, e.g., using flow characteristics for valves. Individual systems are considered as quasi-homogeneous black boxes without spatial resolution. The definition of the system boundaries is one of the first steps in modelling which is an important matter. A lumped-parameter model of an adsorption chiller can e.g., be composed of macroscopic balance equations for adsorber, evaporator, and condenser containing conservation equations of mass and energy. The mass in the individual apparatus only changes by entering and leaving streams according to the process setup whereas the total mass is constant since adsorption chillers are closed systems. The energy of the individual apparatus changes due to heat transfer to and from the surroundings and via convective energy transport across the system boundaries. The number of individual systems increases if the level of detail increases, whereby the system boundaries do not necessarily have to represent the physical dimensions of the apparatus. It is often appropriate to consider phases with different physical properties as separate systems that are connected via interphase mass, energy, and momentum transport. The formulation of interphase fluxes between such imagined system boundaries cannot be motivated by connecting, physical armatures. Therefore, transfer coefficients (e.g., heat or mass transfer coefficient) are used to describe the interphase fluxes of adjacent phases accounting for the transfer resistance and thus is a measure of the kinetics of the transfer.

The adsorber can e.g., be divided into individual systems describing heat transfer fluid, passive mass, the adsorbent composites, and a free gas phase as shown in Figure 3-2, with the advantage of assigning individual kinetics to the respective interphase fluxes. By summarizing the conservation equations of the individual phases, a black-box model of the adsorber is obtained in terms of fluxes across the apparatus boundaries.

Subsequently, lumped-parameter conservation equations of energy and mass for the individual phases are presented. Furthermore, lumped-parameter models for evaporator and condenser are used completing the lumped-parameter model of the adsorption chiller. In the remainder of the

thesis, all model equations are written in specific quantities. The quantities are related to the cross-sectional area of the adsorbent composites.

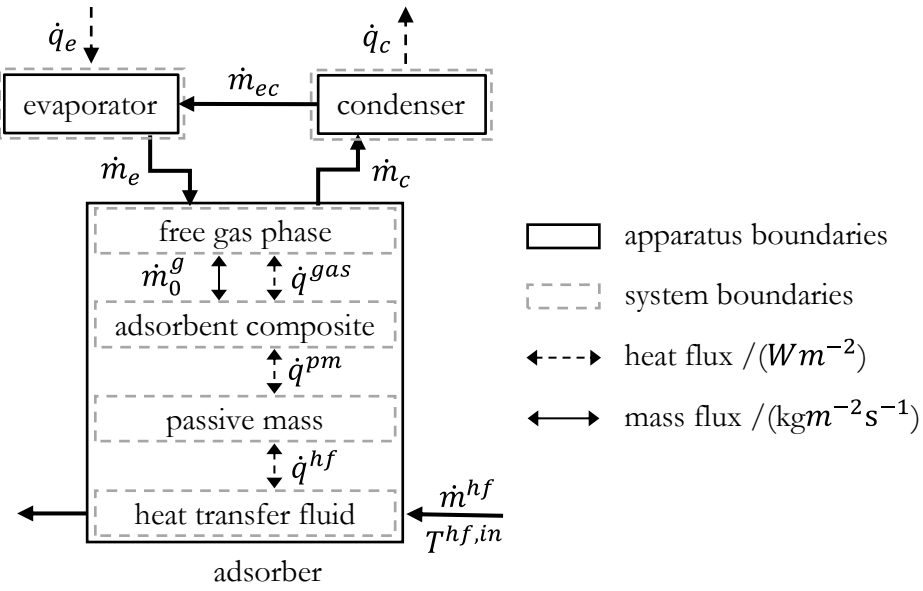

Figure 3-2: Macroscopic level modelling approach of an adsorption chiller containing adsorber, evaporator, and condenser. The adsorber is subdivided into four individual systems coupled with interphase fluxes.

The heat required for desorption and released by adsorption is transferred from or to the surroundings via the heat transfer fluid which is modelled as an ideal stirred tank without spatial resolution. In the adsorption half cycle (pre-cooling and evaporation steps), the inlet temperature is below the outlet temperature and vice versa in the desorption half cycle (pre-heating and condensation steps). The mass flux of the heat transfer fluid (hf) is constant and thus, only an energy balance is required, which, in terms of temperature, is given as follows

$$m^{hf} c_p^{hf} \frac{\partial T^{hf}}{\partial t} = \dot{m}^{hf} c_p^{hf} \left(T^{hf,in} - T^{hf}\right) - \dot{q}^{hf}. \tag{3-6}$$

The heat flux $\dot{q}^{hf}$ referred to the cross-sectional area of adsorbent composites (in units Wm_{comp}^{-2}) is the interphase flux exchanged with the adjacent heat exchanger wall (passive mass, pm) with the temperature difference as driving force and the heat transfer coefficient k^{hf}

$$\dot{q}^{hf} = k^{hf} (T^{hf} - T^{pm}). \tag{3-7}$$

The temperature of the Hex changes due to heat transfer to or from the heat transfer fluid and the adsorbent composites

$$m^{pm} c_p^{pm} \frac{\partial T^{pm}}{\partial t} = \dot{q}^{hf} - \dot{q}^{pm}, \tag{3-8}$$

with the heat flux between adsorbent and passive mass of Hex

$$\dot{q}^{pm} = k^{pm}(T^{pm} - T). \tag{3-9}$$

Here, k^{pm} includes the heat transfer between adsorbent composite and Hex as well as the heat conductivity of the Hex.

In the lumped parameter model approach, the adsorbent composites containing heat conducting additive, adsorbent, adsorbate, and adsorptive are regarded as quasi-homogeneous system without spatial resolution of the transport processes. Its total mass changes by the total adsorption and desorption fluxes. The temperature of the adsorbent composites T depends on the heat exchange with the Hex ($\dot{q}^{pm}$), the enthalpy input of the entering mass flux and the source or sink of the adsorption or desorption enthalpy ($\Delta_{ads}h$). In the adsorber, a free gas phase encloses the adsorbent composites. In a technical adsorption chiller, the adsorber is designed with a minimal volume of the free gas phase reducing the mass and energy hold-up. Therefore, the mass fluxes entering and leaving the composites ($\dot{m}_0^v$) are approximately the fluxes exchanged with evaporator and condenser.

The lumped-parameter energy balance of the adsorbent composites for adsorption and desorption in terms of temperature can be formulated as follows

Adsorption:
$$\left(X m^s c_p^{ad} + m^s c_p^s + m^{ha} c_p^{ha}\right)\frac{\partial T}{\partial t} = \dot{m}_0^v \, \Delta_{ads}h + \dot{q}^{pm} + \dot{m}_0^v \, c_{p,e}^v (T_e - T), \tag{3-10}$$

Desorption:
$$\left(X m^s c_p^{ad} + m^s c_p^s + m^{ha} c_p^{ha}\right)\frac{\partial T}{\partial t} = \dot{m}_0^v \, \Delta_{ads}h + \dot{q}^{pm}. \tag{3-11}$$

The accumulation terms contain contributions from the dry adsorbent, heat conducting additive, and adsorbate; the energy hold-up of the adsorptive phase in the voids and micropores is negligibly small. If the free gas phase in the adsorber is neglected, the change of mass of the adsorbent composites solely depends on the interphase transfer flux between the adsorber and evaporator or condenser $\dot{m}_0^v$ in units $kgm_{comp}^{-2}s^{-1}$. In terms of loading, the mass balance can be formulated with a (macroscopic) linear-driving force approach summarizing all kinetic resistances in the adsorbent composites. The difference between equilibrium loading at bulk conditions and adsorbent loading serves as the driving force

$$m^s \frac{dX}{dt} = \dot{m}_0^v = m^s k_{LDF}^{macro}\left(X_{eq} - X\right). \tag{3-12}$$

In the evaporation step, the equilibrium loading is a function of adsorbent temperature and evaporator pressure $X_{eq}(T, p_e)$. While the adsorbent is regenerated, equilibrium loading is a function of adsorbent temperature and condenser pressure $X_{eq}(T, p_c)$. The linear driving force parameter k_{LDF}^{macro} in $1/s$ describes the total transport resistance of the composites in terms of an integral transfer resistance. For thin composites with homogeneous temperature, pressure, and loading the lumped-parameter approach is sufficient. However, for large gradients and differences in the dynamic states, which is the case for thick layers with large transport resistance, the overall kinetic cannot be described with a lumped-parameter approach.

For a first evaluation of the process performance, the thermodynamic limiting case can be evaluated assuming local adsorption equilibrium either by using a large transfer resistance parameter k_{LDF}^{macro} or by using the total derivative of the adsorption isotherm. Then, the equilibrium mass balance can be formulated in terms of the loading X with the total differential of the equilibrium loading $X_{eq}(T, p)$ with p being evaporator or condenser pressure, respectively

$$m^s \frac{dX}{dt} = m^s \left(\left(\frac{\partial X_{eq}}{\partial p} \right)_T \frac{dp}{dt} + \left(\frac{\partial X_{eq}}{\partial T} \right)_p \frac{dT}{dt} \right). \tag{3-13}$$

The adsorber can be described as a black-box system using a lumped-parameter approach, where the total mass changes only by the amount adsorbed or desorbed during the adsorption and desorption steps. Therefore, equations (3-12) or (3-13) can be used as the total mass balance of the adsorber. For the total energy balance of the black-box model, the single balances are summed up. Hence, the energy conservation equation of the adsorber contains contributions from heat transfer across the adsorber boundary, a source/ sink term for adsorption/ desorption heat, and in the case of adsorption, a term describing superheating of adsorptive from evaporator to adsorber temperature

Adsorption:
$$\left(X m^s c_p^{ad} + m^s c_p^s + m^{ha} c_p^{ha} + m^{pm} c_p^{pm}\right) \frac{\partial T}{\partial t} = \dot{m}_0^v \Delta_{ads} h + \dot{m}^{hf} c_p^{hf} \left(T^{hf,in} - T^{hf}\right) + \dot{m}_0^v c_{p,e}^v (T_e - T), \tag{3-14}$$

Desorption:
$$\left(X m^s c_p^{ad} + m^s c_p^s + m^{ha} c_p^{ha} + m^{pm} c_p^{pm}\right) \frac{\partial T}{\partial t} = \dot{m}_0^v \Delta_{ads} h + \dot{m}^{hf} c_p^{hf} \left(T^{hf,in} - T^{hf}\right). \tag{3-15}$$

If the heat transfer fluid temperature is constant (e.g., large hold-up or velocity), the hf-phase can be neglected reducing the equation for conservation of total energy of the adsorber to

Adsorption:
$$\left(Xm^s c_p^{ad} + m^s c_p^s + m^{pm} c_p^{pm}\right)\frac{\partial T}{\partial t} = \dot{m}_0^v \Delta_{ads} h + \dot{q}^{hf} + \dot{m}_{rf}^0 c_{p,e}^v (T_e - T), \tag{3-16}$$

Desorption:
$$\left(Xm^s c_p^{ad} + m^s c_p^s + m^{pm} c_p^{pm}\right)\frac{\partial T}{\partial t} = \dot{m}_0^v \Delta_{ads} h + \dot{q}^{hf}. \tag{3-17}$$

In the process simulations carried out in this thesis, the free gas phase in the adsorber is neglected due to its negligible influence on a technical scale. However, for the validation of the mathematical process model with small-scale dynamic experiments (see Appendix C.1), taking the gas-phase hold-up into account is inevitable. Then, the conservation equations of the adsorbent composites are formulated by using boundary variables from the free gas-phase (pressure, temperature) instead of evaporator or condenser variables. In terms of mass density ϱ^{gas}, the conservation of mass in the free gas-phase can be formulated as follows

$$V^{gas}\frac{\partial \varrho^{gas}}{\partial t} = A_{comp}(\dot{m}_{e/c} - \dot{m}_0^v), \tag{3-18}$$

with the total volume of the free gas-phase V^{gas}, the mass fluxes exchanged between evaporator and adsorber $\dot{m}_e$, or adsorber and condenser $\dot{m}_c$. If the mass hold-up in the free gas phase is considered, valve equations can be used describing the fluxes between the adjacent apparatus by e.g., using linear transfer resistances with the pressure differences as the driving force

$$\dot{m}_{e,c} = \beta_{e,c}\left(p_{e,c}^{sat} - p^{gas}\right). \tag{3-19}$$

If a specific valve type is modelled, $\beta_{e,c}$ can be formulated so that the opening and closing characteristics are reproduced. In the validation of the mathematical model in Appendix A, $\beta_{e,c}$ are fitting parameters. If the mass hold-up in the free gas phase is considered, $\dot{m}_0^v$ describes the mass flux between adsorbent composites and free gas phase related to the composites cross-sectional area A_{comp}. Otherwise, it describes the fluxes between the adjacent apparatus as outlined previously. The energy hold-up in the free gas phase can be modelled using a lumped-parameter energy conservation equation

$$\left(\varrho^{gas} V^{gas} c_p^{gas} - \frac{\varrho^{gas} V^{gas} R}{MW}\right)\frac{\partial T^{gas}}{\partial t} = A_{comp}(\dot{m}_e c_{p,e}(T_e - T^{gas}) - \dot{m}_0^v c_p^v (T - T^{gas}) + \dot{q}^{gas}) + \frac{R}{MW} T^{gas} V^{gas}\frac{\partial \varrho^{gas}}{\partial t}. \tag{3-20}$$

The first two terms on the right-hand side are relevant if the adsorptive enters the free gas phase. For mass fluxes leaving the free gas phase, these terms are zero. The last term on the right-hand side results from the work performed on the system and $\dot{q}^{gas}$ describes the heat exchange between adsorbent composite surface and free gas phase by radiation

$$\dot{q}^{gas} = \alpha^{gas}(T - T^{gas}). \tag{3-21}$$

The methodology used for deriving a lumped-parameter model of the adsorber can also be applied for the evaporator and condenser. Instead of the adsorbent composites, the evaporator and condenser contain liquid refrigerant. By neglecting the gas hold-up, the mass balances for evaporator and condenser in units $kgm_{comp}^{-2}s^{-1}$ are

$$\frac{\partial m_e}{\partial t} = \dot{m}_{ec} - \dot{m}_e, \tag{3-22}$$

$$\frac{\partial m_c}{\partial t} = \dot{m}_c - \dot{m}_{ec}. \tag{3-23}$$

Here, $\dot{m}_{ec}$ is the flux of liquid refrigerant from the condenser to evaporator, and $\dot{m}_e$ and $\dot{m}_c$ are directly given by $\dot{m}_0^v$, when neglecting the adsorber gas phase. The conservation equations for the energy of heat transfer fluid and passive mass are equivalent to equations (3-6) and (3-8). The energy balances of the refrigerant contain the heat of evaporation or condensation instead of the heat of adsorption or desorption. When neglecting the gas hold-up, the energy balances are given as follows

$$m_e c_{p,e}^l \frac{\partial T_e}{\partial t} = -\dot{m}_e \Delta_{evap} h(T_e) + \dot{q}_e^{pm} + \dot{m}_{ec} c_{p,c}^l (T_c - T_e), \tag{3-24}$$

$$m_c c_{p,c}^l \frac{\partial T_c}{\partial t} = \dot{m}_c \Delta_{evap} h(T_c) + \dot{q}_c^{pm} + \dot{m}_c c_{p,des}^v (T_{des} - T_c). \tag{3-25}$$

The last terms in equations (3-24) and (3-25) describe the energy input by the reflux from the condenser to evaporator and the cooling of adsorptive from desorption to condensation temperature, respectively. In equivalence to the procedure demonstrated for the adsorber, conservation equations for the total energy of evaporator and condenser can be formulated.

If evaporator and condenser are assumed to be isothermal and in steady-state, the heat flux provided to the evaporator, and heat to be dissipated from the condenser can directly be calculated as follows

$$\dot{q}_e = \dot{m}_e \Delta_{evap} h(T_e) - \dot{m}_{ec} c_{p,c}^l (T_c - T_e), \tag{3-26}$$

$$\dot{q}_c = \dot{m}_c \Delta_{evap} h(T_c) + \dot{m}_c c_{p,des}^v (T_{des} - T_c). \tag{3-27}$$

These formulations are convenient if the kinetics of the evaporator and condenser are not of interest. Since the process simulations in this work are subjected to the goal of developing structured adsorber composites and novel process designs, the kinetic influences of the

evaporator and condenser are neglected and thus equations (3-26) and (3-27) are used to evaluate process performance instead of the dynamic conservation equations previously introduced. However, the dynamic conservation equations are required and adapted for validation of the total process model in Appendix C.1.

3.2.2 Thermodynamic/ steady-state model of adsorption refrigerators

In this section, the simplest type of model is briefly introduced. As previously discussed, to evaluate the performance of adsorption heat pumps, the varying temperature levels need to be considered with energy-flux equations for the four steps shown in the Clausius-Clapeyron diagram in Figure 1-1. The formulations result from the lumped-parameter model described in section 3.2.1.

Pre-Cooling:
$$\dot{q}_{cool} = \left(X_{min} m^s c_p^{ad} + m^s c_p^s + m^{pm} c_p^{pm}\right) \frac{dT}{dt}, \tag{3-28}$$

Adsorption:
$$\dot{q}_{ads} = \left(X m^s c_p^{ad} + m^s c_p^s + m^{pm} c_p^{pm}\right) \frac{dT}{dt} - m^s \frac{dX}{dt} \Delta_{ads} h - m^s \frac{dX}{dt} c_{p,e}^l (T_e - T), \tag{3-29}$$

Pre-Heating:
$$\dot{q}_{heat} = \left(X_{max} m^s c_p^{ad} + m^s c_p^s + m^{pm} c_p^{pm}\right) \frac{dT}{dt}, \tag{3-30}$$

Desorption:
$$\dot{q}_{des} = \left(X m^s c_p^{ad} + m^s c_p^s + m^{pm} c_p^{pm}\right) \frac{dT}{dt} - m^s \frac{dX}{dt} \Delta_{ads} h. \tag{3-31}$$

While pre-cooling and pre-heating only contain energy contributions from sensible heat, adsorption and desorption steps also contain latent heat due to the phase change from adsorptive to adsorbate and vice versa. The adsorption step further includes a term accounting for superheating of adsorptive from evaporator temperature to adsorption temperature.

To minimize entropy production due to irreversibility and thus optimize the thermodynamic efficiency, as much sensible and latent heat as possible needs to be recovered. Schwamberger et al. [118]–[120] introduced a thermodynamic analysis that provides the heat recovery potential for adsorption cooling machines depending on the material pair, adsorber parameters, and temperature levels. In the present thesis, the method is applied to the Dubinin-Astakhov isotherm. The following section gives a brief overview of the method, and its application is outlined in Appendix D.1.

The state of the adsorbent can be described by two of the three dynamic states pressure, temperature, and loading. Thus, the differential, path-dependent heat (δq), which is transferred

to the adsorber during the desorption cycle and removed during the adsorption cycle, can be described by partial derivatives of two of these dynamic states, e.g.,

$$\delta q = \left(\frac{\delta q}{\delta T}\right)_p dT + \left(\frac{\delta q}{\delta p}\right)_T dp. \tag{3-32}$$

Using the chain rule, equation (3-32) can be rewritten to

$$\delta q = \left(\frac{\delta q}{\delta T}\right)_p dT + \left(\frac{\delta q}{\delta X}\right)_T \left(\frac{\partial X}{\partial p}\right)_T dp. \tag{3-33}$$

The first term describes the differential, path-dependent change of heat with a change in temperature at constant pressure. The pressure $p = f(T, X(T))$ is a function of temperature T and loading $X(T)$, which is a function of temperature itself. Using this dependency, the first term in equation (3-33) can be separated into two parts. The first part describes the differential change of heat with the temperature at constant loading. The second part contains the differential change in the heat with a change in loading and, additionally, the dependence of the loading on temperature

$$\delta q = \left[\left(\frac{\delta q}{\delta T}\right)_X + \left(\frac{\delta q}{\delta X}\right)_T \left(\frac{\partial X}{\partial T}\right)_p\right] dT + \left(\frac{\delta q}{\delta X}\right)_T \left(\frac{\partial X}{\partial p}\right)_T dp. \tag{3-34}$$

<u>Adsorption half-cycle:</u>

The adsorption cycle contains the isosteric pre-cooling and the isobaric adsorption/ evaporation steps. The differential heat transferred during the adsorption cycle can be written in terms of the heat flows shown in Figure 1-1

$$\begin{aligned} q_{cool+ads} &= \int_{Ads} \delta\, q = \underbrace{q_{cool}}_{isoster} + \underbrace{q_{ads}}_{isobar} \\ &= \int_{t_0}^{t_1} \dot{q}_{cool}(T, X_{min}, p(T, X_{min}))\, dt + \int_{t_1}^{t_2} \dot{q}_{ads}(T, X(p_e, T), p_e)\, dt. \end{aligned} \tag{3-35}$$

The heat q_{cool} is removed in the isosteric pre-cooling step at X_{min} and q_2 is removed in the isobaric adsorption step at evaporator pressure p_e. Using the first formulation in equation (3-32) and the heat flow from equation (3-28), the isosteric step can be formulated as

$$\int_{t_0}^{t_1} \dot{q}_{cool}\, dt \equiv q_{cool} = \int_{T_0}^{T_1} \left(\frac{\delta q}{\delta T}\right)_{X_{min}} dT = \int_{T_0}^{T_1} \left(X_{min} m^s c_p^{ad} + m^s c_p^s + m^{pm} c_p^{pm}\right) dT. \tag{3-36}$$

It contains sensible heat removed from adsorbate, adsorbent, and heat exchanger. Schwamberger [120] introduced a necessary driving temperature difference ΔT for the heat transfer, which can be varied during the thermodynamic analysis. The highest efficiency can theoretically be achieved with a driving temperature difference of $\Delta T = 0K$, which is physically not feasible. Using the driving temperature difference, the starting temperature of the pre-cooling step T_0 can be calculated from the maximal available regeneration temperature

$$T_0 = T_{des}^{max} - \Delta T. \tag{3-37}$$

In analogy, the starting temperature of the adsorption step T_1 can be evaluated using the maximal adsorption temperature

$$T_1 = T_{ads}^{max} + \Delta T. \tag{3-38}$$

T_{ads}^{max} needs to be obtained iteratively and describes the temperature at which the equilibrium loading $X(p_e, T)$ is equal to the loading $X_{min}(p_c, T_{des}^{max})$.

Using the formulation introduced in equation (3-34) and the heat flux from equation (3-29), the isobaric adsorption/ evaporation step can be formulated, which contains contributions from sensible and latent heat

$$\begin{aligned} \int_{t_1}^{t_2} \dot{q}_{ads}\, dt \equiv q_{ads} &= \int_{T_1}^{T_2} \left(\frac{\delta q}{\delta T}\right)_{p_e} dT \\ &= \int_{T_1}^{T_2} \Big\{ \left(X(p_e, T) m^s c_p^{ad} + m^s c_p^s + m^{pm} c_p^{pm}\right) \\ &\quad - m^s \left(\Delta_{ads} h(X(p_e, T), T) + c_{p,e}^l (T_e - T)\right) \left(\frac{\partial X}{\partial T}\right)_{p_e} \Big\} dT. \end{aligned} \tag{3-39}$$

In analogy to above, the minimal adsorption temperature T_2 can be calculated with a driving temperature difference from the minimal available boundary temperature

$$T_2 = T_{ads}^{min} + \Delta T. \tag{3-40}$$

Desorption half-cycle:

The desorption cycle contains the isosteric pre-heating step (at X_{max}) and the isobaric regeneration step (at p_c), where the adsorber is connected to the condenser. The heat transferred during the desorption cycle can be written as follows

$$q_{heat+des} = \int_{Des} \delta q = \underbrace{q_{heat}}_{isoster} + \underbrace{q_{des}}_{isobar} = \int_{t_2}^{t_3} \dot{q}_{heat}(T, X_{max}, p(T, X_{max}))\, dt + \int_{t_3}^{t_4} \dot{q}_{des}(T, X(p_c, T), p_c)\, dt. \tag{3-41}$$

With the formulation for the differential heat introduced in equation (3-34), the heat input for the isosteric pre-heating step can be written as

$$\int_{t_2}^{t_3} \dot{q}_{heat}\, dt \equiv q_{heat} = \int_{T_2}^{T_3} \left(\frac{\delta q}{\delta T}\right)_{X_{max}} dT = \int_{T_2}^{T_3} \left(X_{max} m^s c_p^{ad} + m^s c_p^s + m^{pm} c_p^{pm}\right) dT. \tag{3-42}$$

In equivalence to the other temperatures, T_3 can be calculated with the driving temperature difference for the heat transfer and the minimal temperature of the desorption step. T_{des}^{min} needs to be calculated iteratively and describes the temperature, at which the equilibrium uptake $X(p_c, T)$ is equal to the loading $X_{max}(p_e, T_{ads}^{min})$.

The last, isobaric desorption step partly contains sensible heat contributions as well as latent heat contributions from the endothermic desorption. Using the heat flux introduced in equation (3-31), the desorption step can be formulated to

$$\int_{t_3}^{t_4} \dot{q}_{des}\, dt \equiv q_{des} = \int_{T_3}^{T_4} \left(\frac{\delta q}{\delta T}\right)_{p_c} dT = \int_{T_3}^{T_4} \left\{\left(X(p_c, T) m^s c_p^{ad} + m^s c_p^s + m^{pm} c_p^{pm}\right) - m^s \left(\Delta_{ads} h(X(p_c, T), T)\right) \left(\frac{\partial X}{\partial T}\right)_{p_c}\right\} dT. \tag{3-43}$$

The first term in the integral describes the sensible heat contributions and the second term contains the latent heat dissipated by desorption. Due to the cyclic process, T_4 is equal to T_0.

In dynamic models, the evaporation energy required in the evaporator q_e can be calculated by integrating the heat flux $\dot{q}_e$ over the cycle time. In the thermodynamic model, with the maximal loading difference ΔX and the energy provided from the condenser due to recirculation of condensate, q_e is directly obtained from

$$q_e = m^s \Delta X \left(\Delta_{evap} h(T_e) - c_{p,c}^l (T_c - T_e)\right). \tag{3-44}$$

3.2.3 Microscopic level - Equations of change for adsorbent composites (distributed-parameter model)

Microscopic models aim to obtain information about temperature, velocity, pressure, and concentration profiles within a small region of a macroscopic apparatus or process. For the application of the classical conservation equations of continuum theory, the smallest systems must contain enough molecules so that fluctuations do not play a role and an averaging over the considered volume is justified. In the case of adsorption chillers, the microscopic transport phenomena of mass and energy within the adsorbent composites are well understood, which raises the question of why a model at the microscopic level is necessary, with the obvious disadvantages of a higher computational cost and effort for the parameterisation of the model? On the one hand side, the performance of adsorption chillers is strongly dependent on the coupled heat and mass transfer within the adsorbent, which is accompanied by large gradients, requiring the application of a model at the microscopic level. On the other hand, a model at the microscopic level is more generally valid and can be adapted to varying composite dimensions without introducing a new integral transport resistance k_{LDF}^{macro}, as is necessary for the lumped-parameter model. With the objective of a combined material and process development pursued in this work, the use of a microscopic model for the adsorbent composites is thus valid, even though the spatial resolution requires parametrisation with transport properties determined with some experimental effort. Aiming to keep the focus on the transport processes in the composites, the remaining phases are kept as simple as possible, which is why only one further macroscopic lumped-parameter equation is used describing the Hex of the adsorber (equation (3-8)). As described in section 3.2.1, evaporator and condenser are regarded as isothermal, steady-state apparatus and thus, equations (3-26) and (3-27) are used. Since the computational effort strongly increases with increasing model-dimensionality, a one-dimensional microscopic model is used spatially resolving the transport processes over the layer thickness of the consolidated composites, and a linear-driving force approach is applied to condense the intraparticle transport into an effective approach. This results in a "1 + 0 - dimensional" model approach, where the coupling between intraparticle pores and interparticle void is achieved via boundary conditions. Thus, the smallest scale resolved is the µm-scale. The interconnections between adsorber and evaporator as well as adsorber and condenser are considered in the boundary conditions of the consolidated composites.

Transferring the "1 + 0 - dimensional" modelling approach to the adsorbent composites investigated in this work, as discussed in section 2.4, the following abstracted phases can be identified: The interparticle void space with porosity ε^{ma}, the primary particle space with $\tilde{\varepsilon}^{s}$, and

the heat additive phase with ε^{ha}. The primary particles include the solid adsorbent skeleton as well as adsorbate and adsorptive in the micropores. It is assumed, that mass transport over the height of the adsorbent composites exclusively occurs via adsorptive transport in the void space and that the void porosity, as well as void widths, remains constant for different loadings. Adsorption takes place in the form of micropore volume-filling in the primary particles with dynamically and (over the composite height) spatially varying adsorbate concentrations. Heat transport in the composites is mainly due to heat conduction in the skeletal adsorbent phase as well as the heat additive phase and, depending on the loading, to a certain extent in the adsorbate phase. Due to the high porosity of technical adsorbent composites, the volume fraction of solid adsorbent is commonly small which results in low effective thermal conductivities often below 1 W/m/K which is why adding highly conducting heat additive is advantageous. The following requirements thus arise for the microscopic modelling approach of the consolidated adsorbent composites:

- Derivation of spatial equations of change for mass and energy for all phases.
- Formulation of boundary conditions for the spatially resolved balances.

To reduce the number of energy equations a local quasi-homogeneous temperature is assumed in the modelling approach. Thus, the energy balances of adsorptive, adsorbate, adsorbent, and heat conducting additive are combined into a spatially resolved, quasi-homogeneous energy balance. The model is set up with the volume fractions of the individual phases being a function of the spatial coordinate, which is necessary for the context of heterogeneous material design. Here, the main underlying assumptions and an overview of the derivation are outlined.

Figure 3-3 shows the conceptional system to be modelled containing the individual phases of adsorptive in macropores (void), adsorptive in micropores, adsorbate in micropores, solid adsorbent, and heat additive.

Concerning 3D-structured adsorbent composites with spatially varying volume fractions of heat additive, adsorbent primary particles, and macroscopical transport channels (see section 6.1), a generally valid model is derived with the volume fractions being a function of space. Furthermore, besides space, the volume fractions of adsorbate and adsorptive in the micropores are functions of time due to transient increase and decrease of loading. With the assumption of adsorption exclusively taking place in the micropores, the adsorbate and adsorptive phases can be combined into the micropore phase with volume fraction ε^{mi} without having to worry about the time variation of these phase fractions. Thus, a fictitious, time-depending adsorbate density $\tilde{\varrho}^{ad}$

is modelled, which describes the mass of adsorbate per micropore volume, which is further converted to the loading X.

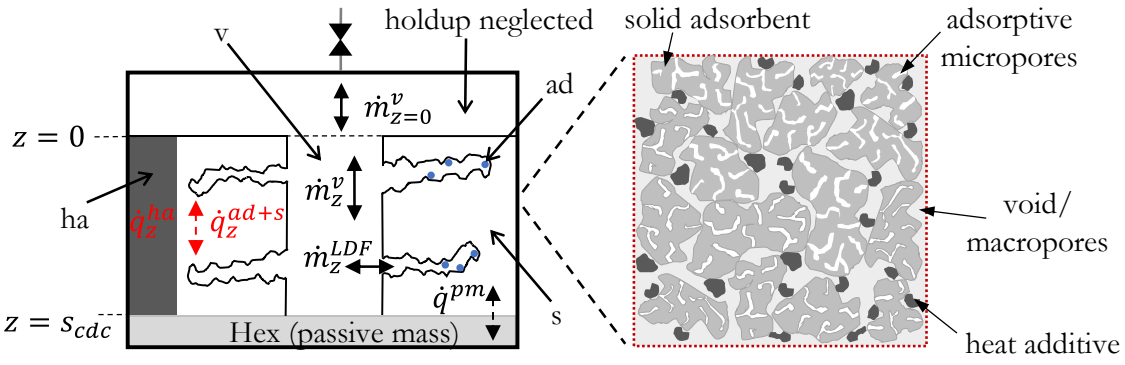

Figure 3-3: Model sketch with the exchanged mass fluxes and heat fluxes (left); local section of an adsorbent composite containing microporous adsorbent particles, interparticle void, and heat additive (right).

Subsequently, the one-dimensional equations of continuity of the individual phases are considered, generally applicable to the material models investigated in this work which is followed by the same procedure for the energy conservation equations. The discretization scheme of the modelled domain is shown in Figure D-1. The model is validated with small-scale experiments which are outlined in Appendix C.

3.2.3.1 Equation of continuity of adsorbent composites

The main underlying assumption in the derivation of the continuity equations is one-dimensional gas transport in the macropores and thus, partial differential equations are obtained. Axial transport in the micropores is neglected resulting in accumulation – source term ODEs for the adsorbate concentration. This approach is used to model mass transport in the macropores resulting in spatially one-dimensional adsorptive concentration profiles over the height of the consolidated adsorbent composites. Micropore transport and kinetic as well as adsorption kinetic is not resolved in detail but rather modelled with an effective driving-force approach.

The equation of continuity describes the time rate of change of mass density in a fixed point in space [102] by the net rate of mass addition

$$\frac{\partial \varrho}{\partial t} + \underbrace{\nabla \cdot \varrho \vec{v}}_{\nabla \cdot \vec{\dot{m}}} = 0. \tag{3-45}$$

Subsequently, the equations of continuity in one spatial coordinate are set up separately for the individual phases shown in Figure 3-3.

The adsorptive density ϱ^v in the interparticle void changes due to the net flux across the element boundaries. It is composed of the net flux exchanged with neighbouring void elements and the flux across the interface of void space and apparent adsorbent particles. The adsorptive flux between interparticle void space and micropores $\dot{m}^{v-mi,v}$ accounts for the adsorption or desorption rate calculated with a linear-driving force approach. With the volume fraction of the void space $\varepsilon^{ma} = V^{ma}/V_{comp}$ and the adsorbent composites width L_x, the one-dimensional continuity equation of adsorptive in the voids results as follows

$$\varepsilon^{ma}\frac{\partial \varrho^v}{\partial t} + \frac{\partial \varepsilon^{ma}\dot{m}_z^v}{\partial z} + \frac{1}{L_x}\dot{m}^{v-mi,v} = 0. \tag{3-46}$$

For 3D-structured adsorbent composites, the void porosity can change with the height and thus ε^{ma}(z) is a function of space. However, assuming adsorption in the void space being negligible, the void volume fraction remains constant throughout the process, and hence, ε^{ma} is no function of time.

Adsorption predominantly occurs in the micropores of the primary particles due to volume filling. The grade of filling strongly depends on the dynamically and spatially varying temperature, pressure, and loading conditions. Therefore, the adsorbate volume-fraction $\varepsilon^{ad}(z,t) = V^{ad}/V_{comp}$ is a function of space and time. The mass flux $\dot{m}^{mi,v-ad}$ accounts for mass transfer across the interface between the adsorbate phase and micropores adsorptive phase. No mass is transferred over the adsorbate-adsorbent interface and hence, $\dot{m}^{ad-s} = 0$. Axial mass flux in the micropores, either in adsorptive or adsorbate phase, e.g., surface diffusion, is neglected, and hence the mass adsorbed solely changes by the rate of adsorption or desorption. Applying these assumptions, the continuity equation of adsorbate is given by

$$\frac{\partial \varepsilon^{ad}(z,t)\varrho^{ad}}{\partial t} - \frac{1}{L_x}\dot{m}^{mi,v-ad} = 0. \tag{3-47}$$

However, resolution of the time-dependency of the adsorbate volume-fraction is inconvenient. This can be overcome by neglecting the holdup in the adsorptive micropores, which is very small compared to the adsorbate mass. Since the dynamic variation in adsorbate volume is equal to the negative change in micropore adsorptive volume,

$$\frac{dV^{ad}}{dt} = -\frac{dV^{mi,v}}{dt}, \tag{3-48}$$

the micropore volume fraction ε^{mi} is only a function of space

$$\varepsilon^{mi}(z) = \varepsilon^{mi,v}(z,t) + \varepsilon^{ad}(z,t). \tag{3-49}$$

Therefore, for the model derivation, it is more convenient to use the apparent adsorbate density $\tilde{\varrho}^{ad}$ (mass of adsorbate referred to the volume of the micropores) which is equal to the adsorbate density ϱ^{ad} in the limiting case of filled micropores. Using $\tilde{\varrho}^{ad}$ is advantageous since the volume of the micropores is stationary whereas the adsorbate volume dynamically changes throughout the process. The apparent and true adsorbate densities can be transferred into each other using the ratios of adsorbate to micropore volume-fraction

$$\tilde{\varrho}^{ad} = \frac{\varepsilon^{ad}(z,t)}{\varepsilon^{mi}(z)}\varrho^{ad}. \tag{3-50}$$

Accordingly, the adsorbate continuity equation can be formulated using the volume fraction of the micropores $\varepsilon^{mi} = V^{mi}/V_{comp}$, transferring the boundary condition to the interface between micropores and interparticle void space

$$\varepsilon^{mi}\frac{\partial\tilde{\varrho}^{ad}}{\partial t} - \frac{1}{L_x}\dot{m}^{v-ad} = 0. \tag{3-51}$$

For 3D-structured adsorbent composites, the volume-fraction of the adsorbent primary-particle phase is a function of the spatial coordinate z. Therefore, the local micropore volume fraction and thus the volumetric adsorption capacity is also a function of space. This gets more obvious when using the practical (mass) loading X instead of $\tilde{\varrho}^{ad}$. Using the loading X and the spatial dependent bulk-density $\varrho^{bulk}(z)$, the experimentally accessible mass of the adsorbent phase M^s and the composite volume V_{comp} are introduced.

$$\varepsilon^{mi}(z)\tilde{\varrho}^{ad} = \varepsilon^{mi}(z)\frac{M^s(z)X}{V^{ad}} = \frac{M^s(z)X}{V_{comp}} = X\varrho^{bulk}(z). \tag{3-52}$$

Using equation (3-52), the micropore continuity equation in terms of loading follows to

$$\varrho^{bulk}\frac{\partial X}{\partial t} - \frac{1}{L_x}\dot{m}^{v-ad} = 0. \tag{3-53}$$

To describe the adsorption and desorption rate exchanged between macropores and micropores $\dot{m}^{v-ad}$ in $[kg/m^2/s]$, a linear driving force (LDF-) approach is used, with the difference of

equilibrium loading and loading serving as driving force. By using the LDF-approach, the total transport resistance of the adsorbent particles is transferred into the boundary surface. By comparing equations (3-53) and (2-47), the boundary condition between macropores and micropores can be identified

$$\dot{m}^{v-ad}\frac{1}{L_x} = k_{LDF}(X^{eq} - X)\underbrace{\frac{M^s}{\Delta y \Delta z}\frac{1}{L_x}}_{M^s/V_{comp}} = k_{LDF}(X^{eq} - X)\varrho^{bulk}. \tag{3-54}$$

Hence, the micropore continuity equation can be written as

$$\varrho^{bulk}\frac{\partial X}{\partial t} = k_{LDF}(X^{eq} - X)\varrho^{bulk}. \tag{3-55}$$

By applying the boundary condition $\dot{m}^{v-ad} = \dot{m}^{v-mi,v}$ on the continuity equation (3-46) of the void space, it finally results to

$$\varepsilon^{ma}\frac{\partial \varrho^v}{\partial t} + \frac{\partial \varepsilon^{ma}\dot{m}_z^v}{\partial z} + \varrho^{bulk}\frac{\partial X}{\partial t} = 0, \tag{3-56}$$

describing the mass density of adsorptive in the interparticle void or macropores of the consolidated adsorbent composites. The Dusty-Gas model is used as the transport approach to describe the mass flux density $\dot{m}_z^v$ with an effective mass transport parameter as transport property (see equation (4-12)).

3.2.3.2 Equation of change for energy

In analogy to the continuity equations, the equations of change for the energy are derived for the individual phases shown in Figure 3-3, which are subsequently coupled with boundary conditions. In addition, it is assumed that the temperature variance over the height of the consolidated composites is much larger than in one cross-sectional layer of the composites, and thus, the energy balances of the individual phases are combined into a quasi-homogeneous energy balance. This approach is common and has some advantages. First, the model size is reduced and second, the transport resistances between the individual phases are not explicitly modelled, for which otherwise suitable approaches would have to be used or experiments conducted.

The equation of change for volume-specific internal energy ϱu (without viscous dissipation) in units $Jm^{-3}s^{-1}$ is given as follows [102]

$$\frac{\partial \varrho u}{\partial t} + \nabla \cdot (\varrho u \vec{v}) + \nabla \cdot \vec{q} + p\nabla \cdot \vec{v} = 0. \tag{3-57}$$

The term $p\nabla \cdot \vec{v}$ represents a reversible mode of energy interchange and describes the interconversion from mechanical into thermal energy. $\nabla \cdot \vec{q}$ is the gradient of the heat flux vector and $\nabla \cdot (\varrho u \vec{v})$ describes "the rate of energy addition per unit volume by convective transport". A more useful formulation of the energy equation is obtained by introducing the specific enthalpy h and in the next step the temperature. With $u = h - p/\varrho$ and the mass flux $\vec{\dot{m}} = \varrho \vec{v}$,

$$\frac{\partial \varrho h}{\partial t} - \frac{\partial p}{\partial t} + \nabla \cdot \left(\vec{q} + \vec{\dot{m}} h\right) - \vec{v} \nabla p = 0. \tag{3-58}$$

In the following sections, the formulation from equation (3-58) is used to formulate energy equations for the individual phases. Subsequently, these equations are summarized to obtain the spatial depending, quasi-homogeneous energy equations of the adsorbent composites in which the adsorption enthalpy occurs as a source term. In equivalence to the continuity equations, the individual energy equations are formulated with spatially dependent volume fractions.

The volume fraction of the heat additive phase for a one-dimensional material is given by $\varepsilon^{ha} = V^{ha}/V_{comp}$. The total differential of the specific enthalpy as a function of temperature and pressure is given as follows

$$dh = \underbrace{\left(\frac{\partial h}{\partial T}\right)_p}_{c_p} dT + \left(\frac{\partial h}{\partial p}\right)_T dp, \tag{3-59}$$

with the specific heat capacity c_p. Energy transport in the heat additive is exclusively by thermal conduction and the heat additive is independent of pressure, thus the energy balance is given by

$$\varepsilon^{ha} \varrho^{ha} c_p^{ha} \frac{\partial T^{ha}}{\partial t} + \frac{\partial \varepsilon^{ha} \dot{q}_z^{ha}}{\partial z} - \frac{\dot{q}^{ha-s}}{L_x} = 0. \tag{3-60}$$

Energy transport across the interface between heat additive and adsorbent $\dot{q}^{ha-s}$ is eliminated with boundary conditions in the summation to the quasi-homogeneous equation.

In equivalence to the heat additive phase, energy transport in the solid adsorbent phase exclusively occurs due to heat conduction

$$\tilde{\varepsilon}^s \tilde{\varrho}^s c_p^s \frac{\partial T^s}{\partial t} + \frac{\partial \varepsilon^s \dot{q}_z^s}{\partial z} + \frac{\dot{q}^{s-ha} - \dot{q}^{s-ad}}{L_x} = 0. \tag{3-61}$$

Here, $\tilde{\varepsilon}^s\tilde{\varrho}^s$ is used which is the apparent volume fraction times the apparent density of the primary particles having the same value as $\varepsilon^s\varrho^s$, but which is experimentally more easily accessible.

Adsorption predominantly occurs in the micropores of the porous primary adsorbent particles due to volume-filling depending on the local pressure and temperature conditions. Therefore, the adsorbate volume-fraction $\varepsilon^{ad}(z,t)$ and micropores adsorptive volume-fraction $\varepsilon^{mi,v}(z,t)$ related to the composite volume are functions of space and time. In analogy to the continuity equation, the energy equation for the adsorbate is formulated related to the stationary micropore volume rather than the dynamic varying adsorbate volume. The energy holdup in the micropore-adsorptive phase is small compared to the contributions from adsorbate and can thus be neglected. Furthermore, since the micropore adsorptive phase rather contributes to the spatial transport nor contains a sink term, it exclusively consists of the accumulation term and fluxes across the adjacent interfaces, which are vanishing when summing up the individual energy equations to the quasi-homogeneous energy equation. For an ideal fluid, the differential specific enthalpy is given as follows

$$dh = c_p dT + \frac{1}{\varrho} dp. \tag{3-62}$$

Applying the beforementioned assumptions on equation (3-58), the adsorbate energy equation in terms of apparent adsorbate density $\tilde{\varrho}^{ad}$ is given by

$$\varepsilon^{mi}\left(h^{ad}\frac{\partial\tilde{\varrho}^{ad}}{\partial t} + \tilde{\varrho}^{ad}c_p^{ad}\frac{\partial T^{ad}}{\partial t}\right) + \frac{\partial\varepsilon^{mi}\tilde{q}_z^{ad}}{\partial z} + \frac{\dot{q}^{\,ad-s} - (\dot{m}h)^{\,ad} + (vp)^{\,ad}}{L_x} = 0. \tag{3-63}$$

In equivalence to the apparent adsorbate density $\tilde{\varrho}^{ad}$ (equation (3-50)), the apparent or rather effective heat conduction in the micropores $\tilde{q}_z^{ad}$ is correlated with the heat conduction in the adsorbate phase via the volume fractions of adsorbate and micropores

$$\tilde{q}_z^{ad} = \frac{\varepsilon^{ad}(z,t)}{\varepsilon^{mi}(z)}\dot{q}_z^{ad}. \tag{3-64}$$

With equation (3-52), the adsorbate energy equation is expressed in terms of mass loading X

$$\varrho^{bulk}h^{ad}\frac{\partial X}{\partial t} + \varrho^{bulk}c_p^{ad}X\frac{\partial T^{ad}}{\partial t} + \frac{\partial\varepsilon^{mi}\tilde{q}_z^{ad}}{\partial z} + \frac{\dot{q}^{\,s-ad} - (\dot{m}h)^{\,ad} + (vp)^{\,ad}}{L_x} = 0. \tag{3-65}$$

Finally, the energy equation for the interparticle void space with volume fraction ε^{ma} contains the accumulation term and transfer contributions across the interfacial boundaries. Assuming

ideal gas behaviour with the differential enthalpy $dh = c_p dT$, the energy equation of the interparticle void space is given by

$$\left(\varepsilon^{ma}\varrho^v c_p^v - \varepsilon^{ma}\frac{R}{MW}\varrho^v\right)\frac{\partial T^v}{\partial t} + \left(\varepsilon^{ma}h^v - \varepsilon^{ma}\frac{R}{MW}T^v\right)\frac{\partial \varrho^v}{\partial t} + \varepsilon^{ma}\dot{m}_z^v c_p^v\frac{\partial T^v}{\partial z} + h^v\frac{\partial \varepsilon^{ma}\dot{m}_z^v}{\partial z} - v_z^v\frac{\partial \varepsilon^{ma}p}{\partial z} + \frac{(\dot{m}h)^v}{L_x} - \frac{(vp)^v}{L_x} = 0. \tag{3-66}$$

Equations (3-60), (3-61), (3-65), and (3-66) are describing the energy equations of the individual phases shown in Figure 3-3 on the left. If the individual temperatures are of interest, these balances can be solved separately and coupled via boundary conditions. However, assuming the temperature differences with the z-coordinate being large compared to the temperature differences in adjacent phases on the same height level, a quasi-homogeneous energy equation can be derived. Therefore, the temperature is exclusively a function of z and not of the individual phases

$$T \equiv T^v|_z = T^{ad}|_z = T^s|_z = T^{ha}|_z. \tag{3-67}$$

For coupling of the individual energy equations, the following set of boundary conditions is used

$$\begin{aligned} \dot{q}^{s-ha} - \dot{q}^{ha-s} &= 0, \\ \dot{q}^{ad-s} - \dot{q}^{s-ad} &= 0, \\ (\dot{m}h)^v - (vp)^v - (\dot{m}h)^{ad} + (vp)^{ad} &= 0. \end{aligned} \tag{3-68}$$

Furthermore, the enthalpy difference between adsorbate enthalpy h^{ad} and adsorptive enthalpy h^v is the adsorption enthalpy introduced in equation (2-27)

$$\Delta_{ads}h = h^{ad} - h^v. \tag{3-69}$$

Using these relations and the continuity equation (3-56), the individual energy equations are summed up to the quasi-homogeneous energy equation in the unit $Jm_{comp}^{-3}s^{-1}$

$$\left(\varepsilon^{ha}\varrho^{ha}c_p^{ha} + \tilde{\varepsilon}^s\tilde{\varrho}^s c_p^s + \varrho^{bulk}Xc_p^{ad} + \varepsilon^{ma}\left(\varrho^v c_p^v - \frac{R\varrho^v}{MW}\right)\right)\frac{\partial T}{\partial t} - \varepsilon^{ma}\frac{RT}{MW}\frac{\partial \varrho^v}{\partial t} + \varrho^{bulk}\Delta_{ads}hk_{LDF}(X^{eq} - X) + \frac{\partial(1-\varepsilon^{ma})\dot{q}_z^{ha+s+ad}}{\partial z} + \varepsilon^{ma}\dot{m}_z^v c_p^v\frac{\partial T}{\partial z} - v_z^v\frac{\partial \varepsilon^{ma}p}{\partial z} = 0. \tag{3-70}$$

The term $v_z^v\frac{\partial \varepsilon^{ma}p}{\partial z}$ is often quite small and negligible compared to the adsorption enthalpy and heat conduction terms. For the effective thermal conductivity λ^{eff} in the gradient of the effective heat conduction $\dot{q}^{eff}$

$$\frac{\partial(1-\varepsilon^{ma})\dot{q}_z^{ha+s+ad}}{\partial z} = \frac{\partial \dot{q}^{\,eff}}{\partial z} = -\frac{\partial\left(\lambda^{eff}(z)\frac{\partial T}{\partial z}\right)}{\partial z}, \tag{3-71}$$

the approaches derived in section 2.4 are used. Especially for the application of 3D-structured adsorbent composites, the spatial dependency of the effective thermal conductivity is of crucial importance which needs to be considered when discretizing the gradient of the heat conduction. For the equilibrium loading X^{eq} in the linear driving-force approach, the Dubinin-Astakhov adsorption isotherm introduced in section 2.1.2 is used. For the adsorptive mass flux in the interparticle voids $\dot{m}_z^v$, the Dusty-Gas model introduced in sections 2.2.5 and 4.4.2 is used as transport approach.

3.2.3.3 Boundary conditions

For solving the set of partial differential equations (equations (3-56), (3-28)), a set of boundary conditions for the upper and lower layer of the adsorbent composites is required. For the bottom layer ($z = s_{cdc}$) of the adsorbent composites (CDC = carbide derived carbon), no-flux mass and Neumann energy boundary conditions are applied

$$\dot{m}^v|_{z=s_{cdc}} = 0, \tag{3-72}$$

$$\left.\frac{\partial T}{\partial z}\right|_{z=s_{cdc}} = \frac{k^{pm}}{\lambda_{eff}}\left(T^{pm} - T|_{z=s_{cdc}}\right). \tag{3-73}$$

The energy boundary condition is obtained by using the equality of the heat fluxes $\dot{q}^{\,pm} = \dot{q}^{\,eff}$. For the boundary conditions at the interface of adsorbent composites and gas phase ($z = 0$), it is necessary to distinguish between the adsorption and the desorption mode of the adsorber. To check whether the check valves are open or closed, the pressure differences between adsorber and evaporator, and adsorber and condenser are evaluated, respectively. In the evaporation step, a check valve is open when $p_e^{sat} > p^v|_{z=0}$ and in the condensation step, if $p_c^{sat} < p^v|_{z=0}$. In pre-cooling and pre-heating, the check valves are closed. Therefore, the following density Neumann and Dirichlet boundary conditions and temperature Neumann and Danckwerts [121] boundary conditions apply to the adsorber in the adsorption half cycle

$$\left.\frac{\partial \varrho^v}{\partial z}\right|_{z=0} = 0 \qquad if\ p_e^{sat} < p^v|_{z=0} \tag{3-74}$$

$$\varrho^v|_{z=0} = \frac{p_e^{sat} MW}{RT|_{z=0}} \qquad if\ p_e^{sat} \geq p^v|_{z=0} \tag{3-75}$$

$$\left.\frac{\partial T}{\partial z}\right|_{z=0} = 0 \qquad if\ p_e^{sat} < p^v|_{z=0} \tag{3-76}$$

$$\dot{m}^v|_{z=0} c_{p,e}(T|_{z=0} - T_e) = \left.\left(\dot{m} c_p^v \frac{\partial T}{\partial z} + \frac{\partial \dot{q}}{\partial z}\right)\right|_{z=0} \qquad if\ p_e^{sat} \geq p^v|_{z=0}. \tag{3-77}$$

In the pre-heating and condensation steps (desorption half cycle), the following Neumann and Dirichlet density and Neumann temperature boundary conditions apply to the top layer of the adsorbent composites

$$\left.\frac{\partial \varrho^v}{\partial z}\right|_{z=0} = 0 \qquad if\ p_c^{sat} > p^v|_{z=0} \tag{3-78}$$

$$\varrho^v|_{z=0} = \frac{p_c^{sat} MW}{T^v|_{z=0} R} \qquad if\ p_c^{sat} \leq p^v|_{z=0} \tag{3-79}$$

$$\left.\frac{\partial T}{\partial z}\right|_{z=0} = 0. \tag{3-80}$$

3.2.3.4 Summary of microscopic model equations and boundary conditions

	Adsorber
Heat transfer fluid	Adsorption: $T^{hf} = T_{ads}^{min}$ Desorption: $T^{hf} = T_{des}^{max}$
Energy balance Hex	$m^{pm} c_p^{pm} \frac{\partial T^{pm}}{\partial t} = \dot{q}^{hf} - \dot{q}^{pm}$
Mass balance of adsorbent comp.	$\varepsilon^{ma} \frac{\partial \varrho^v}{\partial t} + \frac{\partial \varepsilon^{ma} \dot{m}_z^v}{\partial z} + \varrho^{bulk} \frac{\partial X}{\partial t} = 0$
Energy balance of adsorbent comp.	$\left(\varepsilon^{ha} \varrho^{ha} c_p^{ha} + \tilde{\varepsilon}^s \tilde{\varrho}^s c_p^s + \varrho^{bulk} X c_p^{ad} + \varepsilon^{ma}\left(\varrho^v c_p^v - \frac{R \varrho^v}{MW}\right)\right)\frac{\partial T}{\partial t}$ $- \varepsilon^{ma} \frac{RT}{MW} \frac{\partial \varrho^v}{\partial t} + \varrho^{bulk} \Delta_{ads} h k_{LDF}(X^{eq} - X)$ $+ \frac{\partial (1 - \varepsilon^{ma}) \dot{q}_z^{ha+s+ad}}{\partial z} + \varepsilon^{ma} \dot{m}_z^v c_p^v \frac{\partial T}{\partial z} - v_z^v \frac{\partial \varepsilon^{ma} p}{\partial z} = 0.$

BC top layer adsorbent comp.	$\left.\frac{\partial \varrho^v}{\partial z}\right\|_{z=0} = 0$	$if\ p_e^{sat} < p^v\|_{z=0}$
	$\varrho^v\|_{z=0} = \frac{p_e^{sat} MW}{RT\|_{z=0}}$	$if\ p_e^{sat} \geq p^v\|_{z=0}$
	$\left.\frac{\partial T}{\partial z}\right\|_{z=0} = 0$	$if\ p_e^{sat} < p^v\|_{z=0}$
	$\dot{m}^v\|_{z=0} c_{p,e}(T\|_{z=0} - T_e) = \left(\dot{m} c_p^v \frac{\partial T}{\partial z} + \frac{\partial \dot{q}}{\partial z}\right)\Big\|_{z=0}$	$if\ p_e^{sat} \geq p^v\|_{z=0}$
BC bottom layer adsorbent comp.	$\dot{m}^v\|_{z=s_{cdc}} = 0$	
	$\left.\frac{\partial T}{\partial z}\right\|_{z=s_{cdc}} = \frac{k^{pm}}{\lambda_{eff}}\left(T^{pm} - T\|_{z=s_{cdc}}\right)$	

	Evaporator
Energy balance of refrigerant	$\dot{q}_e = \dot{m}_e \Delta_{evap} h(T_e) - \dot{m}_{ec} c_{p,c}^l (T_c - T_e)$
	$T_e = const.$

	Condenser
Energy balance of refrigerant	$\dot{q}_c = \dot{m}_c \Delta_{evap} h(T_c) + \dot{m}_c c_{p,des}^v (T_{des} - T_c)$
	$T_c = const.$

4. Experimental Characterization of carbonaceous adsorbents

For the application in technical devices, the adsorbent is applied in a variety of ways ranging from loose grains or consolidated beds over binder-based coatings to in-situ directly synthesized adsorbents [33]. All shapes have their pros and cons which can be summarized to the antagonistic behaviour concerning mass transport, heat transport, and adsorption capacity. Depending on the shape of the technical adsorbents used, only the material model must be adapted. However, for the application of a combined material and process design, the shape of the adsorbent is of subordinate importance. The methods presented in this work can be applied to any form of adsorbent.

In this work, exemplarily consolidated composites with cuboid shape are investigated, since they can be easily manufactured with varying compositions, e.g., amount and type of adsorbent, additive, and binder. In addition, consolidated composites are promising to improve the performance of adsorption heat transformers [35]. In many studies, the focus was laid on the production of consolidated adsorbent composites with a binder, sometimes adding heat-conducting material, all aiming to either improve heat or mass transport as well as the compactness to increase the volumetric adsorption capacity of the AdHex [19], [28], [122], [123]. However, increasing one parameter is mostly accompanied by a decrease of another. Finally, there is always the question of the adsorbent composition and how the adsorbent should be designed, which should be answered by taking the specific application and mode of operation into account.

In this chapter, the material models introduced in section 2.4 are parameterised by experiments. The parameterised material models can subsequently be applied in the mathematical models of an adsorption refrigerator outlined in chapter 3. The aim is to identify structure-property correlations and thus to correlate the material and transport parameters with the composites composition and to identify the competing material properties in large parameter space. For that purpose, carbonaceous adsorbents are investigated in powdered shapes, and in addition, consolidated composites with different compositions are experimentally characterized. In particular, the following material parameters are identified in this chapter to parameterise the material models: parameters of Dubinin-Astakhov adsorption isotherm (w_0, E, n), Dusty-Gas model parameters (B_0^{eff}, D_{MeOH}^{Kn}), thermal conductivity and specific heat capacity of the adsorbent

($\tilde{\lambda}^s, c_p^s$), bulk and skeleton densities (ϱ^{bulk}, ϱ^{skel}), macro- and micropore porosity ($\varepsilon^{ma}, \varepsilon^{mi}$), and macro- and micropore size (d^{ma}, w_p).

This chapter is outlined as follows: Initially, the investigated adsorbent composites and their production routine are introduced. Subsequently, the characterisation methods and results obtained for selected samples are presented, starting with the inter- and intraparticle pore analysis. This is followed by characterization of the adsorption capacity, mass transport capability as well as the thermal conductivity of the consolidated composites. Most of the methods and materials investigated in this chapter have been published in short by Träger et al. [34]. Here, more detailed insight and more results are presented.

The reader is informed that this chapter does not need to be read to understand the following chapters.

4.1 Adsorbent and production of consolidated composites

In this work, two different powdered carbonaceous adsorbents are investigated, namely, Titanium carbide-derived carbon (Ti-CDC, short: CDC) and a commercial activated carbon (AC; VWR Chemicals; charcoal activated (vegetable-based); technical [34]). Consolidated composites of these adsorbents were investigated in the context of applicability for adsorption refrigeration. In a DFG funded project[2], CDCs were chosen as adsorbents since their potential as model materials with tuneable properties and a high reproducibility during the synthesis has been demonstrated in several applications [34]. The synthesis of the CDCs, characterisation of the powdered adsorbents, as well as the preparation of the consolidated composites, was carried out by the Etzold working group[3], particularly during the Ph.D. thesis of L. Träger [124]. In the following, this work is briefly reproduced.

Among others, CDC primary particles were synthesised by chlorination of titanium carbide powder, showing a good performance in the application of adsorption. Synthesis of CDC has two main technical advantages: The overall shape of the carbide is retained during chlorination

[2] DFG – Deutsche Forschungsgemeinschaft (German Research Foundation) – project number: NI 932/10-1 & ET 101/11-1

[3] Technical University of Darmstadt, Department of Chemistry, Ernst-Berl-Institut für Technische und Makromolekulare Chemie, 64287 Darmstadt, Germany, www.etzoldlab.de

and the pore size distribution can be adjusted by the choice of the precursor carbide and chlorination temperature [125]. For details of the reactive extraction of titanium carbide see Träger et al. [34], [124]. Among others, microporous CDC-powders with particle fractions of 50-75 µm and 75-150 µm were produced, to investigate the influence of particle size. The maximal particle size of the activated carbon was 80 µm. Based on the powdered active materials, consolidated cuboid adsorbent composites were prepared with different types and amounts of binders and types and amounts of heat conduction additives in a binder-based approach. In detail, sodium carboxymethyl cellulose (CMC) with usually 2 wt% and polytetrafluoroethylene (PTFE), with usually 15 wt% have been investigated as binders. Furthermore, boron nitride (BN), silver (Ag) and graphite powder (C) with varying amounts have been investigated as heat conducting additives. The suspensions containing adsorbent, binder, binder-solvent and thermal conductive additive were cold pressed uniaxially in a hydraulic laboratory press to form the cuboid consolidated adsorbent composites. The composites with dimensions of 45 x 15 mm with varying thickness have been produced at ambient temperature and 363 bar with a hydraulic lab press. In addition to the adsorbent preparation, experimental characterisations were conducted in the Etzold working group on the carbonaceous composites regarding the influence of binder on the BET surface, the interparticle void distribution, mechanical stability as well as effective thermal conductivity [124].

Partly, some of the results are reproduced in the present work and some measurements were repeated for comparison and completion of the effective material models. The respective results and methods are marked if they do not correspond to an own contribution. However, the experimental focus of this thesis was laid on the characterisation of the consolidated composites regarding their applicability for adsorption refrigeration using methanol as the refrigerant. To identify structure-property correlations, several consolidated composites with varying compositions were investigated for methanol adsorption capacity and effective mass transport. Additionally, thermal diffusivity and specific heat capacity were measured for selected samples. Table B-1 in Appendix B gives an overview of the samples examined in this work and the measurements carried out.

4.2 Pore analysis of powdered active materials and consolidated composites

The number of molecules a porous material can adsorb from a bulk gas phase is directly linked to the internal surface area of the pore walls, or in microporous adsorbents, to the micropore

volume. Consequently, knowledge of these quantities is of great interest in the characterization of porous materials. It is assumed that a major part of the adsorption capacity is attributed to the pore network in the primary particles (mainly micropores in the CDCs; micropores and mesopores in the AC), whereas adsorption on the outer particle surface and adsorption in the voids of the composites is negligible. Besides adsorption capacity, the internal pore volume of the particles or rather the particle porosity is of interest since a high porosity is advantageous for mass transfer but disadvantageous for heat transfer. Furthermore, the pore size distribution (or the mean pore width) is crucial concerning the mass transport in the primary particles. The beforementioned material quantities can be obtained from the measurement of the powdered carbon active materials. However, concerning the applicability in technical processes, powdered adsorbents are unpractical, requiring adsorbent agglomerates or consolidated composites of adsorbents. These consolidated composites consist of the active carbon material, binders and may additionally be enriched with heat-conducting additives, which poses further questions regarding the material properties. Do the binders and heat-conducting additives influence the adsorption capacity as well as mass and heat transfer rates in the consolidated adsorbent? And if so, is it possible to identify structure-property correlations? To address these questions, the focus of material characterization is on the study of consolidated composites with varying compositions.

The material parameters, concerning the powdered active materials, are determined by nitrogen physisorption measurements and their evaluation by classical methods. These measurements and characterizations were part of the Ph.D. thesis of L. Träger [124] and were published in a joint publication [34]. The results and methods are only briefly summarized here (see section 4.2.1) to provide an understanding of the derivation of the effective material models of the consolidated composites at the various scales and the origin of the material parameters as well as to parameterise the material models. In particular, the analysis of the powdered active materials delivers the following parameters required for the effective material models: volume fraction of micropores (ε^{mi}) and average micropore size (w_p).

Furthermore, characterisation measurements related to the application in the adsorption refrigeration process were carried out on consolidated composites with the aim to further parameterise the effective material models outlined in section 2.4. The void network between powdered adsorbent-particles (also termed macropores in this work) was investigated with mercury intrusion revealing the macroporosity (ε^{ma}) and mean width of transport pores (d^{ma}) in the consolidated composites. In addition, skeleton (ϱ^{skel}) and bulk density (ϱ^{bulk}) are obtained from these measurements and a BET surface area analysis is conducted for selected samples.

4.2.1 Characterization of powdered carbon active material

Nitrogen physisorption experiments and classical evaluation methods (e.g., BET method) are still widely disseminated in the characterization of porous materials, despite their questionable applicability in the presence of micropores and the advantages provided by computational methods. Already in 2001, concerning the developments in computational methods, Sing questioned, why the BET method is still used for the characterization of microporous materials [62]. And, it is evident, that DFT (and related methods), as well as molecular dynamics simulations, are powerful when correct assumptions are met [126]. Thus, besides experimental characterization, computational methods are nowadays state of the art in the characterisation of microporous materials e.g., [126], [127], which, however, is not part of this work. The interested reader is referred to the extensive work concerning DFT methods in porous media e.g., provided by Landers et al. [128].

Still, especially for new materials with unordered, heterogeneous pore structures, classical methods give a quick, first insight and the quantities obtained from nitrogen physisorption experiments are still useful fingerprints of porous materials [20], [57], [62], [129], [130].

Nitrogen physisorption measurements on AC- and CDC-samples with varying binders were conducted during the Ph.D. thesis of L. Träger [124]. Two experiments with relevant binder and amount of binder are reproduced here and the evaluation with the BET method and Gurvich rule examined. The nitrogen physisorption measurements were performed with a Quantachrome (Quadrasorb SI) at 77 K over the complete range of relative pressure $\phi = p/p_{sat} = 0 - 1$. Degassing of the samples was initially performed under fine vacuum at 120 °C for 22 h [34]. Figure 4-1 shows the adsorption isotherms in terms of adsorbed volume and molecules per mass adsorbent as a function of relative pressure in normal (top) and semi-logarithmic scale (bottom) for the CDC and AC powdered material.

The CDCs exhibit isotherms that can be classified between Type I(b) and Type II and the AC shows rather isotherms of Type I(a) and IV(a) according to the IUPAC classification [48], [57] with a small hysteresis (a marginal hysteresis can also be identified in the CDC isotherms). The adsorption capacity of AC is lower than that of CDC, with the smaller CDC particles having a slightly higher capacity than the larger particles, which may be due to the larger external surface area or better accessibility to the internal porosity.

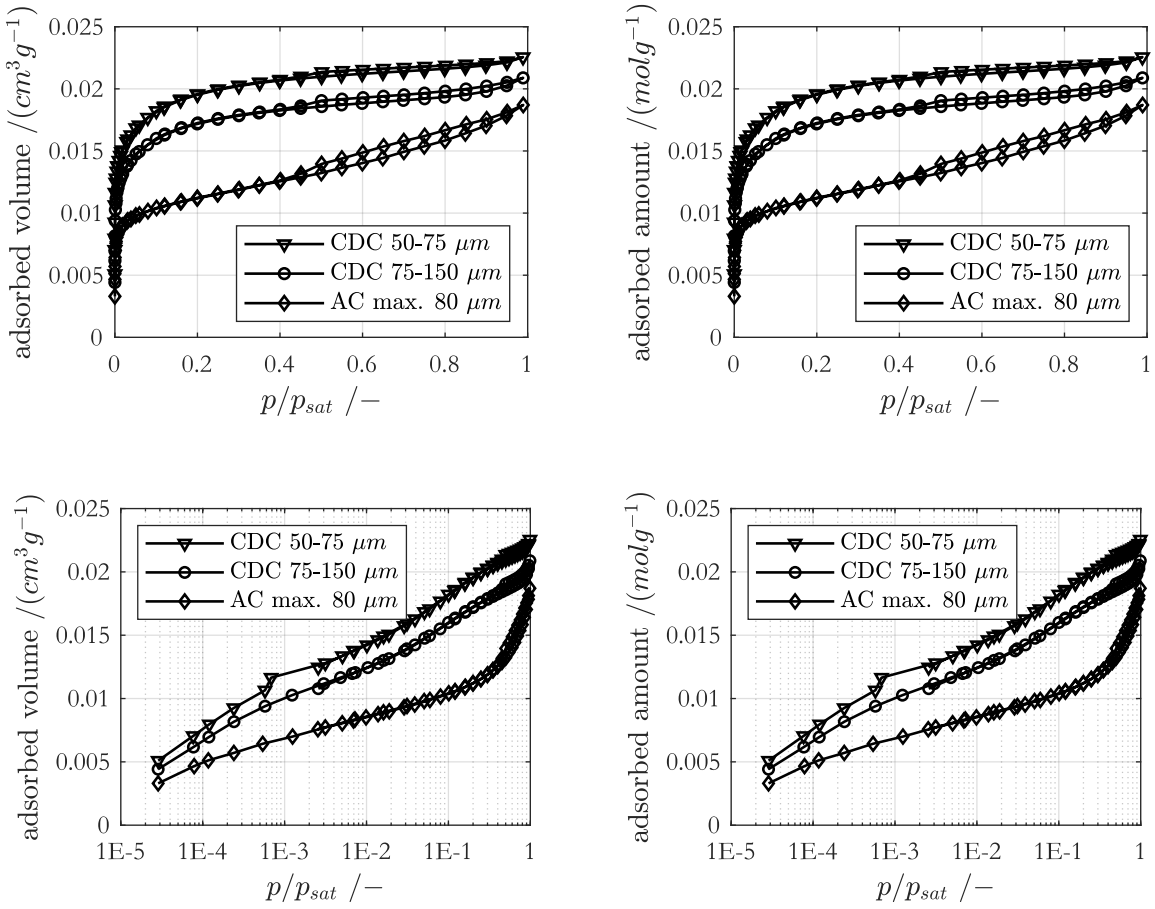

Figure 4-1: Adsorption isotherms of AC and CDC with different particle fractions as a function of relative pressure. Left in terms of volume adsorbed and on the right in terms of amount adsorbed. In the two graphs below, the abscissa is shown semi-logarithmically.

However, it is difficult to pinpoint with certainty the exact reason. A superposition of several effects is also conceivable. All the presented isotherms exhibit a steep rise at low relative pressures indicating adsorption in micropores, e.g., volume filling. With increasing relative pressure, the adsorbed amount in the CDCs continues to increase slightly, indicating adsorption at the external surface or to some extend in mesopores which are present in addition to micropores. No specific relative pressure can be assigned to the transition from volume filling to the external surface and mesopore adsorption, however, since the adsorbed amount increases only slightly from approx. $\phi = 0.2$, it is predominantly micropores that contribute to the intraparticle porosity. In AC, on the other hand, the transition from micropore volume filling to the external surface and mesopore multilayer adsorption occurs more sharply and is already at a very low relative pressure of about $\phi = 0.02$. At this point, the adsorbed amount in the AC is significantly lower than in the CDCs indicating a lower micropore volume. The increase in

loading with increasing relative pressure is larger for the AC than that for the CDCs, which conversely indicates a larger mesopore volume and/ or external surface.

As the preceding discussion shows, identifying a unique isotherm type is often difficult. In fact, for microporous materials, one usually obtains a composed isotherm of Type I and II (which arises from micropores and outer surface) or Type I and IV (which arises from micropores and mesopores) [66].

By applying the BET method to the nitrogen physisorption measurements obtained by Träger [124], the specific internal surface area (for microporous materials more appropriately termed apparent surface area [57]) can be determined. Furthermore, using the Gurvich rule, the micropore volume and average pore size can be calculated when assuming a slit pore geometry. The application of the BET method requires a prior determination of the linear BET range. According to Thommes et al. [57], the linear range is evaluated by using the linear form of the BET isotherm from equation (2-15) which is exemplified here for the CDC sample with a smaller particle fraction (50-75 µm). By plotting the left-hand side versus the relative pressure, the BET plot in Figure 4-2 (left) is obtained.

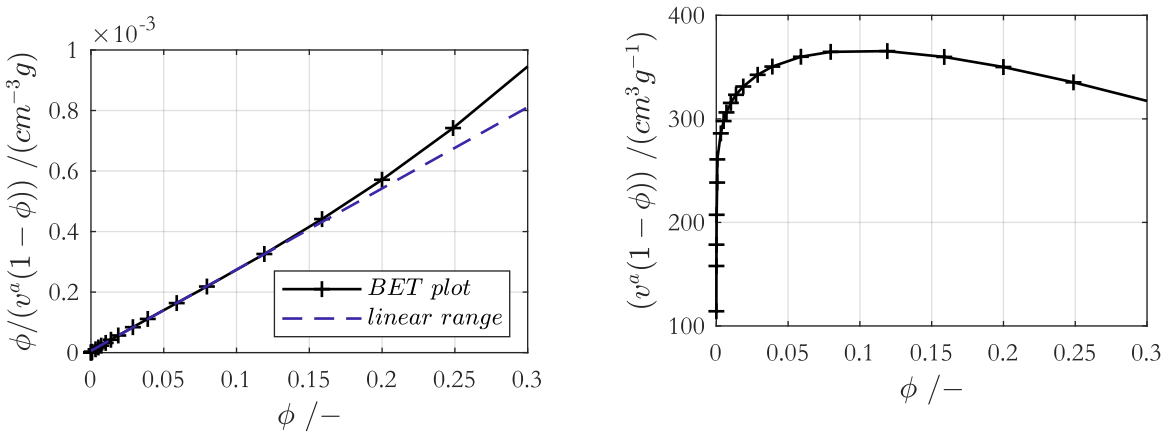

Figure 4-2: BET plot (left) with the linear range and determination of the monotonously increasing range of the BET-plot with $\phi = p/p_{sat}$ (right) for the sample CDC 50-75 µm.

Furthermore, the linear range is indicated, however difficult to identify. For this reason, a plot of the denominator of the left-hand side of equation (2-15) versus the relative pressure is more appropriate as shown in Figure 4-2 (right). The upper limit of the BET range for this CDC sample can thus be identified at approx. $\phi = 0.12$. For the lower limit, Brunauer-Emmet-Teller originally proposed $\phi \sim 0.05$. In the present work, the lower limit is chosen to $\phi = 0.01$ which guarantees that enough measurement points are considered for the fit. It was verified that the exact value of the lower limit has no influence on the resulting fit parameters if the lower, non-

linear region of the BET plot is excluded. The identical procedure was used to determine the BET range for the other samples.

From the BET equation in the linear form (equation (2-15)) the monolayer capacity $v_m^{v,ad}$ and parameter b were obtained followed by calculation of the specific equivalent BET surface area a^s (equation (2-16)), using the cross-sectional area occupied by one adsorbed nitrogen molecule $\sigma_{m,N_2} = 0.162nm^2$ [57]. Assuming a slit pore geometry (two parallel pore walls each with specific surface area $a^s/2$), the mean (micro-) pore width is finally calculated by

$$w_p = \frac{2v_p}{a^s}, \tag{4-1}$$

with the specific internal volume v_p (intraparticle pore volume per mass adsorbent). The internal volume (for microporous solids, the term "micropore volume" is not appropriate and is better termed "saturation capacity" [66]) of pores in microporous materials is an important characteristic parameter. Concerning experimental methods, the Gurvich rule is still state of the art in determining the saturation capacity [131]. Even though in practice, the plateau of the adsorption isotherm is rarely horizontal and, thus, a sharp distinction between micropore and mesopore adsorption is difficult [57]. The Gurvich rule is a quick method, to get an idea of the intraparticle pore volume of adsorbent materials with a predominantly microporous nature. In this method, the density of the adsorbed molecules is assumed to be identical to a hypothetical liquid phase at bulk conditions without taking the shape of the intraparticle pore network into account and regardless of the surface chemistry of the adsorbent [131]. Thus, the intraparticle pore volume with respect to the adsorbent mass is calculated by

$$v_p = \frac{max(v^{v,ad})MW_{N_2}}{\varrho_{N_2}^l v_0} = \frac{X^{sat}}{\varrho^l}, \tag{4-2}$$

using the specific adsorbed gas volume close to saturation (in the present work, $\phi \approx 1$ is used). X^{sat} is the specific loading with filled (saturated) intraparticle pore volume in units mass adsorbate per mass adsorbent and MW is the molar weight. The liquid density of nitrogen is $\varrho_{N_2}^l = 0.808\ gcm^{-3}$. With the apparent particle density $\varrho_{app,par}$ in kg^s/m_{par}^3, the particle porosity in m_p^3/m_{par}^3 is (included are all intraparticle pores which could be micropores and mesopores)

$$\varepsilon_{p,par} = v_p \varrho_{app,par}. \tag{4-3}$$

The particle density is the apparent density of a single particle obtained with a non-wetting fluid, e.g., by mercury intrusion, (volume of accessible and non-accessible pores included). However, concerning the effective material models (section 2.4) and differential equations of the microscopic level model describing the consolidated composites (section 3.2.3), $\varepsilon_{p,par}$ is not of great interest. Rather the particles pore volume related to the consolidated composite volume $\varepsilon^{mi} \equiv \varepsilon_{p,comp}$ in m^3_{mi}/m^3_{comp} is needed, given by

$$\varepsilon^{mi} \equiv \varepsilon_{p,comp} = \frac{V_p}{V_{comp}} = v_p \varrho^{bulk}. \tag{4-4}$$

The bulk density of the consolidated composite ϱ^{bulk} can either be obtained by measurement of the macroscopic lengths to calculate the composite volume and dividing it by its mass. Or more sophisticated using the bulk density obtained from mercury intrusions at an applied pressure of 1 bara (see section 4.2.2). X^{sat}, n^{ad} or $v^{v,ad}$ are classically obtained from N_2 physisorption measurements, just before it starts to adsorb at the outer particle surface. For microporous adsorbents with a well-defined, horizontal plateau (e.g., Type I isotherm), the exact ratio of ϕ is not of great importance. However, as stated above, in the presence of mesopores a clear distinction between micro- and mesopore adsorption and, thus, a clear determination is difficult. Typically, $v^{v,ad}$ is obtained at a ratio of ϕ of $0.9 - 0.95$ which includes any pores smaller than $20 - 40\ nm$ [127], [131], resulting in an internal pore volume containing micro- and mesopores. Furthermore, especially in the presence of ultra-micropores the size of the adsorptive molecule is of importance since some voids cannot be accessed while still contributing to the internal pore volume, which can be analysed using the molecular probe method [129]. As a reason, Ongari et al. proposed the term 'occupiable pore volume', since this is the volume obtained from experiments and which should be used to compare results obtained by DFT methods [127]. An alternative experimental method to estimate the internal pore volume is the Dubinin-Radushkevich-method [132]. However, there are some inaccuracies which is why the Gurvich rule is more reliable and disseminated [62].

A summary of the values determined for the three samples examined in this section is given in Table 4-1. The CDC sample with the small particles has the largest adsorption capacity (as discussed previously) accompanied by the largest 'equivalent BET surface area', internal volume, and the smallest average pore width.

Table 4-1: Characteristic values of the investigated powdered carbon active materials obtained from N2 physisorption experiments and evaluated with the BET method and the Gurvich rule.

	CDC 50-75 µm	CDC 75-150 µm	AC max. 80 µm
$BET\ range\ /-$	0.01-0.12	0.01-0.12	0.01-0.08
$v_m^{v,ad}(BET)/(cm^3g^{-1})$	372	327	213
$b(BET)/-$	459	425	681
$a^s(BET)/(m^2g^{-1})$	1619	1423	927
$v_p/(cm^3g^{-1})$	0.78	0.72	0.65
w_p/nm	0.97	1.02	1.40

4.2.2 Characterization of consolidated composites containing carbon active material, binder, and heat-conducting additive

Quantities in the macropore range are not obtained by gas sorption measurements which is why other methods are needed to characterize the larger pore ranges. A standard experimental procedure to obtain these quantities is mercury intrusion which is thus complementary to gas sorption procedures for characterization of porous media. However, one should not expect to attain the same results in the overlapping range, when using two different methods with very different underlying models [51]. In mercury intrusion measurements, liquid mercury is forced into the voids and pores of the porous sample by increasing external pressure. With increased pressure, more and more voids and then pores in the primary particles can be filled by the liquid mercury. Since the interparticle voids are generally larger than pores in the individual particles, these voids are filled at lower pressures and hold more mercury than intraparticle pores. In other words, the intrusion rate of mercury with rising pressure is greater while the voids are filled compared to the intrusion rate when the intraparticle pores are filled [51]. As a result of this, the completion of interparticle void filling can be identified on the intrusion curve by an abrupt change in the filling rate. From this inflection point, the total volume of the interparticle voids and following the macroporosity as well as the void widths can be identified.

The external pressure p directly correlates with the void width d^{ma}, the angle of contact Θ ($\Theta_{\mathrm{Hg}} = 140°$) between liquid mercury and solid surface as well as the surface tension σ ($\sigma_{Hg} = 0.48\ N/m$) which was suggested by Washburn in 1921 [133]

$$r^{ma} = \frac{d^{ma}}{2} = -\frac{2\sigma}{p} cos\Theta. \tag{4-5}$$

The Washburn equation concisely correlates the pressure required to force a non-wetting liquid with surface tension σ into an equivalent circular capillary with a radius r^{ma} or diameter d^{ma} [51]. Due to the non-wetting behaviour, mercury is ideally suited for use in intrusion experiments to characterize porous media.

For a mercury intrusion measurement, a porous sample is initially placed in a vacuum chamber and evacuated allowing all adsorbed contaminants to be removed. While still under vacuum, the sample chamber is filled with mercury creating a system containing the dry, porous sample, the non-wetting liquid mercury, and its vapor. The value of the bulk density is obtained at the point before the mercury starts to enter the voids of the consolidated sample (at approx. 100 mbar abs.). For further initialization, the pressure is increased to ambient allowing the liquid phase to enter large fractures with diameters above $d^{ma}(1\ bar) = 6\ \mu m$ [52]. Subsequently, the sample container is placed in a pressure chamber, where the pressure could be increased up to 400 MPa [51]. By increasing the pressure up to this value, mercury is forced into pores down to about $d^{ma} = 3\ nm$ according to the Washburn equation. The volume intruded into the porous sample when increasing the pressure from p_i to p_{i+1} corresponds to the volume of pores in the size range from d_i^{ma} to d_{i+1}^{ma}. To obtain the correct volumes, the intrusion process needs to equilibrate before increasing the pressure to the next level and probing the next smaller pores. Measurement of the intruded volume can be obtained from the volume decrease in a capillary attached to the pressure chamber. The correlation of increasing pressure and intruded volume is called intrusion curve whereas the extrusion curve is obtained when decreasing the pressure and measuring the corresponding extruded volumes. Figure 4-3 (left) shows the intrusion and extrusion curves of a compacted CDC composite with primary particle sizes of 50-75 µm and 2 wt% of CMC binder (sample P_{68}, termed "Exp_{CDC}") as function of pressure. In addition, the pressure corrected intrusion curve is plotted. Due to the high pressures applied in a mercury intrusion experiment, the differing compressibility of mercury, porous sample, and pressure chamber needs to be considered. The (manual) correction factors were provided by the

experimental laboratory[4] that carried out the intrusion measurements. Thus, the corrected intruded volume results to

$$v_{int,corr} = v_{int} - pC_{Hg,p}, \tag{4-6}$$

where p is in units MPa an v_{int} in mm^3/g. With increasing pressure and smaller intruded pores, the compressibility of mercury, porous sample, and the pressure chamber is of relevance. Figure 4-3 (right) shows the specific intruded volume (non-corrected) as a function of the void radius.

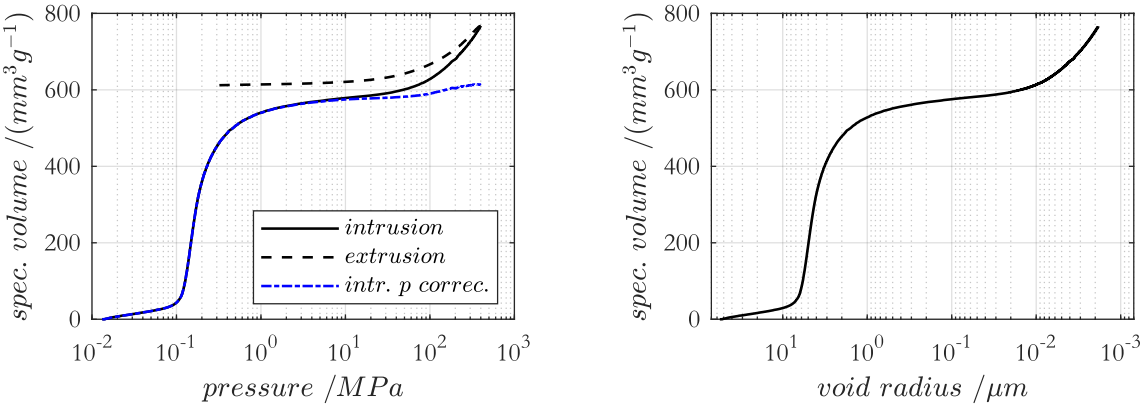

Figure 4-3: Specific void volume of a consolidated CDC composite with particle size of 75-150 µm and 2 wt% CMC binder (sample P_{68}, termed "Exp_{CDC}") as function of pressure (left) and void radius (right).

The correlation between intrusion pressure and void radius is directly obtained from the Washburn equation. With a pressure of up to approx. 400 MPa, the mercury could access pores down to an equivalent pore diameter of 3.7 nm for this CDC sample, and thus, interparticle voids (macropores) and some of the intraparticle pores (mesopores) are covered. The interparticle void volume can be determined from the transition from mercury void filling to the filling of the intraparticle pore network, at the inflection point, by an abrupt decrease in the mercury intrusion rate [51]. However, the determination of distinctive inflection points from the intrusion curves obtained for the samples investigated in the present work is not possible. The transition from interparticle void to intraparticle pore filling takes place in the form of a continuous transition

[4] Zeta Partikeltechnik: pressure correction factors: $C_{Hg,p} = 0.38\ mm^3/(gMPa)$ (CDC 75-150 µm, 2 wt% CMC) and the same value assumed for (CDC 50-75 µm, 2 wt% CMC), $C_{Hg,p} = 0.33\ mm^3/(gMPa)$ (CDC 75-150 µm, 2 wt% CMC, 10 wt% BN).

rather than at the defined point as can be identified from Figure 4-3. Therefore, a different approach is used, starting from the skeletal density, which is explained in detail further below. Applying this procedure, the inflection point for the intrusion curve shown in Figure 4-3 can be identified at an approximate intrusion pressure of $p_{infl} = 0.46\ MPa$ corresponding to a specific void volume of approximately $v_{int}(p_{infl}) = 500\ mm^3 g^{-1}$ and an equivalent void radius of $r_{infl}^{ma}(p_{infl}) = 1.58 \mu m$.

A further step in evaluating the mercury intrusion measurements includes the identification of the modal void radius which is obtained by differentiating the specific intruded volume by the logarithmic void radius. The resulting curve is shown in Figure 4-4 together with the specific intruded volume as a function of void radius.

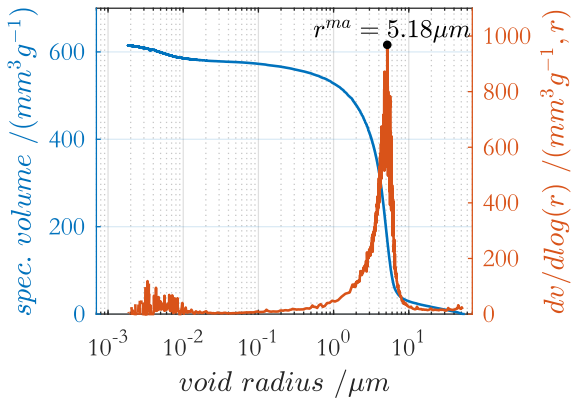

Figure 4-4: Specific void volume and differential void volume distribution as a function of the void radius of a CDC composite with a particle size of 75-150 µm and 2 wt% CMC binder. The indicated point represents the modal void radius.

The modal radius of (macropores) voids for this CDC sample can be identified to $r^{ma} = 5.18\ \mu m$ which is assumed to be the average radius of the interparticle voids. This quantity serves as a characteristic value describing the macropore size and is needed in the effective material model to describe the mass flux in the consolidated composites with the Dusty-Gas model. Furthermore, from Figure 4-4 the macropore range can be identified as being the pore range which predominantly contributes to the all-over specific void volume as well as a minor contribution from pores in the lower mesopore range (around 2-10 nm).

For the parameterisation of the effective material models introduced in section 2.4, in addition, adsorbent particle and interparticle void porosity, as well as densities, are needed. Especially, the (micro-) pore porosity $\varepsilon^{mi} \equiv \varepsilon_{p,comp}$ and void porosity ε^{ma} related to the composite volume as

well as the true adsorbent density ϱ_{true} and bulk density ϱ^{bulk} are required. To obtain the beforementioned quantities, the apparent density of the particles at the inflection point $\varrho_{app,par}(p_{infl})$ is identified. The apparent density as a function of the specific intruded volume can be calculated by

$$\varrho_{app}(d^{ma}) = \frac{1}{1/\varrho^{bulk} - v_{int}(d^{ma})}. \tag{4-7}$$

By identifying the intruded volume $v_{int}(p_{infl})$ at the inflection point, just before the mercury enters the primary particle, the apparent particle density can be obtained by

$$\varrho_{app,par}(p_{infl}) = \varrho_{app}\big(v_{int}(p_{infl})\big), \tag{4-8}$$

which is used to evaluate the particle porosity $\varepsilon_{p,par}$ in equation (4-3) and the void porosity ε^{ma} by the following relation

$$\varepsilon^{ma} = \frac{V^{ma}}{V_{comp}} = v_{int}(p_{infl})\varrho_{bulk} = 1 - \frac{\varrho_{bulk}}{\varrho_{app,par}(p_{infl})}. \tag{4-9}$$

As indicated in section 4.2.1, particle porosity is not of great interest for the effective material models of the consolidated composites. Rather, the volume of intraparticle pores related to the composite volume ε^{mi} in equation (4-4) is needed. For this as well as for equation (4-9) the bulk density ϱ^{bulk} is used which was obtained from the mercury intrusion measurement at initial state at $p \approx 0.01\ MPa$.

The later discussion reveals the difficulty of identifying the proper value of the void porosity ε^{ma} which is directly related to the inflection point and thus depends on the quality of its determination. Due to the difficulty of defining an exact pressure of the inflection point from the intrusion curve, an approach is used going the reversed way. In addition to mercury intrusion, a helium pycnometer was used for two selected CDC samples to determine the skeleton density ϱ_{skel} (or true density ϱ_{true} if no closed pores exist) independently. The underlying principle of the measurements is the displacement of a gas in a known volume by a solid sample. Generally, a pycnometer contains two isothermal chambers of known volume one of which is evacuated and contains the porous sample. The other chamber is filled with a weak- or non-adsorbable gas with a molecular size as small as possible. For this purpose, helium has proven to be a suitable gas (adsorption rates of helium at atmospheric pressure and room temperature are neglected). When connecting the two chambers, the resulting equilibrium pressure is above the pressure in an equivalent experiment without a solid sample. From the pressure difference and ideal gas

assumption, the skeleton volume and following the skeleton density can be determined. This independently obtained skeleton density with the helium pycnometer (ϱ_{skel}) together with the specific pore volumes obtained from N_2 physisorption v_p (see Table 4-1) are subsequently used, to identify the inflection points on the mercury intrusion curves using the following relation

$$\varrho_{skel} = -\frac{\varrho_{app,par}(p_{infl})}{\varepsilon_{p,par} - 1} = -\frac{1}{v_p - 1/\varrho_{app,par}(p_{infl})}. \tag{4-10}$$

Summarizing, Table 4-2 shows the values for three consolidated composites with different particle sizes and amounts of heat conducting additive. The characteristic values in the first three rows are directly obtained from the mercury intrusion curve respectively the measurements with the Helium pycnometer. The characteristic values in the subsequent rows were calculated in post-processing using the method described above.

The following identifications can be revealed. The bulk density increases when using smaller primary particles (CDC 50-75 µm vs. CDC 75-150 µm) directly resulting in a void half-width (r^{ma}) reduced by a factor of approx. 3. Similarly, the addition of 10 wt% BN heat conducting additive increases the bulk density due to partial filling of the void volume ($d_{BN} \approx 1\mu m$ [34]). As a result, the void half-width slightly decreases (CDC 75-150 µm vs. CDC 75-150 µm with BN). Since the skeleton density of boron nitride ($\varrho_{skel,BN} = 1.9\ gcm^{-3}$ [134]) is below the skeleton density of CDC ($\varrho_{skel,CDC} = 2.27\ gcm^{-3}$ [134]) consequently, a lower skeleton density of the thermal conductivity enhanced composite results. With equations (4-4) and (4-9) the particle porosity related to the volume of the consolidated composite ($\varepsilon_{p,comp} = \varepsilon_{mi}$) and the void ($\varepsilon^{ma}$) can be determined, respectively. The void porosity of the composite with a large particle fraction is the highest which directly correlates with the smallest bulk density. Equivalently, the smaller particle causes a somewhat more compact bed density resulting in a significantly reduced void porosity. Due to the boron nitride additive partially filling the voids, the macroporosity is also significantly reduced, which however can also partly be explained by the comparably large pore porosity of this sample. The sample with the small particle fraction is the one with the highest pore porosity directly related to adsorption capacity. This link could already be drawn in the analysis of the nitrogen physisorption results.

Finally, it must be emphasised, that the division in particle pore and void porosity is not straightforward and definitive, due to its dependence on the definition of the inflection point. Rather the total porosity can be taken as the correct value since its determination solely depends on the measurement of the bulk density and skeleton density with the helium pycnometer.

However, it must be kept in mind, that skeleton density was determined with helium as a probe molecule which is not able to enter closed pores or pores with size below its molecular diameter.

Table 4-2: Characteristic values of the investigated consolidated composites of CDC adsorbent with varying particle sizes, binder, and additive directly obtained from mercury intrusion measurements and with a helium pycnometer (first three rows). In the post-processing calculated characteristic values using the N_2 physisorption results from section 4.2.1 (last five rows).

	CDC 50-75 µm, 2 wt% CMC	CDC 75-150 µm, 2 wt% CMC	CDC 75-150 µm, 2 wt% CMC, 10 wt% BN (~1 µm)
$\varrho_{bulk}/\left(g\ cm_{comp}^{-3}\right)$ $(Hg\ int.@\ p \approx 0.01\ MPa)$	0.63	0.60	0.66
$r^{ma}/\mu m\ (Hg\ int.)$	1.79	5.18	4.47
$\varrho_{skel}/(g\ cm_s^{-3})\ (He\ pyc.)$	-	2.27	2.17
$\varrho_{skel}/(g\ cm_s^{-3})\ (eq.\ (4\text{-}10))$	2.26	2.27	2.17
$\varepsilon^{ma}/(m_v^3 m_{comp}^{-3})\ (eq.(4\text{-}9))$	0.23	0.3	0.22
$\varepsilon_{p,comp}/(m_p^3 m_{comp}^{-3})\ (eq.(4\text{-}4))$	0.49	0.43	0.48
$\varepsilon_{total}/\left(m_{v,p}^3 m_{comp}^{-3}\right)$	0.72	0.73	0.7
$\varrho_{app,par}/\left(g\ cm_{par}^{-3}\right)$ $(Hg\ int.@\ infl.point, eq.(4\text{-}8))$	0.82	0.86	0.85

Typical characteristic values for activated carbons are given by [55], which are comparable to the values obtained for the CDC carbon active material with nitrogen physisorption and mercury intrusion.

4.3 Adsorption capacity of active carbon composites for methanol

The adsorption characteristics of methanol on carbon active adsorbents can be well described by the Dubinin-Astakhov adsorption isotherm which is the model of choice in this thesis. It contains three fitting parameters (w_0, E, n) which can be determined with uptake measurements and parameter fitting. Regarding the design of adsorbent composites, with varying amount of

inert and active material, correlating the adsorption capacity w_0 with the proportion of the carbon active material is necessary. Intuitively, one would assume a linear dependence of adsorption capacity and adsorbent content. Whether this relationship proves to be correct, or whether high proportions of inert additive or binder block some of the adsorption sites is investigated in this section.

4.3.1 Manometric measurement setup for determining adsorption isotherms

The methanol adsorption capacity of different carbon active consolidated composites was determined at 30 and 90 °C with an automated apparatus consisting of a liquid methanol tank and a thermally controlled vapor reservoir coupled to an absolute pressure transducer (MKS Baratron 121A, 1000 mbar). The experimental plant works with the static manometric principle of measurement [135] and the setup is schematically shown in Figure 4-5. It consists of ultra-high vacuum components to minimize gas leakage. All relevant components are embedded in an actively, temperature-controlled (external thermostat), isothermal aluminium bed. The temperature of the sample holder can further be actively controlled with a second, external thermostat. A temperature-controlled pressure transducer serves to detect the MeOH vapour pressure in the vapor reservoir. A Turbo-molecular pump is coupled via valve V6 with the vapor reservoir to enable a high vacuum initial for each experiment.

The static manometric principle of measurement is based on the determination of changes in pressure of calibrated gas volumes due to adsorption. However, in contrast to gravimetric techniques, measurement points at high relative pressures cannot be obtained.

Each equilibrium measurement is initialized by slowly dosing methanol vapor up to a defined pressure level into the vapor reservoir with known volume, which is maintained at a constant temperature. The amount of methanol can be calculated assuming ideal gas behaviour and varied by varying the initial pressure level. By opening the valve V4 methanol vapor flows into the previously evacuated sample chamber and starts to adsorb on the adsorbent. Due to adsorption, the pressure decreases until equilibrium is reached. The amount adsorbed can be determined by the difference of vapor initially dosed into the vapor reservoir and the amount remaining in the vapor phase in equilibrium. The adsorption isotherm is constructed by repeating the equilibrium measurement with different equilibrium pressures. To obtain the correct amount adsorbed, the volume of the dead space must be known, which can be obtained by pre-calibration of the sample volume and subtracting the skeleton density of the adsorbent. However, the sample volumes are negligibly small compared to the volumes of the vapor reservoir and sample chamber which is why the dead space of the skeleton adsorbent is neglected.

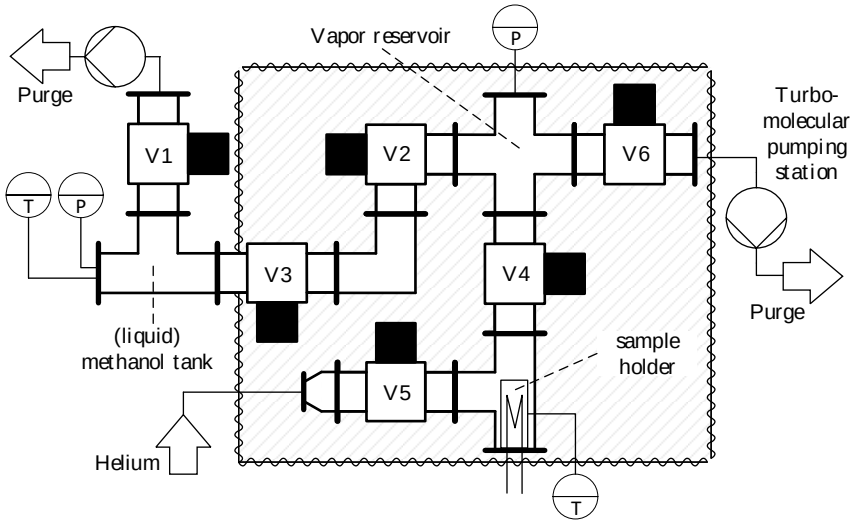

Figure 4-5: Schematic sketch of the experimental plant for measurements of methanol adsorption on carbon active composites.

The execution of the experiments consists of the following steps. After evacuating the setup with a turbo-molecular pumping station (≈ 10^{-4} mbar) and desorbing the sample on the sample holder, vaporous methanol is dosed into the vapor reservoir via V2 and V3 up to certain vapour pressure. The MeOH is provided from the methanol tank. When opening valve V4, methanol enters the sample chamber and is adsorbed on the sample. After a certain time, the equilibrium is reached, and the amount adsorbed can be calculated from the chamber volumes and the pressures at the beginning of the experiment and in equilibrium. The sample preparation consisted of degassing at 180 °C for 5 h under fine vacuum and subsequent weighing. The dried carbon active composite was attached to thin metal plates utilizing an indium foil (Goodfellow; 0.25 mm) or a double-sided, thermal conducting adhesive tape (Dreyer Systems GmbH, Thermal Tape DS-TAP-P-A2-1.2-0.10, $\lambda = 1.2\,W/m/K$). The centre temperature of the metal plate was measured using a thermocouple inserted into a small hole in the metal plate. The top temperature of the carbon active composites was measured with another thermocouple adjusted with thermal conducting paste. The mounted metal plate was placed on a temperature-controlled sample holder utilizing a liquid metal pad (Coollaboratory) to provide a reasonable thermal contact. Subsequently, before the first measurement, in situ degassing of the fully assembled sample at 90°C under high vacuum was conducted. Figure 4-6 shows a picture of the sample holder with an attached consolidated CDC composite, thermocouples, and thermal conducting paste.

Figure 4-6: Sample holder for the equilibrium plant consisting of the temperature-controlled sample holder, metal plate, thermocouples, and consolidated CDC-composite.

In the manometric measurement principle applying a dosing procedure, the systematic errors in the measured amount of gas are cumulative. Besides, with increasing initial pressure, the remaining amount of methanol in the dead space that is not adsorbed becomes more and more important [57]. Therefore, beforehand every single experiment, the measurement cell was evacuated, and the sample desorbed to generate identical initial conditions (for microporous samples, <1 Pa is desirable [57]). To obtain measurement points at higher relative pressures, step experiments were used, where the equilibrium pressure of the previous experiment served as initialization of the subsequent experiment. However, due to the accumulative errors in manometric experiments, no more than two-step experiments were conducted.

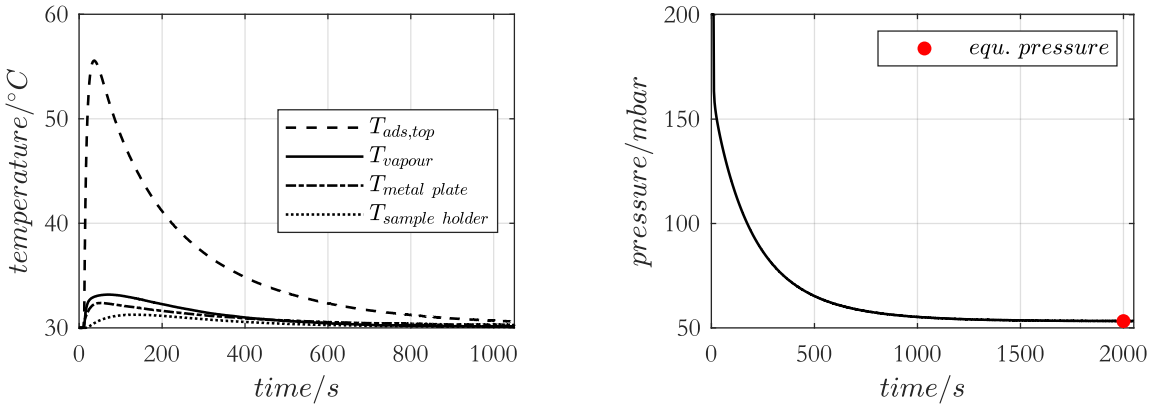

Figure 4-7: Transient temperature and pressure profiles obtained in a manometric measurement. The equilibrium pressures are used to parameterize the Dubinin-Astakhov isotherm model. Exemplarily, the plots are shown for sample P_{68} (Exp_{CDC}) (see Table B-1) and an experiment conducted with an initial temperature of 30°C and initial pressure of 200 mbar.

The measurement procedure explained previously results in transient pressure and temperature curves, exemplarily shown in Figure 4-7, which were obtained for sample P_{68} (Exp_{CDC}) at 30°C and an initial pressure of 200 mbar.

By evaluating the equilibrium points with the DA-model (equations (2-18) and (2-23)), and plotting adsorbed volumes versus corresponding adsorption potentials, the characteristic curve is obtained. Figure 4-8 (top) exemplarily shows the characteristic curve of a sample with CDC primary particles size between 50-75 µm with 2 weight percent of CMC binder and 10 weight percent of silver additive (P_{48}).

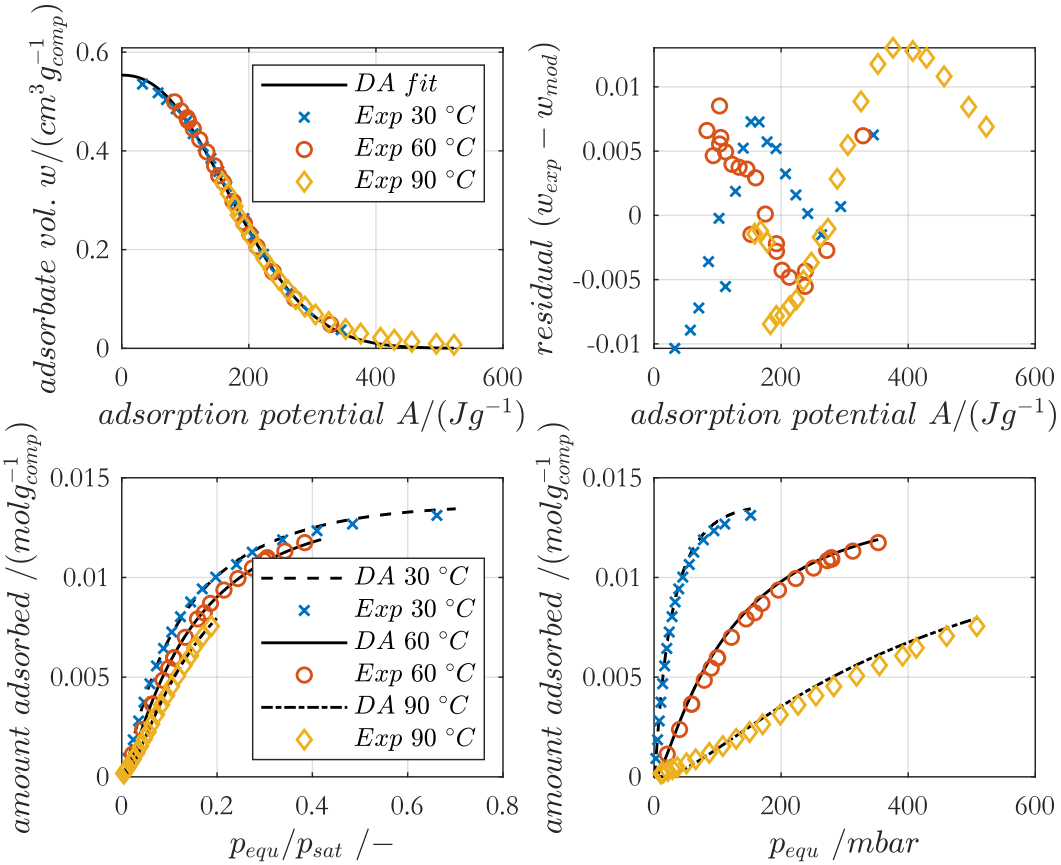

Figure 4-8: Dubinin-Astakhov isotherm fit with equilibrium measurements at 30 °C, 60 °C, and 90 °C as well as the residuals (top). Adsorption isotherms as a function of relative pressure and equilibrium pressure (bottom). Exemplarily, the plots are shown for sample P_{48} with CDC primary particles size between 50-75 µm, with 2 wt% of CMC binder and 10 wt% of silver.

The maximal adsorbate volume with respect to the compound mass is approximately $0.553\ cm^3/g_{comp}$. Exemplarily, isotherms at 30°C, 60°C and 90°C were measured for this specific sample. It is obvious, that the measurements at 60°C do not provide any additional

information than the measurements at the other temperatures. Therefore, to reduce the number of experiments for the remaining samples, the equilibrium measurements were exclusively conducted at 30°C and 90°C. In addition, the residual of experimental and model adsorbate volume shows a very good agreement of experiments and Dubinin-Astakhov model with deviations below 1.5%. Furthermore, the adsorption isotherms as functions of relative and absolute equilibrium pressures are shown in Figure 4-8 (bottom). Due to the manometric measurement principles and for the high-temperature measurements due to the setup limitation of maximal 1 bara, the experiments could not be executed to the saturation limit.

4.3.2 The characteristic curve in the Dubinin formalism

The Dubinin-Astakhov model was applied to the experimental equilibrium measurements of the carbon active consolidated composites. The experimental equilibrium point, and characteristic curve can be related to the mass of the composite or the carbon active mass.

Figure 4-9 shows characteristic curves obtained for sample P_{68} (Exp_{CDC}) (see Table B-1) related to composite mass (left) and CDC-mass (on the right). Due to the small amount of inert additive (2 wt% of CMC binder) the intersection with the ordinate is similar. The specific maximum (micro-) pore volume is $w_0 = 0.603\ cm^3 g_{comp}^{-1}$. In comparison, the specific micropore volume obtained with nitrogen physisorption and evaluated with the BET method for CDC-powder with the same particle size (50-75 µm) was $v_p = 0.78\ cm^3 g^{-1}$ (see Table 4-1).

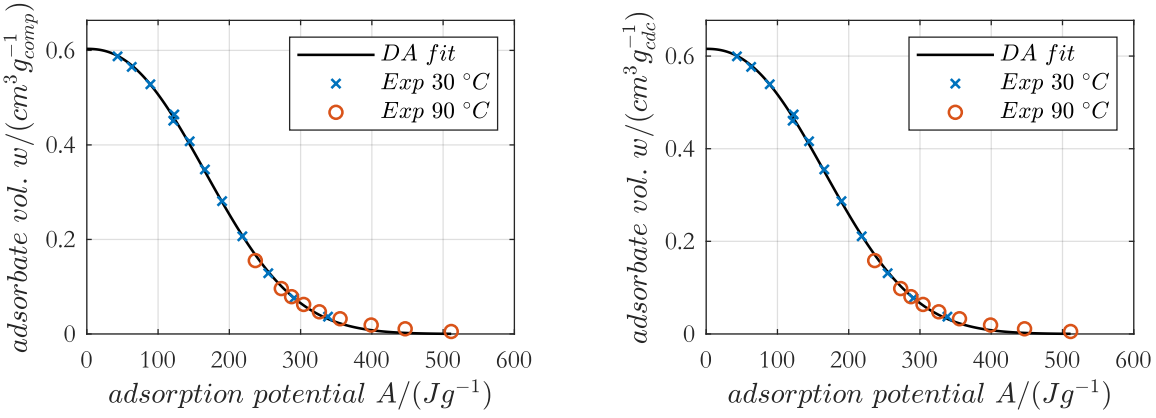

Figure 4-9: Characteristic curve in the Dubinin formalism related to absolute composite mass (left) and CDC mass (right) as a function of the adsorption potential A for sample P_{68} (Exp_{CDC}). The fitted parameters result to $w_0 = 0.603\ cm^3 g_{comp}^{-1}$, $E = 212.5\ Jg^{-1}$ and $n = 2.32$.

The deviation in the specific micropore volume of > 20 % between methanol adsorption measurements on the composites and nitrogen physisorption on powdered primary particles is significant and cannot be completely explained by the addition of the extra binder mass. Due to the mixing with the binder and shaping process of the composites, pore-blockage appears to some extend reducing the accessible micropore volume. This was confirmed by a loss in BET surface areas of about 10% of consolidated composites compared to powdered primary particles [34]. In addition, the nitrogen molecule can access smaller pores compared to methanol due to its smaller molecular diameter ($\sigma_{MeOH} = 0.42nm$ [136], $\sigma_{N_2} = 0.364nm$).

Besides CDC samples, the activated carbon samples were investigated in manometric equilibrium measurements. Figure 4-10 shows the characteristic curves obtained for an AC-sample with 10 wt% of CMC binder (P_{80}) referred to the composite (left) and carbon active mass (right), respectively. The maximum pore volume is smaller than for the CDC sample and $w_0 = 0.397\, c\, m^3 g_{comp}^{-1}$.

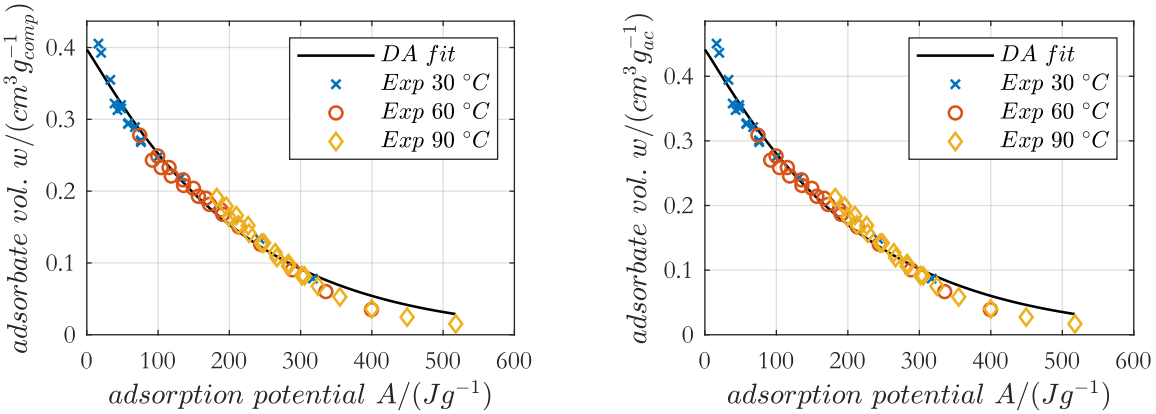

Figure 4-10: Characteristic curve in the Dubinin formalism related to absolute composite mass (left) and activated carbon mass (right) as a function of the adsorption potential A for AC sample P_{80}. The fitted parameters result to $w_0 = 0.397\, cm^3 g_{comp}^{-1}$, $E = 209.7\, Jg^{-1}$ and $n = 1.07$.

This trend was already investigated in the nitrogen physisorption measurements, at which the pore volume was obtained to $v_p = 0.65\, cm^3 g^{-1}$ (see Table 4-1). Similar as for the CDC measurements, the pore volume for the AC is significantly smaller comparing the two methods. However, the loss in pore volume is almost 40 % which cannot solely be explained by the higher amount of inactive CMC binder and the accompanying increased pore blockage. Another possible reason for the large deviation is the more mesoporous character of the AC for which the

underlying idea of micropore volume filling in the Dubinin-Astakhov formalism loses its basis. This assumption is supported by the non-optimal fit of the DA isotherm to the AC equilibrium measurements which deviates especially in the range of smaller adsorption potentials and thus underestimates the micropore volume.

The fitted DA parameters obtained for the CDC- and AC- samples are summarized in Table 4-3.

Table 4-3: DA parameters for CDC-sample P_{68} (Exp_{CDC}) and AC-sample P_{80} obtained from methanol equilibrium measurements with the manometric method.

	$w_0/(cm^3 g_{comp}^{-1})$	$E/(J g^{-1})$	$n/-$
$P_{68}(Exp_{CDC})$	0.603	212.5	2.32
$P_{80,ac}$	0.397	209.7	1.07

4.3.3 Maximum pore volume for different carbon active composites with varying inertia proportion

For the correlation of adsorbent volume fraction with adsorption capacity which is required in the effective material models, several CDC and AC consolidated composites with varying amounts and types of binder and heat additive were investigated regarding their adsorption capacity for methanol. Figure 4-11 shows the maximum pore volume w_0 referred to the composite mass for the CDC samples (left) and the AC samples (right) as a function of the weight fraction of the carbon active material.

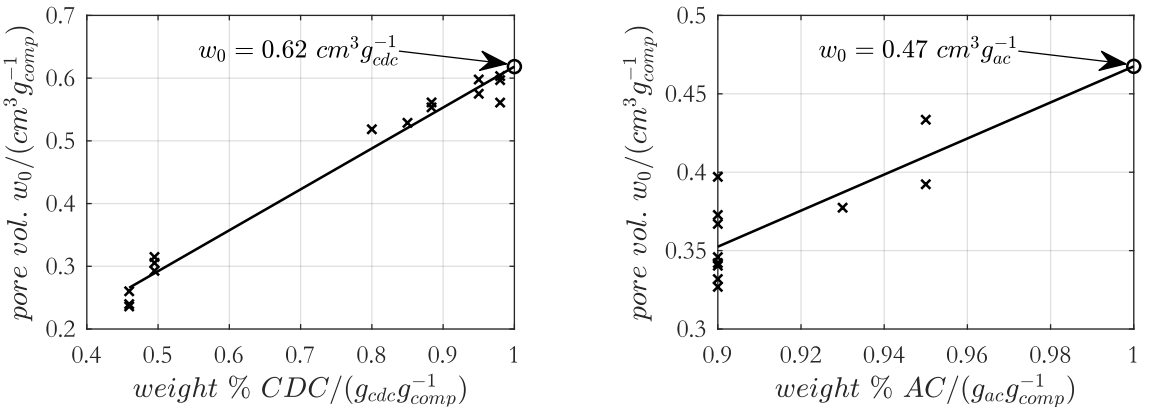

Figure 4-11: Maximum specific (micro-) pore volume referred to the composite mass as a function of weight fraction of carbon active material. On the left for CDC and AC on the right.

The maximum pore volume per composite mass linearly scales with the weight fractions of the respective carbon active material. The maximum pore volume is theoretically obtained without additive at a carbon active proportion of 1 being approximately 25% greater for CDC than for the AC. This is an unsurprising result already investigated by many authors e.g., [28]. Consequently, the maximum specific pore volume referred to the composite mass can be determined by scaling the experimentally obtained value by the mass fraction of active adsorbent material as introduced in the effective material models

$$w_0 = w_0^{exp} \frac{\varepsilon^s \varrho^s}{\varepsilon^s \varrho^s + \varepsilon^{ha} \varrho^{ha}}. \tag{4-11}$$

4.4 Mass transfer of non- or weak-adsorbing gases in consolidated adsorbent composites of active carbon materials

Besides the intraparticle porosity of the microporous adsorbent particles, the consolidated composites contain interparticle porosity which mainly consists of macropores. Depending on the layer thickness of the composites, the primary particle size, the pressure conditions (50-200 mbar using methanol as adsorptive in adsorption cooling [21]) as well as the effective thermal conductivity, the mass transfer in the interparticle voids can be limiting. The aim of the mass transport measurements is the determination of the transport parameters parametrising the Dusty-gas Model (B_0^{eff}, D_{MeOH}^{Kn}) and the identification of correlations between composites composition and effective mass transport parameters. Theoretically, when using the DGM, the transport resistance linearly scales with the layer thickness of the consolidated plates, whereas the transport parameters are independent of the layer thickness. The mass transfer measurements are used to verify these relations.

Mass transfer properties of different CDC and AC composite for non-adsorbable gases at different temperatures were measured with a flow-through setup. The experiments were evaluated using the DGM taking Knudsen diffusion and viscous flow into account.

4.4.1 Experimental setup for flow-through experiments

A simple permeation setup was used to determine single-component gas effective transport parameters of the consolidated samples. A schematic sketch of the setup can be seen in Figure 4-12. In the experiments, non-adsorbable gases were passed through the composites using a mass flow controller (Bronkhorst EL-Flow Prestige FG-200CV). The pressure drop over the samples was measured with two absolute pressure gauges (MKS Baratron 627F, P1: 1000 mbar, and P2:

100 mbar). The sample holder was immersed in a thermostat, allowing measurements at different temperatures to extract the temperature dependence of the mass transport parameters. A vacuum pump was installed at the end of the flow pipe to provide a low vacuum at the downstream side of the sample. Pressure P2 served as a control variable for the control valve. With this setup, measurements with varying Knudsen numbers were possible by applying different pressure levels (adjustment to pressure P2), temperature levels and volume flows. Furthermore, the gas species can be varied allowing for a variation in molecular mass which is also affecting the flow regime. At the applied pressure levels, the investigated gases (He, Ar, N_2, CO_2) are non- or weakly-adsorbable.

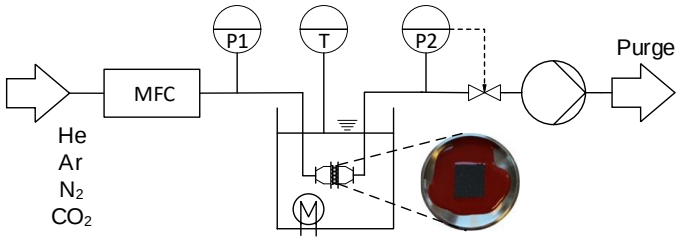

Figure 4-12: Schema of the simplified flow-through setup to measure pressure drops over the samples and determine effective mass transport properties with the DGM for consolidated adsorbent composites. The schema was reproduced from Träger et al. [34].

Before the experiments, the samples were cut to the dimensions of the sample holder and fixed gas-tight with silicone (Wacker Elastosil E10) to avoid bypass flow. Due to its high viscosity, the silicone does not penetrate the porous samples. This is a prerequisite to prevent pore blockage and was investigated at the contact surface with an optical microscope and REM. The samples prepared in this way were then installed in the flow-through setup. The system control allows automated operation, whereby measuring routines with varying settings can be carried out. An experiment was finished when the relative deviation of the pressure with time was in a steady state. Depending on the settings and the sample thickness and density, the duration of an experiment could take up to hours.

4.4.2 Gas transport through consolidated composites: Evaluation of permeation experiments with the DGM

Each experiment results in a unique set of data containing the temperature, pressures, and volume flow rate of the adjusted gas. Together with geometrical data of the respective sample, this data can be used and evaluated with the Dusty-Gas model providing an effective diffusion coefficient that contains Knudsen-diffusion and (effective) permeability [83], [89], [99]. This

approach accounts for additive superposition of transport in the transition regime between continuous Darcy flow and Knudsen diffusion. For a pure, non-adsorbable gas, the mass flow densities of viscous flow and Knudsen diffusion add up to the all-over, one-dimensional gas transport in the consolidated composites with an effective mass transport coefficient D^{eff} and the spatial gas density $\frac{d\varrho^g}{d\xi}$ as driving force (see equation (2-50) with ideal gas law)

$$\dot{m} = -D^{eff}\frac{d\varrho^g}{d\xi} = \dot{m}^g\varepsilon^g. \tag{4-12}$$

The mass flux $\dot{m}$ is related to the cross-sectional area of the consolidated sample whereas $\dot{m}^g$ is related to the cross-sectional area of the transport pores. The void porosity $\varepsilon^g \equiv \varepsilon^{ma}$ was obtained from mercury intrusion (see section 4.2.2). The effective diffusion coefficient is [83]

$$D^{eff} = \underbrace{\frac{\varepsilon^g}{\tau}D^{Kn}(T)}_{D^{Kn,\,eff}} + \underbrace{\frac{\varepsilon^g}{\tau}B_0}_{B_0^{eff}}\frac{p}{\eta}, \tag{4-13}$$

with effective permeability B_0^{eff} for a porous composite material, τ the tortuosity, and η the dynamic viscosity. Theoretically, B_0^{eff} is independent of gas species and temperature and thus, different experiments with the same sample should result in identical values. However, the size of the gas molecules plays a role to some extent, which is discussed in detail below. The effective Knudsen diffusion coefficient $D^{Kn,\,eff}$ depends on temperature and gas species (see equation (2-41)). Extracting the temperature and molar mass is convenient to isolate the structure dependencies for comparison of different experiments. Furthermore, for application in the simulations, extraction of the temperature-independent part is appropriate

$$D_j^{Kn,eff} = \frac{\varepsilon^g}{\tau}\frac{d_{pore}}{3}\sqrt{\frac{8R}{\pi MW_j}}\sqrt{T} = D_j^{Kn,const}\left(MW_j\right)\sqrt{T} = D^{Kn,const}\sqrt{\frac{T}{MW_j}}. \tag{4-14}$$

In a further step, the effective Knudsen-diffusion coefficient for methanol molecules $D_{MeOH}^{Kn,eff}$ is calculated from the experimental results by linear interpolation.

The permeation experiments for each sample were carried out with four different gases (He, Ar, N_2, CO_2) with a wide variety of molecular masses. For each gas, the experiments were carried out with three temperatures and in each case for six different mean pressures. For evaluation of the experiments, the DGM (see equation (A-42) in the derivation) needs to be formulated in a form, where the measured variables and macroscopical geometries can be inserted. Instead of the molar flux $\dot{n}_j$, the molar flow in mol/s is used with the cross-sectional area of the sample A_{comp}

$$\dot{N}_j = \dot{n}_j A_{comp} \varepsilon^g. \tag{4-15}$$

Furthermore, the pressure gradient is linearized, and the average pressure is used for p

$$\frac{dp}{d\xi} = \frac{\Delta p}{\Delta \xi}, \tag{4-16}$$

$$p \approx \frac{p_1 + p_2}{2}. \tag{4-17}$$

Using these relations, equation (A-42) can be reformulated

$$\frac{RT\Delta\xi\dot{N}_j}{\Delta p A_{comp}} = \frac{\varepsilon^g D_j^{Kn}}{\underbrace{\tau}_{D_j^{Kn,eff}}} + \underbrace{\frac{\varepsilon^g}{\tau} B_0}_{B_0^{eff}} \frac{1}{\eta} \frac{p_1 + p_2}{2}. \tag{4-18}$$

Applying equation (4-14) and $\dot{n}_j = \dot{N}_j / A_{comp}$, the Knudsen-related, temperature-independent part can be extracted

$$\frac{R\sqrt{T}\Delta\xi\dot{n}_j}{\Delta p} = \underbrace{D_j^{Kn,eff}/\sqrt{T}}_{D_j^{Kn,const}} + \frac{B_0^{eff}}{\eta\sqrt{T}} \frac{p_1 + p_2}{2}. \tag{4-19}$$

Equation (4-18) or (4-19) can now be used for the identification of the effective permeability from the slope (multiplied with the kinetic viscosity) and the effective or constant part of the Knudsen diffusion coefficient from the intersection with the ordinate.

4.4.3 Results of permeation experiments with consolidated composites

Using the evaluation strategy presented in section 4.4.2, permeation experiments of four different gases at different flow regimes can be evaluated. First, experiments conducted with sample P_{68} (Exp_{CDC}) are discussed in detail. Subsequently, transport parameters of 9 different samples are compared and conclusions are drawn concerning structure-property correlations. The independence of layer thickness was investigated for an AC sample and the results are outlined in Appendix B.2.3.

4.4.3.1 Consolidated composite with CDC particle size of 50-75 µm

Experiments were performed with the sample P_{68} (Exp_{CDC}) using He, Ar, N_2, CO_2, at three temperatures with six different flow rate conditions. Volumetric flow rates at standard conditions ($273.15K$, $10^5 Pa$) of $3,4,5,7,8,9 \frac{mL_N}{min}$ were adjusted resulting in different pressure conditions depending on the transport resistance of the sample and the adjusted downstream pressure p_2. In

steady-state, temperature, volumetric flow rate, and pressures were detected. The resulting set of data was evaluated using the DGM and visualized in Figure 4-13 using equation (4-18) (figures on the left) and equation (4-19) (figures on the right).

From the classic form of the DGM (equation (4-18)), the effective Knudsen-diffusion coefficient is obtained as a function of temperature and the molar mass of the gas species j. The higher the temperatures and the lower the molar mass, the larger is $D_j^{Kn,eff}$. Therefore, the largest value is obtained for He at $90°C$ and the smallest value for CO_2 at $30°C$. As the temperature increases, the slope (B_0^{eff}/η) decreases, which is due to the increasing viscosity. Using equation (4-19), the temperature-independent part of the Knudsen-diffusion coefficient $D_j^{Kn,const}$ can be obtained resulting in a uniform intersection with the ordinate. This evaluation serves as a validation of the experiments, which worked very well for the samples studied. Again, the dependency of the molar mass can be obtained from $D_j^{Kn,const}$. In a final step, this dependency can be eliminated using equation (4-14), yielding the exclusively structure-dependent part of the Knudsen diffusion coefficient $D^{Kn,const}$.

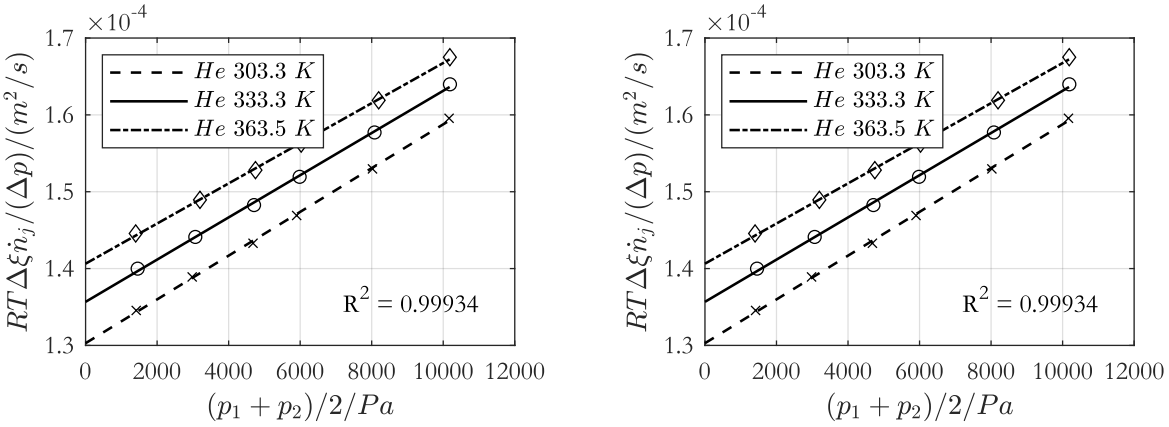

Figure 4-13: Results of permeation experiments for sample P_{68} (Exp_{CDC}) ($d_{par} = 50 - 75\ \mu m$) with He at 30, 60 and 90°C. Left: Evaluation with the classic DGM in equation (4-18). Right: Evaluation with temperature-independent ordinate from equation (4-19). (Further results with N_2, Ar and CO_2 are outlined in Appendix B.2.)

Following the kinetic theory of gases, the Knudsen diffusion coefficient is linearly dependent on the square root of the reciprocal of the molar mass (equation (2-41)), as can be seen in Figure 4-14 (left). This linear dependency is used to calculate the respective Knudsen diffusion coefficient of methanol. Furthermore, the value that depends purely on the structure of the sample can be calculated. The $D^{Kn,const}$obtained for all experiments for sample P_{68} (Exp_{CDC})

are plotted in Figure 4-14 (right) versus the respective fraction of molar mass and temperature. The results are consistent with theory with a relative deviation below 3% compared to the averaged value of $\overline{D}^{Kn,const}$.

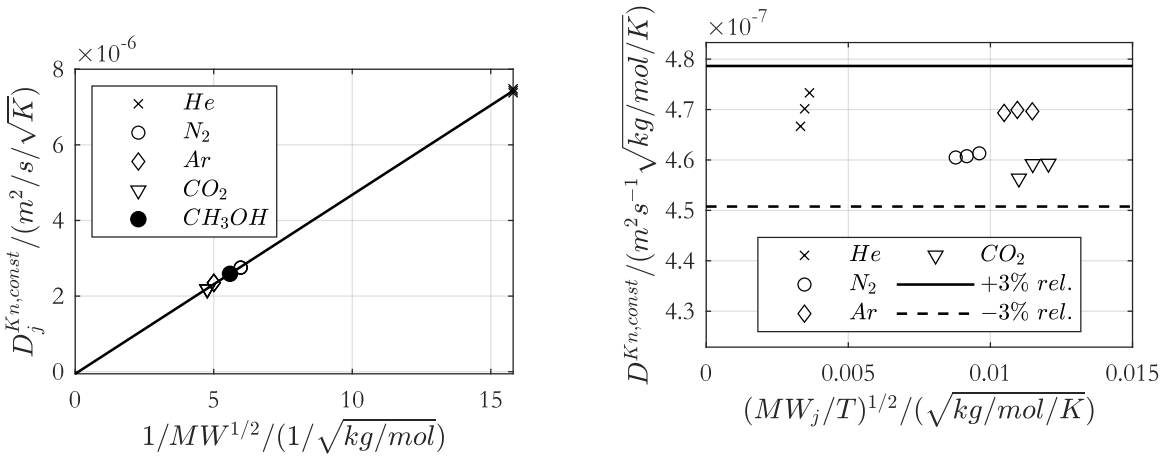

Figure 4-14: Validation of the Knudsen diffusion coefficient for the sample P_{68} (Exp_{CDC}) according to Graham's law (equation (2-42)) with temperature-independent part of the Knudsen diffusion coefficients $D_j^{Kn,const}$ (left). The value for methanol was obtained by linear interpolation on the molar mass. (Right) The constant part of the Knudsen diffusion coefficient according to equation (4-14) for different gases and temperatures and the 3% relative deviations from the averaged $\overline{D}^{Kn,const}$.

Finally, the calculated effective permeabilities for each temperature and gas are visualized in Figure 4-15. Theoretically, B_0^{eff} should be independent of temperature and gas species since it solely depends on the structure of the sample.

This is true for regular structures with narrow pore size distributions. However, the herein investigated carbon composites are complex in structure and non-ideal. For this reason, a linearly decreasing dependency of B_0^{eff} with increasing size of the molecules (molar mass) was observed for all samples investigated. Do et al. [89] give a possible explanation of this trend. Due to the nonideal slit-like pore geometries in consolidated beds of activated carbons, an increase in diffusion flow paths for smaller molecules is possible, especially in microporous carbons. Especially in very thin slits, small molecules such as helium can still be transported convectively, while mass transport of larger molecules such as argon at the same pressure and temperature conditions is predominantly by Knudsen flow. Using the linear dependency, the effective permeability for the molecular mass of methanol is obtained by linear interpolation.

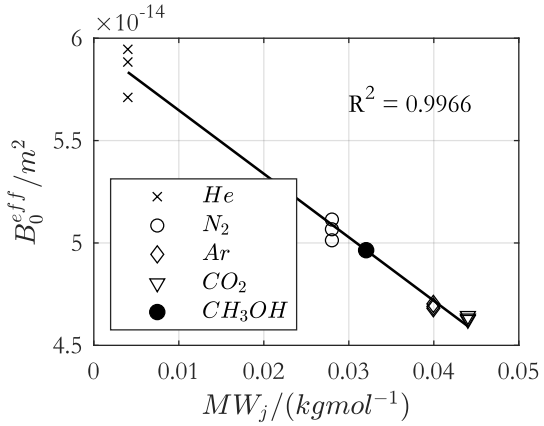

Figure 4-15: Effective permeability in dependency of gas species for sample P_{68} (Exp_{CDC}). Experiments with three temperatures were conducted for each gas species. The smaller the gas molecules, the more transport pores are available for mass transport in the viscous flow regime. Effective permeability for molecules of the molar mass of Methanol was obtained by linear interpolation.

Although the effect of gas molecule size on effective permeability is relevant (approximately 20% higher for He than for CO_2) and not negligible, the composition of the composite (adsorbent particle size and shape as well as additive) has a considerably larger influence as will be shown in section 4.4.3.2. The resulting $D_j^{Kn,const}$ and temperature-averaged $\overline{B}_0^{eff}$ are listed in Table 4-4.

Table 4-4: Temperature independent Knudsen-diffusion coefficients and temperature-averaged effective permeabilities for measured gases obtained for sample P_{68} (Exp_{CDC}) (CDC 2wt% CMC). The values for Methanol are calculated.

Gas species	$D_j^{Kn,const}$ $/(m^2/s/\sqrt{K})$	$\overline{B}_0^{eff}/m^2$
He	$7.4 \cdot 10^{-6}$	$5.8 \cdot 10^{-14}$
N_2	$2.8 \cdot 10^{-6}$	$5.1 \cdot 10^{-14}$
Ar	$2.4 \cdot 10^{-6}$	$4.7 \cdot 10^{-14}$
CO_2	$2.2 \cdot 10^{-6}$	$4.6 \cdot 10^{-14}$
CH_3OH	$2.6 \cdot 10^{-6}$	$4.96 \cdot 10^{-14}$

4.4.3.2 Variation of CDC composite composition

For the parameterisation of the effective material models, one aim is to investigate the dependencies of the composite compositions on the transport properties due to a varying

interparticle structure. Therefore, the mass transport of 9 consolidated CDC composites with different amounts and types of binder and heat conducting additive have been investigated in flow-through experiments (see Table B-1) and effective permeabilities and Knudsen diffusion coefficients were determined. The structure-property relations were subsequently determined by using the definition of the effective Knudsen diffusion coefficient in equation (4-14).

Equation (4-14) can be rewritten so that the structural parameters are on the left-hand side and the remaining variables are on the right-hand side. Thus, a quantity can be extracted which contains the structured dependency and consists of void porosity $\varepsilon^g \equiv \varepsilon^{ma}$, tortuosity τ of the voids, and mean void width d^{ma}

$$\frac{\varepsilon^{ma}}{\tau} d^{ma} = 3D_j^{Kn,eff} \sqrt{\frac{\pi MW_j}{8RT}}. \tag{4-20}$$

With the void porosity and the width of transport pores from Hg-porosimetry, the tortuosity factor τ can be calculated. The structural parameter ($\varepsilon^{ma} d^{ma}/\tau$) is used to compare (temperature-averaged) effective permeabilities obtained for methanol $\overline{B}_0^{eff}(CH_3OH)$ for the different samples which are shown in Figure 4-16. It can be concluded, that the higher the void porosity and width and the lower the tortuosity, the larger the effective permeability. Interestingly, the effective permeability correlates linearly with the structural parameter.

According to Hagen-Poiseuille law in equation (2-32), the effective permeability should rather scale with $d^{ma\,2}$. However, this law is valid for a cylindrical tube, giving a hint of the non-ideal structure of the investigated CDC samples.

Generally, the tendency of greater permeabilities with an increasing structural parameter can be explained by larger voids. The transport parameters and structural parameters for the nine investigated consolidated CDC-plates are listed in Table B-3 which reveal the following findings: CDC-composites prepared with the smaller particle fraction (50–75 μm) tend to have lower effective permeabilities and Knudsen diffusivities compared to the ones with larger primary particles (75–150 μm). The results are in accordance with the common understanding that smaller voids between the particles (lower values for $\varepsilon^{ma} d^{ma}/\tau$) have a detrimental effect on the mass transport. Moreover, the utilization of additives additionally hampers the mass transport because the interparticle porosity is further reduced. As can be observed for sample P_{61} (50–75 μm; 2wt% CMC; 50 wt% BN), this effect can even lower the mass transport properties by about two orders of magnitude. In other words, the high amount of BN particles clogs the transport pores to a large extent revealing the influence of the competing structure-property dependencies.

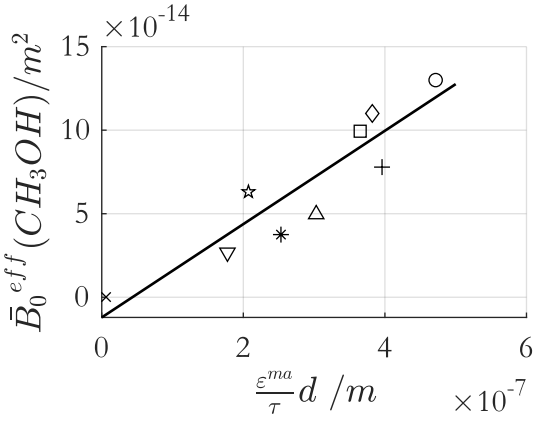

Figure 4-16: Temperature-averaged effective permeabilities (calculated for methanol) as a function of the void structural parameters $\varepsilon^{ma} d^{ma}/\tau$ for 9 CDC composites with different amounts and types of binder and heat additive (see Table B-1).

The previously outlined investigations motivated the formulations for the mass transport parameters in the effective material model introduced in section 2.4.

4.5 Heat capacity, thermal diffusivity, and thermal conductivity of consolidated composites of active carbon materials

The thermal conductivity of CDC samples with and without heat-conducting additive has been measured by Träger et al. with the transient hot bridge technique [34]. For comparison in this work, a few samples were investigated with the laser flash method [137] to obtain thermal diffusivities and differential scanning calorimetry to obtain specific heat capacities.

Differential Scanning Calorimetry (DSC)[5] [138] measurements were conducted with carbonaceous powders obtained by pulverizing the consolidated samples (CDC & AC) to determine specific heat capacities. A thermal gravimetric analysis (TGA) of the CDC provided information on the transient, temperature-dependent mass change rate. The measurement was conducted with a temperature increasing rate of 10 K/min. Up to 140°C, a mass loss of around 3% could be obtained which can mainly be attributed to the desorption of water previously adsorbed from moisture in ambient air. Between 140°C and 500°C, a further mass loss of 8 % was detected which can be attributed to the evaporation of volatile components. For the DSC

[5] Differential Scanning Calorimetry (DSC) and thermal diffusivity (LFA) measurements were conducted at the "Institut für Kunststofftechnik" (IKT) at the University of Stuttgart. The explanations, measurements strategy and results were provided by the IKT.

measurements, the carbonaceous samples were pre-heated, and in-situ dried in the DSC measurement cell at 120°C for 10 min, to remove adsorbed species. Following, without opening the cell, the DSC measurement was conducted with four CDC samples and one AC-sample, with different compositions and primary particle sizes. In the measurements, the temperature was increased from 20°C to 100°C with an increasing rate of 10 K/min. After the DSC measurements, the sample weight was measured and used for determining the specific heat capacities. Besides specific heat capacity, thermal diffusivities α^{eff} of consolidated samples were measured with the laser flash method [137] using a Netzsch LFA 447[5]. In equivalence to the DSC measurements, the samples were pre-heated at 120°C for 30 min to remove adsorbed species. Afterward, thermal diffusivities were measured at 25°C, 50°C, 75°C, and 100°C at atmospheric pressure.

Figure 4-17 on the left shows the specific heat capacities from the DSC measurements for sample P_{68} (Exp_{CDC}). The measurement points can be approximated reasonably well with a linear fit. Results obtained for the other CDC samples are qualitatively equivalent.

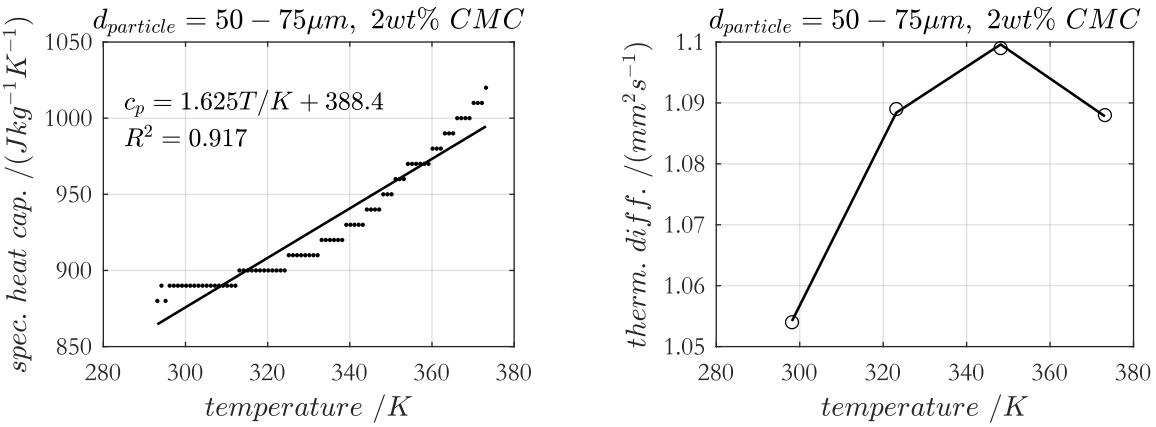

Figure 4-17: Measurement results of specific heat capacity and thermal diffusivity as a function of temperature for CDC-sample P_{68} (Exp_{CDC}) with $d_{par} = 50 - 75$ µm.

The fitted linear equations are summarized in Table B-5. The thermal diffusivities of the sample P_{68} (Exp_{CDC}) obtained by the laser flash method are shown on the right in Figure 4-17 indicating a minor dependency on temperature. Averaged thermal diffusivities of the CDC- and AC-samples are also listed in Table B-5.

Using thermal diffusivity, specific heat capacity, and bulk density ϱ^{bulk}, the effective thermal conductivity can be calculated [108]

$$\lambda^{eff}(T) = \alpha^{eff}(T)\varrho^{bulk}c_p(T). \tag{4-21}$$

The respective bulk densities were determined by weighing and measuring the dimensions of macroscopic AC samples and by mercury intrusion (see section 4.2.2) for the CDC samples. The derived effective thermal conductivity includes contributions of the solid adsorbent matrix λ^s and of dry air λ^g, located in the macro- and micropores of the samples during the thermal diffusion measurement. Assuming parallel phases weighted with their volume fractions, the thermal conductivity of the solid adsorbent matrix is obtained by

$$\lambda^s = \frac{\lambda^{eff} - \lambda^g\left(\varepsilon^{ma} + \varepsilon^{mi}\right)}{1 - \varepsilon^{ma} - \varepsilon^{mi}}. \tag{4-22}$$

Alternatively, the apparent thermal conductivity of the microporous particles $\tilde{\lambda}^s$ related to the particle volume fraction $\tilde{\varepsilon}^s$ in m^3_{par}/m^3_{comp} can be used, given by

$$\tilde{\lambda}^s = \frac{\lambda^{eff} - \lambda^g\left(\varepsilon^{ma} + \varepsilon^{mi}\right)}{1 - \varepsilon^{ma}}. \tag{4-23}$$

Effective thermal conductivities and thermal conductivities of the dry adsorbent particles of the sample P_{68} (Exp_{CDC}) are shown in Figure 4-18. A linear equation correlates the measurement reasonably well. This linear correlation is used for the effective material models introduced in section 2.4 as well as in the process simulations. Additionally, linear correlations of the effective thermal conductivities of the other CDC- and AC samples are summarized in Table B-5.

Some summarizing conclusions can be drawn comparing the thermal conductivities for the different samples which are following the conclusions drawn by Träger et al. [34]: The thermal conductivities of the consolidated CDC composites are two to three times greater than that of the consolidated AC- composites. Concerning the CDC samples, larger primary particle sizes (75-150 µm) increase thermal conductivity compared to composites with smaller primary particles (50-75 µm). The addition of Boron Nitride to the CDC-samples only slightly increases thermal conductivity. However, a proportional increase suggested by the effective material model with parallel phases cannot be observed which is due to the non-percolating Boron Nitride phase. Therefore, the material model developed from effective medium theory is more appropriate to describe the effective thermal conductivity of composites with statistically added heat additives.

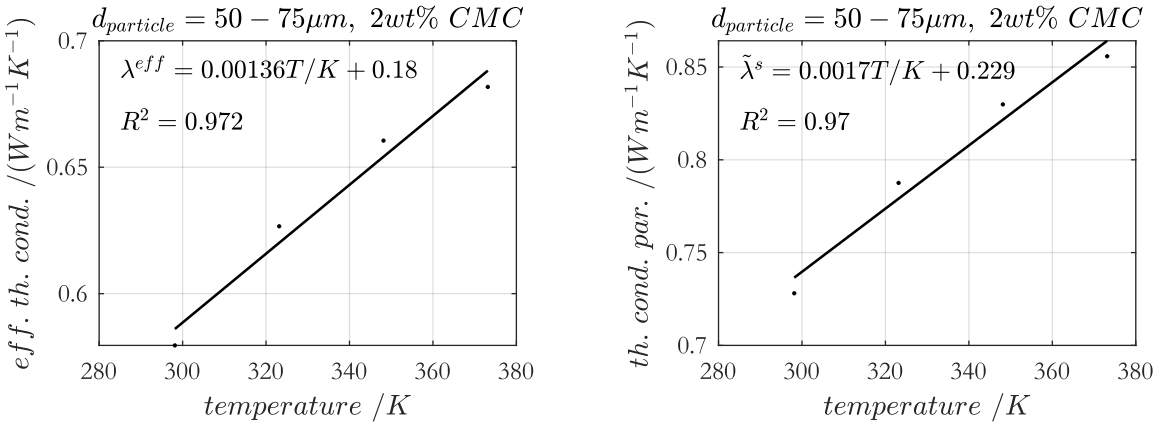

Figure 4-18: Effective thermal conductivity of sample P_{68} (Exp_{CDC}) calculated with equation (4-21) (left); Corresponding thermal conductivity of dry adsorbent particles $\tilde{\lambda}^s$ obtained with equation (4-23) (right).

4.6 Summary

For the combined material and process development, plausible material models are required in addition to reliable process models. In the course of this work, the effective material models were motivated in part by the findings of experimental investigations of various adsorbent composites. For this purpose, it was necessary to characterize many composites with different compositions and to derive structure-property correlations from the experimental findings. The composites were produced by the project partner at the University of Darmstadt[3] and characterizations of powdered samples were carried out, from which the parameters related to the primary particles could be derived. In this work, the characterization of powdered samples was partially repeated to confirm the experimental results. For the application in technical devices, the adsorbent needs to be temperature controlled by a Hex. For that, the application of powdered samples is not suitable. Therefore, the adsorbent must be provided in a condition so that it can be well contacted with the Hex for which cuboid adsorbent composites were selected. Besides, for the active material carbide-derived carbons as well as activated carbons have been chosen. In addition to the powder-based parameters, the effective material parameters of the adsorbent composites are crucial for the application of sufficient process models.

In this chapter, besides powdered-based characterisations, several composites were investigated for methanol adsorption, effective interparticle mass transport, and effective thermal conductivity. The main findings are:

- Methanol adsorption capacity correlates linearly with the fraction of adsorbent and thus, additives and binders do not block any adsorption sites.
- Depending on the process conditions and void widths, besides viscous flow, Knudsen diffusion occurs in the composites.
- The greater the primary particle and additive sizes, the greater the void widths and thus the better the mass transport through the void network.
- Effective thermal conductivity is only slightly improved by adding heat additives, even at high total mass fractions, which is due to the fact, that the additives do not reach the percolation threshold, and possibly binder acts as a thermal resistor.

Finally, two completely characterized composites were selected, whose material data are the basis for parameterisation of the material and process models in the further course of the work. The total parameter set characterizing these two samples is summarized in Appendix B.4.

5. Combined Material and Process Design for 2-Bed adsorption chillers

The methods, results, figures, and discussions presented in this chapter were partly published by the author of this thesis [139]. Some sections are taken verbatim from the publication and are reproduced here.

In this chapter the distributed parameter model introduced in section 3.2.3 is used for process simulations of the idealized two-bed adsorption refrigeration process (see Figure 1-1), solely taking transport hindrance in the composites into account. Initially, the underlying mathematical model is briefly repeated. The process model is initially parameterized with the material parameters of the CDC composite with 2 wt% CMC binder given in Table B-6 (P_{68} (Exp_{CDC})). The subsequent results section begins with a discussion of the spatial and dynamic profiles in cyclic steady-state (CSS). After that, a two-step optimization approach and objective function are introduced which are applied to optimize cycle time and layer thickness, taking the Pareto-optimal behaviour of process efficiency and power density into account, which results in a global optimal Ragone-plot. This optimization approach is used more frequently in the remainder of this thesis.

In a further step, the experimentally investigated material parameters of a CDC composite with 10 wt% of boron nitride heat additive and 2 wt% of CMC binder (P_{67} (Exp_{CDC+BN})) were inserted in the process model and the process simulations were repeated. By adding inert heat-conducting BN to the composites, the adsorption capacity is reduced. However, the experiments outlined in chapter 4 reveal a slight increase in heat and mass transfer (see Table B-6). A comparison of the simulations conducted with Exp_{CDC} and Exp_{CDC+BN} reveals whether the decrease in adsorption capacity is overcompensated by improved transport characteristics.

Finally, the effective material models introduced in section 2.4 are applied and the volume fractions of heat additive ε^{ha} as well as interparticle voids ε^{ma} are varied representing different compositions of the composites.

5.1 Distributed parameter model of two-bed adsorption refrigerator

The governing equations for the conservation of mass and energy of an idealized two-bed adsorption cooling process were developed in chapter 3. For clarity, the used equations are briefly referenced. The model for the adsorber consists of partial differential equations describing the CDC composites ($ads + ad + v + ha$) and an ordinary differential equation for the passive mass of piping (pm). The model is completed with algebraic equations describing the isothermal evaporator and condenser.

Mass and energy transport are spatially resolved over the height of the CDC composites (coordinate z). In terms of methanol vapor density (ϱ^v) and temperature (T), the conservation equations of mass and energy as well as the respective boundary conditions are summarized in section 3.2.3.4. For the experimentally investigated CDC composites, the terms referring to heat additive (ha) are neglectable. These terms are relevant for simulations with varying composite compositions. Furthermore, the passive mass of the Hex is considered using equations (3-7)-(3-9). For the process simulations, the heat transfer resistance between heat transfer fluid, passive mass, and adsorbent composites are neglected to not limit the overall process kinetic. In the process simulations, no additional equation is solved for the heat transfer fluid. It is rather assumed to be isothermal by directly applying the specified temperatures according to Table 3-1.

Finally, to exclusively investigate the kinetical effects of the transport within the adsorbent composites, evaporator and condenser are modelled as isothermal apparatus using the algebraic equations (3-26) and (3-27) to evaluate the cooling power and heat flux dissipated in the condenser.

The set of partial differential equations is reduced to a differential-algebraic system by discretizing the spatial derivatives using the finite volume method. The discretized process model is dynamically solved using the ode15s solver in MATLAB. Details of the numerical discretization, solution approach, and process boundary conditions are outlined in Appendix D.1 and D.2.

5.2 Simulation results of experimentally characterized CDC composites

Initially, simulation results are discussed which were obtained with the distributed parameter model parameterized with the experimental characterized CDC composites (Exp_{CDC}). The

material parameters used for parameterization are given in Table B-6. Subsequently, the effective material models introduced in section 2.4 are applied to vary the composition of the composite and to conduct a combined material and process optimization.

Spatial and dynamic profiles – from initialization to CSS

Simulations with the one-dimensional process model provide spatially distributed temperature, pressure, and loading profiles across the thickness of the CDC composites. Figure 5-1 shows the spatial profiles of the adsorption half cycle (pre-cooling and evaporation steps) as well as in the desorption half cycle (pre-heating and condensation steps) of one cycle in CSS. In addition to the initial and final spatial profiles (in black), profiles evenly distributed over time are shown (in grey). Exemplarily, the simulations were conducted with a short cycle time of $t_{cyc} = 150s$ and with composite layer thickness of $8\,mm$. In cyclic steady state, the initial profiles in the adsorption half cycle are identical to the final profiles of the desorption half cycle.

The initial temperature profile in the adsorption half cycle is shown on the top-left side. Due to switching of the temperature boundary condition in the heat transfer fluid from T_{des} to T_{ads}, the temperature sharply decreases in the lower layers of the CDC composites (at 8 mm). During the entire adsorption step of 75s (half of the cycle time), the temperature continuously decreases whereby the upper layers experience a smaller and significantly slower decline in temperature than the lower layers. On the one hand, this is due to the heat transport resistance of the CDC composites and, on the other hand, due to the exothermic adsorption that occurs preferentially in the upper layers. The pressure profiles are qualitatively identical to the temperature profiles. However, the final pressure profile is reached slightly faster than the final temperature profile indicating a heat transfer limitation. Initially, the pressure in the top layer of the CDC composites exceeds the pressure of the evaporator and thus the connecting valve remains closed. The decreasing temperature in the lower layers induces a rise in adsorption potential which leads to methanol adsorption from the interparticle voids accompanied by a sharp decrease in the lower layer pressure. This leads to desorption in the upper layers and thus reallocation of methanol from the top to the bottom layers of the CDC composites. Consequently, the loading in the upper layers is initially reduced whereas the lower layers experience an increase in methanol loading. As soon as the pressure of the evaporator exceeds the top layer pressure, the connecting valve opens giving rise to a mass flux from the evaporator to the adsorber and, therefore, a cooling production.

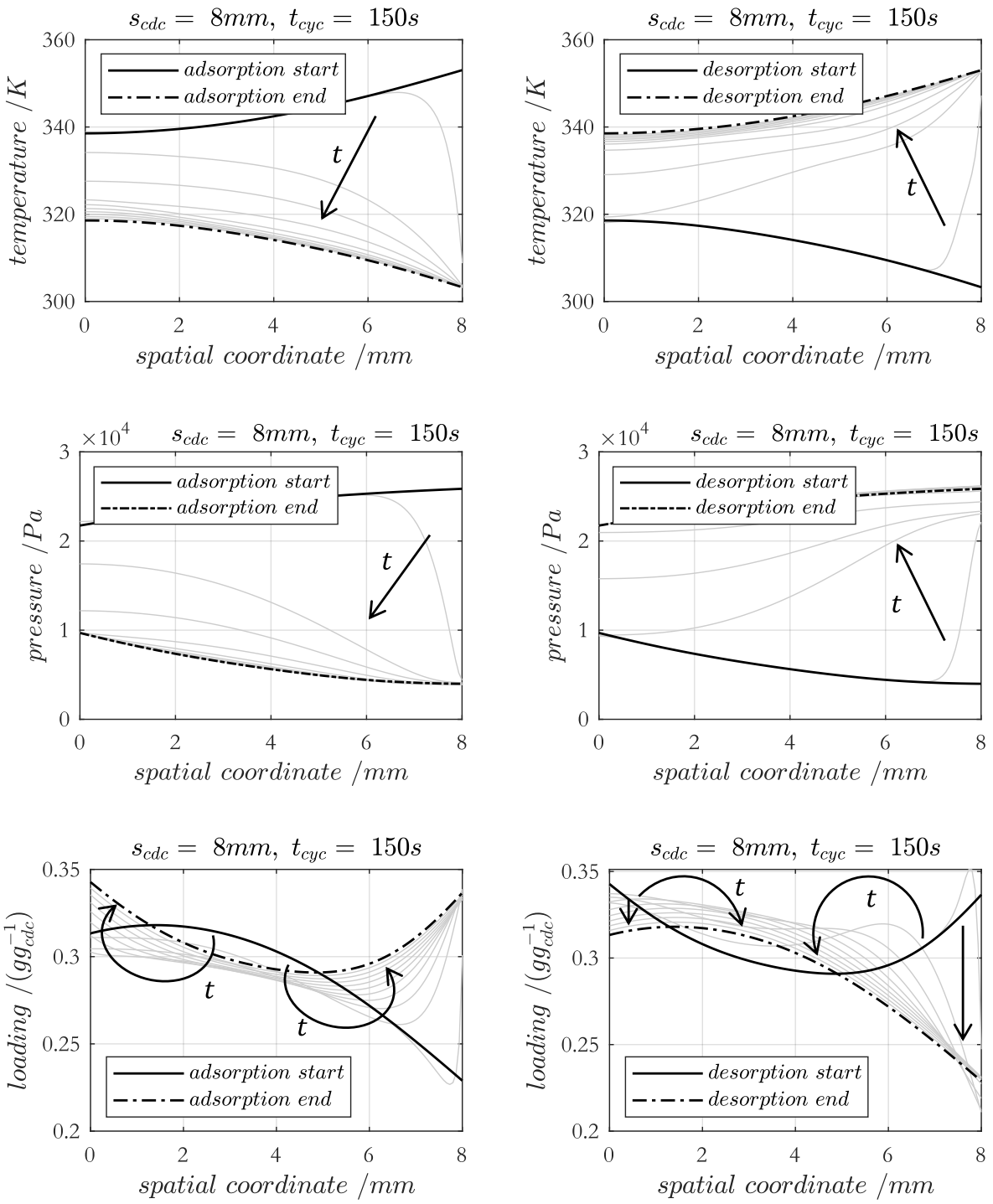

Figure 5-1: Spatial temperature, pressure, and loading profiles in CSS obtained with simulations of the two-bed adsorption refrigeration process with cycle time of $t_{cyc} = 150s$ and for a layer thickness of CDC composites of $8\ mm$. The plots on the left-hand side show the profiles of the pro-cooling and evaporation steps (adsorption) during the first half of the cycle; the plots on the right-hand side show the spatial profiles of the pre-heating and condensation steps (desorption) in the second half of the cycle.

The spatial profiles in desorption half cycle are shown on the right-hand side in Figure 5-1. After half of the cycle time (75s), the pre-heating step begins by changing the temperature boundary condition from T_{ads}^{min} to T_{des}^{max} (see Table 3-1), causing the temperature in the CDC composites to rise abruptly. Like in the adsorption half cycle, initially, the check valves in the adsorber are closed. Therefore, the sharp temperature rise accompanied by a decrease in adsorption potential leads to a reallocation of methanol from the lower to the middle and top layers of the CDC composites as well as an increase of interparticle void pressure. Once the top layer pressure exceeds condenser pressure, the connecting valve opens, and with time, the upper layers are preferentially regenerated.

In addition, the transient temperature and pressure profiles of the different layers of the CDC composites are shown in Figure 5-2. Here, the top layer and average temperature profiles as well as the top and bottom layer pressure profiles are highlighted.

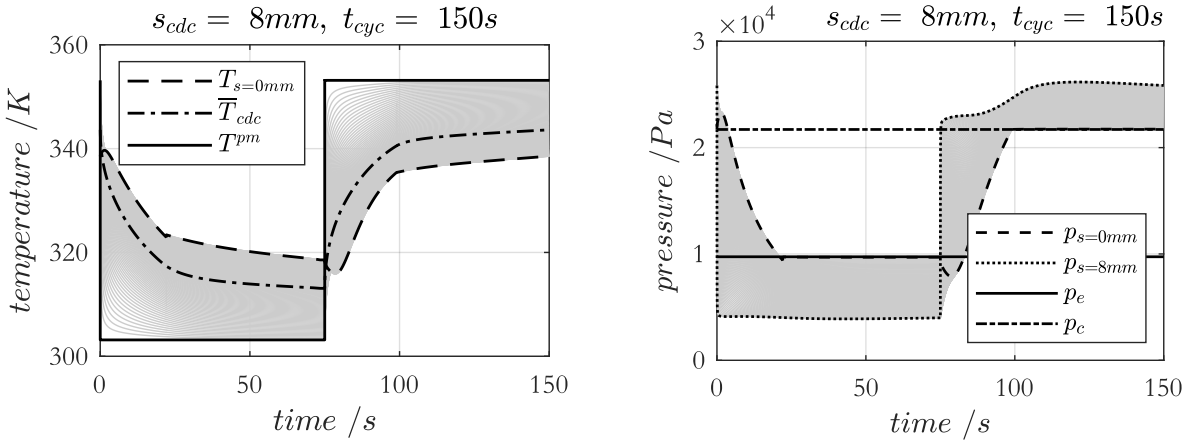

Figure 5-2: Transient and spatial temperature and pressure profiles in cyclic steady state. Each grey line shows the transient profile of another spatial discretization layer.

Since the heat transfer fluid is idealized and assumed to be isothermal in the individual half-cycles and the heat transfer between fluid and Hex flat tubes is not limiting, the passive mass temperature experiences a step-like temperature profile. The temperatures of the different CDC composite layers follow the temperature of the heat exchanger with a delay. After approximately 20s, the upper layer pressure ($s = 0\ mm$) reaches evaporator pressure, and the valve opens initializing the adsorption step. At this point, the top layer temperature profile experiences a bend due to the exothermic adsorption. After the half-cycle time, the temperature boundary condition is changed to T_{des} inducing the pre-heating step. After approximately 100 s, the upper layer

pressure reaches condenser pressure, and the condensation step begins which is accompanied by a bend in the top layer temperature profile due to the endothermic desorption.

Depending on the set of parameters used, several cycles are required until a cyclic steady state is reached. Figure 5-3 shows loading profiles from initialization to CSS for different layer thicknesses and cycle times. Process simulations with short cycles and with CDC composites with a large transport resistance (large layer thickness) require the most cycles to reach CSS.

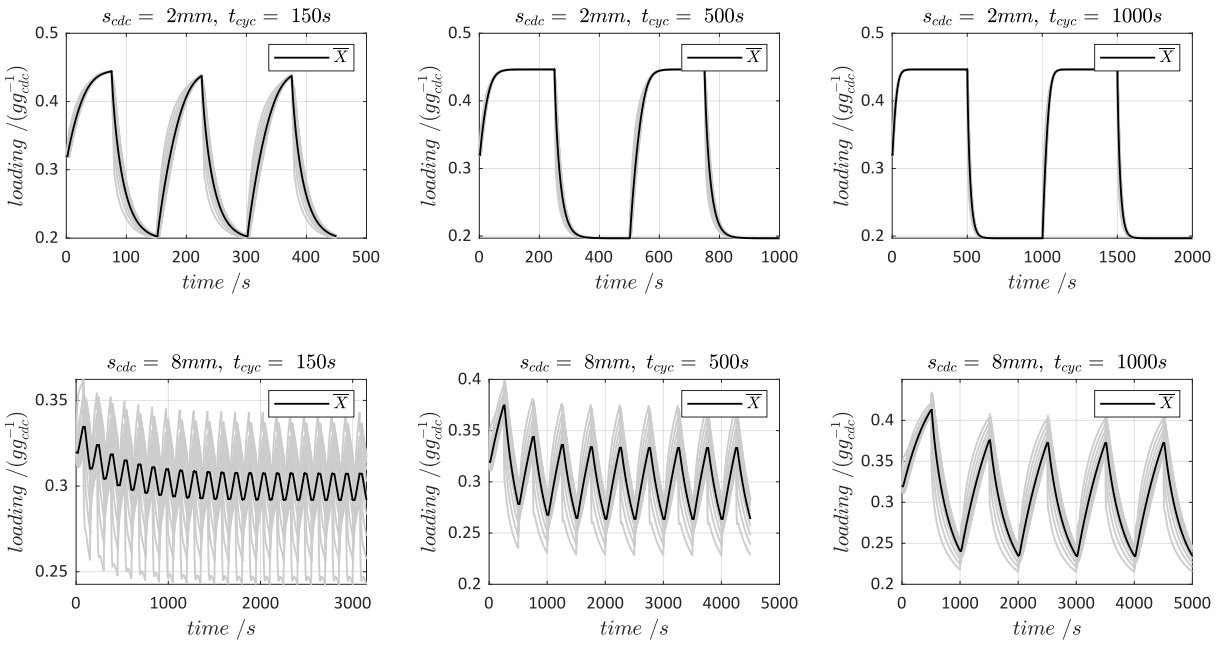

Figure 5-3: Averaged (in black) and spatially distributed (in grey), transient loading profiles from initialization to cyclic steady state for simulations with a layer thickness of the CDC composites of 2 mm as well as 8 mm and process cycle times of 150 s, 500 s, and 1000 s.

To reduce the simulation times, determining the CSS with a sufficient criterion is necessary (see equations (D-9) and (D-10)).

When using thin CDC composites, the averaged equilibrium loading is reached in approximately 100 s after switching between adsorption/desorption and vice versa. The difference between equilibrium loading in adsorption and desorption is approx. 0.24 g/g_{cdc} which is given by the adsorption isotherm. Therefore, cycle times longer than 200s do not provide any improvement in terms of COP and are accompanied by a reduction in SCP. In contrast, when using thick CDC composites (8 mm) and the same cycle time of 150s, the adsorption equilibrium is not reached. The advantage of thicker layers (greater ratio of active to passive mass) concerning the process efficiency comes into play with longer cycle times, as the available adsorption capacity is better

utilized. However, the specific power continuously decreases with longer cycle times and thus determination of the optimal layer thickness and process operation point requires taking this Pareto-optimality into account.

Objective function and workflow for performance optimization

The main criteria for evaluating adsorption chillers are criteria for efficiency, like COP, and specific cooling power, like SCP. The Pareto-optimality of process efficiency and power density can be treated by a combined cost function, e.g., as suggested by Pons [140], by optimization of COP using a prescribed SCP. In detail, the procedure is twofold with the optimization of the process cycle time t_{cyc} and the layer thickness of CDC composites s_{cdc} (steps 1 and 2). For the combined material and process development, the approach is extended by two material parameters (volumetric proportions of interparticle voids ε^{ma} and heat conducting additive ε^{ha}) in steps 3 and 4 to additionally optimize the composite's composition

$$\underbrace{\left(\frac{\partial COP}{\partial t_{cyc}}\right)_{SCP}}_{1} = \underbrace{\left(\frac{\partial COP}{\partial s_{cdc}}\right)_{SCP}}_{2} = \underbrace{\left(\frac{\partial COP}{\partial \varepsilon^{ma}}\right)_{SCP}}_{3} = \underbrace{\left(\frac{\partial COP}{\partial \varepsilon^{ha}}\right)_{SCP}}_{4} = 0. \tag{5-1}$$

The workflow of the two-step optimization approach is outlined in Figure 5-4. The three temperature levels, prescribed SCP and the specific mass of the Hex are input parameters for the process simulations.

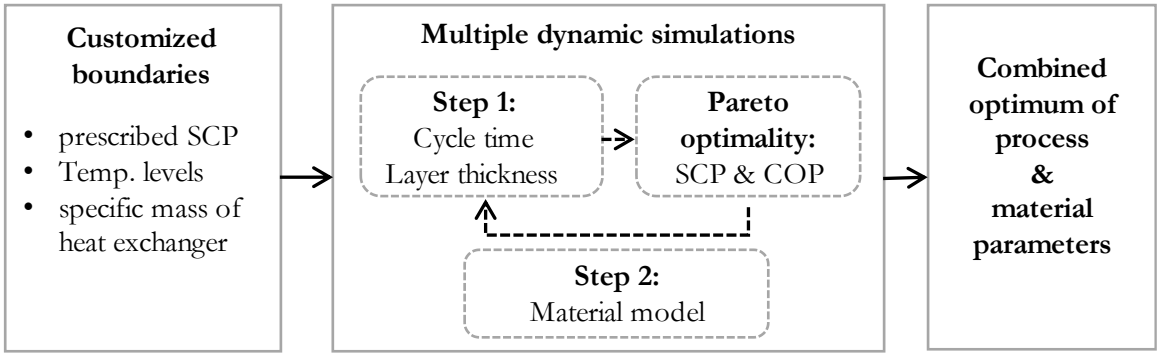

Figure 5-4: Workflow of the optimization approach taking the Pareto-optimality of efficiency and power density into account. Additionally, by varying the composite's composition utilizing the effective material models, a combined process and material optimization is conducted.

In the first step, cycle time and composite layer thickness are varied in a wide range for a given material composition. For each unique combination, the distributed parameter model (microscopic level model) is dynamically solved for CSS. In a post-processing step, for different

prescribed SCP, a pair of optimal cycle time and layer thickness corresponding to the maximal COP are identified. If the adsorbent costs are crucial and/or heating energy is freely available, a high cooling power density would be aimed at. However, this would be accompanied by a rather low optimal COP, thin layer thickness, and short cycle times. On the other hand, if the process efficiency is the main objective, the process would be operated with a low SCP, thick layers, and long cycle times.

In addition, structured composites can be investigated by applying the material models outlined in section 2.4. For every prescribed SCP, different optimal composite's composition with corresponding optimal layer thickness and cycle time can be identified resulting in a global optimal curve.

Optimization of cycle time and layer thickness for experimentally characterized CDC composites

In the first step, a parameter variation is carried out to determine the maximum achievable COP^{max} for a prescribed SCP in the two-dimensional parameter space concerning process cycle time and layer thickness. Exemplarily, this procedure is described with simulations conducted with the experimentally characterized CDC composites without heat additive ($\varepsilon^{ha} = 0$, samples termed Exp_{CDC}, see Table B-6). The cycle time is varied in a wide range between 20s and 2000s. Exemplarily, Figure 5-5 shows the results for a layer thickness of 5 mm and 8 mm. Besides COP and SCP obtained from the process simulations, the thermodynamic ideal COP^{theo} and SCP^{theo} are shown which are obtained from equations (3-1) and (3-5).

For long cycle times, adsorption equilibrium and thus the theoretical COP^{theo} and SCP^{theo} are reached. Whereas COP is monotonously increasing with cycle time, SCP shows an optimum and declines with longer cycle times. For thicker layers, adsorption equilibrium is reached at longer cycle times due to longer transport paths followed by reduced transport dynamics. However, the increased ratio of active adsorbent to passive mass of Hex increases the process efficiency, which underlines the Pareto-optimality between energy efficiency and power density. This trade-off is common for many energy-transformation and -storage technologies and is often visualized in Ragone-plots, by plotting efficiency vs. power density or vice versa e.g., [16], [141]. An operating point in favour of a large power density is always accompanied by a loss of energy efficiency or vice versa.

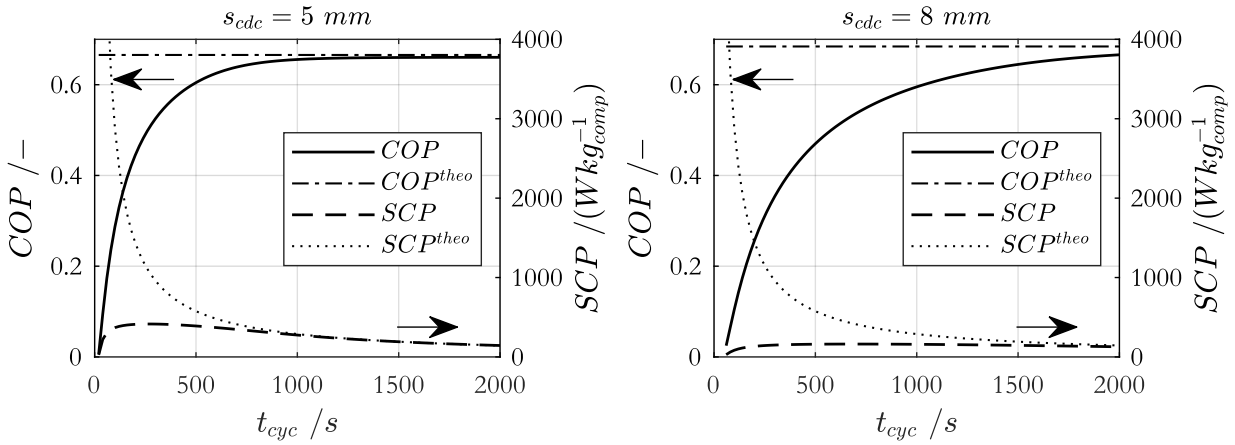

Figure 5-5: COP and (composite mass-specific) SCP as a function of cycle time for CDC composites without heat additive ($\varepsilon^{ha} = 0$) and with layer thickness of 5 mm and 8 mm evaluated with equations (1-1) and (1-2). In addition, the thermodynamic theoretical values calculated with equations (3-1) and (3-5) are shown.

By repeating the simulations and post-processing procedure for different layer thicknesses of the CDC composites between 1 mm and 9 mm, several Pareto-frontiers are obtained. Depending on the prescribed SCP, an optimal COP^{opt} with an associated cycle time can be extracted from each of these data sets. Exemplarily, Figure 5-6 shows the obtained COP^{opt} as function of the layer thickness for a prescribed SCP of 500 W/kg. In addition, the maximal COP^{max} as well as the theoretical efficiency obtained in the thermodynamic equilibrium is shown. In this example, the maximal COP is reached with a layer thickness of 3.7 mm with a process cycle time of 539 s.

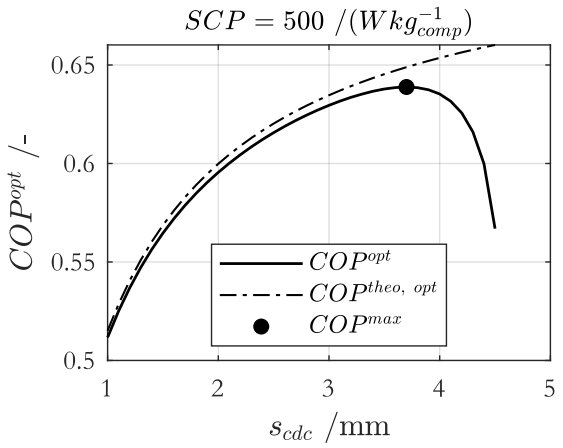

Figure 5-6: Maximum achievable COP^{max} in the two-dimensional parameter space concerning cycle time and layer thickness exemplary for a prescribed SCP of 500 W/kg.

This analysis leads to a maximum achievable COP^{max} for a given material in the two-dimensional parameter space. Furthermore, this analysis reveals increasing transport limitations with thick layers and the increasing divergence from thermodynamic equilibrium. In this example, the transport dynamics of CDC composites thicker than 4.5 mm are too low to provide the prescribed SCP.

Variation of the CDC composite composition

In addition to cycle time and layer thickness, further degrees of freedom are given by the material concerning the composite's composition. In this section, a comparison between experimentally characterized CDC composites with ($\varepsilon^{ha} > 0$) and without ($\varepsilon^{ha} = 0$) increased thermal conductivity is conducted. Therefore, the previously outlined workflow is repeated for the CDC composites with 10wt% BN ($\varepsilon^{ha} > 0$, samples termed Exp_{CDC+BN}, see Table B-6) and the optimization routine is conducted for a wide range of prescribed SCPs. The optimization results are visualized in a Ragone-plot with each point on the curve accompanied with a unique optimal set of layer thickness and cycle time. Figure 5-7 shows the optimization results obtained for the two experimentally characterized CDC samples. The optimal cycle times (right) are independent of the sample, which is due to the proportionality of SCP and cycle time (see equation (1-2)). The Ragone-plot (left) shows convex profiles which are obtained due to the fact, that besides cycle time, the layer thickness is optimized at each point. When using a constant layer thickness (here exemplarily 1.5 mm), the curves are concave, and only in a small region of prescribed SCPs, the maximal efficiency is achieved which underlines the necessity of applying combined optimization of process and material parameters.

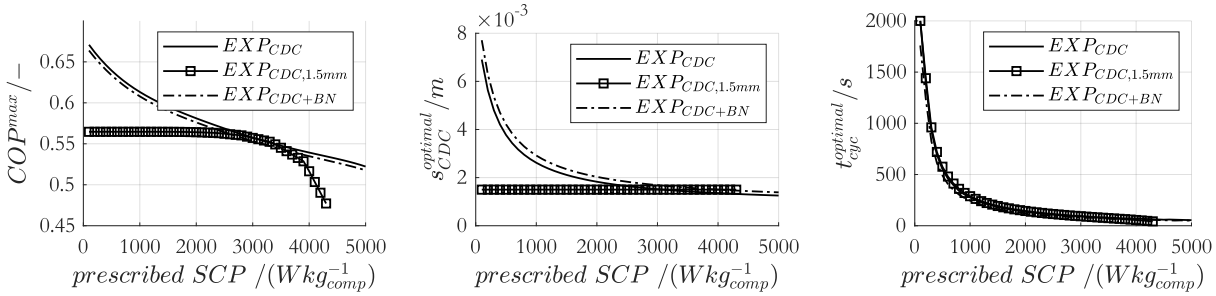

Figure 5-7: Ragone-plot of maximal efficiency (COP) as a function of prescribed power density (left) accompanied with optimal layer thickness (middle) and optimal cycle time (right). Material parameters from experimentally characterized CDC composites with and without BN additive (see Table B-6) were investigated in the process simulations.

Increasing the thermal conductivity by statistically adding BN to the CDC composites leads to a minor reduction in efficiency for prescribed SCPs. On the one hand side, the enhanced thermal conductivity is accompanied by reduced heat transport resistance which is why slightly thicker composite layers are preferred. However, the reduced adsorption capacity cannot be overcompensated by the increased thermal conductivity resulting in lower efficiencies. Therefore, for the experimentally produced CDC composites, statistically adding heat additive accompanied by a large reduction of adsorption capacity is detrimental to the overall process performance.

Still, heat and mass transfer resistances are present in the adsorbent composites limiting the process performance. The question is how to reduce these resistances without significantly reducing the adsorption capacity? This question is addressed in the subsequent section by utilizing the effective material models introduced in section 2.4.2.

5.3 Simulation results with effective medium theory and percolating heat additive

To reduce heat and mass transfer resistances of the adsorbent composites, the material space is extended by two additional material parameters. For better mass transfer, the volume fraction of interparticle void space ε^{ma} can be increased and for a higher thermal conductivity, the volume fraction of the heat conducting additive ε^{ha} can be increased. In the remainder, two different effective material models are introduced in the process model, in each case with the goal of identifying the optimal composite composition for different prescribed SCPs. In both material models, a variation of the volume fractions is directly linked with a variation in mass and heat transport parameters as well as adsorption capacity. The heat additive phase with volume fraction ε^{ha} consists of an aluminium alloy (AlSi10Mg(Fe)) with the parameters listed in Table 5-1.

Table 5-1: Material parameters of aluminium alloy (AlSi10Mg(Fe)) heat additive phase [116].

$c_p^{ha}/(Jkg^{-1}K^{-1})$	910
$\lambda^{ha}/(Wm^{-1}K^{-1})$	140
$\varrho^{ha}/(kgm^{-3})$	2680

Initially, the effective material model obtained from effective medium theory is introduced in the process model. However, as the discussions in section 2.4.2.1 and the visualization of the material parameter space in Figure 2-7 showed, even a small increase in the effective thermal conductivity requires a large amount of heat conducting additive (e.g., $\varepsilon^{ha} > 0.12$ for $\lambda^{eff} > 1 Wm^{-1}K^{-1}$).

Furthermore, a strong dependency of the effective thermal conductivity on the void fraction ε^{ma} was investigated in that model. As a reason of that, the simulation results obtained with the effective medium theory model are not discussed in detail but rather the final Ragone-plots are compared in the end of this section.

However, the simulation results obtained with the second material model (with the percolating heat additive phase), which was introduced in section 2.4.2.2, are subsequently discussed in detail. With that model, the best-case composition is investigated by introducing linear, percolating heat conducting structures into the CDC composites. As the discussions in section 2.4.2.2 and the visualization of the material parameter space in Figure 2-9 indicate, with that model, only a minor fraction of heat conducting additive is sufficient to increases the effective thermal conductivity significantly (e.g., $\varepsilon^{ha} > 0.025$ for $\lambda^{eff} > 5 W m^{-1} K^{-1}$).

Figure 5-8 (left) shows surface plots of the process efficiency COP^{max} for variable material compositions exemplarily for a prescribed specific cooling power of 500 W/kg. In addition, the same plot is shown on the right using the effective transport parameters as the axis. As a reminder, in that visualization, cycle time and layer thickness are already optimized for each material composition.

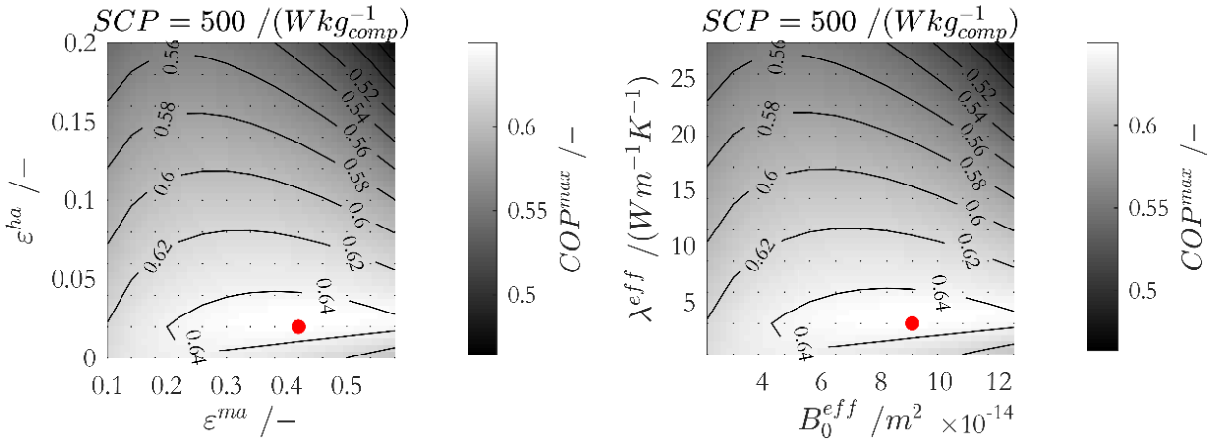

Figure 5-8: COP^{max} as function of the volume fractions (left) and as a function of the transport parameters (right) for a prescribed power density of 500 W/kg. Each point is accompanied by an ideal cycle time and layer thickness. In this case, the optimal void fractions are $\varepsilon^{ma} = 0.42$ and $\varepsilon^{ha} = 0.02$. The simulations were conducted with the linear material model with percolating heat additive phase outlined in section 2.4.2.2.

The evaluation of the objective function in equation (5-1) reveals a non-trivial optimum. For this prescribed power density, the application of the model with percolating heat additive results in a

maximal achievable efficiency of approx. 0.65. Even a small amount of percolating heat additive increases the effective thermal conductivity enough to shift the transport limitation in the direction of mass transfer. It follows that the effective permeability is too small which requires an increase of the void fraction ε^{ma}. The maximal efficiency (maximum of COP^{max}) is obtained with the optimal combination of transport parameters and adsorption capacity. Further increasing the transport parameters leads to a loss in adsorption capacity which cannot be overcompensated. Furthermore, it should be mentioned that the function is very flat in the region of the optimum and forms a plateau rather than a distinctive optimum. On one side, even a small amount of highly conducting additive significantly increases the effective thermal conductivity, but due to its high density also significantly decreases the adsorption capacity (see Figure 2-9). On the other hand, varying the void porosity changes the adsorption capacity only slightly, since no inert mass is added or removed. As a result, the gradients of the maximal efficiency are steep with the variation of ε^{ha} and flat with variation of ε^{ma}. Therefore, COP^{max} only divers slightly in the region of the optimum when varying the transport parameters.

Finally, the previous material optimization step is repeated for a wide range of prescribed SCPs and the optimal efficiencies are determined, which results in a Ragone-plot of the type already discussed in Figure 5-7. Each point on the global-maximal curve is accompanied by a unique set of optimal void fraction, fraction of heat conducting additive, layer thickness, and cycle time. Figure 5-9 shows COP^{max} (left) and s_{cdc}^{opt} (right) as functions of the prescribed SCP for the experimentally characterized CDC composites Exp_{CDC} which has already been discussed in the previous section 5.2. In addition, the simulation results obtained with the effective medium material model (effective medium theory) and with the linear material model with percolating heat additive are shown. The optimal cycle times are equal to the results in Figure 5-7 (right).

Two conclusions can be drawn from the simulation results. First, the findings from section 5.2 are confirmed that the statistical addition of heat additives does not result in an improvement of the process performance. Rather, the results obtained with the effective medium theory model are identical to those obtained in the simulations with the experimentally characterized CDC composites (Exp_{CDC}). This can be attributed to the fact that the composites initially exhibit a heat transport limitation, but the statistical addition of heat conducting additive does not overcompensate for the loss of adsorption capacity. Accordingly, an optimum volume fraction of additive of $\varepsilon^{ha} = 0$ results in the entire range of prescribed SCP. Due to the heat transport limitation and the negligible dependency of the adsorption capacity on ε^{ma} (see Figure 2-7 on the right), the optimum ε^{ma} in the entire range of prescribed SCP also results at $\varepsilon_{exp}^{ma} = 0.23$.

The second conclusion regards the results obtained with percolating heat additive phase. The effect of decreasing the transport resistance of the CDC composites by using linear, percolating heat transfer structures is directly reflected in significantly increased optimal layer thicknesses. In contrast, there is a small reduction in adsorption capacity due to the addition of the inert aluminium alloy, which however is overcompensated by the increased layer thickness. Therefore, the composites with percolating heat additives have a favourable active to passive mass ratio, resulting in improved efficiencies in the whole SCP region.

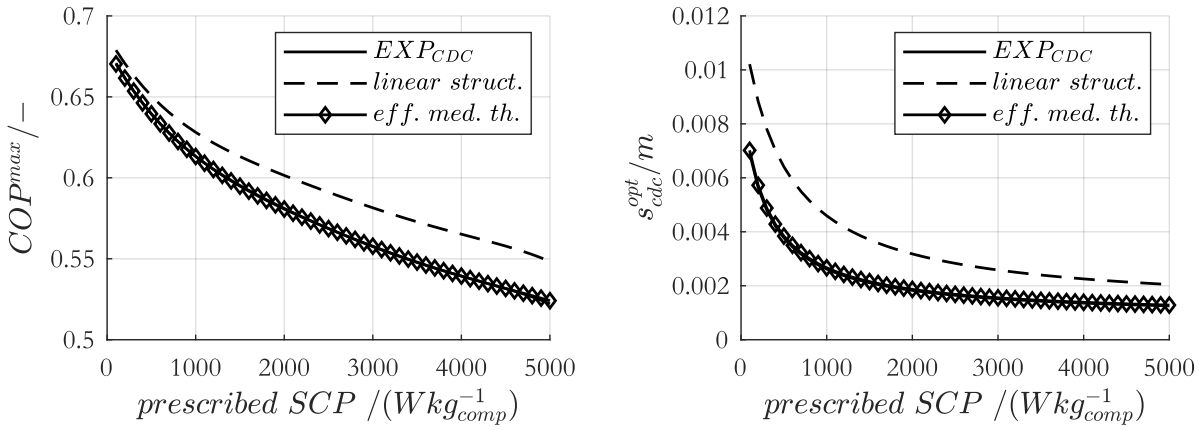

Figure 5-9: Comparison of COP^{max} obtained from simulations with the experimentally characterized CDC composites (Exp_{CDC}), with the effective medium theory model (eff. med. th.), and with the percolating heat additive model (linear struct.). For the percolating heat additive model, the optimum composition is always in the region of $\varepsilon^{ma} = 0.42$ and $\varepsilon^{ha} = 0.02$ for all prescribed power densities. In addition, the optimal layer thicknesses are shown (right).

Even though percolating heat-conducting structures and increased void fractions are beneficial, due to the flat, plateau-like region in the vicinity of the optimum material composition (see Figure 5-8) varying the material contributes only slightly to further improving process performance. Throughout the whole SCP region, the material optimum obtained with the linear, percolating material model is around $\varepsilon^{ma} = 0.42$ and $\varepsilon^{ha} = 0.02$, with a tendency to higher values, when larger SCPs are prescribed and therefore, a faster kinetic is required.

The previous discussion underlines the necessity of optimizing the composition of adsorbent composites for the application in adsorption heat pumps. However, adding heat additive that is statistically distributed in the composite does not provide an advantage since the required amount to reach the percolation threshold is large and the loss of active material cannot be overcompensated by the increased thermal conductivity. Therefore, percolating structures, for

increasing thermal conductivity as well as mass transfer improvement, is more target oriented. Simulations with the material model with linear percolating heat additive phase revealed a significant efficiency improvement without sacrificing specific power density. These findings are the motivation to investigate the material design of 3D-structured adsorbents in more depth. In chapter 6, triangular prism-shaped, percolating aluminium ribs are used to improve the thermal conductivity of activated carbon composites. In addition, macroscopical mass transfer channels are investigated to improve mass transport.

5.4 Summary

Usually, research activities have been devoted to either the improvement of process properties or the study of adsorbent properties. However, separating material and process-related research results in local rather than global optima.

In the context of a combined process and material design, process simulations of a simple 2-bed adsorption chiller setup have been conducted. Besides, material-related parameters (composite composition, layer thickness) process parameters (cycle time) have been varied over a wide range. In a post-processing routine, the optimal set of parameters has been identified taking the Pareto-optimality of process efficiency and power density into account.

In this chapter, the procedure was carried out in two steps. Initially, material parameters of experimentally characterized CDC composites have been used in the dynamic process simulations to introduce the whole optimization routine and poke the point of Pareto-optimality of efficiency and power density. It could be concluded, that statistically adding heat conducting additives to adsorbent composites cannot overcompensate the loss of active material. This has been shown by utilizing the material parameters of two experimentally manufactured and characterized CDC composites in the process simulations.

In the second step, the combined material and process development has been extended to the structural parameters of virtual adsorbents by investigating composites with percolating heat-conducting structures with varying compositions. This was the first time that the focus was placed on structured materials and the great potential was indicated. Due to the percolating heat additive and additionally providing a degree of freedom concerning the mass transfer, heat, and mass transfer resistance of the composites could be reduced. By that, the post-processing optimization routines reveal thicker optimal adsorbent layers and thus, the ratio of active to passive Hex mass can be improved. As a direct consequence, the process efficiency increases without sacrificing the specific power density.

6. Material Design in Adsorption cooling by 3D-structuring

In the simulation studies in chapter 5, material parameters of experimentally manufactured CDC composites were considered. A first variation of the composite's composition and structure was already investigated. It was shown that a considerable increase in efficiency can be achieved with the aid of percolating heat additive phase, which is mainly due to the thicker composite layers which can be utilized due to increased thermal conductivity. With the aim of combined material and process optimization, in this chapter the approach of 3D-structured adsorbent composites is revisited. Physically motivated geometries that offer low resistance to the heat and mass flows in the adsorbent composites are investigated. Since the breakthrough of adsorption heating or cooling devices is directly linked to poor adsorbent performance, a leap in development concerning heat and mass transfer improvement is inevitable to become competitive [4].

Regarding the consolidated composite adsorbent type, only with a large amount of statistically added heat additive, the percolation threshold is reached, and the thermal conductivity can be increased significantly. The high proportion of heat additive is accompanied by a reduction of the specific adsorption capacity and often by a reduction of the mass transport to such an extent that these disadvantages are out of proportion to the increased thermal conductivity, which was shown and intensively discussed in section 5.2. To tackle this issue, mass transfer channels can be introduced into the consolidated composite enhancing the mass transport and thus the performance of adsorption heat transformers. Ammann et al. indicated the mass transport in SAPO-34 zeolite coatings to be the limiting factor for the rate of water adsorption and thus introduced uniformly spaced, linear channels of width 75 µm into the coating, doubling the water sorption rate [141]. Improving the adsorbent permeability is target-oriented if the mass transfer has been identified as the mechanism limiting the process. By adding mass transfer channels, at some point, the main limitation is shifted from mass transport to heat transport. Thus, optimal composition and design of adsorbent composites are subject to an optimization problem requiring a quantitative method comparing heat and mass transfer limitations [16].

With 3D-structuring of adsorbent composites is aimed at improving the performance of the AdHex system for the application in solid sorption chillers, without sacrificing efficiency or power density. The investigation procedure is twofold. In the first step, triangular prism-shaped ribs are introduced to improve the thermal conductivity of the composites. The cross-sectional area of these ribs increases from the top to the bottom of the composites. The rib's shape is

physically motivated by an increasing heat flux towards the Hex. Enhancing mass transfer is enabled by introducing inverted, triangular-shaped macroscopical channels laterally staggered to the ribs. The channel's shape is also physically motivated by a decreasing mass flux towards the Hex. An effective material model is developed to describe the spatially varying transport and adsorption characteristic which is applied in process simulations of a 2-bed adsorption chiller. The simulation and evaluation procedure are equivalent to that discussed in chapter 5.

In a second, experimental step, 3D-printed aluminium alloy ribs are applied in the composites, which was motivated by the simulation findings. In addition, vertical macroscopical mass transport channels laterally staggered to the ribs are introduced. Experimentally prepared, 3D-structured adsorbent composites are investigated in a small-scale adsorption chiller.

6.1 3D-structuring – Theoretical investigation

The methods, results, figures, and discussions presented in this section were already partly published by the author of this thesis [142].

The benefit of structuring is initially investigated with a theoretical approach. First, an effective material model is introduced for the aid of describing the triangular prism-shaped ribs. This effective model is furthermore plugged into the distributed process model of a 2-bed adsorption chiller introduced in section 3.2.3 and dynamically solved in process simulations. By conducting parameter variations over a wide range of process and material parameters and analysing the simulation results in a post-processing step, a global optimum is obtained concerning the process and material parameters.

6.1.1 Material model of 3D-structured adsorbent composites

The triangular geometry of the composites is described with an effective material model, taking the local volumetric compositions of the composites into account. A scheme of the structures is shown in Figure 6-1 which contains macroscopical, triangular prism-shaped heat-conducting ribs and macroscopical mass transport channels with an inverted triangular shape.

A macroporous consolidated adsorbent bed consisting of microporous adsorbent primary particles is attached to the ribs using a binder. The (quasi-) homogeneous adsorbent bed is equivalent to the consolidated composites without heat additive (see Figure 2-5) and thus, the same effective material model is used for this phase (presented in section 2.4.1).

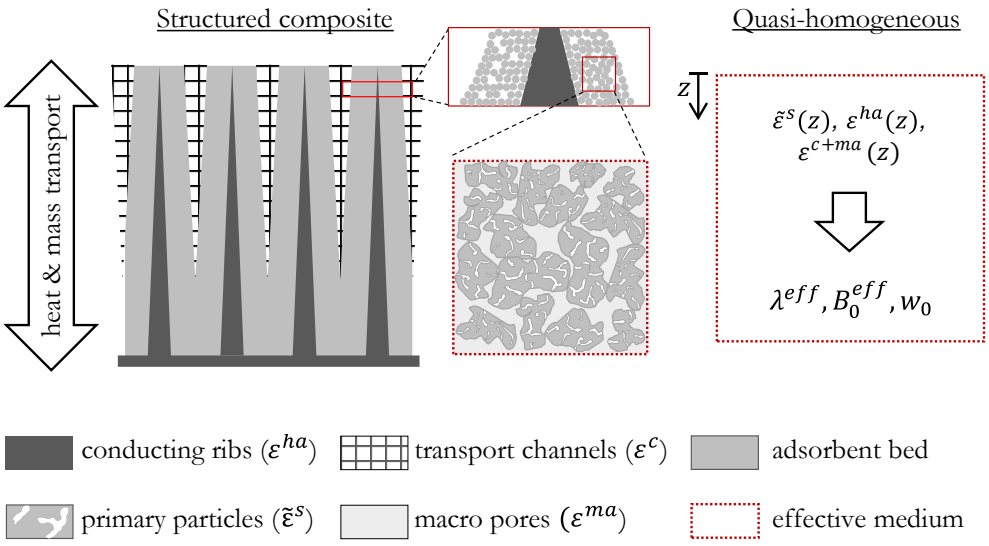

Figure 6-1: Structured adsorbent composite with triangular heat-conducting ribs, inverted triangular mass transfer channels, and consolidated microporous adsorbent particles.

The utilization of triangular prism-shaped geometries is motivated by the physical transport processes occurring in the application in an adsorption heat pump. The structured composites are attached to a heat exchanger with their bottom side. The heat flux increases from the top to the bottom (or decreases from the bottom to the top) of the composites which is due to accumulation of heat of adsorption (or due to heat required for desorption). It is desirable to have a homogeneous temperature distribution over the composite's height, which is established as quickly as possible (to achieve a homogeneous loading distribution). Therefore, the effective thermal conductivity should increase from the top to the bottom which is achieved by the triangular prism-shaped heat conducting ribs. For the same reason, the amount of adsorbent is reduced at the upper side of the composites by introducing inverted triangular mass transfer channels. This ensures that the adsorption heat released at the top or the heat required for desorption can be supplied or dissipated quickly. Another reason for the macroscopic transport channels is to provide sufficient adsorptive pressure over the height of the structure which is essential when applying very thick layers. In the effective model, it is assumed that the pressure in mass transfer channels is constant and thus mass transfer is not limited here. Therefore, the width of the channels only influences the released or required heat of adsorption or desorption due to a variable amount of adsorbent. However, the penetration depth of the channels plays an essential role, since this determines the length of the adsorbent bed, in which mass transport takes place exclusively in the interparticle voids (macropores) and thus, mass transport limitation is possible. The height and width of the heat-conducting ribs, as well as mass transport channels,

are parameters that are optimized in the process simulations. The determination of these parameters results in an optimization problem.

To develop an effective material model of these 3D-structured composites, the geometrical parameters describing ribs and mass transport channels are correlated with the local volume fractions of the individual phases. Figure 6-2 shows the smallest repeating unit of the structured composites and structuring examples with high thermal conductivity, mass transfer capability, and adsorption capacity. The geometry of the structured composite is described with four independent geometrical parameters describing the width and heights of the transport channels and heat-conducting ribs. In detail, these parameters describe

- ε_{top}^{c}: Fraction of mass transport channel at top of the structured composite.
- $1 - s^{c}$: Normalized height of the mass transport channel.
- $\varepsilon_{bottom}^{ha}$: Fraction of the heat conducting ribs at the bottom of the composite.
- s^{ha}: Normalized height of the heat conducting ribs.

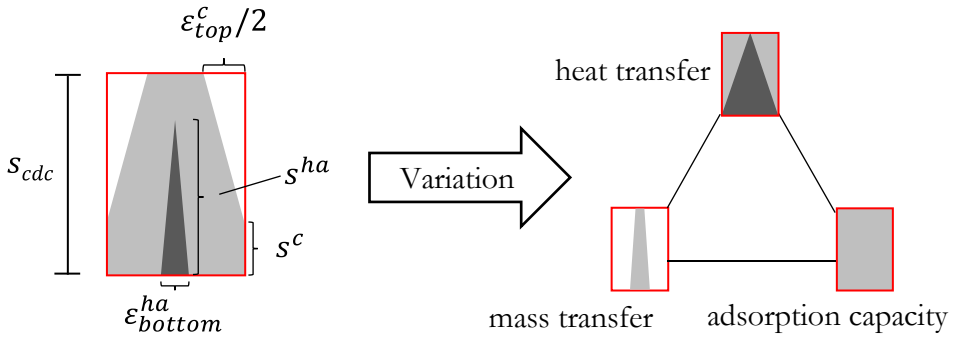

Figure 6-2: Geometrical interpretation of the triangular structured composite with four independent geometrical parameters (left) and three examples of structuring generated by varying the geometrical parameters with high thermal conductivity, mass transfer capability, and adsorption capacity.

The spatial porosity distribution over the height of the structure is calculated using linear correlations resulting in a porosity matrix, which contains the volume fractions of ribs ($\varepsilon^{ha}(z)$), mass transport channels plus voids in adsorbent bed ($\varepsilon^{c+ma}(z)$), and primary adsorbent particles ($\tilde{\varepsilon}^{s}(z)$) in every layer of the composite. This serves as input for the material model and is used to calculate the spatially distributed material and transport parameters. These, in turn, are the input variables for the process model. The short pseudo-algorithm used to calculate the porosity matrix is given in Appendix D.3. Since all phases are percolating, the effective model approach

combining parallel and serial phases introduced in sections 2.4.1 and 2.4.2.2 can be applied. However, the spatial variation of the volume fractions requires an adaption of the equations as shown below.

The porosity matrix contains information upon the spatial distribution of $\tilde{\varepsilon}^s(z)$, $\varepsilon^{c+ma}(z)$, and $\varepsilon^{ha}(z)$ over the height of the structured composites, which are used to calculate the material and transport parameters as follows

$$\varepsilon^s(z) = \tilde{\varepsilon}^s(z)\left(1 - \frac{\varepsilon_{exp}^{mi}}{1-\varepsilon_{exp}^{ma}}\right), \tag{6-1}$$

$$\varrho^{bulk}(z) = \varepsilon^s(z)\varrho^s + \varepsilon^{ha}(z)\varrho^{ha}, \tag{6-2}$$

$$w_0(z) = w_0^{exp}\frac{\varepsilon^s(z)\varrho^s}{\varepsilon^s(z)\varrho^s + \varepsilon^{ha}(z)\varrho^{ha}}, \tag{6-3}$$

$$\tilde{\lambda}^{ad+s+ha}(z) = \frac{\varepsilon^{ha}(z)}{\tilde{\varepsilon}^s(z)+\varepsilon^{ha}(z)}\lambda^{ha} + \frac{\tilde{\varepsilon}^s(z)}{\tilde{\varepsilon}^s(z)+\varepsilon^{ha}(z)}\left(\tilde{\lambda}^s(z) + \frac{X(z)\lambda^{ad}}{\tilde{\varepsilon}^s(z)}\right). \tag{6-4}$$

Where the macroscopical transport channels are penetrating the structure, it is assumed that mass transport is not limiting. In regions without mass transport channels (z-position $> 1 - s^c$), the effective permeability and the constant parts of the Knudsen-diffusion coefficient are calculated in equivalence with equations (2-68) and (2-69)

$$B_0^{eff}(z) = \frac{\varepsilon^{ma}(z)B_{0,exp}^{eff}}{\varepsilon_{exp}^{ma}}, \tag{6-5}$$

$$D^{Kn,const}(z) = \frac{\varepsilon^{ma}(z)D_{exp}^{Kn,const}}{\varepsilon_{exp}^{ma}}. \tag{6-6}$$

For the sake of comparison with the simulations conducted in chapter 5, the identical material parameters have been applied here. The adsorbent related parameters are taken from the experimentally characterized CDC-composites (EXP_{CDC}) listed in Table B-6. For the heat conducting ribs, the material parameters from the aluminium alloy listed in Table 5-1 are applied. The temperature levels and the passive mass of the Hex flat tubes are considered with the values listed in Table 3-1.

6.1.2 Optimization function

Here, the methodical procedure for the optimization of the classical 2-bed adsorption refrigeration process is presented, whereby a virtual material design of 3D-structured composites

is carried out, and, at the same time, the process parameters are considered. An overview of the procedure is given in Figure 6-3.

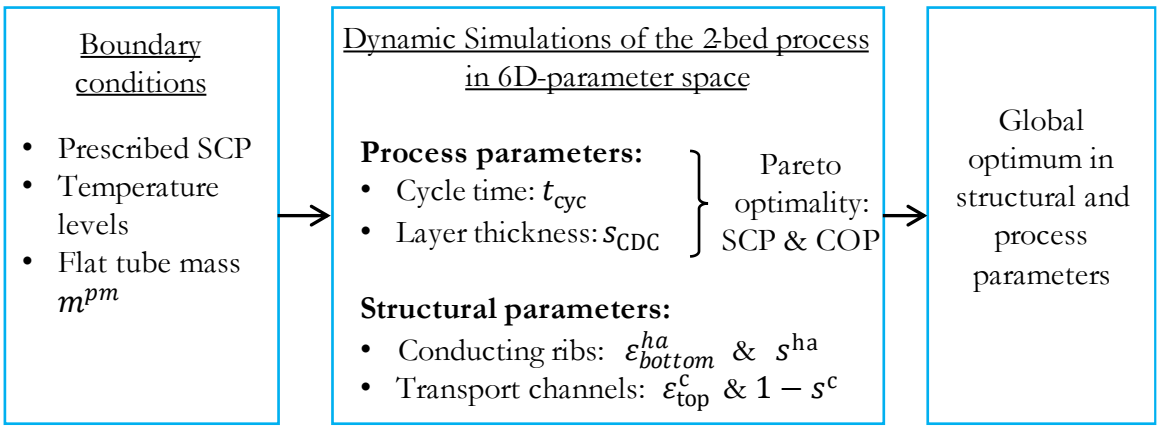

Figure 6-3: Methodical procedure for combined optimization of geometric structure and process parameters for the 2-bed adsorption refrigeration process taking the Pareto-optimality of COP and SCP into account.

Consideration for different user requirements and a prediction of the global optimum in the entire parameter space is performed. On the material side, the structuring of composites is optimized. In addition, on the process side, the cycle time and the layer thickness of the composites are considered. For the optimization of the 6-dimensional parameter space, a suitable objective function is required. Identical to chapter 5, the parameter combination that maximizes the COP is searched for a given SCP.

To compare the different parameter combinations, the process model presented in section 3.2.3 is solved in dynamic simulations up to the cyclic steady state. The objective function of the optimization is formulated as follows

$$\underbrace{\left(\frac{\partial COP}{\partial t_{cyc}}\right)_{SCP}}_{1} = \underbrace{\left(\frac{\partial COP}{\partial s_{cdc}}\right)_{SCP}}_{2} = \underbrace{\left(\frac{\partial COP}{\partial \varepsilon_{top}^{c}}\right)_{SCP}}_{3} = \underbrace{\left(\frac{\partial COP}{\partial s^{c}}\right)_{SCP}}_{4} = \underbrace{\left(\frac{\partial COP}{\partial \varepsilon_{bottom}^{ha}}\right)_{SCP}}_{5} = \underbrace{\left(\frac{\partial COP}{\partial s^{ha}}\right)_{SCP}}_{6} = 0. \tag{6-7}$$

6.1.3 Process simulations

In addition to the operating and process parameters, the structuring of the composites provides several degrees of freedom for the optimization of thermal heat pumps. The presented steps for

process parameter optimization are repeated for differently structured CDC composites, which enables the identification of the global optimum in the 6-dimensional parameter space. In equivalence to the optimization procedure introduced in section 5.2, all parameters were varied to optimize the COP for a prescribed SCP. Since the methodology is identical, optimization of cycle time and layer thickness will not be discussed in detail here. The focus is rather laid on the optimal 3D-structuring of the composites.

Subsequently, the effect of the macroscopic transport channels is discussed, initially for a fixed dimension of the heat-conducting ribs as shown in Figure 6-4. In a further step, the dimension of the heat-conducting ribs is additionally optimized. Finally, the global optimal curve is discussed by comparing the differently structured composites.

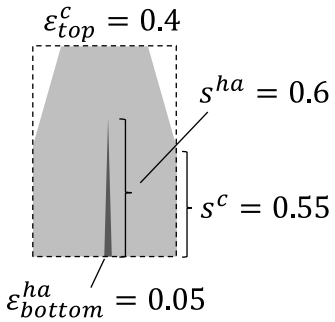

Figure 6-4: Exemplary 3D-structured adsorbent composite with triangular heat-conducting ribs and macroscopical mass transport channels.

6.1.3.1 Optimization of mass transport channels

In addition to the width, the penetration depth of the transport channels plays a role in optimum structuring. If the transport channels penetrate the composites completely, mass transfer is not limiting. However, the large volumetric proportion of transport channels is at the expense of the adsorbent primary particle phase, which deteriorates the ratio of active to passive mass. Conversely, if the transport channels are chosen too small, the adsorbent will be inadequately and unevenly loaded from top to bottom. To investigate these influences, the fraction of macroscopic mass transport channels at the top (ε_{top}^{c}) and their height ($1 - s^{c}$) were varied over a wide range, dynamic simulations of the 2-bed process were performed up to the cyclic steady state, and for each parameter set, the cycle time and layer thickness were optimized. Figure 6-5 shows results of the optimization exemplarily for the 3D-structured composite as shown in Figure 6-4. The left figure shows the maximum achievable COP^{max} for these ribs as a function of the transport channel parameters. On the right, the corresponding optimized layer thicknesses are shown.

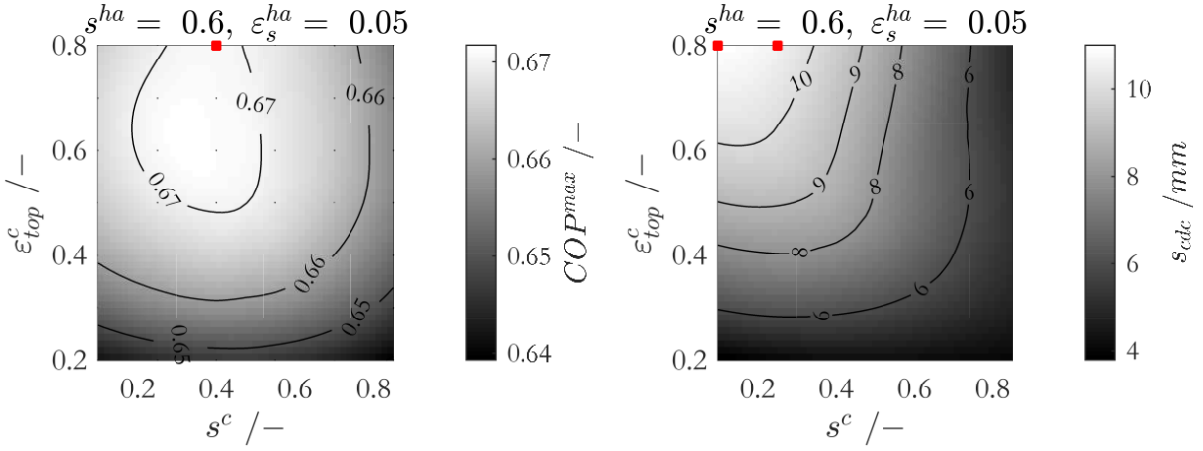

Figure 6-5: Left: Maximum achievable COP^{max} as a function of the transport channel parameters exemplarily for the heat-conducting ribs shown in Figure 6-4. The corresponding layer thicknesses are plotted on the right. The optimization was carried out for a prescribed SCP of $500\ Wkg^{-1}$.

In the parameter space under investigation, the maximal COP is a weak function of the optimal transport channel parameters and thus showing a flat plateau in the vicinity of the optimum. In this example, the maximum COP is 0.67 obtained with very wide transport channels ($\varepsilon_{top}^c = 0.8$) penetrating the structured composites more than half ($s^c = 0.4$). Conversely, if the channel width is small ($\varepsilon_{top}^c < 0.4$), it means that the composites contain a large amount of active adsorbent in the upper layers to adsorb methanol. The heat generated during adsorption (and desorption energy required for desorption) must be transported over the entire layer thickness of the composites, with the corresponding transport resistance. Thus, large thicknesses cannot be used for composites with insufficient channel width (ε_{top}^c), which can be seen in Figure 6-5 on the right. As the channel width increases (and the volume fraction of active adsorbent decreases), thicker and thicker composites can be used, which also leads to an improvement of efficiency.

6.1.3.2 Optimization of heat transfer ribs

Finally, the 3D-structuring of the heat-conducting ribs is optimized. Besides their height, the width plays a decisive role in the kinetics of the overall process. Figure 6-6 shows the results of the global optimization of COP and the layer thickness of the 3D-structured composites in the 6D parameter space, for a prescribed SCP of 500 W/kg. The plots are shown as a function of the rib's width at the bottom of the composites ($\varepsilon_{bottom}^{ha}$) and their normalized height (s^{ha}).

By optimizing the heat-conducting ribs, the optimum layer thicknesses can be increased, resulting in a further increase in the COPs. A maximum COP of approx. 0.676 can be achieved with a layer thickness of the structured composites of approx. 13 mm. The ribs should totally penetrate the composite ($s^{ha} = 1$) and should be very thin ($\varepsilon_{bottom}^{ha} = 0.05$) for the prescribed SCP of 500 W/kg. The thin ribs are sufficient because the thermal conductivity of the percolating aluminium alloy ribs is already very high ($\lambda^{ha} = 140\ Wm^{-1}K^{-1}$).

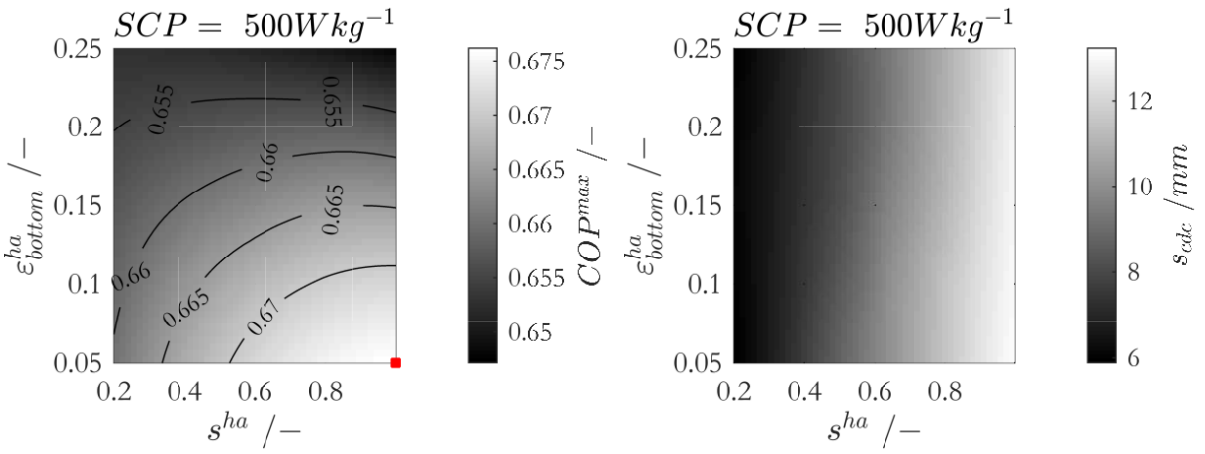

Figure 6-6: Global optimum of structural and process parameters for a prescribed specific cooling power of $SCP = 500\ W/kg$. At each point, layer thickness, cycle time, and mass transfer channels are optimized. Left: Maximum achievable COP as a function of the structural parameters of the heat-conducting ribs. Right: The corresponding layer thicknesses.

6.1.3.3 Global optimal curves

Finally, the prescribed SCP is varied over a wide range to consider different applications (high power density or high efficiency) and the previous analysis is repeated. To gain an understanding of the interplay between heat conduction and mass transfer, differently 3D-structured triangular materials, as shown in Figure 6-7, were investigated in the process simulations. The non-structured material (EXP_{CDC}) has already been introduced in section 5.2 and the results are reproduced here to show the great impact of 3D-structured adsorbents.

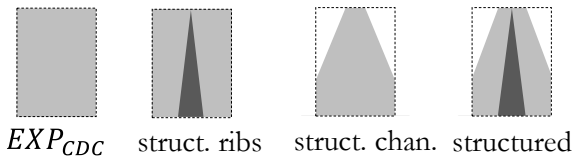

Figure 6-7: Schematical representation of the four varied structural designs. Starting from a composite

without structuring (EXP_{CDC}), solely introduction of heat conducting ribs as well as solely mass transfer channels were investigated. Finally, 3D-structured composites with improved mass and heat transport were investigated.

Figure 6-8 shows the optimal layer thicknesses as well as cycle times obtained by applying the optimization function from equation (6-7) in post-processing on the total data set. Initially, the transport kinetics is limited by the mass transport and as a result, thicker optimal layers can be realized by introducing macroscopic mass transfer channels. However, both, channels as well as ribs only result in slightly thicker layers. In the case of improved thermal conductivity, mass transport is limiting, which is why an increase in the size of the ribs does not contribute to a higher COP. In equivalence, larger mass transfer channels are not expedient if the thermal conductivity is limiting the overall kinetics. Therefore, a combined optimization is necessary which is reflected in a dramatically improved layer thickness of the 3D-structured composites. As already discussed previously, since cycle time is proportional to the prescribed SCP, the optimal values of the differently structured composites do not differ from each other.

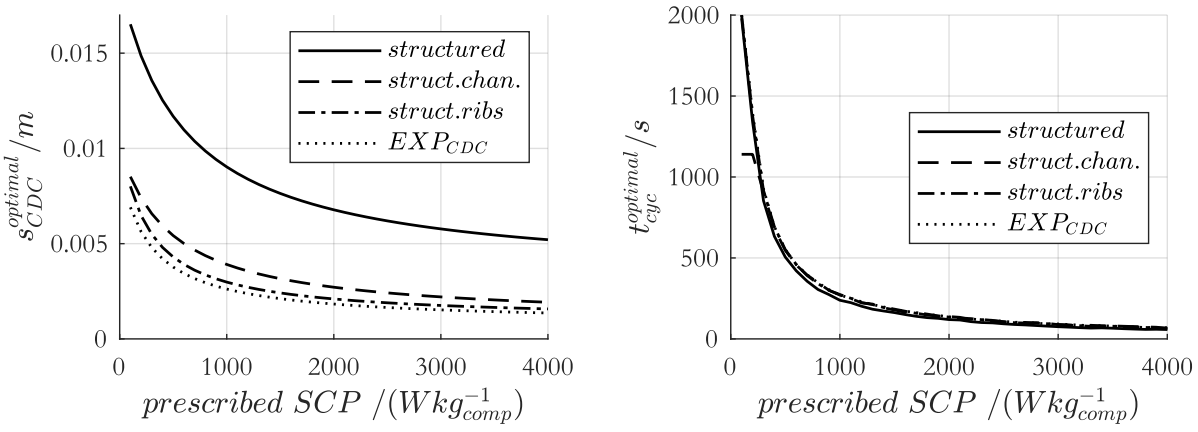

Figure 6-8: Optimal composite layer thickness and process cycle time as a function of the prescribed SCP for three differently 3D-structured composites and non-structured composites.

The preceding descriptions are directly reflected in the COP. The Ragone-plot in Figure 6-9 shows the maximum COP vs. prescribed power density for the four different composites. In addition, the different structuring is visualized for selected SCPs. The improvement of the achievable COP due to the 3D-structuring is remarkable. By reducing the transport resistances, the layer thickness can be increased to such an extent that an increase in the COP of up to 15% is possible in the high power density range (at SCP=4000 W/kg) if compared to the non-structured composites. With increasing SCP, the maximum COP decreases, although the decrease is much

smaller for the 3D-structured than for the non-structured CDC composites. Large SCPs are mainly achieved by reducing the layer thickness and by very short cycle times. This is accompanied by the increasing influence of passive mass due to the reduction in cycle time and layer thickness, which explains the reduction of efficiency.

Achieving high power densities requires the evaporation of as much refrigerant as possible in a short time. Heat-conducting ribs that totally penetrate the composites ($s^{ha} = 1$) are required to ensure that the released adsorption heat is well removed, with thicker ribs preferred for higher SCPs. Similarly, larger transport channels are required for higher power densities.

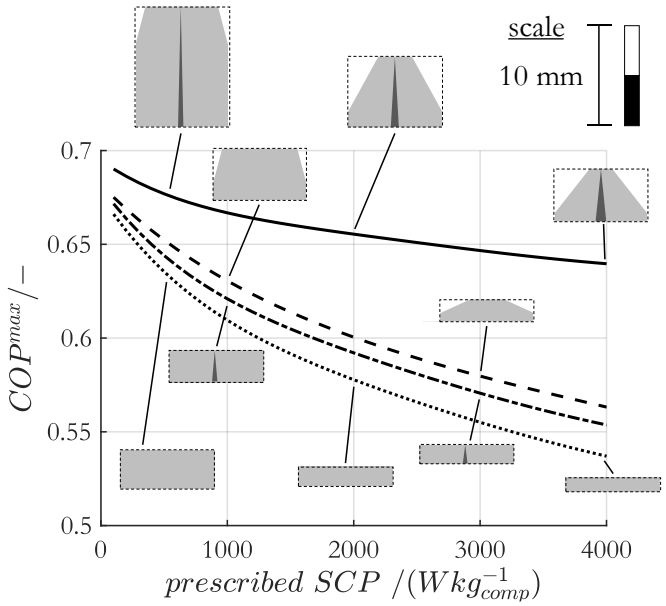

Figure 6-9:Maximum COP as a function of the prescribed SCP. The optimal structuring and layer thicknesses are shown for the different composites exemplarily for different SCPs.

In this section, a combined process and material development was introduced to optimize adsorption heat pumps, which includes the optimization of process parameters and a virtual material design of 3D-structured adsorbent composites. Exemplarily, the method was applied to the classical 2-bed adsorption refrigeration process but can be transferred to arbitrary process designs and process parameters. The cycle time and the thickness of the adsorbent composites were optimized as process-relevant variables. Transfer this methodology to further parameters is directly applicable. On the material side, the 3D-structuring of the adsorbent composites consisting of heat-conducting ribs, mass transport channels, and active adsorbents was aimed at, for which a geometric material model was introduced. With this method, a global optimum for the process can be identified under the given boundary conditions, which would not be possible

by neglecting either process or material parameters. Furthermore, the method reveals the significant potential of virtual material design for structurally optimized adsorbent composites.

6.2 3D-structuring - Experimental investigations

The methods, results, figures, and discussions presented in this chapter were partly published by the author of this thesis [143]. Some sections are taken verbatim from the publication and are reproduced here.

The results of the process simulations in the previous section motivated the experimental investigation of 3D-structured adsorbent composites. In this section, the idea of material design is experimentally applied using heat-conducting aluminium alloy ribs and macroscopical mass transfer channels for the application in adsorption chillers. Instead of carbide-derived carbon, the activated carbon adsorbent introduced in chapter 4 is used as the active material. Starting from a suspension based on activated carbon primary particles, water, and binder, the preparation procedure of consolidated composites with varying structures is briefly summarized below. The samples were prepared by the Etzold working group[6] and the preparation procedure is described in detail in [143].

6.2.1 Preparation of structured and unstructured consolidated adsorbent composites

The general procedure of producing the 3D-structured composites follows in equivalence to the descriptions outlined in the introduction of chapter 4. Following, the procedure is briefly summarized.

3D printed aluminium alloy (AlSi10Mg(Fe)) ribs

With the aid of the process simulations, promising rib structures were identified. The optimum heat-conducting ribs should fully penetrate the composites and be as thin as possible to avoid introducing too much passive mass. These findings were the basis for the experimentally fabricated aluminium ribs, for which technical and CAD drawings have been made as shown in Figure 6-10. In addition to the information from the process simulations, the constraints from the manufacturing process of the ribs and the final composites have been incorporated into the

[6] Technical University of Darmstadt, Department of Chemistry, Ernst-Berl-Institut für Technische und Makromolekulare Chemie, 64287 Darmstadt, Germany, www.etzoldlab.de

design. Besides, care has also been taken to ensure that the aluminium-structure has ribs at both ends to give stability to the composites. The triangular prism-shaped ribs have been 3D printed using selective laser melting (SLM) out of an aluminium alloy (AlSi10Mg(Fe)) on a support by "FKM Sintertechnik GmbH"[7]. The final 3D-printed rib structure is shown in Figure 6-10 on the right.

Figure 6-10: Technical drawing of ribs geometry on support with dimensions in mm (left); CAD view (middle); aluminium ribs 3D-printed using selective laser melting (SLM).

For the experimental investigation, the flat support of the aluminium ribs is directly applied to the heat exchanger with an adhesive thermal tape. In a later, technical application, the ribs could be directly printed on the Hex to reduce thermal resistance and amount of passive mass.

Preparation of structured consolidated adsorbent composites

The structured composites were prepared by the Etzold working group[6] and the detailed procedure for the preparation was published in [143]. Here, a summary is given.

To guarantee sufficient adherence of the activated carbon on the ribs surface, the activated carbon mass was prepared with 10wt% CMC-binder. The CMC-binder AC mass obtained was then pre-dried in the air at ambient temperature.

For the preparation of the composites with structured heat-conducting ribs, the CMC-binder AC mass was added into a press mold, then the 3D-printed aluminium ribs were pressed into the mass. After pre-compression of the closed press mold, it was compressed in a hot press with a pressure of 20 bar for 15 min at ambient temperature. Afterwards, the compressed composite was removed from the press mold and dried in air at ambient temperature until completely dry. Optionally five vertical channels laterally staggered to the ribs with the depth of 8 mm channels were added afterward using a 350 µm saw blade to obtain structured consolidated composites with mass transport channels and heat-conducting ribs.

[7] FKM Sintertechnik GmbH, Zum Musbach 6, 35216 Biedenkopf, https://www.fkm.net/?lang=en

With these methods the four different sample types were prepared: 'non-structured' (unstructured consolidated composites), 'channels' (structured consolidated composites with mass transport channels), 'ribs' (structured consolidated composites with heat-conducting ribs), and 'ribs + channels' (3D-structured consolidated composites with mass transport channels and heat-conducting ribs).

Figure 6-11 schematically shows the production routines of the four different non-structured and structured AC composites. After preparation, the different samples were investigated in a small-scale chiller setup. To ensure that sufficient active carbon mass is used, two identical samples were tested simultaneously in the laboratory setup.

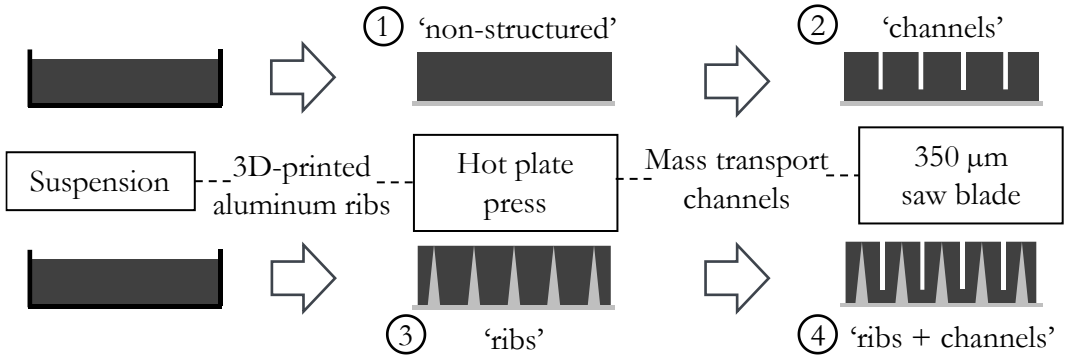

Figure 6-11: Production routine of consolidated composites ① ('non-structured'); composites with enhanced permeability ② ('channels'); with heat-conducting ribs ③ ('ribs'); with ribs and mass transfer channels ④ ('ribs + channels') [143].

The experimentally produced composites are shown in Figure 6-12. Partially the ribs are still visible. However, it can be stated that the composites were very stable and that the adsorbent layers adhered very well to the rib walls. After the drying step, the vertical mass transfer channels could be easily introduced into the composites.

The geometrical parameters and material parameters of the four different samples are listed in Table 6-1. Even though produced in the same hot press with the same press mold, the compound's cross-sectional area is not identical. Equivalently, the composites layer thickness slightly deviates. Within the limits of experimental inaccuracies, the geometries of the specimens are nevertheless comparable.

In the simulation studies so far, the power density has been related to the composite mass. Due to the aluminium base plate of the structured composites, the composite mass is not a useful reference value in this case. Instead, the cross-sectional area of the composites is used as a

reference, which is also of great technical relevance to minimize the total apparatus expenditure (less heat exchanger area).

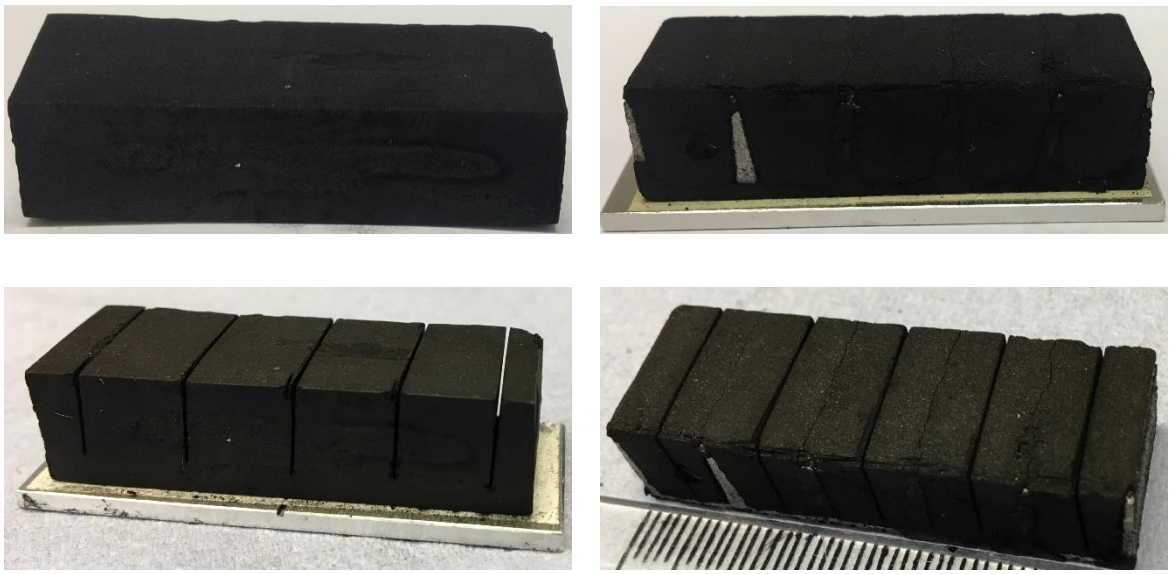

Figure 6-12: Activated-carbon and CMC-binder based adsorbent-composites. Non-structured composite (①, 'non-structured', top left), structured composite with mass transfer channels (②, 'channels', bottom left), structured composite with heat-conducting aluminium ribs (③, 'ribs', top right), and structured composite with heat-conducting ribs and mass transfer channels (④, 'ribs + channels') [143].

Table 6-1: Parameters of the four different, experimentally produced AC-composites. In each case, the sum (A_{comp}, V_{comp}, M_{AC+CMC} and M_{ribs}) or mean value (s_{comp}) of two identical samples are listed.

	①, 'non-structured'	②, 'channels'	③, 'ribs'	④, 'ribs + channels'
A_{comp}/cm^2	13.26	13.26	13.6	13.6
s_{comp}/mm	10.73	10.73	10.45	10.45
V_{comp}/cm^3	14.2	14.2	14.2	14.2
M_{AC+CMC}/g	7.16	6.93	6.1	5.86
M_{ribs}/g	-	-	6.75	6.75

6.2.2 Experimental setup – Laboratory-scale adsorption chiller

For the experimental investigation of gram-scale adsorbent composites in the adsorption refrigeration cycle, a novel setup has been developed and realized in a laboratory plant. This setup allows for cyclic experiments with gram scale adsorbent composites under varying pressure and temperature conditions as well as evaporation and condensation times, according to the refrigeration cycle introduced in section 1.1. The dynamic behaviour of the cyclic process can be investigated revealing information upon the influencing process parameters, e.g., cycle time and temperature boundaries. Furthermore, adsorbent composites with varying compositions and structuring can be investigated and compared in this laboratory plant. The lab-scale apparatus has been designed and built containing adsorber, evaporator, condenser, and two mass flow meters (MFM) as the main components allowing to measure the overall kinetic of the AdHex system. The high vacuum components are interconnected with small flange (ISO-KF) bellows hoses, pipes, and valves according to the flow chart in Figure 6-13. The vacuum-tight design of the plant prevents the entry of ambient air and enables cyclical operation of the process. The whole setup is placed in a temperature-controlled container to exclude temperature fluctuations and prevent condensation of refrigerant in the connecting pipes.

Dynamic, gravimetric measurements within vacuum components require great effort in terms of equipment and temperature control is difficult. In addition, gravimetric determination of adsorption rates of temperature-controlled, gram-scale adsorbents is subject to significant fluctuations due to circulating heat transfer fluid. Therefore, an indirect measurement principle of the adsorption rate has been chosen by detecting the volume flow of vaporous methanol between adsorber and condenser as well as evaporator and adsorber using MFMs. Mathematical integration of the exchanged mass flow with time yields the total mass evaporated or condensed in one cycle. Furthermore, the integral mass can be used to calculate the specific cooling power and cooling efficiency. The advantage of the small-scale experimental setup is a fast investigation of new adsorbents and structured adsorbent composites in gram-scale at arbitrary process conditions in a real cycle of the adsorption cooling process, thus revealing fast information of the performance of newly designed materials.

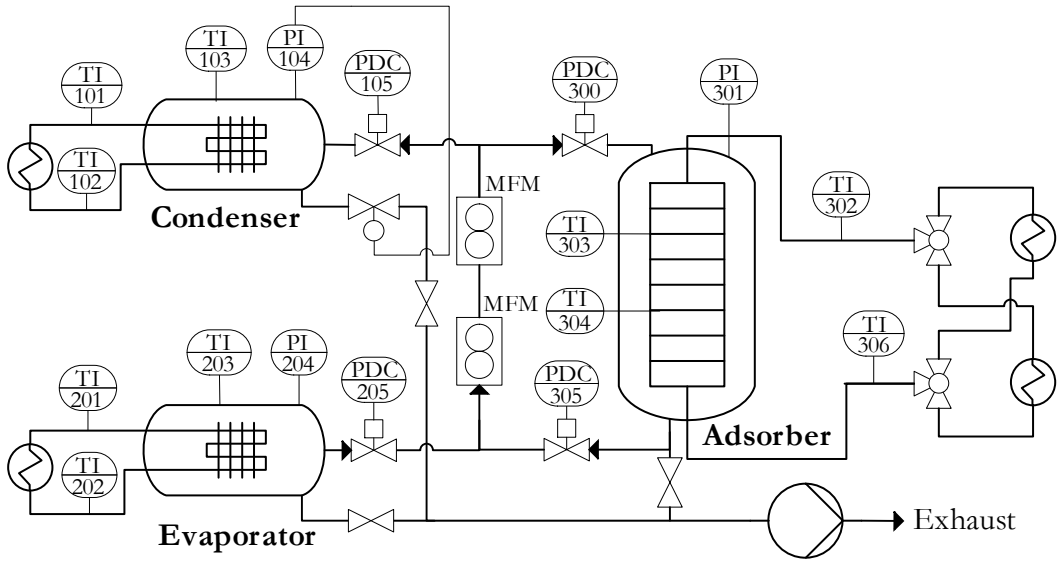

Figure 6-13: Process flow diagram of the gram-scale laboratory plant containing condenser, evaporator, adsorber with the adsorbent composites, and two MFM.

Adsorber

The adsorber is the main component of the laboratory plant realized as a DN100 cylinder with a small flange ISO-KF25 connection to the MFMs. The nozzles of the heat exchanger are led out on both sides of the cylinder through the ISO-K DN100 clamping flanges using vacuum feedthrough. The heat exchanger is designed as an aluminium hexagon with round pipe nozzles on both sides for sealing the vacuum feedthroughs using O-rings. The hexagonal design and aluminium material of the heat exchanger resulted from the specification of several criteria: flat surfaces to enable the best possible contacting of the adsorbent composites, good machinability, low specific heat capacity as well as high thermal conductivity, vacuum feedthrough easily possible, flexibility for quick installation and modification. Figure 6-14 shows the heat exchanger with two non-structured AC composites and aluminium supports attached using thermal adhesive tape.

Two identical VWR® Refrigerated Circulating Baths 13271-108 are used to temperature-control the AdHex. To ensure smooth and fast switching between adsorption and desorption, two electro-pneumatic 3-way ball valves are installed. In cyclic process operation, the 3-way valve connected to the output of the thermostats is switched a few seconds before the input valve, which corresponds exactly to the residence time of the heat transfer fluid in the hose system and the heat exchanger. This prevents the thermostats from cooling down or heating up too much due to the exchange of heat transfer fluid. Thus, only the temperature control of the passive

adsorber mass during the change between adsorption and desorption leads to the cooling or heating of the thermostats. Two thermocouples of type-T are installed to measure the temperature at the interface of adsorbent composites to the heat exchanger. Additionally, an MKS Baratron® Type 627F absolute pressure transducer is assembled to monitor and control the adsorber pressure. The adsorber is connected in two different ways with the MFMs via electro-pneumatic bellows valves. During the evaporation phase, the valve connected with the MFMs output is open and during the condensation phase, the valve connected to the MFMs input is open, so that the flow direction is the same.

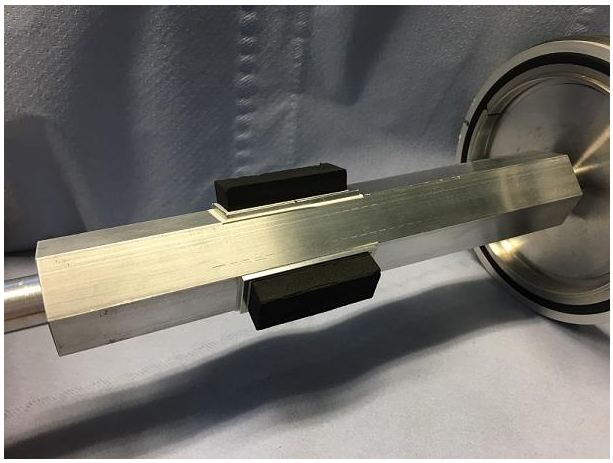

Figure 6-14: Hex of the laboratory setup to investigate adsorbent composites under dynamic process conditions of the adsorption refrigeration process. The heat exchanger is an aluminium hexagon with a heat transfer tube with an internal diameter of 10 mm. Additionally, the Hex ends were turned round in a lathe to obtain pipe nozzles with an outer diameter of 12 mm which serve as vacuum feedthrough. Two adsorbent composites (activated carbon) attached to aluminium supports are fixed on the Hex using thermal adhesive tape.

Sample preparation

The adsorbent composites are placed on 2 mm thick aluminium supports using thermal adhesive tape as shown in Figure 6-15. A 0.5 mm horizontal slit is machined into the aluminium support, into which a type-T thermocouple is inserted to measure the temperature between the adsorbent composite and the heat exchanger. The aluminium support and the second layer of thermal tape cause additional resistances for heat transfer. Nevertheless, aluminium supports were used to enable temperature measurement between the sample and the heat exchanger as well as easy exchange of samples in the adsorber. The sample shown in Figure 6-15 is a 3D-structured AC composite with aluminium ribs.

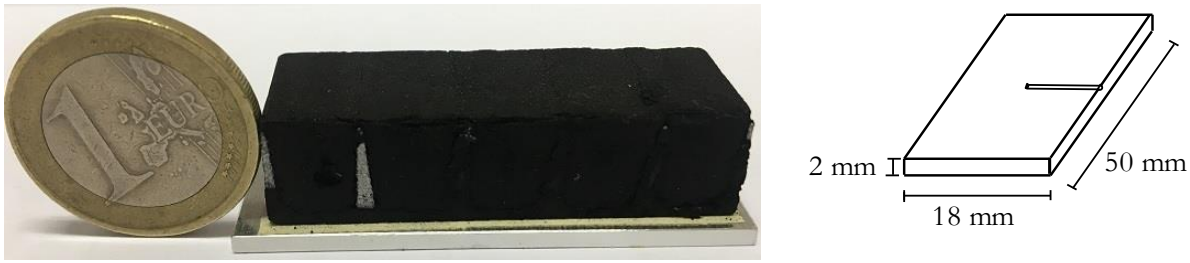

Figure 6-15: 3D-Structured AC composite with heat-conducting aluminium ribs attached using thermal adhesive tape on a 2 mm thick aluminium support with horizontal slit for the thermocouple (left). Dimensions of the aluminium support (right).

Mass flow meter

To determine transient adsorption and desorption rates during evaporation and condensation periods, two MFMs Bronkhorst® low-Δp-flow F101D are used for low-pressure drop applications. The interconnection of adsorber, evaporator, and condenser are designed in such a way that the MFMs are always flown through in the same direction. To enable accurate determination of the volumetric flow rates over a wide range, one MFM is calibrated with a range of $0 - 2000\ ml_N/min$ and the other with $0 - 200\ ml_N/min$ to reduce the dependence of the measurement inaccuracy on the set maximal value. In the order of magnitude of the examined volume flows, the measuring error is $\pm\ 0.5\%$ of the measured value plus $\pm\ 0.1\%$ of the set maximum value.

Evaporator

The evaporator is realized as a union tee of the small flange series ISO-KF40. One of the ports is used as inspection glass, the second one for the vacuum feedthrough of the heat exchanger, and the third for the connection to the MFMs. The heat exchanger is constructed as a spindle with an inner piping diameter of 4 mm. The temperature of the heat exchanger is controlled with a JULABO Corio CD-200f thermostat. Temperature measurements with type-K thermocouples are installed at the inlet and outlet of the heat exchanger. Additionally, a type-T thermocouple is installed in the evaporator detecting the liquid methanol temperature. For monitoring and controlling the pressure, a temperature-controlled MKS Baratron® Type 627F absolute pressure transducer is used. The evaporator is separated from the MFMs by an electro-pneumatic bellows valve controlled to the differential pressure between the evaporator and the adsorber. To remove carrier gas after initially filling with liquid methanol, the evaporator can be evacuated with a Pfeiffer vacuum HiCube 80 Eco pump via a manual bellows valve. All connections to the evaporator are carried out as ISO-KF16 piping units.

Condenser

The condenser is realized like the evaporator but with two union tee ISO-KF40 installed to use two different heat exchangers improving the condensation and assuring almost isobaric condensation pressure. The heat exchangers are temperature-controlled using a VWR® Refrigerated Circulating Bath AD15R-30. Like the evaporator, the condenser is separated from the MFMs by an electro-pneumatic bellows valve controlled to the differential pressure between adsorber and condenser. To prevent the component from an accumulation of carrier gas throughout experiments with several cycles, an electromagnetic proportional valve is installed connecting the condenser with the vacuum pump.

Process control unit

The process control is realized with control units and a programmable logic controller (PLC) from Gantner Instruments Test & Measurement GmbH. The whole cyclic adsorption refrigeration process can be performed in automated operation mode revealing information upon the cyclic behaviour from initialization to cyclic steady state. After cooling the adsorber, the cycle starts with the evaporation period as soon as the pressure in the adsorber is equal to the pressure in the evaporator. This period depends on the hold-up volume of the adsorber gas phase. The two valves connecting the adsorber and evaporator open, giving rise to a gas flow through the MFMs which is adsorbed from the adsorbent. After an individually adjusted duration of evaporation, the heat transfer fluid circuit in the adsorber heat exchanger is abruptly switched over inducing the heating period. The desorption process starts as soon as the pressure in the adsorber is equal to the pressure in the condenser. The two valves connecting the adsorber and condenser open which gives rise to a volume flow through the MFMs condensing in the condenser. In equivalence to the evaporation duration, the condensation time can individually be chosen on the user interface.

The measurements in the laboratory adsorption chiller provide information upon the evaporated and condensed volume flow rates, which can be used to calculate the heat flows in the evaporator and condenser. Since the laboratory plant is not optimized for the minimal hold-up in the adsorber free gas phase, when using gram scale adsorbent samples, significant amounts of adsorptive are adsorbed from the free gas phase or desorbed to the free gas phase during the cooling and heating period. The duration of the heating and cooling period depends on the adjusted evaporation and condensation time, the mass of adsorbent in the system as well as the kinetic of the respective sample. Thus, to compare adsorbent composites with different weight and kinetical behaviour, the integral adsorbed and desorbed methanol mass during the cooling and heating period is considered in addition to the mass flow exchanged with evaporator and

condenser for evaluation of process performance. In the application of an adsorption chiller, kg amounts of adsorbent would be applied, and the free gas phase hold up would be minimized, reducing the cooling and heating period to a negligible short duration compared to the total cycle time.

6.2.2.1 Measurement procedure and evaluation

The volumetric norm-flow rate $\dot{V}^N$ in ml^N/min measured with the MFMs is transferred to the mass flow rate assuming ideal gas behaviour

$$\dot{M}_{e,c} = \frac{p^N \dot{V}^N MW}{T^N R}. \tag{6-8}$$

Referring this to the cross-sectional area of the composites (A_{comp}), the mass flux $\dot{m}_{e,c} = \dot{M}_{e,c}/A_{comp}$ in kg/m^2 is calculated. The integral evaporated/ condensed mass per unit composite cross-sectional area (or occupied heat exchanger area) is calculated by integrating the mass flux during evaporation and condensation phases with time

$$m_e(t_e) = \int_0^{t_e} \dot{m}_e \, dt, \tag{6-9}$$

$$m_c(t_c) = \int_{t_e}^{t_c} \dot{m}_c \, dt. \tag{6-10}$$

The specific mass adsorbed (m_{cool})/ desorbed (m_{heat}) to/ from the free gas phase during the pre-cooling/ pre-heating period is calculated using the ideal gas law with the pressure difference $\Delta_{ec}p$ between condenser and evaporator

$$m_{cool,heat}(t_{cool,heat}) = \frac{\Delta_{ec} p V^{gas} MW_{MeOH}}{R T^{gas} A_{comp}}. \tag{6-11}$$

For evaluation of the process performance, the hold-up of the gas phase is additionally considered for the calculation of the integral adsorbed and desorbed mass during one cycle. The total specific mass adsorbed during one cycle is obtained as follows

$$m_{ads}(t_{cyc}) = m_e + m_{cool}, \tag{6-12}$$

and the total specific mass desorbed in one cycle is given by

$$m_{des}(t_{cyc}) = m_c + m_{heat}. \tag{6-13}$$

With the evaporation enthalpy $\Delta_{evap}h$, the specific cooling power per unit A_{comp} is given by

$$SCP_A = \frac{m_{ads}(t_{cyc})\Delta_{evap}h}{t_{cyc}}, \tag{6-14}$$

with the cycle time t_{cyc}. In equivalence, the cooling power can be related to the CDC composite mass M_{comp} giving the mass-specific SCP

$$SCP == SCP_M = \frac{M_{ads}(t_{cyc})\Delta_{evap}h}{M_{comp}t_{cyc}}, \tag{6-15}$$

with the total mass adsorbed $M_{ads} = m_{ads}A_{comp}$ during one cycle. The cycle cooling energy per unit A_{comp} or composite mass is given by

$$q_A = m_{ads}(t_{cyc})\Delta_{evap}h = t_{cyc}SCP_A, \tag{6-16}$$

$$q_M = \frac{M_{ads}(t_{cyc})\Delta_{evap}h}{M_{comp}} = t_{cyc}SCP_M. \tag{6-17}$$

Specific cooling power and cooling energy are linearly correlated via cycle time. While SCP shows a maximum at short cycle times, q is optimal when the adsorbent is in equilibrium at very long cycle times. To evaluate the Pareto-optimal behaviour in a combined performance indicator, the product of SCP_A and q_A can be used with units kJ/m^4s, as performed by Ammann et al. [141]. In equivalence, the mass-specific criteria can be used to yield a performance indicator with units $kJ/kg_{comp}^2 s$.

The four samples were investigated in the gram-scale adsorption chiller applying the outlined evaluation procedure. Therefore, dynamic measurements were conducted with the four structured and non-structured samples, and the results obtained in cyclic steady-state were used for the evaluation. In a first step, a constant temperature level was adjusted ($T_e = 15°C$, $T_{ads,c} = 20°C$ and $T_{des} = 90°C$) and the four samples were investigated in experiments with various cycle times and were compared. In a second step, the sample with enhanced permeability and thermal conductivity (④, 'ribs + channels') was investigated at different temperature levels.

6.2.3 Results and discussion

The performance of the four non-structured and structured AC composites is discussed in the following by comparing the results obtained in cyclic steady-state. Details of the dynamic

behaviour from initialization to CSS are outlined in Appendix C.1.2 which is exemplarily discussed for experiments conducted with non-structured CDC composites.

6.2.3.1 Structured vs- non-structured activated carbon composites

Subsequently, results are discussed obtained for experiments conducted with moderate temperature levels of $T_e = 15°C$, $T_{ads,c} = 20°C$ and $T_{des} = 90°C$. Figure 6-16 shows specific cooling power and specific cooling energy vs. cycle time as well as the mass fluxes obtained in CSS exemplarily for evaporation and condensation times of 500 s.

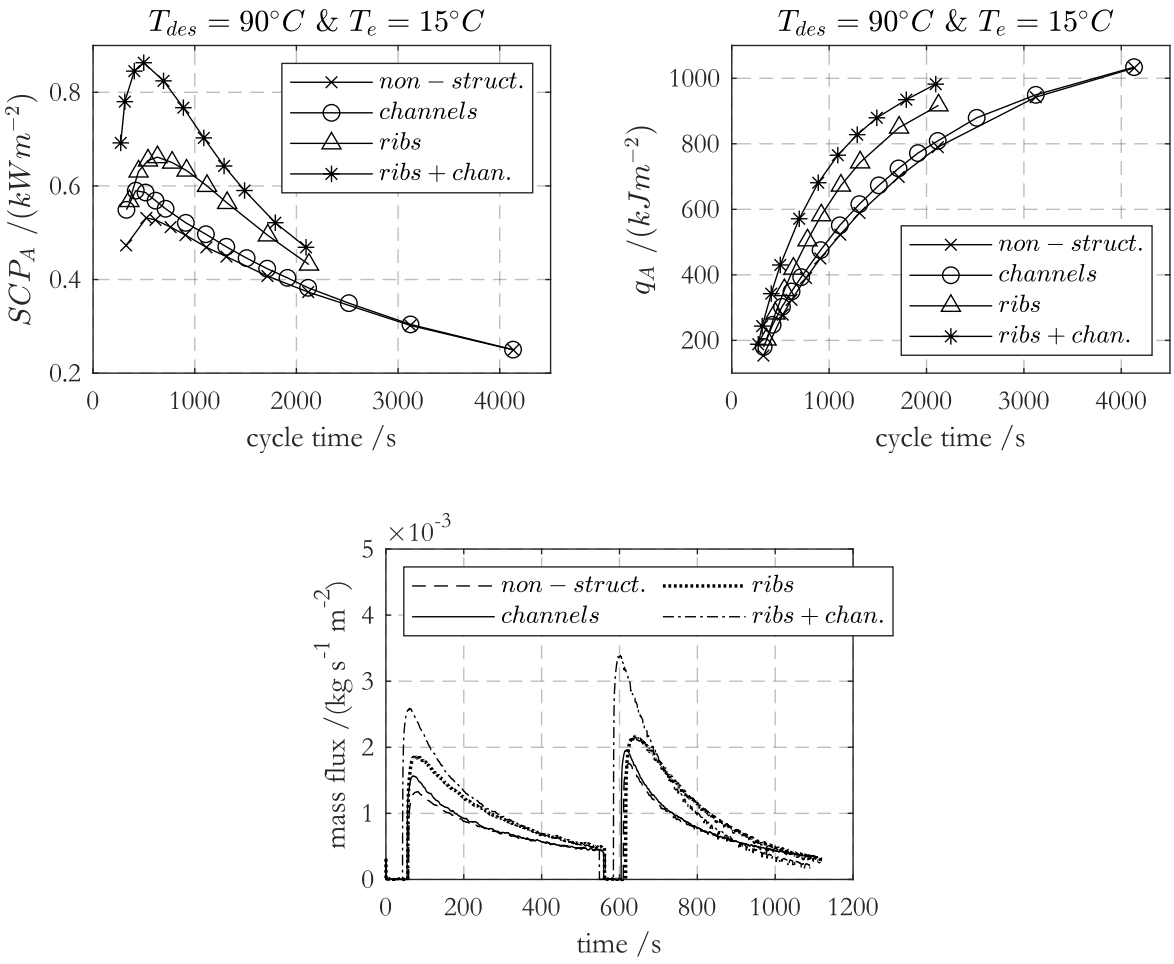

Figure 6-16: Power density and energy density vs. cycle time ($t_{ads} + t_{des}$) for non-structured and structured adsorbent composites for experiments with $T_e = 15°C$, $T_c = T_{ads} = 20°C$, $T_{des} = 90°C$. Additionally, mass fluxes in CSS for $t_e = t_c = 500\ s$ are shown for the non-structured and structured activated carbon composites.

SCP_A is maximal at short cycle times of $t_{cyc} = 300 - 500\ s$, with no clear tendency concerning different structuring. Initially, the non-structured composite exhibits a heat transport limitation,

thus structuring with heat conducting ribs is much more effective in improving SCP_A than introducing mass transport channels. However, by structuring the composite with heat-conducting ribs, the main limitation shifts towards mass transport. Therefore, adding mass transfer channels to the composite with aluminium alloy ribs, a high-performing, 3D-structured composite is produced showing a further significant improvement in SCP_A. The significant increase in specific power is due to the increased transport kinetic. As a result of that, more adsorptive can be adsorbed and adsorbate desorbed with time which is represented in the increased integral mass flux. Contrary to SCP_A, the energy density is monotonously increasing with increasing cycle time. At long cycle times, in equilibrium, q_A reaches the limiting value which is not determined in these experiments. In the same manner as for SCP_A, q_A is increased by the 3D-structuring of the composites and thus a significantly better utilization of the heat exchanger surface area. With the high-performing, 3D-structured composites, a maximal specific cooling power of 900 Watt per square meter of composites could be achieved. Even though the 3D-structuring of the composites with ribs and mass transfer channels has not yet been optimized a significant improvement compared to the unstructured composite could be achieved.

A direct comparison with the results obtained with the thin CDC composites in Appendix C.1.2.2 is not feasible due to the different adsorbent materials used and following the different material parameters. However, by comparing the results, one point can be highlighted. Due to the short transport paths in thin composites, the transport kinetic is much faster compared to thicker composites. Therefore, even without structuring, the CDC composites show a significantly higher power density. However, due to the detrimental ratio of active to passive mass, the specific efficiency is lower than for the thicker, structured activated carbon composites. For a quantitative comparison of different samples, an evaluation criterion combining efficiency and power density is beneficial.

To compare the four different AC composites, the performance is evaluated according to the method outlined in section 6.2.2.1. The overall enhancement in performance due to the application of 3D-structuring can be visualized in a double logarithmic Ragone-plot in which SCP_A is plotted versus q_A. In adsorption technology, such a visualization has been used by Ammann et al. [141]. Figure 6-17 shows a Ragone plot for the four AC samples investigated. Due to the 3D-structuring, the performance ($SCP_A \cdot q_A$) of the composites could be increased from 295 to 538 $kJ^2/m^4/s$ being an improvement of approx. 82% compared to the unstructured composites. Due to the increased kinetic, the optimal cycle time was reduced from 2115 s to 1090 s.

In the Ragone plot, the initial heat transfer limitation can be qualified. Starting from the non-structured composites, only minor improvement was achieved by introducing the mass transfer channels which is reflected in a slightly improved performance from 295 to 311 $kJ^2/m^4/s$ with a slightly shorter optimal cycle time. Introducing the mass transfer channels on one hand side leads to a minor reduction of the amount of active material, but on the other hand side, the surface area for methanol vapor entering the composites has been increased improving the all-over kinetic. Comparing the results of non-structured composite ① to composite no. ③ ('ribs'), the initial heat transfer limitation becomes obvious. By using the triangular prism-shaped ribs, performance could be improved up to 420 $kJ^2/m^4/s$, although a significant amount of passive mass was added to the composites by the ribs. The rib thickness could well have been thinner, as the initial heat transport limitation was overcompensated, which became evident by the additional insertion of mass transport channels to composite no. ③.

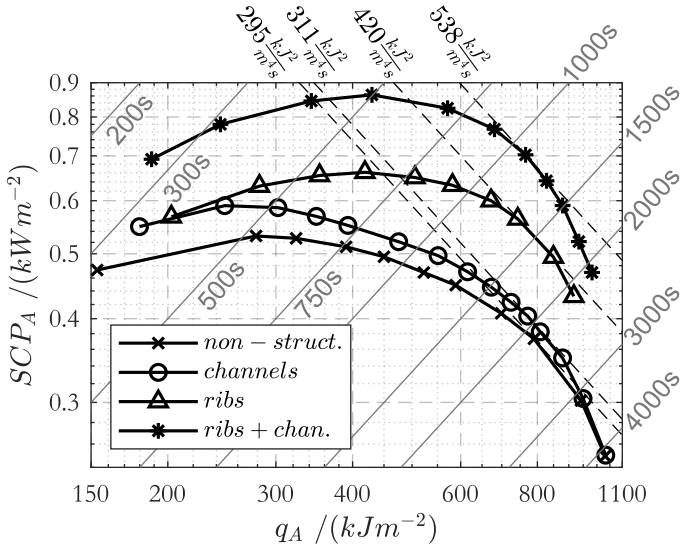

Figure 6-17: Ragone-plot showing specific cooling power vs. energy density related to the composite cross-sectional area for the four samples investigated. The experiments were conducted with temperature levels of $T_e = 15°C$, $T_c = T_{ads} = 20°C$, $T_{des} = 90°C$. The identically adjusted evaporation and condensation times were varied between $t_{e/c} = 100 - 2000\,s$; pre-heating and pre-cooling durations have adjusted variably.

Due to the high adsorption rate in short cycles, the specific cooling power is maximal at short cycle times. However, in short cycles, only a small fraction of the adsorption capacity of the adsorbents is utilized resulting in small efficiencies. This Pareto-optimality between power density and efficiency is common for many energies conversion processes. Depending on the application

and the desired mode of operation, the process can therefore be operated in a power- or efficiency-oriented manner. However, the preceding discussion shows, that regardless of the final operating point, a significant improvement can be realized by using structured composites.

6.2.3.2 High-performer – Influence of temperature boundary conditions

Adsorption heat transformers are used to transfer heat from a low-temperature level to a higher temperature level. Depending on the application, either the lowest temperature level (chiller) or the medium temperature level (heating purpose) is the benefit of the process. In both applications, the temperature levels at which the process is operated are significantly influencing the performance. The lower the temperature differences between evaporator and condenser as well as the higher the temperature differences between adsorption and desorption, the better the performance. However, the temperature levels of the process are determined by the specific conditions of the installation site and the user requirements. Therefore, further experiments have been conducted with the high-performing, 3D-structured adsorbent-composite ④ for varying temperature levels to investigate the influence of the temperature levels on the performance. Figure 6-18 shows experimental results for five temperature levels in a Ragone plot. While the location of the maximal performance is always determined at a cycle time slightly above $t_{cyc} = 1000\ s$, the value of the maximal performance strongly depends on the three temperature levels.

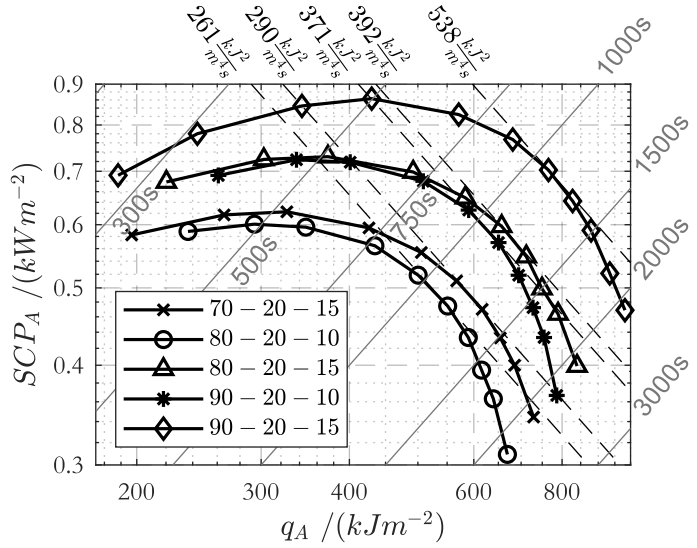

Figure 6-18: Ragone-plot showing power density versus efficiency for the 3D-structured adsorbent-composite (④, 'ribs + channels') for varying temperature levels. The legend shows the temperatures in degree centigrade of desorption - adsorption/ condensation - evaporation.

While higher evaporation and desorption temperatures are beneficial for the process performance, lower re-cooling temperatures are preferable. Even though the pressure difference and thus temperature difference between evaporator and condenser is important, the desorption temperature is crucial for process kinetic and has the strongest influence on the process performance.

6.3 Summary

Low heat and mass transfer properties of technical adsorbents are the main obstacles to the low system performance of adsorption chillers. To gain competitiveness these drawbacks need to be overcome.

Digital material design and 3D-structuring is a very promising tool to develop tailor-made structures which accompany the beneficial attributes of high thermal conductivity as well as mass transfer properties without significantly sacrificing adsorption capacity. In this chapter, digital material design has been used to identify a promising geometrical structure of adsorbent composites. The triangular prism-shaped aluminium ribs have been selected to enhance thermal conductivity and inverted triangular mass transfer channels to increase the mass transfer properties. An effective material model was developed to correlate the spatially variable structuring to effective transport and material parameters. The material model was parameterized with experimentally obtained adsorbent parameters of a non-structured composite and subsequently used in transient, spatially resolved process simulations of a 2-bed adsorption chiller. By varying the five material-related parameters (dimensions of ribs and channels, the layer thickness of composites) and further process-related parameters (cycle time) a combined material and process optimization has been conducted. In post-processing, the optimal set of parameters has been identified applying a cost-function by searching for the maximal efficiency for a prescribed power density. The evaluation of different structure-property combinations was performed using an objective function considering the Pareto-optimal behaviour of SCP and COP. In the whole range under consideration, by 3D-structuring, the process efficiency could be drastically improved compared to non-structured composites. 3D-structuring shows its strengths especially in the range of high power densities, whereby an increase in efficiency of up to 15 % could be achieved. This can be attributed to the fact, that by reducing heat and mass transfer resistance, the optimal layer thickness could be more than doubled without sacrificing process dynamic. By that, the ratio of active to passive mass is improved beneficially, that the influence of the inertia decreases.

The digital material design was the basis for the manufacturing of structured adsorbent composites containing 3D printed triangular prism-shaped aluminium ribs and macroscopical mass transfer channels laterally staggered to the ribs. Four different composites were manufactured to compare the influence of the ribs and the channels. The samples have been investigated in a small-scale adsorption chiller under realistic, cyclic process conditions and evaluated using the cross-sectional specific power and efficiency. It has been shown that the limitation concerning mass and heat transfer should be detected and the initial structuring should be dedicated to lowering the initial limitation. With the experiments, the simulation results could be enforced. Compared to non-structured composites, the process performance (efficiency density multiplied with power density) could be improved up to 87% by 3D-structuring of activated carbon composites.

7. Heat integrated Multiple-bed process setup

The methods, results, figures, and discussions presented in this chapter were partly published by the author of this thesis [144]. Some sections and figures are taken verbatim from the publication and are reproduced here.

Besides improving heat and mass transfer of adsorbents by 3D-structuring, the process performance of adsorption chillers can be improved with sophisticated heat recovery. Internal heat regeneration can be utilized by thermal waves [145] or by multi-bed designs [44]. Both concepts aim to reduce the supply of external heat by internal heat regeneration.

Wang W. et al. and Qu et al. examined the potential of mass and heat recovery and showed that heat recovery significantly increases the coefficient of performance, especially when latent heat is partially recovered [41], [146]. Schwamberger et al. [118], [119], and Schwamberger [120] provided a fundamental, thermodynamic model to evaluate the heat recovery potential of thermally driven heat pumps. It was shown that besides the sensible heat of passive masses, recovering the latent heat of adsorption significantly enhances the process efficiency. Advanced cycles such as the thermal wave cycle [147], adsorber with stratified heat storage [119], the dual-mode cycle, and the multistage cycle with up to six beds show promising results, improving process performance utilizing internal heat regeneration. Another advantage of multi-bed process designs is the reduction of peak temperatures in the evaporator and condenser. Meunier numerically investigated the entropy production of a solid adsorption heat pump in cyclic steady state as function of the number of adsorbers [43] and a thermodynamic analysis of the heat and entropy flows in and out of the heat pump was carried out, revealing a rising efficiency with an increasing number of adsorbers, due to improved heat recovery and reduction of entropy generation. An analysis of the thermal wave regeneration adsorption cycle, using entropic mean temperatures, was provided by Pons revealing similar conclusions [145], [148]. A reduction of driving temperature differences in the heat transfer reduces irreversibility and, thus, improves the process efficiency of adsorption heat pumps. Hence, thermal wave or multi-bed processes are thermodynamically interesting due to a reduction of heat losses [43], [147].

Critoph, proposed a multi-bed approach consisting of 32 closed (integrated) adsorber modules with the advantage of thermal and material separation, which prevents redistribution of adsorbate in the adsorbent bed [44]. Each module consists of a sorption zone and an evaporation/ condensation zone with cyclic varying temperature and pressure environments. Compared to a

classical 2-bed setup with heat recovery, the multi-bed approach is advantageous due to lower temperature differences between the heat sources and heat sinks. The cold heat transfer fluid entering the adsorption zone is partly heated up by exothermic adsorption and partly by absorbing the sensible heat from the modules. The more modules are utilized in a multiple-bed setup, the more efficient the heat regeneration. In the limiting case, the multi-bed setup converges to the approximation of a continuously moving bed which is discussed in detail in the subsequent section.

Moving bed processes are commonly used in chemical, pharmaceutical, and bioprocess industries for recovery, separation, or purification purposes. In the practical application of moving beds, particle attrition due to the transport of the solid phase is disadvantageous. To overcome this shortcoming, the bed movement can be emulated with a Simulated-Moving-Bed (SMB). An SMB consists of a fixed bed or a rotating annular bed of catalyst or adsorbent with many ports for injection of carrier gas, reactant, and withdrawal of the product. The solid bed is stationary, whereas inlet and outlet ports are periodically shifted in the direction of the fluid flow, simulating a true counter current system [149]. As the number of inlet and outlet ports increases, the SMB approach converges to a continuous True-Moving-Bed (TMB), where the reactant and carrier are continuously fed into a downward or rotating moving bed containing the solid phase [150]. In the TMB, all flows are continuous, thus converting the system from an unsteady to a steady-state behaviour. This results in huge advantages concerning simulation effort [151]. Günther et al. applied the TMB approach with a lumped-parameter model of the adsorbent to adsorption cooling machines [152]. Following, this approach is adapted to the distributed parameter model introduced in section 3.2.3. This approach allows efficient simulations of adsorption refrigeration multi-bed processes and evaluation of the heat recovery potential of sensible and latent heat, considering heat and mass transfer in the adsorbent structure. The steady-state character of the TMB approach offers the possibility to vary process parameters with comparatively low simulation effort applying parameter continuation [151]. Besides, the multi-bed design enables efficient heat recovery between modules with a minor driving temperature difference, and thus highly heat integrated process setups are developed and optimized utilizing the maximal amount of latent and sensible heat to be recovered.

The material model for the simulations in this chapter was parameterized with the effective material model introduced in section 2.4.1 and the material parameters of CDC consolidated composites with 2 wt% of CMC binder as summarized in Table B-6 (EXP_{CDC}). However, the methodology of a heat integrated multi-bed process approximated with a TMB can be transferred to other material models.

This chapter is outlined as follows: In section 7.1, the multi-bed process setup and the mathematical models of SMB and TMB are introduced. Followed by that, in section 7.2 simulations of the TMB approximation are compared with the SMB approach and the limiting cases are discussed. In section 7.3, simulation results and first optimizations of the TMB process setup are presented. Finally, in section 7.4 a highly heat integrated process setup is introduced.

7.1 Periodically and continuously operated multi-bed adsorption heat pumps – process setup and modelling approach

The thermodynamic potential for heat recovery in solid sorption heat pumps can be quantified using the thermodynamic model outlined in section 3.2.2 which is based on a lumped-parameter model. Based on the methodology provided by Schwamberger et al. [118], [153], [154], a thermodynamic analysis of the maximum efficiency that can be achieved with an adsorption chiller was performed for the adsorbent – heat exchanger (AdHex) system and temperature conditions investigated in this thesis. The result of the thermodynamic analysis is outlined in detail in Appendix D.4. It reveals a high grade of heat recovery potential partly contributed by sensible heat and partly by latent heat. If the heat recovery potential can be utilized to a large extent, the efficiency of adsorption heat pumps can be improved significantly. A challenging task is to develop process setups to exploit the potential of heat recovery.

In this work, the approach for maximizing process efficiency is to minimize the heat required from the external heat supply by maximizing the internal regeneration of sensible and latent heat and thus maximizing the coefficient of regeneration r

$$r = \frac{q_{hrp}}{q_{des}}, \tag{7-1}$$

where q_{hrp} is the heat density recovered during heat recovery [155]. The higher r, the more heat is recovered.

To achieve this, a multi-bed approach is used with the total amount of adsorbent evenly distributed among individual adsorber modules, which in turn are evenly distributed over time in the adsorption cycle. By discretely switching the heat transfer fluid circuits at a frequency of t_{cyc}/j_{max}, where j_{max} is the total number of adsorber modules, each adsorber runs through the entire cycle once within the cycle time t_{cyc} and in countercurrent to the heat transfer fluid (hf). This simulates a discrete movement of the stationary adsorbers. In the remainder, these setups will be referred to as SMB, following the nomenclature of chromatography [149]. First, such a

counterflow SMB setup is discussed without additional internal heat regeneration, similar to the setup proposed by Critoph [156]. For simplicity, a setup with four adsorber modules (a_1 - a_4) is shown in Figure 7-1, where adsorbers a_1 and a_2 are initially connected to the evaporator and located at positions 1 and 2.

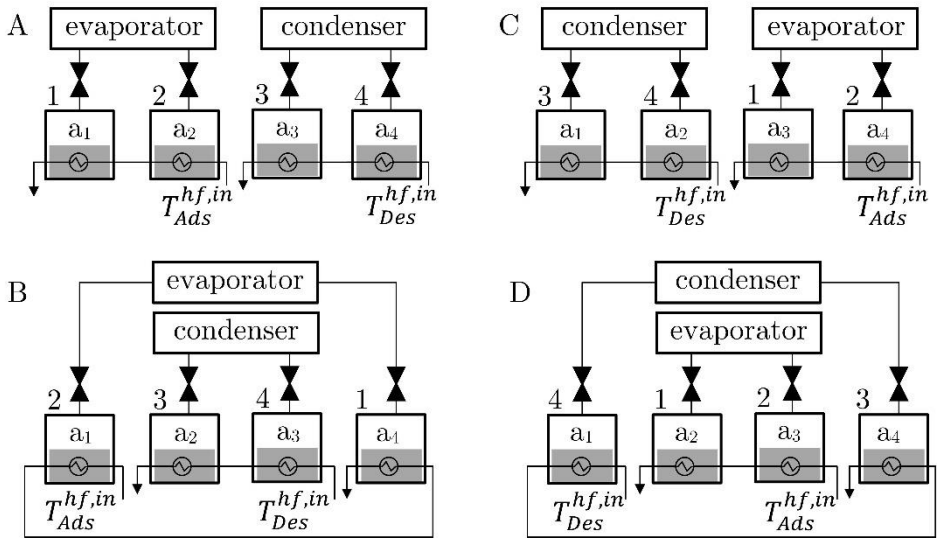

Figure 7-1: SMB design with four separate adsorber modules a_1 - a_4, with two in the adsorption zone and two in the desorption zone. By switching the heat transfer fluid circuit with a frequency of $t_{cyc}/4$ in counterflow to the adsorbers, each module is located once at every position 1-4 within the cycle time t_{cyc}, which simulates a movement of each adsorber through the whole cycle.

Furthermore, adsorbers a_3 and a_4 are initially heated and regenerated and thus connected to the condenser and located at positions 3 and 4. With a frequency of $t_{cyc}/4$ the heat transfer fluid circuits are switched creating new connections until the initial setup is restored after t_{cyc}. With this setup, a considerable amount of the heat recovery potential remains unused. Therefore, a new type of configuration is proposed, which in principle can be divided into two sections: One section, in which adsorbers are temperature-controlled by the external heat transfer fluid circuits in equivalence to the setup shown in Figure 7-1 and a second section, in which the temperature of adsorbers is equilibrated by thermal coupling due to a circular flow of the heat transfer fluid. Within this second section, the internal heat regeneration takes place by transferring sensible and latent heat whereby some adsorbers are heated up and the same number is cooled down. It is assumed that the internal heat transfer between two adsorbers is ideal without heat transfer resistance, e.g., by using a fast-flowing heat transfer fluid. The transfer resistance in the adsorbent, however, is modelled. By thermally coupling two adsorbers at a time with the

minimum possible temperature difference and switching the positions with a frequency of t_{cyc}/j_{max}, this creates a countercurrent heat transfer. The smaller the temperature difference between each of the two thermally coupled adsorbers, the lower is the irreversibility and thus the higher the quality of the heat regeneration. To guarantee heat transfer with a minor temperature difference, a high total number of adsorbers j_{max} is necessary. For simplicity, only six adsorbers $a_1 - a_6$ are shown in Figure 7-2 with the 6 sequential process setups A-F.

Furthermore, the adsorbers are arranged evenly in time throughout the whole cycle at positions 1-6. Here, two of the adsorbers are temperature-controlled with an external heat transfer circuit and the remaining are heated or cooled by internal heat regeneration. In addition to the process setups, the respective position of each adsorber in the thermodynamic cycle is shown in Clausius-Clapeyron diagrams with the heat fluxes belonging to the respective positions. In the initial setup A, adsorber a_1 at position 1 is cooled by dissipating the heat flux $\dot{q}_{1,5}$, which is used to heat adsorber a_5 at position 5. Equivalently in setup B, adsorber a_6 at position 1 is cooled by dissipating the heat flux $\dot{q}_{1,5}$ to heat adsorber a_4 located at position 5, and so on.

The normalized number of adsorbers contributing to the internal heat regeneration is given by

$$y_{hr} = \frac{j_{hr}}{j_{max}}. \tag{7-2}$$

For the setups in Figure 7-2, y_{hr} is $2/3$. As the number of adsorbers increases, the interconnection of the heat transfer fluids and the interconnections between adsorbers and evaporator or condenser become visibly more complex. However, since the goal of the multi-bed design is dedicated to optimizing the efficiency of adsorption chillers by maximizing the value of r (see equation (7-1)), a high number of adsorber modules is required. With a higher number of adsorbers, heat regeneration becomes more efficient due to lower temperature differences between heat source and sink. Depending on the number of adsorbers and their level of detail, the problem to be solved is a large system of partial differential equations. This set of equations must be solved dynamically to calculate a cyclic steady state, requiring a high simulation effort [157]. By increasing the total number of adsorbers in the SMB, the discrete-time intervals of switching t_{cyc}/j_{max} decrease, and thus the discrete movement of the adsorbers approaches a quasi-continuous counterflow movement.

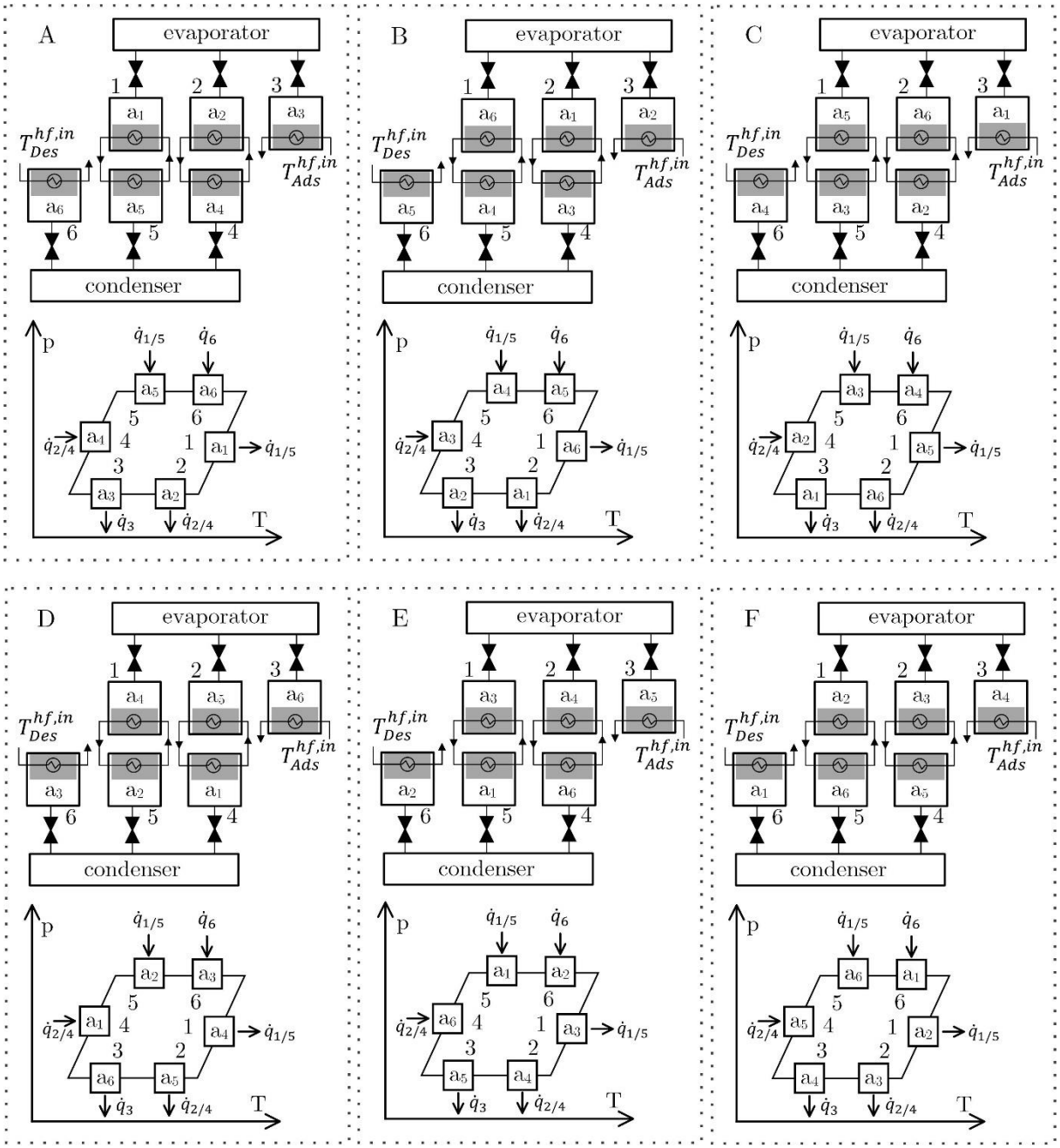

Figure 7-2: Novel process setup of an adsorption chiller with internal heat regeneration. Here, 6 adsorbers are evenly distributed within the cycle, whereby two adsorbers are temperature-controlled with external heat transfer fluid circuits and four adsorbers are thermally coupled for internal heat regeneration. By switching the heat transfer fluid connections with a frequency of $t_{cyc}/6$, each adsorber passes through the whole cycle in a duration of t_{cyc}.

In the limit case of infinite adsorbers, the discrete motion converges to a continuous motion and thus, the transient SMB can be treated as a steady-state TMB as shown in Figure 7-3. Hence, a TMB in adsorption refrigeration applications leads to a continuously varying temperature and

pressure environment for the adsorbent. Although the TMB is considered a continuous bed in the process simulations, no direct material or energy exchange is allowed between the beds of adjacent cells to maintain the analogy to the SMB with the separated adsorber modules, as shown by the dashed lines in Figure 7-3 on the right. However, the energy exchange takes place via the heat transfer fluid circuits.

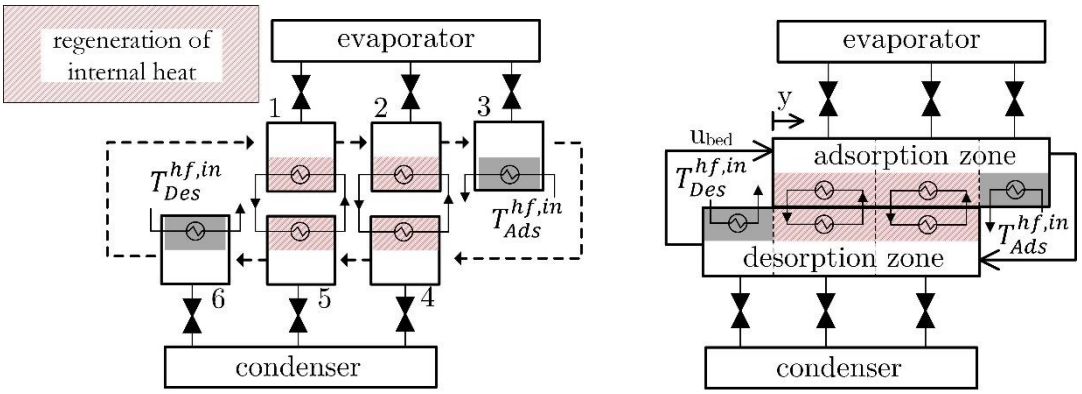

Figure 7-3: Simulated-Moving-Bed with the discrete movement of six adsorbers (left) and True-Moving-Bed with continuously moving adsorption and desorption zone in y-coordinate direction with velocity u^{bed} (right). The sections where the upper (adsorption) zone and the lower (desorption) zone are thermally contacted represent the zones where internal heat regeneration takes place.

One advantage of the multi-bed setup is that in addition to sensible heat, it also enables regeneration of high amounts of latent heat significantly increasing the coefficient of regeneration. While sensible heat of the passive masses is recovered within the whole heat regeneration zone, latent heat is only recovered in sections, where adsorption/ desorption takes place. This is the case when the pressure difference between the evaporator and the respective cells of the adsorption zone is positive and thus, the check valves switch from closed to open. Equivalently, if the pressure difference between the respective cells of the desorption zone and condenser is positive, the check valve switches from close to open.

In the remainder, the simulation results are presented along the spatial coordinate y of the moving bed with a length L^{bed} which is always bisected into desorption and adsorption zone as shown in Figure 7-4. The adsorption zone is located from 0 to $L^{bed}/2$ with the adsorption heat recovery zone from 0 to $L^{hr}/2$. The desorption zone begins at position $L^{bed}/2$ and reaches until the end of the bed at L^{bed} with the desorption heat recovery zone as indicated. In addition, a

schematic temperature profile of the moving bed is shown. In the schematic temperature profile, the advantage of internal heat regeneration is visible. By heating the beginning of the desorption zone ($L^{bed}/2$ to $(L^{bed}+L^{hr})/2$) with sensible and latent heat provided from the adsorption zone, the amount of heat to be supplied from the external heat source is reduced, which significantly increases the process efficiency. As indicated, the temperature of the desorption heat recovery zone is increased by ΔT_{des}^{hr} and the temperature in the adsorption heat recovery zone decreased by ΔT_{ads}^{hr} due to the internal heat regeneration. Due to the higher loading and thus the larger heat capacity at the beginning of the desorption zone, ΔT_{des}^{hr} is smaller than ΔT_{ads}^{hr}.

The decisive parameter for the optimization of the multi-bed design is the normalized length of the heat recovery zone. Since the adsorbent is evenly distributed in the moving bed, the normalized length of the heat recovery zone is given in equivalence to the SMB. It is calculated as the ratio of the length of the heat recovery zone to the total length of the moving bed

$$y_{hr} = \frac{L^{hr}}{L^{bed}}. \tag{7-3}$$

A high value of y_{hr} improves the thermal efficiency of the process, whereas the dynamic and therefore, the specific cooling power decreases.

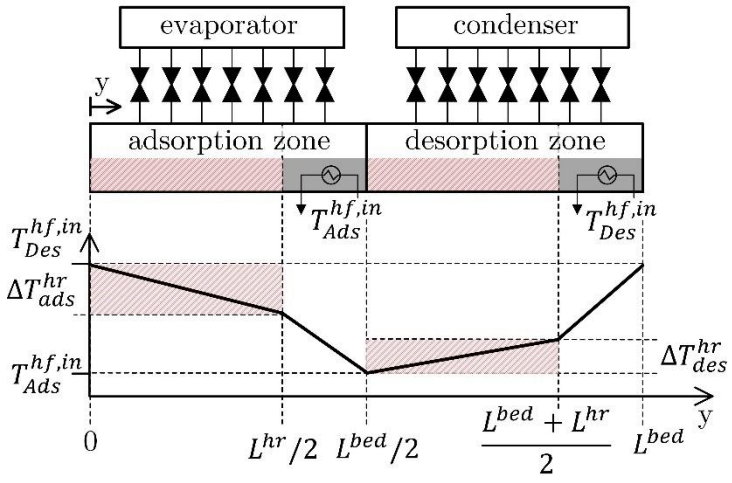

Figure 7-4: Heat recovery setup for multiple bed adsorption chillers approximated with the TMB approach and idealized temperature profile of the moving bed. In addition to the positions in the moving bed, schematically, the temperature levels and temperature differences obtained in the heat regeneration zone (hatched) are shown.

7.1.1 Simulated-Moving-Bed (SMB) model

The SMB model is based on a cascade of j_{max} adsorber (see Figure 7-2 (left) with $j_{max} = 6$) and is basically the same model as introduced in section 3.2.3 with the extension that it accounts for multiple adsorbers with index j. Therefore, in equivalence to equations (3-55), (3-56), and (3-70) a set of partial differential equations can be formulated for adsorbers j, yielding local adsorptive densities (ϱ_j^v), temperatures (T_j) and loadings (X_j) in the adsorbent composites

$$\varepsilon^{ma}\frac{\partial \varrho_j^v}{\partial t} + \frac{\partial \varepsilon^{ma}\dot{m}_{z,j}^v}{\partial z} + \varrho^{bulk}\frac{\partial X_j}{\partial t} = 0 \tag{7-4}$$

$$\left(\varepsilon^{ha}\varrho^{ha}c_{p,j}^{ha} + \tilde{\varepsilon}^s\tilde{\varrho}^s c_{p,j}^s + \varrho^{bulk}X_j c_{p,j}^{ad} + \varepsilon^{ma}\varrho_j^v\left(c_{p,j}^v - \frac{R}{MW}\right)\right)\frac{\partial T_j}{\partial t} - \varepsilon^{ma}\frac{RT_j}{MW}\frac{\partial \varrho_j^v}{\partial t} + \varrho^{bulk}\Delta_{ads}hk_{LDF}\left(X_{eq,j} - X_j\right) + \frac{\partial(1-\varepsilon^{ma})\dot{q}_{z,j}^{ha+s+ad}}{\partial z} + \varepsilon^{ma}\dot{m}_z c_{p,j}^v\frac{\partial T_j}{\partial z} - v_{z,j}^v\frac{\partial \varepsilon^{ma}p_j}{\partial z} = 0, \tag{7-5}$$

$$\frac{\partial X_j}{\partial t} = k_{LDF}\left(X_{eq,j}(T,p) - X_j\right). \tag{7-6}$$

In analogy, the energy conservation equations for the heat exchanger flat tube and the heat transfer fluid at position j can be formulated, respectively

$$m^{pm}c_p^{pm}\frac{\partial T_j^{pm}}{\partial t} = \dot{q}_j^{hf} + \dot{q}_j^{hr} - \dot{q}_j^{pm}, \tag{7-7}$$

$$m^{hf}c_{p,j}^{hf}\frac{\partial T_j^{hf}}{\partial t} = \dot{m}^{hf}c_{p,j}^{hf}\left(T^{hf,in} - T_j^{hf}\right) - \dot{q}_j^{hf}. \tag{7-8}$$

The heat fluxes between heat transfer fluid, passive mass, and adsorbent composite as well as the heat recovery heat flux $\dot{q}_j^{hr}$ at position j are given by

$$\dot{q}_j^{pm} = k^{pm}\left(T_j^{pm} - T_j\big|_{z=s_{cdc}}\right), \tag{7-9}$$

$$\dot{q}_j^{hf} = k^{hf}\left(T_j^{hf} - T_j^{pm}\right), \tag{7-10}$$

$$\dot{q}_j^{hr} = k^{hr}\left(T^{pm}\big|_{\frac{j_{max}+j_{hr}}{2}-j} - T_j^{pm}\right). \tag{7-11}$$

Here, k^{hr} is the heat transfer coefficient between two modules in heat recovery which is chosen largely to not limit the heat transfer. In heat recovery, $\dot{q}_j^{hf} = 0$ and for modules that are not contributing to internal heat regeneration, $\dot{q}_j^{hr} = 0$.

For the adsorbent composites in module j, the same boundary conditions apply as in section 3.2.3.3. The boundary conditions for the dynamic states $\xi_j(z) \equiv \left[X_j(z), \varrho_j^v(z), T_j(z), T_j^{pm}\right]$ of module j are

$$\xi_j^{in} = \begin{cases} \xi_{j_{max}} - 1, j = 0 \\ \xi_{j-1}, j = 1, \dots, j_{max} - 1. \end{cases} \tag{7-12}$$

In analogy to the cycle time t_{cyc} in the two-bed design, the discrete-time intervals in which the adsorber modules are switched can be formulated as a function of the total number of modules j_{max},

$$\tau_{sw} = \frac{t_{cyc}}{j_{max}}, \tag{7-13}$$

with τ_{sw} the residence time of each module at position j. In the SMB approach, each module passes through each position exactly once during one cycle with cycle time t_{cyc}.

The desorption heat flux provided for the modules in the desorption half cycle is obtained in cyclic steady-state, by appending the heat fluxes of each module in desorption mode in the time interval $[0, \tau_{sw}]$. In equivalence, the total desorption heat flux is obtained by taking the desorption heat flux of one module in the total desorption half cycle $\left[t_{cyc}/2, t_{cyc}\right]$ into account. Integration of the desorption heat flux over the cycle time yields the total heat density in the unit energy per cross-sectional area

$$\dot{q}_{des} = \sum\nolimits_j \dot{q}_{j,des}[0, \tau_{sw}] \equiv \dot{q}_{j,des}\left[t_{cyc}/2, t_{cyc}\right], \tag{7-14}$$

$$q_{des} = \int_0^{t_{cyc}} \dot{q}_{des}\, dt. \tag{7-15}$$

The mass fluxes between evaporator/adsorber modules and condenser/desorbing modules are calculated from the sum of mass fluxes leaving ($\dot{m}_c = \sum_j \dot{m}_{j,des,0}^v [0, \tau_{sw}]$) or entering ($\dot{m}_e = \sum_j \dot{m}_{j,ads,0}^v [0, \tau_{sw}]$) the CDC composites at the top layer in the time interval $[0, \tau_{sw}]$. The mass fluxes are used to calculate the evaporator heat flux and heat density

$$\dot{q}_e = \dot{m}_e \Delta_{evap} h(T_e) - \dot{m}_e c_{p,c}^l (T_c - T_e), \tag{7-16}$$

$$q_e = \int_0^{t_{cyc}} \dot{q}_e\, dt. \tag{7-17}$$

7.1.2 True-Moving-Bed (TMB) model

In this work, the steady-state TMB approach is applied on multi-bed adsorption chillers with a distributed parameter model of the adsorbent composites. A model sketch of the TMB and the adsorbent composites is shown in Figure 7-5.

With an increasing number of adsorber beds in the SMB approach, the residence time of an adsorber at one position decreases. In the limit, the discrete movement of the adsorber beds can be treated as a convective flow counter currently to the heat transfer fluid in equivalence to a truly moving bed of adsorbent. This will be denoted as flow along the y-coordinate. The limit consideration of the TMB provides an enormous reduction of the numerical solution effort. While the SMB model needs to be solved dynamically over several cycles until the cyclic steady state is reached, the TMB model is stationary, which only requires finding the steady-state solution. Furthermore, the steady-state nature allows for efficient parameter variations using parameter continuation. For the sake of comparison with the SMB model equations, the following set of equations describing the TMB model is given in their dynamic form. However, when solving the model, the time derivatives are set to zero. A detailed derivation of the TMB conservation equations is outlined in Appendix D.5.

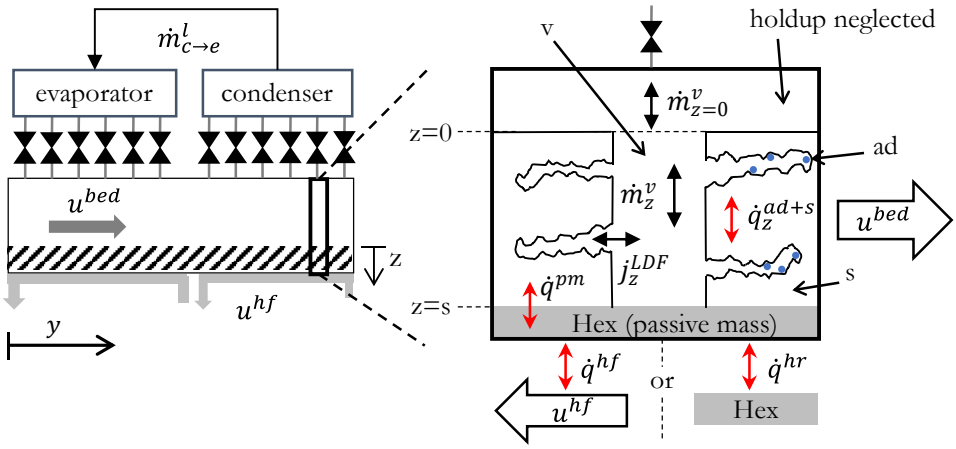

Figure 7-5: True-Moving-Bed containing adsorbent composites and Hex in y-coordinate direction. In addition, the composites are spatially distributed in the z-direction.

Mass and energy balances in terms of methanol vapor density (ϱ^v), temperature (T), and loading (X) in the TMB approach are

$$\varepsilon^{ma}\frac{\partial \varrho^v}{\partial t} + \frac{\partial \varepsilon^{ma}\dot{m}^v_z}{\partial z} + \varrho^{bulk}\frac{\partial X}{\partial t} + u^{bed}\left(\varrho^{bulk}\frac{\partial X}{\partial y} + \varepsilon^{ma}\frac{\partial \varrho^v}{\partial y}\right) = 0, \tag{7-18}$$

$$\left(\varepsilon^{ha}\varrho^{ha}c_p^{ha}+\tilde{\varepsilon}^{s}\tilde{\varrho}^{s}c_p^{s}+\varrho^{bulk}c_p^{ad}X+\varepsilon^{ma}\left(\varrho^{v}c_p^{v}-\frac{R\varrho^{v}}{MW}\right)\right)\frac{\partial T}{\partial t}-\varepsilon^{ma}\frac{RT}{MW}\frac{\partial\varrho^{v}}{\partial t}+$$
$$\Delta_{ads}h\varrho^{bulk}\frac{\partial X}{\partial t}+\Delta_{ads}h\varrho^{bulk}\frac{\partial X}{\partial y}+u^{bed}\left(\varepsilon^{ha}\varrho^{ha}c_p^{ha}+\tilde{\varepsilon}^{s}\tilde{\varrho}^{s}c_p^{s}+\varrho^{bulk}Xc_p^{ad}+\right. \tag{7-19}$$
$$\left.\varepsilon^{ma}\left(\varrho^{v}c_p^{v}-\frac{R\varrho^{v}}{MW}\right)\right)\frac{\partial T}{\partial y}-u^{bed}\varepsilon^{ma}\frac{RT}{MW}\frac{\partial\varrho^{v}}{\partial y}+\frac{\partial(1-\varepsilon^{ma})\dot{q}_z^{ha+s+ad}}{\partial z}+\varepsilon^{ma}\dot{m}_z^{v}c_p^{v}\frac{\partial T}{\partial z}=0,$$

$$\varrho^{bulk}\left(\frac{\partial X}{\partial t}+u^{bed}\frac{\partial X}{\partial y}-k_{LDF}\left(X_{eq}(T,p)-X\right)\right)=0. \tag{7-20}$$

The terms with u^{bed} account for convective mass and energy transport of the adsorbent composites, adsorptive and adsorbate in moving bed direction. With a fixed bed length L^{bed}, the residence time of each segment j in the moving bed is given by

$$\tau^{bed}=\frac{L^{bed}}{u^{bed}}, \tag{7-21}$$

which is in equivalence to t_{cyc} in the single adsorber or SMB approach.

To complete the TMB model, balance equations for the heat exchanger and heat transfer fluid are required. Like the balances of the adsorbent composites, an additional transport in y-direction occurs, which accounts for convective energy transport of the passive flat-tubes

$$m^{pm}c_p^{pm}\frac{\partial T^{pm}}{\partial t}=\dot{q}^{hf}+\dot{q}^{hr}-\dot{q}^{pm}-u^{bed}m^{pm}c_p^{pm}\frac{\partial T^{pm}}{\partial y}. \tag{7-22}$$

The above-mentioned equations ((7-18)-(7-20), (7-22)) describe the conservation of mass and energy in a continuously moving bed with velocity u^{bed}, consisting of Hex flat tubes and adsorbent composites with spatially varying loadings and temperatures. To ensure counterflow, the energy balance of the heat transfer fluid is written with the sign of the fluid velocity u^{hf} being opposite u^{bed} (see Figure 7-5 on the right)

$$m^{hf}c_p^{hf}\frac{\partial T^{hf}}{\partial t}=-u^{hf}m^{hf}c_p^{hf}\frac{\partial T^{hf}}{\partial y}-\dot{q}^{hf}. \tag{7-23}$$

Identical boundary conditions as for the single adsorber model (see section 3.2.3.3) can be used for the adsorbent composites (z-coordinate).

The equations for the TMB contain first-order derivatives in y (convective transport terms). Therefore, periodic boundary conditions for the states of the inlet $\xi(z,y=0)\equiv[X(z,y=0),\varrho^{v}(z,y=0),T(z,y=0),T^{pm}(y=0)]$ are used

$$\xi(z, y = 0) = \xi(z, y = L^{bed}). \tag{7-24}$$

The spatial derivatives in the mathematical models of SMB and TMB are discretized with the finite volume method. The resulting DAEs are implemented in the object-oriented modelling environment ProMoT/ Diana and dynamically solved to cyclic steady state (SMB) or to obtain consistent initial values (TMB). In addition, the time derivatives in the TMB model are set to zero obtaining a large set of nonlinear algebraic equations which can be solved with a significant reduction in computational effort. Details of the discretization, implementation, simulation environment, and simulation parameters are given in Appendix D.2.

7.2 Process simulations of multi-bed adsorption chillers with SMB approach and TMB approximation

In this section, multi-bed adsorption refrigerators are investigated with a varying number of adsorber modules. The material model of (quasi-) homogeneous composites without heat additive introduced in section 2.4.1 and material parameters summarized in Table B-6 are used.

Exemplarily, the steady-state solutions of transient SMB simulations are investigated for a constant layer thickness of the adsorbent composites of 1 mm, a cycle time of 100 s, and heat transfer velocity of $u^{hf} = -0.25 m/s$. Furthermore, a continuously moving multi-bed adsorption heat pump is regarded using the TMB approximation and compared with the SMB approach. The convergence of the SMB solution to the TMB solution is shown for a high number of SMB-modules.

The loading distribution in the adsorbent composites is mainly dictated by the local pressure and temperature conditions. Therefore, the loading profiles are shown as a representative example in Figure 7-6 versus normalized cycle time (SMB) and bed length (TMB).

In addition to the spatially distributed profiles of the SMB, the spatially averaged loading obtained with SMB and TMB are shown. The convergence of the SMB solution with an increasing number of adsorber modules to the TMB solution is evident. For a high number of SMB modules (50 modules for this set of parameters), the loading profiles of SMB and TMB are almost equivalent. The same statement applies to the other state variables such as temperatures and pressures in the adsorbent composites.

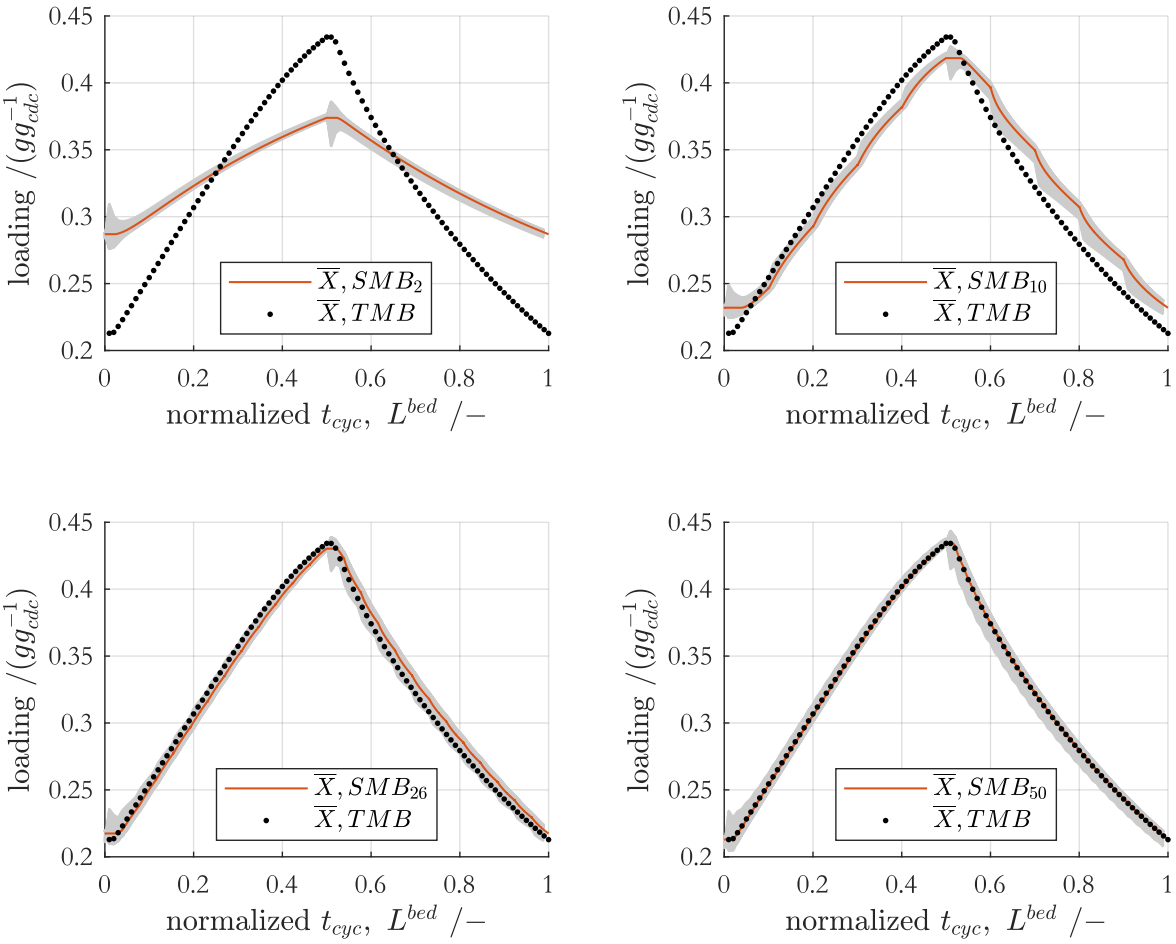

Figure 7-6: Comparison of loading profiles vs. normalized cycle time in the cyclic steady state obtained with the SMB approach for 2, 10, 26, and 50 adsorber modules. The gray area represents the spatial distribution of loading in the adsorbent composites (discretized with $N_z = 30$ grid points), and the average loading for the SMB approach is also shown (solid line). In addition, the spatially averaged (over the composite layer thickness) loading profile for the TMB approximation (discretized with $N_y = 100$ grid points) is plotted versus the normalized bed length. The model parameters were set to $u^{hf} = -0.25\ m/s$, $s_{cdc} = 1\ mm$ and $\tau^{bed} = 100\ s$.

The unsteady, step-like behaviour of the temperature profile in the heat transfer fluid, which results from the discrete switching of adsorber modules, is damped in the spatially averaged load profiles. The discrete intervals become more visible when, for example, considering the dynamic states of the lowest layers of the adsorbent composites. Alternatively, the mass fluxes at the top layer can be regarded. Resulting from the density gradients in the top layers of the adsorbent composites, the mass fluxes exchanged between evaporator and adsorber modules as well as desorbing modules and condenser are further used to compare SMB and TMB. Figure 7-7 shows

the mass fluxes of SMB and TMB at the top layer of the adsorbent composites, revealing the transient, unsteady behaviour due to the discrete shifting of the SMB modules. In contradiction to the averaged loading profiles, however, a discrepancy between the TMB and SMB approach can still be seen with a high total number of 50 SMB modules, which becomes smaller and smaller with an increasing number of adsorbers.

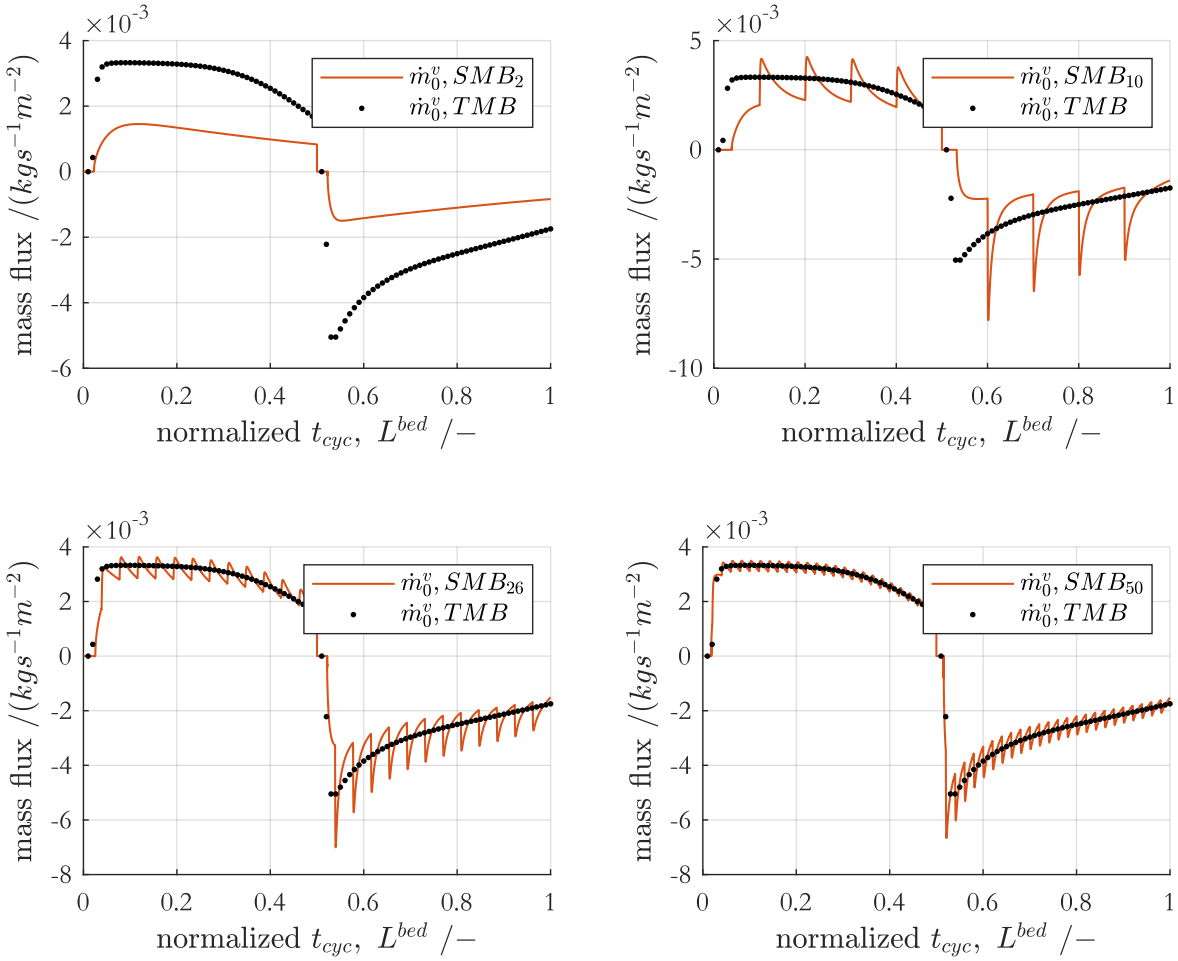

Figure 7-7: Mass fluxes entering the top layer of the CDC composites in one module as a function of normalized cycle time in cyclic steady state in the SMB. The number of SMB modules is increased and chosen in equivalence to Figure 7-6. Additionally, the mass fluxes in the TMB approximation are shown. The model parameters were set to $u^{hf} = -0.25\ m/s$, $s_{cdc} = 1\ mm$ and $\tau^{bed} = 100\ s$.

Due to the higher pressure and temperature levels, the kinetics of mass and heat transfer are larger during desorption. As a result, the amplitudes in the mass flux of adsorbers in the desorption zone (x-axis≥0.5, connected to condenser) are larger than of adsorbers in the

adsorption zone (x-axis<0.5, connected to evaporator). However, in the steady-state, the integral masses entering the adsorption zone and leaving the desorption zone are equal.

Furthermore, the comparison of efficiency and power density between SMB and TMB approaches reveals an integral statement. Figure 7-8 shows COP and SCP for the TMB as well as for the SMB as a function of the number of SMB modules. Especially the SCP strongly depends on the number of modules showing the benefit of a multi-bed setup. For the chosen set of parameters, the SCP could be increased by a factor of approximately 2.5 by increasing the number of modules from 2 to 50. The beneficial effect on the COP is less pronounced. Both, COP, and SCP of the SMB are showing the converging trend towards the TMB solution with an increasing number of modules. The number of adsorbers needed in the SMB to approach the TMB solution depends on the set of simulation parameters. A higher heat transfer fluid velocity e.g., allows the SMB to approach the TMB solution with fewer adsorbers.

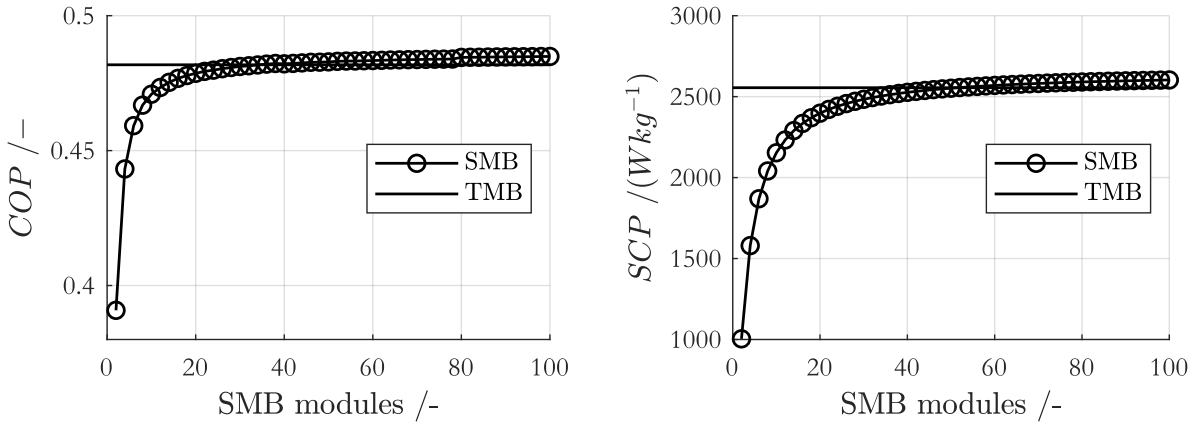

Figure 7-8: COP and SCP obtained for the steady-state TMB approximation and the SMB approach as a function of the number of SMB modules for simulations with $u^{hf} = -0.25\ m/s$, $s_{cdc} = 1\ mm$ and $\tau^{bed} = 100\ s$.

For a high number of SMB modules for which the discrete switching approaches a quasi-continuous movement, the solution of the TMB slightly underestimates the integral solution of the SMB, which is attributed to numerical diffusion. The convective transport terms in the TMB approach are discretized with a first-order upwind scheme guaranteeing numerical stability. This is accompanied by slight smearing of the profiles known as numerical diffusion. This effect can be decreased by increasing the number of grid points in y-direction in the TMB approach. However, without changing the discretization scheme, numerical diffusion cannot be avoided. Due to the low influence of numerical diffusion on the TMB solution and the considerable

advantage due to lower computational effort, the numerical diffusion in the TMB approach was accepted. To show that the TMB is the limiting case of the SMB, simulations of the TMB are shown in Appendix D.6, which are discretized with the method of characteristics, whereby no convective transport terms are used.

Even though the TMB approximation slightly underestimates the SMB solution for a high number of adsorber modules, the significantly lower simulation effort justifies this approach. The simulation results shown and discussed in detail in the following sections were all conducted with the TMB approximations.

7.3 Properties of a continuous Multi-Bed Adsorption Cooling Process simulated with the TMB approach

In this section, the TMB process setup is discussed in detail and the influence of different process parameters is investigated. In section 7.3.1, the influence of the heat transfer fluid velocity is discussed exemplarily for one set of bed residence time and composite layer thickness. Following that, spatial profiles of temperature and loading in the adsorbent composites are shown. This section is completed by investigating simulation results obtained by parameter continuation of the layer thickness and bed residence time and a discussion of their influence on COP and SCP. In principle, the optimization routine is in equivalence to the procedure conducted for the 2-bed process in chapter 5.

7.3.1 Variation of heat transfer fluid velocity

Following, the influence of the heat transfer fluid velocity u^{hf} is investigated in the TMB approach. In equivalence to section 7.2, the residence time of the moving bed and the composites layer thickness were chosen to $\tau^{bed} = 100s$ and $s_{cdc} = 1mm$. Figure 7-9 shows profiles of the averaged loading, heat transfer fluid temperature, and mass flux at the composite's top layer versus the normalized bed length. The heat transfer fluid velocity is varied from -0.25 to $-1m/s$. For slow velocities, this has a limiting effect on the overall process kinetics. Conversely, the overall process kinetics is not limited when the heat transfer fluid is transferred with a high velocity. Then, the process kinetics is limited by the heat and mass transfer in the adsorbent composites. If u^{hf} is limiting, the resulting profiles are linear due to the linear contribution of u^{hf} to the heat exchange between hf, pm and composites. For fast u^{hf}, the limiting processes are heat and mass transfer in the adsorbent composites which are non-linear transport processes resulting in non-linear profiles of temperature and loading.

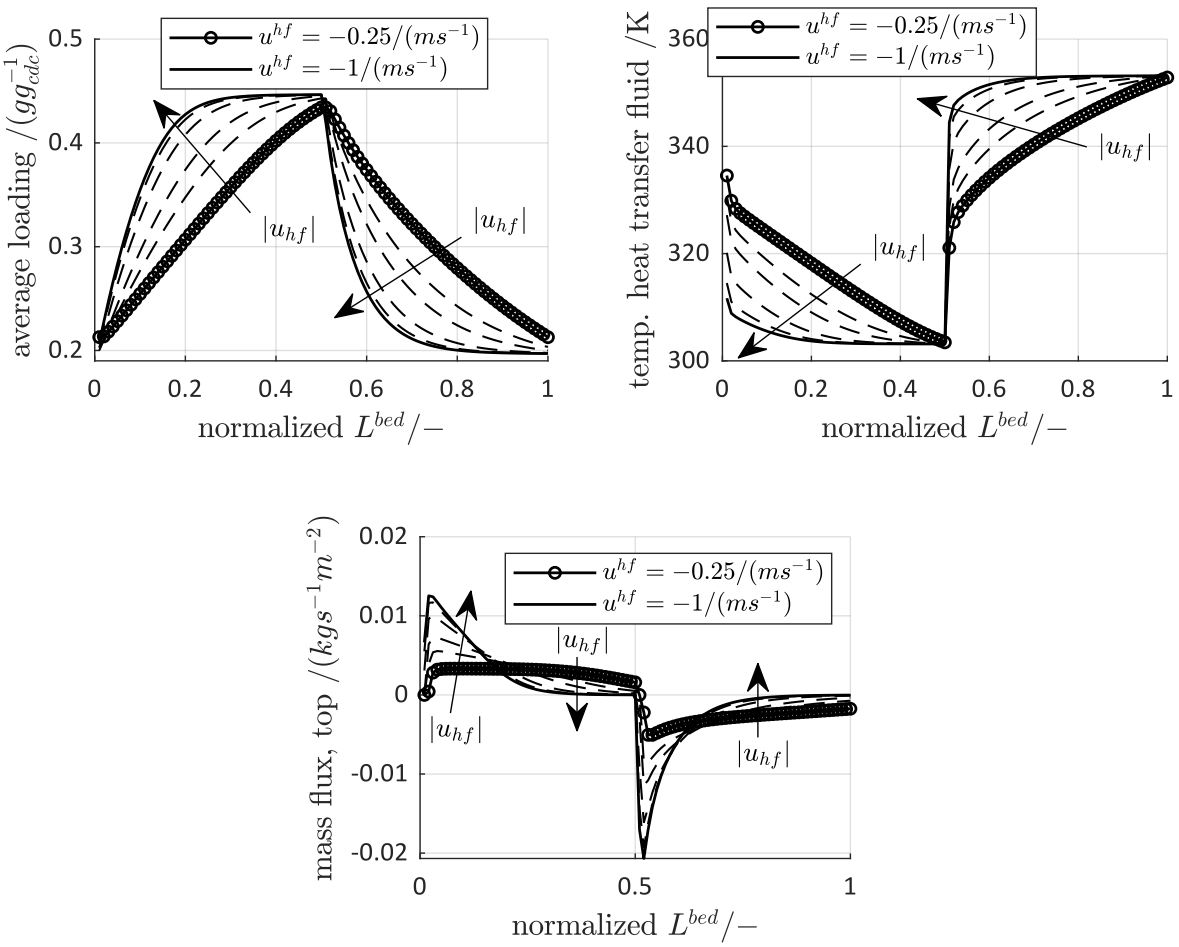

Figure 7-9: Loading, the temperature in the heat transfer fluid, and top layer mass flux in the TMB approach versus normalized length of the moving bed. The heat transfer fluid velocity $|u^{hf}|$ is varied (0.25, 0.3, 0.35, 0.5, 0.75 and 1 m/s). The residence time in the moving bed and layer thickness of the adsorbent composites are the same as in section 7.2 with $\tau^{bed} = 100\ s$ and $s_{cdc} = 1\ mm$.

When the fluid moves with a slow velocity, its residence time in the flat tubes is long enough so that the counter current heat exchange results in an almost linear temperature profile in the heat transfer fluid. Only in the beginning of adsorption (0.0) and desorption zone (0.5), a temperature step can be seen which is due to the cold or hot passive mass of flat-tube and adsorbent coming from adsorption or desorption zone, respectively. With increasing u^{hf}, the temperature profile in the moving bed changes from a linear to a parabolic shape because of the short residence time. In other words, the local contact times between AdHex and heat transfer fluid are too short to exchange enough heat and equilibrate the temperatures resulting in parabolic profiles. As a result, the average loading profiles also transform from almost linearity at $u^{hf} = -0.25\ m/s$ to parabolic shape at $u^{hf} = -1 m/s$.

7.3.2 Further properties of the TMB multi-bed – Steady-state solutions

In this section, steady-state simulation results of the multi-bed process are discussed in detail, where the AdHex moves in counterflow to the heat transfer fluid. The simulations were conducted with the steady-state TMB approximation and with a layer thickness of the CDC composites, bed residence time, and heat transfer velocity of $s_{cdc} = 2mm$, $\tau^{bed} = 100s$, and $u^{hf} = -1m/s$, respectively. The moving bed is equally divided into adsorption and desorption zone with an equivalent length of $L^{bed} = 5\ m$.

Figure 7-10 (top) shows contour plots of the temperature and loading distribution in the adsorbent composites as functions of layer thickness and normalized length of the moving bed. According to the process diagram, the adsorbent is cooled and heated in counterflow to the heat transfer fluid. Additionally, Figure 7-10 (bottom) contains a plot of the temperatures of the heat transfer fluid, flat tubes, and adsorbent composites (averaged and spatially distributed) as well as a plot of the averaged and spatially distributed loading profiles in the composites as a function of the normalized bed length.

The inlet temperatures of the heat transfer fluid (at normalized $L^{bed} = 0.5$ and 1) correspond with the selected ambient temperature levels of $T^{ads} = 303.15K$ and $T^{des} = 258.15K$. Heat transfer resistances between fluid and flat tubes as well as flat tubes and adsorbents are neglected. Consequently, the temperature at the bottom of the composites is equal to the flat tube temperature. The large spatial temperature distribution and as a result the deviation of averaged temperature $\overline{T}_{cdc}$ and flat tube temperature (T^{pm}) is attributed to the low thermal conductivity of the composites. At normalized $L^{bed} = 0$, the adsorbent is cooled by moving in counterflow to the cold heat transfer fluid, which, in turn, is heated by absorbing sensible and latent heat. Due to a large temperature difference, the bed experiences a sudden temperature rise at the beginning of the desorption zone (at normalized $L^{bed} = 0.5$). Due to the counterflow, the temperature of the composites increases in flow direction while the heat transfer fluid shows the opposite behaviour. The sudden increase in temperature causes a large temperature gradient and thus irreversibility. The loading profile depends on the temperature and pressure conditions within the porous CDC composites. In this example, with a layer thickness of $s_{cdc} = 2\ mm$, large spatial gradients exist, revealing the necessity of using a spatially resolved model of the adsorbent.

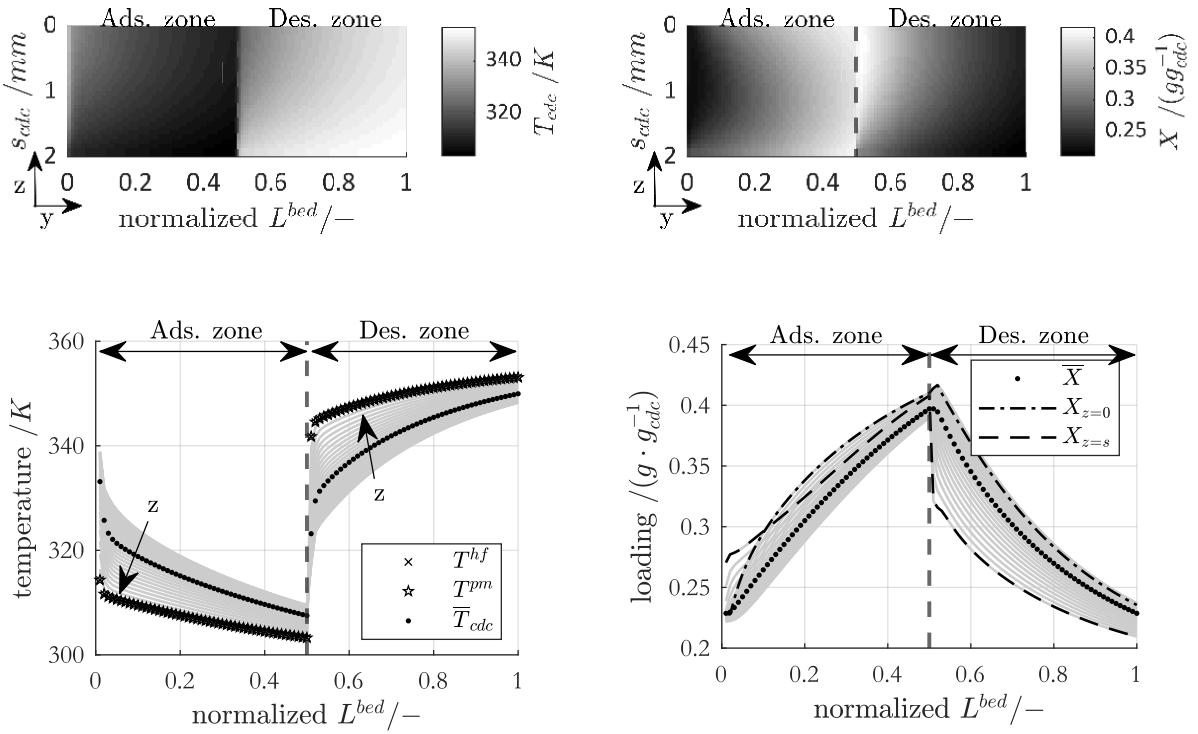

Figure 7-10: Contour plots showing the spatial distribution of temperature and loading in the CDC composites with layer thickness $s_{cdc} = 2\ mm$ (on top). The simulations were conducted with the TMB approximation calculated with a heat transfer fluid velocity of $|u^{hf}| = 1\ m/s$ and a residence time of $\tau^{bed} = 100\ s$. Additionally, temperature profiles of heat transfer fluid (T^{hf}), passive flat tubes (T^{pm}) as well as distributed and averaged temperature profiles of the CDC composites ($\overline{T}_{cdc}$) as well as loading profiles as a function of the normalized bed length are shown (bottom).

While the large spatial temperature gradients are a result of the low thermal conductivity of the CDC composites, the spatial pressure distribution follows from the low permeability of the composites. Figure 7-11 (on the left) shows the pressures of the evaporator and condenser, as well as the averaged and spatially distributed (z-coordinate) pressure profiles of the methanol vapor ($\overline{p}^{v}$) in the interparticle voids. In addition, Figure 7-11 (right) shows the mass flux at different locations in the moving bed between the top layer of CDC composites and evaporator, or condenser, respectively.

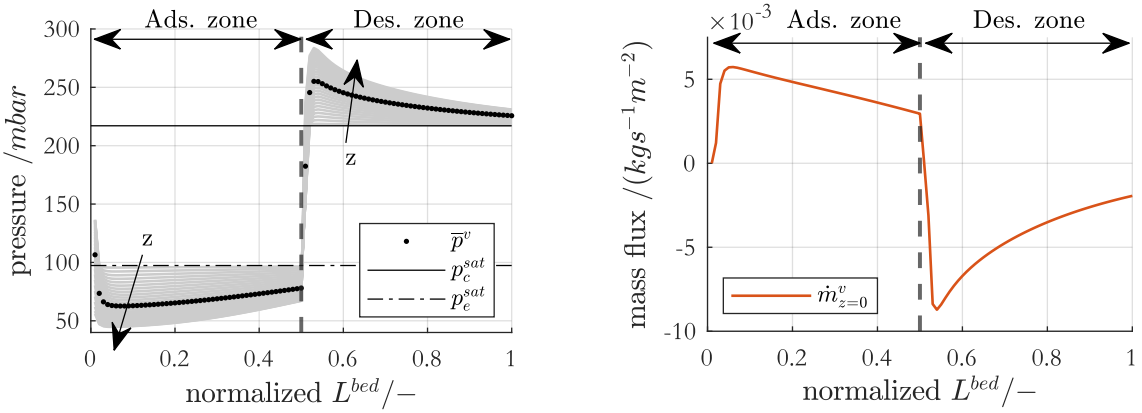

Figure 7-11: Averaged ($\overline{p}^v$) and distributed (in grey) methanol vapor pressure profiles in the interparticle voids of the porous CDC composites, and mass flux exchanged with evaporator and condenser, respectively, as a function of the normalized bed length. Simulation parameters: $s_{cdc} = 2\ mm$, $|u^{hf}| = 1\ m/s$, $\tau^{bed} = 100\ s$.

Due to the sudden cooling at the beginning of the adsorption zone (normalized $L^{bed} = 0$), the adsorption potential increases rapidly, especially in the lower layers of the composite, resulting in strong adsorption. Here, the adsorption flux exceeds the interparticle transport, resulting in a pressure drop in the voids, mainly in the lower layers. As the degree of saturation increases and the adsorption potential decreases, the pressure in the voids approaches the evaporator pressure, and the methanol mass flux decreases. Similarly, at the beginning of the desorption zone (normalized $L^{bed} = 0.5$), the methanol pressure in the voids increases due to the strong heating of the lower layers and the resulting desorption. Since the desorption flux is initially larger than the interparticle transport, an increase in pressure is caused. As the loading decreases, the pressure profile approaches the condenser pressure. With this parameter set, equilibrium has not yet been reached in all adsorbent layers at the end of the adsorption and desorption zone, which is why the exchange mass flux has not yet reached zero at these positions. The larger maximum mass flux in the desorption zone is due to the faster kinetics caused by the higher temperature and pressure levels. This TMB setup without heat recovery results in a COP of 0.52 with a specific cooling power of 1940 W/kg.

7.3.3 Optimal operational and material parameters of the TMB - Optimization of residence time and layer thickness applying parameter continuation

In this section, simulation results of the TMB approach in a wide range of parameter combinations are presented and discussed. Parameter continuation has been used to solve the system of nonlinear algebraic equations (NLAEs) of the steady-state TMB model. The residence time τ^{bed} in the moving bed has been used as the parameter for the continuation to calculate solution branches of the state variables $\boldsymbol{y}(\tau^{bed})$ (see section D.2.3). Additionally, the layer thickness of the adsorbent structures was varied in discrete steps to generate a solution field with a wide variation of these two parameters. Furthermore, three different heat transfer fluid velocities were investigated. With the aid to reduce the parameter space, the temperature boundary conditions, and material parameters of the adsorbent structure were held constant, as listed in Table D-2.

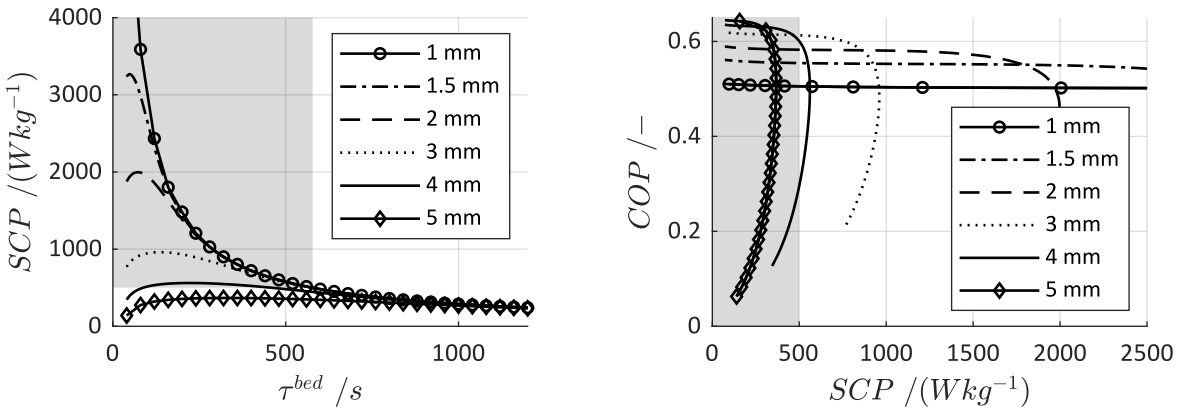

Figure 7-12: Mass-specific cooling power as a function of residence time in the TMB and layer thickness (on the left) and Pareto-optimal behaviour of COP and SCP (on the right). The profiles show simulation results obtained with $\left|u^{hf}\right| = 1\ m/s$.

Aiming to identify the optimal set of operational parameters, an objective function is desired. When either COP or SCP is used as the objective function, either process efficiency or power density is optimized. A cost function is preferred which takes both performance measures into account. Thus, the process and material parameters are sought for which the COP for a given SCP is maximum. Here, the residence time of the moving bed and the layer thickness of the CDC composites are optimized. The number of parameters can be extended for instance by the amount of heat-conducting additive or pore void fraction, as has been shown in chapter 5. Figure 7-12 (left) shows SCP with a variation of residence time τ^{bed} for CDC composites with varying

layer thickness. The grey rectangle indicates the set of parameters to be used to achieve an SCP of at least $500 Wk\,g^{-1}$.

The SCP exhibits an optimum with residence time, the level of which is strongly dependent on the layer thickness. In thick composites, transport paths for mass and energy are long which results in slow kinetics and thus smaller power densities. Due to the higher amount of active adsorbent mass, a process equipped with thicker layers tends to achieve higher efficiencies. While efficiency monotonously increases with τ^{bed} due to better utilization of the adsorption capacity (larger maximal loading difference), the optimal SCP is rather obtained at short residence times. This Pareto-optimality is shown in Figure 7-12 on the right by visualizing COP vs. SCP.

With the specification of a prescribed SCP, the optimal COP^{opt} concerning the residence time can be determined for every set of s_{cdc} and u_{hf}

$$\underbrace{\left(\frac{\partial COP}{\partial \tau^{bed}}\right)_{SCP}}_{1} = 0. \tag{7-25}$$

Exemplarily, Figure 7-13 shows the residence time optimized COP^{opt} for a prescribed SCP of $500 Wk\,g^{-1}$ vs. layer thickness. Depending on the heat transfer fluid velocity, different maximal COP results. The higher $|u^{hf}|$, the better the process kinetics resulting in higher COP^{max} with thicker adsorbent layers.

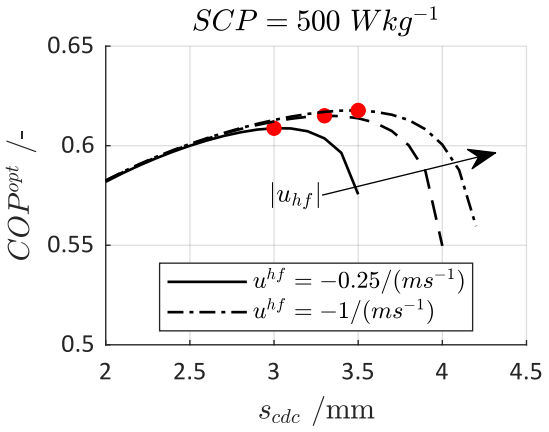

Figure 7-13: Residence time optimized COP^{opt} as function of layer thickness and heat transfer fluid velocity. The maximal COPs for different velocities are indicated.

In a further step, in addition to the residence time, the optimal adsorbent layer thickness is determined for the prescribed SCP

$$\underbrace{\left(\frac{\partial COP}{\partial \tau^{bed}}\right)_{SCP}}_{1} = \underbrace{\left(\frac{\partial COP^{opt}}{\partial s_{cdc}}\right)_{SCP}}_{2} = 0. \tag{7-26}$$

By repeating this procedure for a wide range of specific cooling powers, the optimal process and material parameters are determined as a function of the process operational conditions. By applying equation (7-26) on the parameter field obtained from the continuation simulations, the optimal residence time, layer thickness, and the corresponding COP are determined for three different $|u^{hf}|$. The optimization results are shown in Figure 7-14. Depending on the prescribed SCP, the optimum is a different set of optimal material and process parameters.

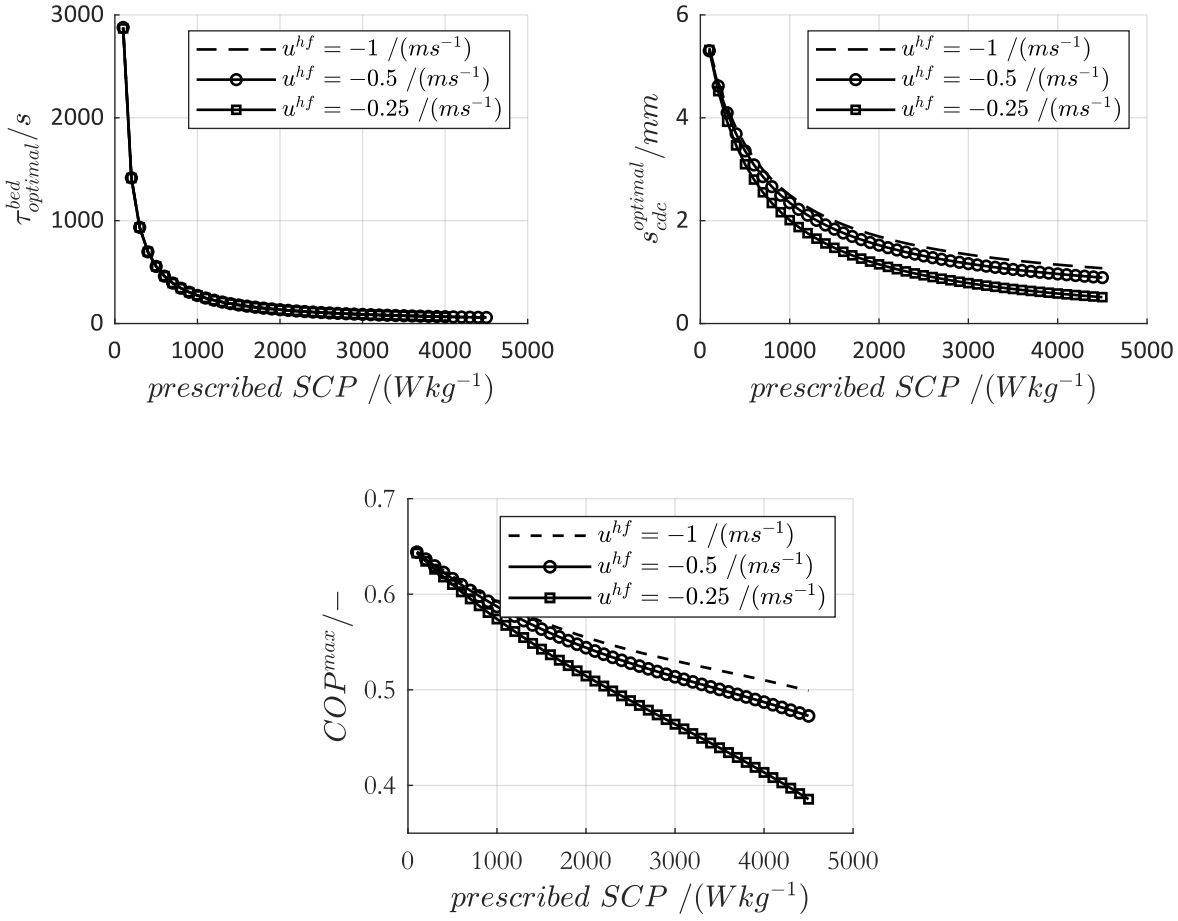

Figure 7-14: Optimized adsorbent residence time in the TMB (top left), composites layer thickness (top right), and resulting COP (bottom) for different $|u^{hf}|$ as function of the prescribed SCP.

The smaller the prescribed cooling power, the less dynamic is required giving rise to long residence times (adsorbent close to equilibrium) and thick layers (beneficial for the ratio of active to passive mass). Consequently, the resulting optimal COPs are higher for smaller prescribed SCP and higher for faster kinetics (larger values of $|u^{hf}|$).

7.4 Multi-bed TMB setup with a high grade of internal heat regeneration

The typical trade-off between efficiency and power density occupied in adsorption heat transformers has extensively been discussed, resulting in low COPs at process conditions with high SCP and vice versa. The reason is the process-related, inevitable temperature swing between adsorption and desorption. Besides active adsorbent mass, passive masses (heat exchanger, fluid, additives) must be heated and cooled cyclically. Thus, adsorber, adsorbent, and adsorbate must undergo the temperature change from adsorption to desorption temperature, albeit at the expense of a high COP. Short cycle times (accompanied by high SCPs) increase transport resistance, which results in lower COPs. So far, the multiple-bed setup was regarded without investigating additional internal heat integration and thus heat recovery between individual modules. Therefore, the thermodynamic limiting efficiency (see Appendix D.4) of an adsorption refrigerator could not be reached so far. To operate the adsorption refrigeration process as close as possible to the limiting efficiency, internal recovery of latent and sensible heat between individual modules is implemented as introduced in section 7.1 (Figure 7-4).

7.4.1 Optimization function

As demonstrated in section 7.3.3, the optimal COP obtained for an operator desired SCP is an adequate cost function optimizing the process performance. In this section, in addition to the moving bed residence time τ^{bed} and the composites layer thickness s_{cdc}, a third parameter y_{hr} (normalized length of heat recovery zone) is varied in the continuation simulations, which extend the parameter space by one dimension. In the post-processing, the simulation results are evaluated with the following cost function

$$\underbrace{\left(\frac{\partial COP}{\partial \tau^{bed}}\right)_{SCP}}_{1} = \underbrace{\left(\frac{\partial COP^{opt}}{\partial s_{cdc}}\right)_{SCP}}_{2} = \underbrace{\left(\frac{\partial COP^{max}}{\partial y_{hr}}\right)_{SCP}}_{3} = 0, \tag{7-27}$$

identifying the maximal COP and optimal material and process operational parameters for a variety of prescribed SCP. This procedure is straightforward and can easily be extended by further variational parameters, e.g., adsorbent design parameters, for a combined determination of optimal process and material composition parameters. However, increasing the parameter space increases the simulation effort exponentially making the application of more profound optimization methods necessary.

7.4.2 Multi-bed adsorption refrigerator with internal heat regeneration

In the following sections, the results of the steady-state TMB approach applied to evaluate the heat-integrated process setup (see Figure 7-4) for multi-bed adsorption cooling machines are presented and discussed. The main task of heat recovery is to reduce the external heat supply to drive the process.

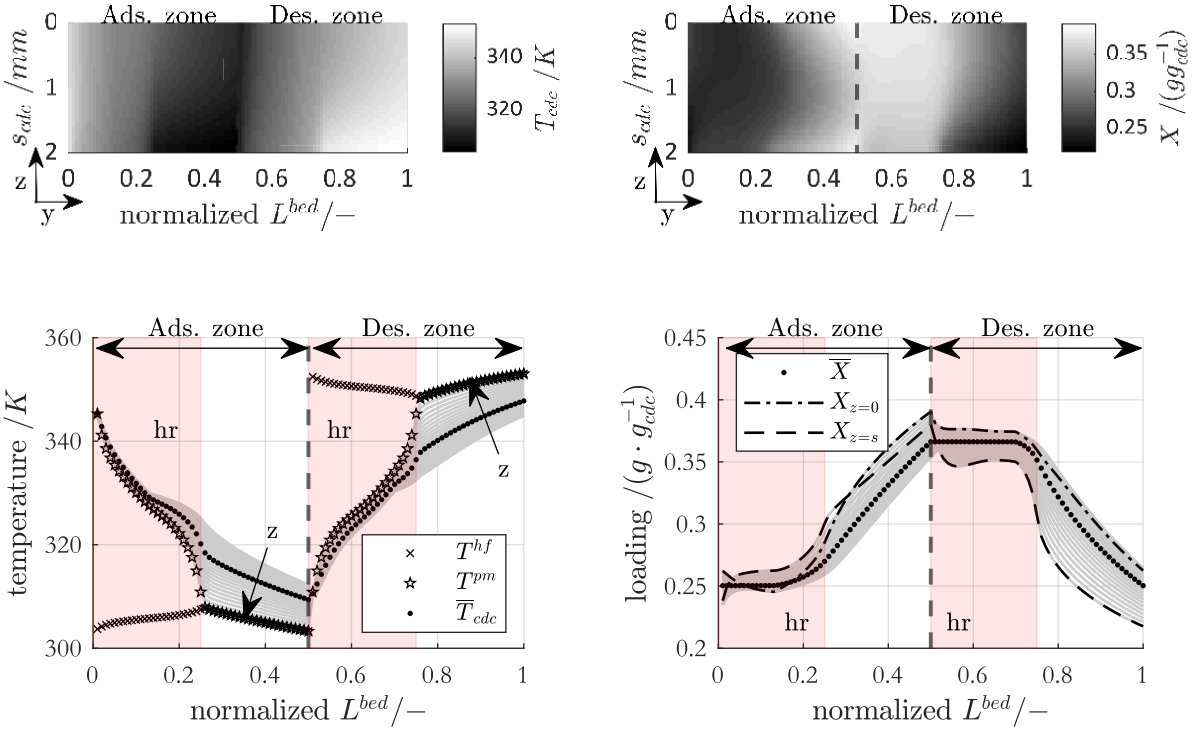

Figure 7-15: Distributed and averaged temperature and loading profiles of the TMB approach calculated with a residence time of $\tau^{bed} = 100\ s$, with normalized length of the heat recovery zone of $y_{hr} = 0.5$, composite layer thickness of $s_{cdc} = 2\ mm$ and heat transfer fluid velocity of $|u^{hf}| = 1\ m/s$. The heat recovery zone (hr) is highlighted with rectangles.

In addition, the temperature profiles are smoothened, and the sudden temperature rise or drop at the beginning of the adsorption and desorption zone is prevented. To achieve this, modules with minimum temperature differences are energetically paired in the heat recovery zone. Thus, sensible, and latent heat from the hot desorption zone can be partially used to heat cold adsorber modules. For comparison, simulations have been conducted with the same set of parameters as for the TMB without heat recovery ($\tau^{bed} = 100\ s$, $s_{cdc} = 2\ mm$, $|u^{hf}| = 1\ m/s$; compare section 7.3.2), additionally regarding a heat recovery zone with $y_{hr} = 0.5$. In this example, half of the modules (normalized $L^{bed} = 0 - 0.25$ and $0.5 - 0.75$) are contributing to heat recovery.

Figure 7-15 shows the resulting temperature and loading profiles as a function of the normalized bed length and the distributed pressure and mass flux profiles are visualized in Figure 7-16.

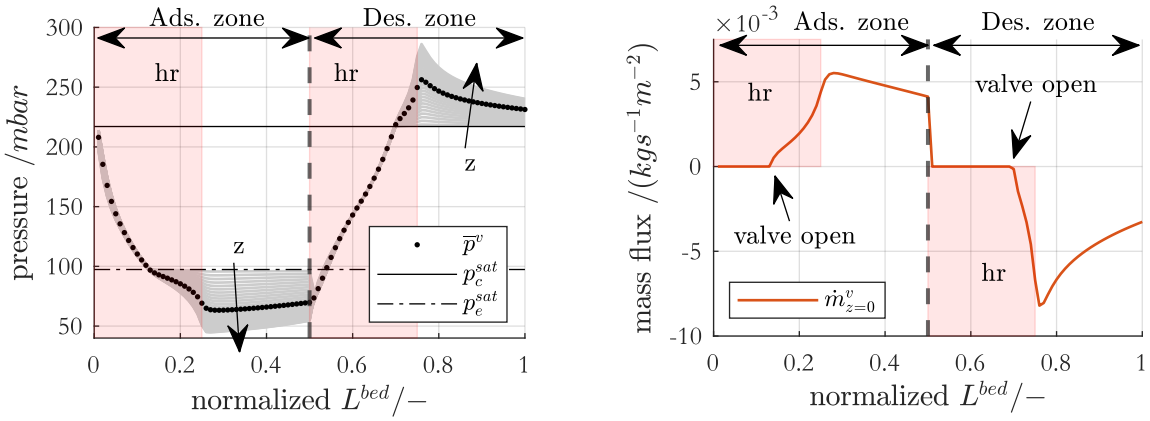

Figure 7-16: Averaged pressure in the macropores of the porous CDC composites and mass flux to the evaporator and from the condenser, respectively, as a function of the normalized position in the moving bed with the normalized length of the heat recovery zone of $y_{hr} = 0.5$.

In the adsorption and desorption heat recovery zone, the heat exchangers of individual modules are in energetic exchange with each other according to the process setup in Figure 7-3, resulting in a mirrored temperature profile in the passive mass. Looking at the spatially distributed temperature plot of the CDC composites (Figure 7-15, top left), four areas of equal size can be identified, representing consecutively the adsorption zone with half heat recovery (norm. $L^{bed} = 0 - 0.25$) and the desorption zone with half heat recovery (norm. $L^{bed} = 0.5 - 0.75$). The temperature profiles in the heat recovery zones are influenced by two effects: heat exchange between the energetically coupled modules and heat absorbed/ released due to desorption or adsorption. At the beginning of the heat recovery zones, the pressure conditions are not yet reached to cause the valves to open. Therefore, no significant adsorption enthalpies are released, or desorption enthalpies are required, and thus the temperature gradients across the layer thickness are very low and the integral loading remains constant. At normalized bed positions 0.13 and 0.7, the pressure conditions are satisfied and the valves connecting evaporator and adsorber modules, and adsorber modules and condenser open, initializing evaporation and condensation. At these points, mass transfer between the apparatuses occurs for the first time, which is induced by the initial adsorption or desorption, causing the spatial profiles of temperature, loading, and pressure to form larger gradients. Since the heat capacity in the adsorption zone is initially smaller (less methanol adsorbed) than at the beginning of the

desorption zone, the temperature decrease occurs faster, which is why the pressure condition in the adsorption zone is reached more quickly. The main advantage of the heat recovery is dedicated to these regions, where the modules are still in heat recovery, but cooling production has already begun and thus, where latent heat is directly being recovered in addition to sensible heat. Towards the end of the heat recovery zones, the temperature of the passive mass increasingly tends towards the temperature of the heat transfer fluid, reaching it at a normalized bed length of 0.25 and 0.75, respectively. From these points on, the spatial profiles of temperature, loading, and pressure are influenced by heat exchange between the heat transfer fluid and the Hex mass, in addition to adsorption and desorption.

The temperature profiles indicate the benefit of internal heat regeneration. Compared to the setup without internal heat regeneration (Figure 7-10), the sudden change in temperature at the beginning of the adsorption and desorption zone is reduced, decreasing entropy production and thus increases thermal efficiency. In addition, the heat supplied from the external heat source could be reduced. However, it should also be noted that the overall temperature difference of the CDC composites, and thus the loading difference and cooling capacity, are reduced compared to the setup without heat recovery. This is because only half of the adsorber bed is in contact with the external heat transfer fluid. In this example, the COP could be increased to 0.825 by applying heat recovery, while the specific cooling power decreases to 1336 W/kg.

The detailed investigation of the physical phenomena occurring in a multi-bed adsorption chiller with heat recovery gives an insight into the complex, coupled behaviour of adsorption, heat, and mass transfer. Nevertheless, the benefit for the process efficiency by applying heat recovery is shown. From the discussions, it appears, that the length of the heat recovery zone is a degree of freedom that needs to be optimized to maximize process efficiency. Following the optimization function in equation (7-27), optimization is conducted for prescribed cooling powers.

7.4.3 Optimal operational and material parameters of the multi-bed adsorption chiller with internal heat regeneration

In section 7.3.3, by applying parameter continuation of the bed residence time and variation of the composite layer thickness, the optimal set of parameters has been identified in a post-processing step. The same procedure is performed in this section additionally varying the normalized length of the heat recovery zone y_{hr}. Finally, in the post-processing, the optimal parameter set is obtained by applying the optimization function in equation (7-27) on the simulation results.

In a first step, for a prescribed SCP the residence time is identified for which the COP is maximal. This evaluation is repeated for the entire parameter space of s_{cdc} and y_{hr}. Exemplarily, the procedure is carried out once for a constant layer thickness and once for a constant heat recovery zone y_{hr} for simulations conducted with heat transfer fluid velocity of $|u^{hf}| = 1\ m/s$. Figure 7-17 shows the respective COP^{opt} with already optimized τ^{bed} as a function of y_{hr} (on the left) and s_{cdc} (on the right) for a prescribed SCP of $500\ Wkg^{-1}$. Exemplarily, for $s_{cdc} = 1.5\ mm$ the maximal COP^{max} is 1.44 at a normalized length of heat recovery zone of $y_{hr} = 0.78$. Similarly, the optimal layer thickness for $y_{hr} = 0.4$ is $s_{cdc} = 0.5\ mm$, with an optimal $COP^{max} = 1.31$. The obtained COPs already indicate the significant benefit on the process efficiency by applying the internal heat regeneration even though the set of parameters has not yet been optimized.

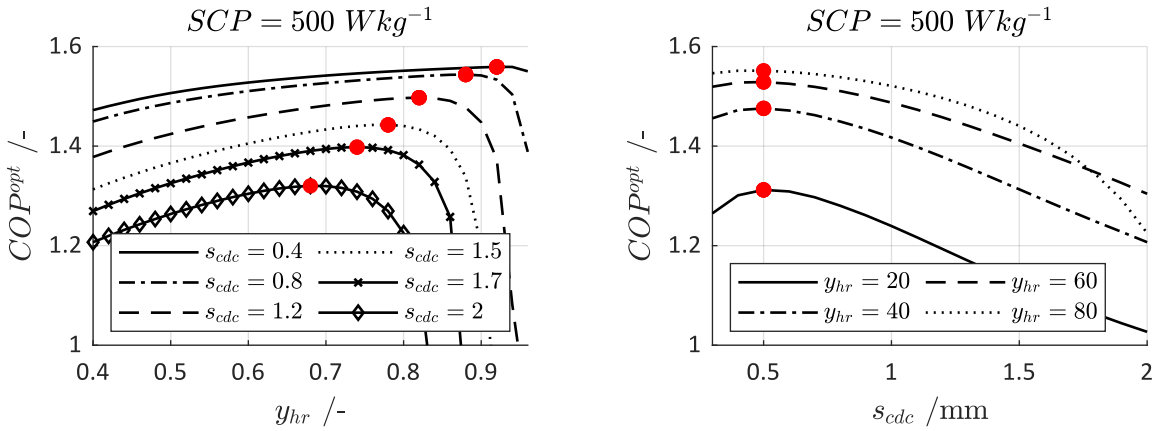

Figure 7-17: Optimal COP for a prescribed SCP of 500 W/kg with a variation of normalized length of heat recovery zone and layer thickness of CDC composites.

To represent the entire parameter space, a plot is used in which the maximum COPs are shown as a function of y_{hr} and s_{cdc} in Figure 7-18 for a prescribed SCP of 500 W/kg. In regions with a short heat recovery zone (small y_{hr}), COP^{max} is relatively insensitive to layer thickness. Here, an increase in y_{hr} is beneficial to improve thermal efficiency. However, if y_{hr} is near to the maximum value of COP^{max}, it is much more sensitive to the layer thickness. It is worth mentioning that the cooling power is mainly influenced by the bed residence time and the layer thickness of the CDC composites, while the thermal process efficiency mainly depends on the length of the heat recovery zone. However, a variation of one parameter is always accompanied by a different set of optimal parameters, which makes the optimization problem challenging. For

a prescribed SCP of 500 W/kg, the maximal COP^{max} results to 1.56 and is achieved with $s_{cdc} = 0.4\ mm$ and $y_{hr} = 0.92$.

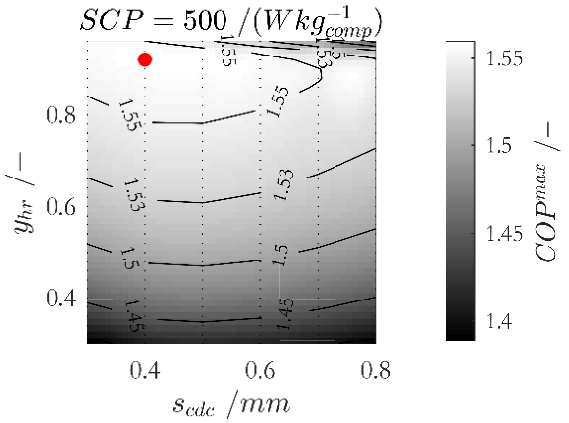

Figure 7-18: Optimal parameter space of COP^{max} as a function of s_{cdc} and y_{hr} for a prescribed SCP of 500 W/kg.

7.4.4 Global optimum: Optimal, characteristic curves for the multiple bed adsorption cooling process with internal heat regeneration

The analysis conducted in section 7.4.3 is repeated for different prescribed SCPs. Subsequently, the influence of the heat transfer fluid velocity u^{hf} is examined. Figure 7-19 shows the maximal achievable COP^{max} for the multi bed setup with internal heat regeneration and, additionally, the set of optimal parameters $\tau^{bed}_{optimal}$, $s^{optimal}_{cdc}$ and $y^{optimal}_{hr}$. At each point, a unique optimal set of parameters exists, consisting of residence time, layer thickness, and normalized length of the heat recovery zone.

The global analysis reveals the Pareto-optimal dependence of COP and SCP. Interestingly, the profiles of COP^{max} and $y^{optimal}_{hr}$ are of the same, almost linear shape, and show similar behaviour with varying SCP and fluid velocity. Therefore, the normalized length of the heat recovery zone can be identified to be the main parameter influencing thermal efficiency. If the prescribed SCP is small ($< 1000\ Wkg^{-1}$), u^{hf} only plays a minor role. However, it becomes more relevant for higher prescribed SCPs. Another interesting observation is that the profiles of $\tau^{bed}_{optimal}$ and $s^{optimal}_{cdc}$ are very similar and strongly nonlinear. These parameters can be identified as the most relevant parameters on the cooling performance. Generally, large values of SCP can only be provided by reducing the layer thickness (reduced transport resistance) or by a reduction of the moving bed residence time. A shorter residence time is accompanied by a greater moving

bed velocity and, thus, a higher heat capacity flow rate, which needs to be removed by the heat transfer fluid. This can be accompanied by increasing the heat capacity flow rate of the heat transfer fluid and, thus, increase the amount of heat that can be provided/ rejected in the desorption/ adsorption zone, respectively. In addition, due to the high grade of internal heat regeneration, the passive masses play no role anymore. Therefore, the optimal layer thicknesses are dramatically decreased to decrease the transport resistances compared to the multi-bed setup without heat regeneration.

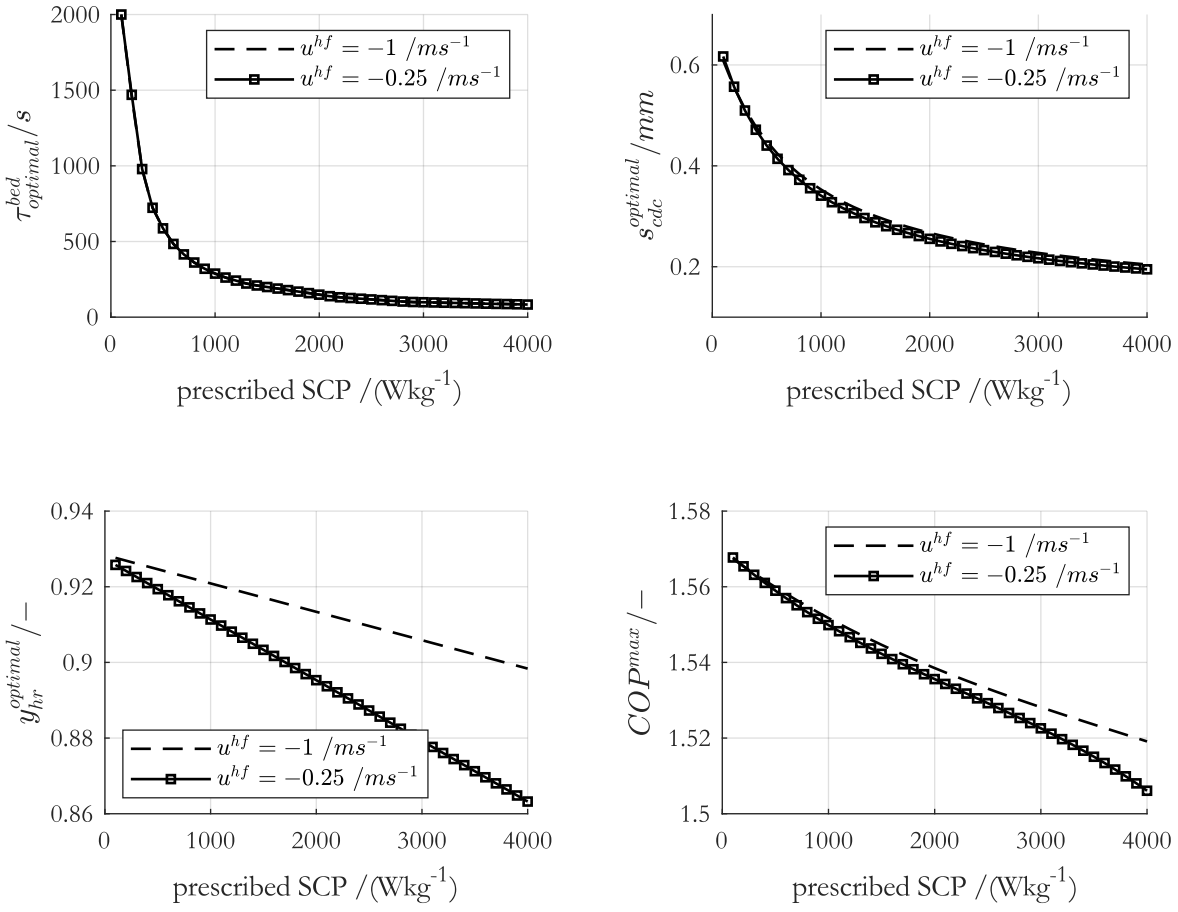

Figure 7-19: Maximal COP^{max} with corresponding optimal $\tau_{optimal}^{bed}$, $s_{cdc}^{optimal}$ and $y_{hr}^{optimal}$ as function of the prescribed SCP and heat transfer fluid velocity.

The thermodynamical optimal efficiency of 1.64 could not be fully achieved (see Appendix D.4), even for small, prescribed SCPs, which is mainly due to two reasons. One reason is the minimal driving temperature difference for the heat transfer, which was assumed to be ideal ($\Delta T = 0K$) in the thermodynamic analysis. The second reason is the number of discretization points in moving bed orientation (y), which is a critical parameter. Simulations with a lumped parameter model

(with no transport limitations) discretized with 200 grid points proved to reach the thermodynamic maximal efficiency. However, when using the distributed parameter model, the computational effort would be too high; hence, a compromise between accuracy and simulation effort has been chosen and a certain amount of numerical diffusion has been accepted.

Nevertheless, the novel multiple bed setup for adsorption refrigeration machines proved to achieve considerable efficiencies that are above 1.5, depending on the prescribed SCP. However, it should be noted that the temperature boundary conditions were chosen moderately. Especially at lower evaporator temperatures, considerable efficiency reductions can be observed using the thermodynamic analysis.

7.5 Summary

Processes that exhibit either transient or local temperature differences are suitable to apply heat integration. In the case of adsorption heat pumps, applying internal heat regeneration is challenging, on one side due to the transient occurrence of heat supply and heat demand and the other side due to the occurrence of latent heat contributions. Either an energetic buffer tank can be utilized, in which the heat is temporarily stored and released when required. Or multi-bed processes are used, which are operated time-shifted in the cycle, allowing heat exchange between individual beds.

In this chapter, the latter approach was investigated with a multi-bed process setup taking advantage of minimal driving temperature differences between individually coupled modules improving the efficiency of heat recovery. A novel process setup has been introduced in which the total amount of adsorbent is evenly distributed among a high number of individual adsorbers which themselves are evenly distributed with time in the thermodynamic adsorption cycle. The strategy of coupling two individual adsorbers was dedicated to reducing the driving temperature differences for heat transfer. With that setup, in addition to sensible heat, a large amount of latent heat of adsorption could be recovered and used to heat and regenerate other adsorbers. The number of adsorbers contributing to internal heat regeneration is a degree of freedom to be optimized to identify the optimal process setup. Besides, cycle time, as well as adsorbent composite layer thickness, are crucial process and material-related parameters to be investigated. With an increasing number of adsorbers, the computational costs increase significantly which makes direct simulations of the individual adsorber beds with spatially distributed material models challenging. Therefore, the limit case of infinite adsorber modules was investigated using a steady-state True-Moving-Bed approach. By that, the computational cost could be dramatically reduced which made a combined process and material investigation feasible.

The heat integrated setup provides an enormous benefit concerning the process efficiency. In the parameter and temperature space regarded, the COP could be more than doubled with values of above 1.5. Since the heat required to heat all sensible masses is equivalently provided by cooling the sensible masses (assuming temperature-independent heat capacities), a significant contribution of these results can be dedicated to the regeneration of latent heat. As matter of fact, this is the main benefit of the novel process setup. Beyond that, due to the neglectable contributions of the sensible heat, the post-processing revealed optimal layer thicknesses which are only one/tenth of the optimum thicknesses obtained for the 2-bed setup in chapter 5. Since the passive masses thus no longer have any disadvantageous influence on the process efficiency, layers with minimum transport resistance are preferred. At this point, however, it must be pointed out that the low optimum layer thicknesses entail a considerable disadvantage. To obtain an adequate system cooling power, very large areas of the heat exchanger are required on which the thin adsorbent layers can be applied, which entails a considerable amount of equipment. Thus, the layer thickness should not be chosen too low to achieve a decent absolute cooling power.

In summary, a significant increase in process performance is achievable using multi-bed processes, especially if a large amount of latent heat is recovered in addition to sensible heat. It can even be stated that clever heat integration represents the greatest lever for optimizing process efficiency under the boundary conditions considered in this work.

8. Conclusion and Outlook

8.1 Summary

In this work, methods are developed and presented to enhance the efficiency of adsorption heat pumps by focusing on the identification of a combined optimum of material and process. Simultaneous investigation and optimization of material and process design are very promising to improve the overall process performance of adsorption chillers. Two main approaches have been identified in this thesis. On the one hand side, 3D-structuring of adsorbent composites to reduced heat and mass transfer resistance, which leads to thicker adsorbent layers and beneficial ratios of active to passive mass. On the other hand, the use of efficient heat integration strategies has proven to be an even greater lever for increasing process efficiency, which was investigated using a multi-bed process setup.

To describe consolidated adsorbent composites consisting of adsorbent primary particles and heat-conducting additives, effective material models are initially presented. The different material models are developed aiming to either describe materials with non-percolating phases, where the heat additive is statistically added to the composites. Or to describe structured composites with percolating phases of primary particles and heat additives. The material models are parameterized with experiments. Therefore, adsorbent composites with different compositions were experimentally characterized for adsorption capacity, permeability, thermal conductivity, and structural parameters to identify composition-property correlations. While methanol adsorption capacity linearly increases with the volumetric fraction of adsorbent, and the permeability increases with larger void spaces, the thermal conductivity is only slightly improved by statistically adding heat additives to the composites. However, theoretical investigations showed that as soon as the heat-conducting phase percolates, the thermal conductivity of the composites increases abruptly, thus structured adsorbents are advantageous.

Aiming to describe the transport hindrance via the height of the composites, a one-dimensionally distributed parameter model is used with which the optimization of composite layer thickness and composition is feasible. This distributed parameter model is inserted in mathematical process models to describe the transient behaviour of adsorption refrigerators. The physical behaviour investigated in experiments in a small-scale adsorption chiller can be reproduced very well with simulations carried out with the distributed process model.

For the combined material and process optimization of a 2-bed adsorption chiller, process simulations with the validated mathematical process model were conducted. In a first step, material parameters of experimentally characterized adsorbent composites without and with statistically added heat conducting additives are investigated in the dynamic process simulations. On the material side, the composites layer thickness, and on the process side the cycle time were varied in wide parameter space. The simulations revealed a Pareto-optimality of process efficiency (COP) and power density (SCP) and thus, a cost function is used to identify the parameter set which optimizes the process efficiency for a prescribed power density. Thick layers of adsorbent and long cycle times are beneficial for the process efficiency, however, to the cost of low SCPs. If high power densities are required, the process should rather be operated with short cycle times and thin layers of composites should be used. In addition, the simulations revealed that statistically adding heat additive to the adsorbent composites does not add value to the process efficiency. Therefore, it can be stated that the slight increase in thermal conductivity due to the statistical addition of a heat additive does not overcompensate for the associated reduction in adsorption capacity. However, the thermal conductivity of the adsorbent composites could be strongly increased by using a percolating heat additive phase. The simulations revealed that percolation of the heat additive is beneficial for the overall process efficiency if the heat transport in the composites is limiting the process efficiency. With increasing thermal conductivity, however, the mass transport becomes the main limitation requiring enhancement of the permeability and therefore optimization of the composites structure.

3D-structuring of adsorbents could be identified as a possibility to improve solid sorption heat pumps. This effect could rather be increased when optimizing the percolating structures for which triangular prism-shaped heat-conducting ribs are applied. In addition, the mass transport is increased by using macroscopical mass transport channels with inverted triangular prism shape laterally staggered to the ribs. The optimal ribs and channels sizes, as well as layer thickness in dependence of the process conditions, were determined in simulations of the 2-bed adsorption chiller. Subsequently, the adsorbent composites with the promising structure were experimentally produced and investigated in a small-scale adsorption chiller underlining the simulation results. Therefore, 3D-structuring of adsorbent composites is a very promising approach to increase the process efficiency of adsorption chillers.

Besides structuring, the thermal swing adsorption refrigeration process offers a great potential for internal heat integration, which is another promising approach to increase the process efficiency. To exploit a high grade of heat regeneration potential, a novel multi-bed setup has been developed. The multi-bed setup is investigated with a Simulated-Moving-Bed approach

containing multiple adsorber beds where the adsorbent is equally distributed in the individual adsorbers which themselves are equally distributed with time in the thermodynamic cycle. To reduce the simulation costs, the Simulated-Moving-bed is approximated with the steady-state True-Moving-Bed approach. The novel setup allows for heat recovery between adsorbers with minimal temperature difference and recovery of sensible as well as latent heat. The great effect of efficient heat recovery is due to the sensible and latent heat lost during the temperature change between desorption and adsorption, which is the largest loss of the process. Thus, reducing this source of loss represents the greatest lever for increasing efficiency. Especially the partial recovery of latent heat of adsorption allows for a great improvement of process efficiency.

8.2 Outlook

The methods presented in this work can be used as guidelines and suggestions for the further optimization of adsorption heat pumps to help gain the competitiveness of this technology. The presented methods can be transferred to other process setups and structured materials whereby even more degrees of freedom can be utilized. For the comparison of different setups and structural designs, the global design diagrams provide a quick indication of the quality of the respective design. Especially in the course of digitalization of material manufacturing, with 3D printing and additive manufacturing, the targeted structuring of materials is promising to become a game-changer for the optimization of process engineering processes.

I. Literature

[1] H. S. Laine, J. Salpakari, E. E. Looney, H. Savin, I. M. Peters, and T. Buonassisi, "Meeting global cooling demand with photovoltaics during the 21st century," *Energy Environ. Sci.*, vol. 12, no. 9, pp. 2706–2716, 2019.

[2] International Energy Agency (IEA), "The Future of Cooling Opportunities for energy-efficient air conditioning," 2018.

[3] International Energy Agency (IEA), "World Energy Outlook 2019," 2019.

[4] Y. I. Aristov, "Adsorptive transformation and storage of renewable heat: Review of current trends in adsorption dynamics," *Renew. Energy*, vol. 110, pp. 105–114, Sep. 2017.

[5] A. Kühn, "Thermally Driven Heat Pumps for Heating and Cooling," 2013.

[6] M. Joemann, "Evaluierung der Wettbewerbssituation solarthermischer und solarelektrischer Kühlsysteme hinsichtlich technischer , energetischer und ökonomischer Aspekte," Ruhr-Universität Bochum, 2015.

[7] H. Z. Hassan, "Energy Analysis and Performance Evaluation of the Adsorption Refrigeration System," *ISRN Mech. Eng.*, vol. 2013, pp. 1–14, Jan. 2013.

[8] S. Maeda, K. Thu, T. Maruyama, and T. Miyazaki, "Critical Review on the Developments and Future Aspects of Adsorption Heat Pumps for Automobile Air Conditioning," *Appl. Sci.*, vol. 8, no. 11, p. 2061, Oct. 2018.

[9] B. Dawoud, M. I. Sohel, A. Freni, S. Vasta, and G. Restuccia, "On the effective thermal conductivity of wetted zeolite under the working conditions of an adsorption chiller," *Appl. Therm. Eng.*, vol. 31, no. 14–15, pp. 2241–2246, 2011.

[10] S. K. Henninger *et al.*, "New materials for adsorption heat transformation and storage," *Renew. Energy*, vol. 110, pp. 59–68, Sep. 2017.

[11] H. T. Chua, K. C. Ng, W. Wang, C. Yap, and X. L. Wang, "Transient modeling of a two-bed silica gel-water adsorption chiller," *Int. J. Heat Mass Transf.*, vol. 47, no. 4, pp. 659–669, 2004.

[12] A. Freni, G. Maggio, F. Cipitì, and Y. I. Aristov, "Simulation of water sorption dynamics in adsorption chillers: One, two and four layers of loose silica grains," *Appl. Therm. Eng.*, vol. 44, pp. 69–77, 2012.

[13] A. Rezk, R. K. Al-Dadah, S. Mahmoud, and A. Elsayed, "Effects of contact resistance and metal additives in finned-tube adsorbent beds on the performance of silica gel/water adsorption chiller," *Appl. Therm. Eng.*, vol. 53, no. 2, pp. 278–284, 2013.

[14] A. Sharafian and M. Bahrami, "Assessment of adsorber bed designs in waste-heat driven adsorption cooling systems for vehicle air conditioning and refrigeration," *Renew. Sustain. Energy Rev.*, vol. 30, pp. 440–451, 2014.

[15] A. Sharafian, K. Fayazmanesh, C. McCague, and M. Bahrami, "Thermal conductivity and contact resistance of mesoporous silica gel adsorbents bound with polyvinylpyrrolidone in contact with a metallic substrate for adsorption cooling system applications," *Int. J. Heat*

Mass Transf., vol. 79, pp. 64–71, 2014.

[16] J. Ammann, P. Ruch, B. Michel, and A. R. Studart, "Quantification of heat and mass transport limitations in adsorption heat exchangers: Application to the silica gel/water working pair," *Int. J. Heat Mass Transf.*, vol. 123, pp. 331–341, 2018.

[17] E. E. Anyanwu and C. I. Ezekwe, "Design, construction and test run of a solid adsorption solar refrigerator using activated carbon/methanol, as adsorbent/adsorbate pair," *Energy Convers. Manag.*, vol. 44, no. 18, pp. 2879–2892, 2003.

[18] L. W. Wang, R. Z. Wang, and R. G. Oliveira, "A review on adsorption working pairs for refrigeration," *Renew. Sustain. Energy Rev.*, vol. 13, no. 3, pp. 518–534, Apr. 2009.

[19] L. W. Wang, Z. Tamainot-Telto, R. Thorpe, R. E. Critoph, S. J. Metcalf, and R. Z. Wang, "Study of thermal conductivity, permeability, and adsorption performance of consolidated composite activated carbon adsorbent for refrigeration," *Renew. Energy*, vol. 36, no. 8, pp. 2062–2066, Aug. 2011.

[20] S. K. Henninger, M. Schicktanz, P. P. C. Hügenell, H. Sievers, and H. M. Henning, "Evaluation of methanol adsorption on activated carbons for thermally driven chillers part I: Thermophysical characterisation," *Int. J. Refrig.*, vol. 35, no. 3, pp. 543–553, 2012.

[21] L. Gordeeva and Y. Aristov, "Dynamic study of methanol adsorption on activated carbon ACM-35.4 for enhancing the specific cooling power of adsorptive chillers," *Appl. Energy*, vol. 117, pp. 127–133, Mar. 2014.

[22] J. W. Wu, S. H. Madani, M. J. Biggs, P. Phillip, C. Lei, and E. J. Hu, "Characterizations of Activated Carbon-Methanol Adsorption Pair Including the Heat of Adsorptions," *J. Chem. Eng. Data*, vol. 60, no. 6, pp. 1727–1731, 2015.

[23] S. K. Henninger, F. Jeremias, H. Kummer, and C. Janiak, "MOFs for use in adsorption heat pump processes," *Eur. J. Inorg. Chem.*, no. 16, pp. 2625–2634, 2012.

[24] Y. I. Aristov, "Challenging offers of material science for adsorption heat transformation: A review," in *Applied Thermal Engineering*, 2013, vol. 50, no. 2, pp. 1610–1618.

[25] F. Meunier, "Adsorption heat powered heat pumps," *Appl. Therm. Eng.*, vol. 61, no. 2, pp. 830–836, Nov. 2013.

[26] Y. I. Aristov, "Concept of adsorbent optimal for adsorptive cooling/heating," *Appl. Therm. Eng.*, vol. 72, no. 2, pp. 166–175, Nov. 2014.

[27] I. S. Girnik, A. D. Grekova, L. G. Gordeeva, and Y. I. Aristov, "Dynamic optimization of adsorptive chillers: Compact layer vs. bed of loose grains," *Appl. Therm. Eng.*, vol. 125, pp. 823–829, 2017.

[28] G. Cacciola, G. Restuccia, and L. Mercadante, "Composites of activated carbon for refrigeration adsorption machines," *Carbon N. Y.*, vol. 33, no. 9, pp. 1205–1210, 1995.

[29] U. Wittstadt, G. Füldner, O. Andersen, R. Herrmann, and F. Schmidt, "A new adsorbent composite material based on metal fiber technology and its application in adsorption heat exchangers," *Energies*, vol. 8, no. 8, pp. 8431–8446, 2015.

[30] L. W. Wang, S. J. Metcalf, R. E. Critoph, R. Thorpe, and Z. Tamainot-Telto, "Thermal conductivity and permeability of consolidated expanded natural graphite treated with sulphuric acid," *Carbon N. Y.*, vol. 49, no. 14, pp. 4812–4819, 2011.

[31] I. I. El-Sharkawy, A. Pal, T. Miyazaki, B. B. Saha, and S. Koyama, "A study on consolidated composite adsorbents for cooling application," *Appl. Therm. Eng.*, vol. 98, pp. 1214–1220, Apr. 2016.

[32] K. Fayazmanesh, C. McCague, and M. Bahrami, "Consolidated adsorbent containing graphite flakes for heat-driven water sorption cooling systems," *Appl. Therm. Eng.*, vol. 123, pp. 753–760, Aug. 2017.

[33] A. Caprì, A. Frazzica, and L. Calabrese, "Recent developments in coating technologies for adsorption heat pumps: A review," *Coatings*, vol. 10, no. 9, pp. 1–24, 2020.

[34] L. Träger, J. Gläsel, M. Scherle, J. Hartmann, U. Nieken, and B. J. M. M. Etzold, "Carbon-Methanol Based Adsorption Heat Pumps: Identifying Accessible Parameter Space with Carbide-Derived Carbon Model Materials," *Chem. Eng. Technol.*, vol. 43, no. 9, pp. 1876–1883, Sep. 2020.

[35] K. Ahmed Rocky, A. Pal, T. Hasan Rupam, M. L. Palash, and B. Baran Saha, "Recent advances of composite adsorbents for heat transformation applications," *Therm. Sci. Eng. Prog.*, p. 100900, Feb. 2021.

[36] F. Akhtar, L. Andersson, S. Ogunwumi, N. Hedin, and L. Bergström, "Structuring adsorbents and catalysts by processing of porous powders," *J. Eur. Ceram. Soc.*, vol. 34, no. 7, pp. 1643–1666, 2014.

[37] H. Steldinger, A. Esposito, K. Brunnengräber, J. Gläsel, and B. J. M. Etzold, "3D Printing: Activated Carbon in the Third Dimension—3D Printing of a Tuned Porous Carbon (Adv. Sci. 19/2019)," *Adv. Sci.*, vol. 6, no. 19, p. 1970114, Oct. 2019.

[38] M. J. Regufe, A. F. P. Ferreira, J. M. Loureiro, A. Rodrigues, and A. M. Ribeiro, "Electrical conductive 3D-printed monolith adsorbent for CO2 capture," *Microporous Mesoporous Mater.*, vol. 278, pp. 403–413, Apr. 2019.

[39] H. Steldinger, "3D Printing of Activated Carbon and Exemplary Application as Adsorbent in the Electric Swing Adsorption," 2020.

[40] T. F. Qu, R. Z. Wang, and W. Wang, "Study on heat and mass recovery in adsorption refrigeration cycles," *Appl. Therm. Eng.*, vol. 21, no. 4, pp. 439–452, 2001.

[41] W. Wang, T. F. Qu, and R. Z. Wang, "Influence of degree of mass recovery and heat regeneration on adsorption refrigeration cycles," *Energy Convers. Manag.*, vol. 43, no. 5, pp. 733–741, 2002.

[42] W. Chekirou, N. Boukheit, and A. Karaali, "Heat recovery process in an adsorption refrigeration machine," *Int. J. Hydrogen Energy*, vol. 41, no. 17, pp. 7146–7157, May 2016.

[43] F. Meunier, "Second law analysis of a solid adsorption heat pump operating on reversible cascade cycles: Application to the Zeolite-water pair," *J. Heat Recover. Syst.*, vol. 5, no. 2, pp. 133–141, 1985.

[44] R. . Critoph, "Simulation of a continuous multiple-bed regenerative adsorption cycle," *Int. J. Refrig.*, vol. 24, no. 5, pp. 428–437, Aug. 2001.

[45] B. B. Saha, S. Koyama, T. Kashiwagi, A. Akisawa, K. C. Ng, and H. T. Chua, "Waste heat driven dual-mode, multi-stage, multi-bed regenerative adsorption system," *Int. J. Refrig.*, vol. 26, no. 7, pp. 749–757, 2003.

[46] F. Ziegler, "Sorption heat pumping technologies: Comparisons and challenges," *Int. J. Refrig.*, vol. 32, no. 4, pp. 566–576, Jun. 2009.

[47] D. M. Ruthven, "Fundamentals of Adsorption Equilibrium and Kinetics in Microporous Solids," in *Adsorption and Diffusion*, vol. 7, no. January 2006, Berlin, Heidelberg: Springer Berlin Heidelberg, 2008, pp. 1–43.

[48] K. S. W. Sing, "Reporting physisorption data for gas/solid systems with special reference to the determination of surface area and porosity (Recommendations 1984)," *Pure Appl. Chem.*, vol. 57, no. 4, pp. 603–619, Jan. 1985.

[49] J. Rouquerol, F. Rouquerol, P. Llewellyn, G. Maurin, and K. Sing, *Adsorption by Powders and Porous Solids - Principles, Methodology and Applications*, 2nd ed. 2013.

[50] J. Rouquerol *et al.*, "Recommendations for the characterization of porous solids (Technical Report)," *Pure Appl. Chem.*, vol. 66, no. 8, pp. 1739–1758, Jan. 1994.

[51] P. A. Webb, "An Introduction To The Physical Characterization of Materials by Mercury Intrusion Porosimetry with Emphasis On Reduction And Presentation of Experimental Data," 2001.

[52] P. Webb, "Volume and Density Determinations for Particle Technologists," 2001.

[53] D. M. Ruthven, *Principles of Adsorption and Adsorption Processes*. 1984.

[54] W. Kast, *Adsorption aus der Gasphase: ingenieurwissenschaftliche Grundlagen und technische Verfahren*. 1988.

[55] D. D. Do, *Adsorption Analysis: Equilibria and Kinetics*, vol. 2, no. Imperial College Press. Imperial College Press, 1998.

[56] F. Lanzerath, "Modellgestützte Entwicklung von Adsorptionswärmepumpen," 2013.

[57] M. Thommes *et al.*, "Physisorption of gases, with special reference to the evaluation of surface area and pore size distribution (IUPAC Technical Report)," *Pure Appl. Chem.*, vol. 87, no. 9–10, pp. 1051–1069, Oct. 2015.

[58] S. Brunauer, L. S. Deming, W. E. Deming, and E. Teller, "On a Theory of the van der Waals Adsorption of Gases," *J. Am. Chem. Soc.*, vol. 62, no. 7, pp. 1723–1732, Jul. 1940.

[59] D. M. Ruthven, *Fundamentals of adsorption equilibrium and kinetics in microporous solids*, vol. 7, no. January 2006. 2008.

[60] I. Langmuir, "THE CONSTITUTION AND FUNDAMENTAL PROPERTIES OF SOLIDS AND LIQUIDS. PART I. SOLIDS.," *J. Am. Chem. Soc.*, vol. 38, no. 11, pp. 2221–2295, Nov. 1916.

[61] H.-J. Bart and U. von Gemmingen, "Adsorption," in *Ullmann's Encyclopedia of Industrial Chemistry*, Weinheim, Germany: Wiley-VCH Verlag GmbH & Co. KGaA, 2005, pp. 1–31.

[62] K. Sing, "The use of nitrogen adsorption for the characterisation of porous materials," *Colloids Surfaces A Physicochem. Eng. Asp.*, vol. 187–188, pp. 3–9, Aug. 2001.

[63] S. Brunauer, P. H. Emmett, and E. Teller, "Adsorption of Gases in Multimolecular Layers," *J. Am. Chem. Soc.*, vol. 60, no. 2, pp. 309–319, 1938.

[64] J. Moellmer *et al.*, "Insights on Adsorption Characterization of Metal-Organic

Frameworks: A Benchmark Study on the Novel soc-MOF," *Microporous Mesoporous Mater.*, vol. 129, no. 3, pp. 345–353, 2010.

[65] M. Thommes, "Physical adsorption characterization of nanoporous materials," *Chemie-Ingenieur-Technik*, vol. 82, no. 7, pp. 1059–1073, 2010.

[66] J. Rouquerol, P. Llewellyn, and F. Rouquerol, "Is the bet equation applicable to microporous adsorbents?," in *Characterization of Porous Solids VII*, vol. 160, 2007, pp. 49–56.

[67] M. Polanyi, "Section III.—Theories of the adsorption of gases. A general survey and some additional remarks. Introductory paper to section III," *Trans. Faraday Soc.*, vol. 28, pp. 316–333, 1932.

[68] A. M. M. Dubinin, "A study of the porous structure of active carbons using a variety of methods," *Q. Rev. Chem. Soc.*, vol. 9, no. 2, p. 101, 1955.

[69] J. S. Bae and D. D. Do, "On the equilibrium and dynamic behavior of alcohol vapors in activated carbon," *Chem. Eng. Sci.*, vol. 61, no. 19, pp. 6468–6477, 2006.

[70] S. K. Henninger, F. Jeremias, H. Kummer, P. Schossig, and H. M. Henning, "Novel sorption materials for solar heating and cooling," *Energy Procedia*, vol. 30, pp. 279–288, 2012.

[71] T. Núñez, "Charakterisierung und Bewertung von Adsorbentien für Wärmetransformationsanwendungen," Albert-Ludwigs-Universität Freiburg, 2001.

[72] M. M. Dubinin and V. A. Astakhov, "Development of concepts of the volume filling of micropores in the adsorption of gases and vapors by microporous adsorbents - Communication 1. Carbon adsorbents," *Bull. Acad. Sci. USSR Div. Chem. Sci.*, vol. 20, no. 1, pp. 17–22, 1971.

[73] K. Wang and D. D. Do, "Characterizing the micropore size distribution of activated carbon using equilibrium data of many adsorbates at various temperatures," *Langmuir*, vol. 13, no. 23, pp. 6226–6233, 1997.

[74] G. Füldner, "Stofftransport und Adsorptionskinetik in porösen Adsorbenskompositen für Wärmetransformationsanwendungen," Albert-Ludwigs-Universität Freiburg im Breisgau, 2015.

[75] I. Medveď and R. Černý, "Surface diffusion in porous media: A critical review," *Microporous Mesoporous Mater.*, vol. 142, no. 2–3, pp. 405–422, Jul. 2011.

[76] D. Bathen and M. Breitbach, *Adsorptionstechnik*. Springer-Verlag Berlin, Heidelberg, New York, 2001.

[77] E. A. Mason and A. P. Malinauskas, *Gas transport in porous media. Dusty-gas model*. Elsevier Science Ltd, 1983.

[78] D. Lasseux and F. J. Valdés-Parada, "On the developments of Darcy's law to include inertial and slip effects," *Comptes Rendus - Mec.*, vol. 345, no. 9, pp. 660–669, 2017.

[79] S. P. Neuman, "Theoretical derivation of Darcy's law," *Acta Mech.*, vol. 25, no. 3–4, pp. 153–170, 1977.

[80] S. Whitaker, "Flow in porous media I: A theoretical derivation of Darcy's law," *Transp. Porous Media*, vol. 1, no. 1, pp. 3–25, 1986.

[81] C. K. Ho and S. W. Webb, *Gas Transport in Porous Media*, vol. 20. Springer Netherlands, 2006.

[82] M. Agnaou, D. Lasseux, and A. Ahmadi, "Origin of the inertial deviation from Darcy's law: An investigation from a microscopic flow analysis on two-dimensional model structures," *Phys. Rev. E*, vol. 96, no. 4, p. 043105, Oct. 2017.

[83] R. Krishna and J. A. Wesselingh, "The Maxwell-Stefan approach to mass transfer," *Chem. Eng. Sci.*, vol. 52, no. 6, pp. 861–911, 1997.

[84] Y. Marcus, "The sizes of molecules-revisited," *J. Phys. Org. Chem.*, vol. 16, no. 7, pp. 398–408, Jul. 2003.

[85] D. Hänel, *Molekulare Gasdynamik*. Berlin/Heidelberg: Springer-Verlag, 2004.

[86] A. D. Kirk, "The range of validity of Graham's Laws," *J. Chem. Educ.*, vol. 44, no. 12, p. 745, Dec. 1967.

[87] O. Šolcová, H. Šnajdaufová, and P. Schneider, "Multicomponent counter-current gas diffusion in porous solids: the Graham's-law diffusion cell," *Chem. Eng. Sci.*, vol. 56, no. 17, pp. 5231–5237, Sep. 2001.

[88] K. Soukup, P. Schneider, and O. Šolcová, "Wicke–Kallenbach and Graham's diffusion cells: Limits of application for low surface area porous solids," *Chem. Eng. Sci.*, vol. 63, no. 18, pp. 4490–4493, Sep. 2008.

[89] H. D. Do, D. D. Do, and I. Prasetyo, "On the surface diffusion of hydrocarbons in microporous activated carbon," *Chem. Eng. Sci.*, vol. 56, no. 14, pp. 4351–4368, Jul. 2001.

[90] S. C. Reyes, J. H. Sinfelt, and G. J. DeMartin, "Diffusion in Porous Solids: The Parallel Contribution of Gas and Surface Diffusion Processes in Pores Extending from the Mesoporous Region into the Microporous Region," *J. Phys. Chem. B*, vol. 104, no. 24, pp. 5750–5761, Jun. 2000.

[91] C. Chmelik, L. Heinke, R. Valiullin, and J. Kärger, "A new view of diffusion in nanoporous materials," *Chemie-Ingenieur-Technik*, vol. 82, no. 6, pp. 779–804, 2010.

[92] A. Kapoor, R. T. Yang, and C. Wong, "Surface Diffusion," *Catal. Rev.*, vol. 31, no. 1–2, pp. 129–214, Feb. 1989.

[93] E. Glueckauf, "Theory of chromatography. Part 10.—Formulæ for diffusion into spheres and their application to chromatography," *Trans. Faraday Soc.*, vol. 51, no. 51, pp. 1540–1551, 1955.

[94] L. J. P. Van Den Broeke and R. Krishna, "Experimental verification of the Maxwell-Stefan theory for micropore diffusion," *Chem. Eng. Sci.*, vol. 50, no. 16, pp. 2507–2522, 1995.

[95] S. W. Hong, S. H. Ahn, O. K. Kwon, and J. D. Chung, "Validity of intra-particle models of mass transfer kinetics in the analysis of a fin-tube type adsorption bed," *J. Mech. Sci. Technol.*, vol. 28, no. 5, pp. 1985–1993, 2014.

[96] S. Sircar and J. R. Hufton, "Why does the linear driving force model for adsorption kinetics work?," *Adsorption*, vol. 6, no. 2, pp. 137–147, 2000.

[97] C. H. Liaw, J. S. P. Wang, R. A. Greenkorn, and K. C. Chao, "Kinetics of fixed-bed adsorption: A new solution," *AIChE J.*, vol. 25, no. 2, pp. 376–381, Mar. 1979.

[98] S. Sircar and J. R. Hufton, "Intraparticle adsorbate concentration profile for linear driving force model," *AIChE J.*, vol. 46, no. 3, pp. 659–660, Mar. 2000.

[99] E. A. Mason, A. P. Malinauskas, and R. B. Evans, "Flow and Diffusion of Gases in Porous Media," *J. Chem. Phys.*, vol. 46, no. 8, pp. 3199–3216, Apr. 1967.

[100] A. A. Askalany, S. K. Henninger, M. Ghazy, and B. B. Saha, "Effect of improving thermal conductivity of the adsorbent on performance of adsorption cooling system," *Appl. Therm. Eng.*, vol. 110, pp. 695–702, Jan. 2017.

[101] A. R. M. Rezk, "Theoretical and experimental investigation of silica gel / water adsorption refrigeration systems," University of Birmingham, 2012.

[102] R. B. Bird, W. E. Stewart, and E. N. Lightfoot, *Transport Phenomena*, Revised 2n. 2007.

[103] K. Pietrak and T. Wiśniewski, "A review of models for effective thermal conductivity of composite materials," *J. Power Technol.*, vol. 95, no. 1, pp. 14–24, 2015.

[104] J. Wang, J. K. Carson, M. F. North, and D. J. Cleland, "A new approach to modelling the effective thermal conductivity of heterogeneous materials," *Int. J. Heat Mass Transf.*, vol. 49, no. 17–18, pp. 3075–3083, 2006.

[105] A. I. I. Radu, T. Defraeye, P. Ruch, J. Carmeliet, and D. Derome, "Insights from modeling dynamics of water sorption in spherical particles for adsorption heat pumps," *Int. J. Heat Mass Transf.*, vol. 105, pp. 326–337, Feb. 2017.

[106] W. Woodside and J. H. Messmer, "Thermal Conductivity of Porous Media. I. Unconsolidated Sands," *J. Appl. Phys.*, vol. 32, no. 9, pp. 1688–1699, Sep. 1961.

[107] VDI, *VDI-Wärmeatlas*, no. 3. Berlin, Heidelberg: Springer Berlin Heidelberg, 2013.

[108] L. W. W. Wang, S. J. J. Metcalf, R. E. E. Critoph, R. Thorpe, and Z. Tamainot-Telto, "Development of thermal conductive consolidated activated carbon for adsorption refrigeration," *Carbon N. Y.*, vol. 50, no. 3, pp. 977–986, Mar. 2012.

[109] Z. Jin, B. Tian, L. Wang, and R. Wang, "Comparison on Thermal Conductivity and Permeability of Granular and Consolidated Activated Carbon for Refrigeration," *Chinese J. Chem. Eng.*, vol. 21, no. 6, pp. 676–682, Jun. 2013.

[110] A. M. Rivero-Pacho, R. E. Critoph, and S. J. Metcalf, "Alternative monolithic/composite carbons for adsorption generators and simulation for optimal performance," *Appl. Therm. Eng.*, vol. 126, pp. 350–357, 2017.

[111] P. L. Kapitza, "Heat Transfer and Superfluidity of Helium II," *Phys. Rev.*, vol. 60, no. 4, pp. 354–355, Aug. 1941.

[112] C. W. Nan, R. Birringer, D. R. Clarke, and H. Gleiter, "Effective thermal conductivity of particulate composites with interfacial thermal resistance," *J. Appl. Phys.*, vol. 81, no. 10, pp. 6692–6699, 1997.

[113] D. C. Venerus and H. C. Oettinger, *Modern Course in Transport Phenomena*. Cambridge University Press, 2018.

[114] A. Eucken, "Allgemeine Gesetzmäßigkeiten für das Wärmeleitvermögen verschiedener Stoffarten und Aggregatzustände," *Forsch. auf dem Gebiete des Ingenieurwesens*, vol. 11, no. 1, pp. 6–20, Jan. 1940.

[115] S. Kirkpatrick, "Percolation and Conduction," *Rev. Mod. Phys.*, vol. 45, no. 4, pp. 574–588, 1973.

[116] N. Hannoschöck, *Wärmeleitung und -transport*. Berlin, Heidelberg: Springer Berlin Heidelberg, 2018.

[117] A. Pesaran, H. Lee, Y. Hwang, R. Radermacher, and H.-H. H. Chun, "Review article: Numerical simulation of adsorption heat pumps," *Energy*, vol. 100, pp. 310–320, Apr. 2016.

[118] V. Schwamberger, C. Glück, and F. P. Schmidt, "Modeling and transient analysis of a novel adsorption cycle concept for solar cooling," *30th ISES Bienn. Sol. World Congr. 2011, SWC 2011*, vol. 4, no. January, pp. 2919–2927, 2011.

[119] V. Schwamberger, A. Desai, and F. P. Schmidt, "Novel Adsorption Cycle for High-Efficiency Adsorption Heat Pumps and Chillers: Modeling and Simulation Results," *Energies*, vol. 13, no. 1, p. 19, Dec. 2019.

[120] V. Schwamberger, "Thermodynamische und numerische Untersuchung eines neuartigen Sorptionszyklus zur Anwendung in Adsorptionswärmepumpen und -kältemaschinen," 2016.

[121] P. V. Danckwerts, "Continuous flow systems. Distribution of residence times," *Chem. Eng. Sci.*, vol. 2, no. 1, pp. 1–13, Dec. 1953.

[122] Z. JIN, B. TIAN, L. WANG, and R. WANG, "Comparison on Thermal Conductivity and Permeability of Granular and Consolidated Activated Carbon for Refrigeration," *Chinese J. Chem. Eng.*, vol. 21, no. 6, pp. 676–682, Jun. 2013.

[123] A. Pal, K. Uddin, K. Thu, and B. B. Saha, "Activated carbon and graphene nanoplatelets based novel composite for performance enhancement of adsorption cooling cycle," *Energy Convers. Manag.*, vol. 180, no. August 2018, pp. 134–148, 2019.

[124] L. Träger, "Untersuchung des zugänglichen Parameter- raumes für geformte Adsorbentien in der Anwendung der Adsorptionskältemaschine am Beispiel karbidabgeleiteter Kohlenstoffe," Friedrich-Alexander-UniversitätErlangen-Nürnberg, 2020.

[125] P. Becker, F. Glenk, M. Kormann, N. Popovska, and B. J. M. Etzold, "Chlorination of titanium carbide for the processing of nanoporous carbon: A kinetic study," *Chem. Eng. J.*, vol. 159, no. 1–3, pp. 236–241, 2010.

[126] K. A. Cychosz and M. Thommes, "Progress in the Physisorption Characterization of Nanoporous Gas Storage Materials," *Engineering*, vol. 4, no. 4, pp. 559–566, Aug. 2018.

[127] D. Ongari, P. G. Boyd, S. Barthel, M. Witman, M. Haranczyk, and B. Smit, "Accurate Characterization of the Pore Volume in Microporous Crystalline Materials," *Langmuir*, vol. 33, no. 51, pp. 14529–14538, Dec. 2017.

[128] J. Landers, G. Y. Gor, and A. V. Neimark, "Density functional theory methods for characterization of porous materials," *Colloids Surfaces A Physicochem. Eng. Asp.*, vol. 437, pp. 3–32, 2013.

[129] M. Helmich, M. Luckas, C. Pasel, and D. Bathen, "Characterization of microporous activated carbons using molecular probe method," *Carbon N. Y.*, vol. 74, pp. 22–31, Aug. 2014.

[130] C. Bläker, J. Muthmann, C. Pasel, and D. Bathen, "Characterization of Activated Carbon Adsorbents – State of the Art and Novel Approaches," *ChemBioEng Rev.*, vol. 6, no. 4, pp. 119–138, 2019.

[131] J. A. Mason, M. Veenstra, and J. R. Long, "Evaluating metal–organic frameworks for natural gas storage," *Chem. Sci.*, vol. 5, no. 1, pp. 32–51, 2014.

[132] C. Nguyen and D. D. Do, "The Dubinin-Radushkevich equation and the underlying microscopic adsorption description," *Carbon N. Y.*, vol. 39, no. 9, pp. 1327–1336, 2001.

[133] E. W. Washburn, "Note on a Method of Determining the Distribution of Pore Sizes in a Porous Material," *Proc. Natl. Acad. Sci.*, vol. 7, no. 4, pp. 115–116, Apr. 1921.

[134] Accuratus - Ceramic Corporation, "Boron Nitride Engineering Properties." [Online]. Available: https://www.accuratus.com/boron.html. [Accessed: 26-Feb-2020].

[135] A. Gorbach, M. Stegmaier, and G. Eigenberger, "Measurement and Modeling of Water Vapor Adsorption on Zeolite 4A—Equilibria and Kinetics," *Adsorption*, vol. 10, no. 1, pp. 29–46, 2004.

[136] A. Perera, F. Sokolić, and L. Zoranić, "Microstructure of neat alcohols," *Phys. Rev. E - Stat. Nonlinear, Soft Matter Phys.*, vol. 75, no. 6, pp. 1–4, 2007.

[137] W. J. Parker, R. J. Jenkins, C. P. Butler, and G. L. Abbott, "Flash Method of Determining Thermal Diffusivity, Heat Capacity, and Thermal Conductivity," *J. Appl. Phys.*, vol. 32, no. 9, pp. 1679–1684, Sep. 1961.

[138] E. S. Watson and M. J. O'Neill, "US Patent 3,263,484 differential microcalorimeter," 1962.

[139] M. Scherle and U. Nieken, "Simultaneous Optimization of Process Operational and Material Parameters for a 2-Bed Adsorption Refrigeration Process," *ChemEngineering*, vol. 4, no. 2, p. 31, 2020.

[140] M. Pons and Y. Feng, "Characteristic parameters of adsorptive refrigeration cycles with thermal regeneration," *Appl. Therm. Eng.*, vol. 17, no. 3, pp. 289–298, Mar. 1997.

[141] J. Ammann, B. Michel, A. R. Studart, and P. W. Ruch, "Sorption rate enhancement in SAPO-34 zeolite by directed mass transfer channels," *Int. J. Heat Mass Transf.*, vol. 130, pp. 25–32, 2019.

[142] M. Scherle and U. Nieken, "Simulative Untersuchung strukturierter Adsorbens-Komposite für die adsorptive Kühlung," *KI - Kälte, Luft, Klimatechnik*, pp. 50–55, 2021.

[143] M. Scherle, T. A. Nowak, S. Welzel, B. J. M. Etzold, and U. Nieken, "Experimental study of 3D – structured adsorbent composites with improved heat and mass transfer for adsorption heat pumps," *Chem. Eng. J.*, vol. 431, no. November, p. 133365, Mar. 2022.

[144] M. Scherle, J. Liedtke, and U. Nieken, "Optimal sequencing and adsorbent design of multi-bed adsorption chillers," *Appl. Therm. Eng.*, vol. 200, no. March 2021, p. 117689, Jan. 2022.

[145] M. Pons, "Analysis of the adsorption cycles with thermal regeneration based on the entropic mean temperatures," *Appl. Therm. Eng.*, vol. 17, no. 7, pp. 615–627, 1997.

[146] T. F. Qu, R. Z. Wang, and W. Wang, "Study on heat and mass recovery in adsorption refrigeration cycles," *Appl. Therm. Eng.*, vol. 21, no. 4, pp. 439–452, 2001.

[147] M. Pons, "Global analysis of refrigerative adsorption cycles with thermal regeneration (non-uniform temperature)," *Int. J. Refrig.*, vol. 20, no. 6, pp. 411–420, Jan. 1997.

[148] M. Pons, "Second Law Analysis of Adsorption Cycles With Thermal Regeneration," *J. Energy Resour. Technol.*, vol. 118, no. 3, pp. 229–236, Sep. 1996.

[149] T. Aida and P. L. Silveston, *Cyclic Separating Reactors*. Oxford, UK: Blackwell Publishing Ltd, 2005.

[150] F. Lode, M. Mazzotti, and M. Morbidelli, "Comparing true countercurrent and simulated moving-bed chromatographic reactors," *AIChE J.*, vol. 49, no. 4, pp. 977–990, 2003.

[151] V. M. Zahn, M. Mangold, M. Krasnyk, and A. Seidel-Morgenstern, "Theoretical analysis of heat integration in a periodically operated cascade of catalytic fixed-bed reactors," *Chem. Eng. Technol.*, vol. 32, no. 9, pp. 1326–1338, 2009.

[152] P. Günther, P. Kunz, R. Stierle, G. Eigenberger, and U. Nieken, "Prozesssimulation einer Adsorptionskältemaschine: True-Moving-Bed-Approximation," *Chemie Ing. Tech.*, vol. 86, no. 1-2, pp. 112–118, Feb. 2014.

[153] V. Schwamberger, "Thermodynamische und numerische Untersuchung eines neuartigen Sorptionszyklus zur Anwendung in Adsorptionswärmepumpen und -kältemaschinen," Karlsruher Institut für Technologie (KIT), 2016.

[154] V. Schwamberger, A. Desai, and F. P. Schmidt, "Novel adsorption cycle for high-efficiency adsorption heat pumps and chillers: Modeling and simulation results," *Energies*, vol. 13, no. 1, 2019.

[155] D. C. Wang, Y. H. Li, D. Li, Y. Z. Xia, and J. P. Zhang, "A review on adsorption refrigeration technology and adsorption deterioration in physical adsorption systems," *Renew. Sustain. Energy Rev.*, vol. 14, no. 1, pp. 344–353, Jan. 2010.

[156] R. E. Critoph, "Multiple bed regenerative adsorption cycle using the monolithic carbon–ammonia pair," *Appl. Therm. Eng.*, vol. 22, no. 6, pp. 667–677, Apr. 2002.

[157] V. M. Zahn, C. U. Yi, and A. Seidel-Morgenstern, "Analysis and demonstration of a control concept for a heat integrated simulated moving bed reactor," *Chem. Eng. Sci.*, vol. 66, no. 20, pp. 4901–4912, 2011.

[158] K. Wu, X. Li, C. Wang, W. Yu, and Z. Chen, "Model for surface diffusion of adsorbed gas in nanopores of shale gas reservoirs," *Ind. Eng. Chem. Res.*, vol. 54, no. 12, pp. 3225–3236, 2015.

[159] P. Pršlja, E. Lomba, P. Gómez-Álvarez, T. Urbič, and E. G. Noya, "Adsorption of water, methanol, and their mixtures in slit graphite pores," *J. Chem. Phys.*, vol. 150, no. 2, 2019.

[160] V. Eyberg, "Experimentelle Charakterisierung des Stofftransports von nicht adsorbierbaren Gasen durch poröse Materialien durch Einkomponentenpermeationsversuche an einer Diffusionszelle," 2019.

[161] MATLAB, *9.9.0.1467703 (R2020b)*, 2020b ed. Natick, Massachusetts: The MathWorks Inc., 2020.

[162] R. Eymard, T. Gallouët, and R. Herbin, "Finite volume methods," in *Computing*, vol. VII, no. Part 3, 2000, pp. 713–1018.

[163] Y. Yang, M. Li, S. Shu, and A. Xiao, "High order schemes based on upwind schemes with modified coefficients," *J. Comput. Appl. Math.*, vol. 195, no. 1–2, pp. 242–251, 2006.

[164] M. Krasnyk, "DIANA - An object oriented tool for nonlinear analysis of chemical processes.," Otto-von-Guericke-Universität Magdeburg, 2008.

[165] P. Deuflhard and A. Hohmann, *Numerische Mathematik 1*. De Gruyter, 2018.

[166] M. Mangold, D. Khlopov, G. Danker, S. Palis, V. Svjatnyj, and A. Kienle, "Development and Nonlinear Analysis of Dynamic Plant Models in ProMoT /Diana," *Chemie Ing. Tech.*, vol. 86, no. 7, pp. 1107–1116, Jul. 2014.

[167] M. Krasnyk, K. Bondareva, O. Milokhov, and K. Teplinskiy, "The ProMoT / Diana Simulation Environment," *16th European Symposium on Computer Aided Process Engineering and 9th International Symposium on Process Systems Engineering*. pp. 445–450, 2006.

[168] A. C. Hindmarsh *et al.*, "Sundials," *ACM Trans. Math. Softw.*, vol. 31, no. 3, pp. 363–396, 2005.

[169] A. Acrivos, "Method of Characteristics Technique. Application to Heat and Mass Transfer Problems," *Ind. Eng. Chem.*, vol. 48, no. 4, pp. 703–710, Apr. 1956.

Appendix A.

A.1 Derivation of the Linear-Driving Force approach

The classical LDF approach introduced by Glueckauf [93] can formally be derived by balancing the moles in the pores of a spherical adsorbent particle with a radius R_{par} with the adsorptive concentration c^v and adsorbate concentration c^{ad} [97], [98]

$$\nabla \cdot \dot{n}^{mi} = -\frac{\partial (c^v + c^{ad})}{\partial t}. \tag{A-1}$$

The total intraparticle flux is generally expressed using the gradients of the chemical potential in adsorptive (μ^v) and adsorbate (μ^{ad}), respectively, [90]

$$\dot{n}^{mi} = -\frac{B^v}{N_A} c^v \nabla \mu^v - \frac{B^S}{N_A} c^{ad} \nabla \mu^{ad}. \tag{A-2}$$

with the mobilities B^v and B^S defined as diffusion velocity per unit force and with Avogadro's number N_A. Adsorption and desorption of molecules is fast compared to transport in the gas or adsorbate phase, which is why the assumption of local thermodynamic equilibrium is satisfied ($\mu^v = \mu^{ad}$). With the chemical potential of an ideal adsorptive (gas)

$$\mu^v = \mu_0 + RTln(c^v k_B T) = \mu_0 + RTln(p^v), \tag{A-3}$$

and with the Boltzmann constant $k_B = R/N_A$, the mobilities can be expressed in terms of the diffusion coefficients in gas and adsorbed phase, respectively

$$D^v = B^v k_B T, \tag{A-4}$$

$$D_0^S = B^S k_B T. \tag{A-5}$$

D_0^S denotes the surface diffusivity at zero loadings as introduced in section 2.2.3. Assuming local thermodynamic equilibrium and substituting equations (A-3)-(A-5) into (A-2), the total intraparticle flux can be reformulated

$$\dot{n}^{mi} = -\left(D^v + D_0^S \frac{c^{ad}}{c^v} \right) \nabla c^v. \tag{A-6}$$

Equation (A-6) can be used if the gradient in the adsorptive concentration is known. Alternatively, the flux can be formulated with the gradient in adsorbate concentration using the total derivative (assuming local isothermal conditions)

$$\nabla c^{ad} = \left(\frac{\partial c^{ad}}{\partial c^{v}}\right)_{T} \nabla c^{v}. \tag{A-7}$$

The partial derivative describes the gas concentration or pressure dependency of the adsorption isotherm. Substituting equation (A-7) into (A-6) yields

$$\dot{n}^{mi} = -\left(\frac{D^{v}}{\left(\frac{\partial c^{ad}}{\partial c^{v}}\right)_{T}} + D_0^{S} \underbrace{\frac{c^{ad}/c^{v}}{\left(\frac{\partial c^{ad}}{\partial c^{v}}\right)_{T}}}_{Darken-factor} \right) \nabla c^{ad}, \tag{A-8}$$

with the Darken-factor as introduced in equation (2-44) and D_0^S the surface diffusivity at zero loading [75]. (Note: Depending on the desired driving force, the flux can be described using either equation (A-6) or (A-8), taking care to use the appropriate formulations for the diffusion coefficients deviating by the factor $1/(\partial c^{ad}/\partial c^{v})_{T}$). With the loading $X = c^{ad}(MW\varepsilon_{par}/\varrho_{par})$ instead of the adsorbate concentration, the flux in the formulation of equation (A-8) is given by

$$\dot{n}^{mi} = -\frac{1}{\varepsilon_{par}}\left(\widetilde{D}^{mi}\right)\nabla X, \tag{A-9}$$

with the intraparticle or micropore diffusion coefficient

$$\widetilde{D}^{mi} = \frac{D^{v}\varepsilon_{par} + D_0^{S}\frac{X}{c^{v}}\frac{\varrho_{par}}{MW}}{\left(\frac{\partial X}{\partial c^{v}}\right)_{T}}, \tag{A-10}$$

which contains adsorptive and surface diffusivity. ε_{par}, ϱ_{par} are the porosity and apparent density of the primary particle, and MW the molar mass of the adsorptive. The corrected surface diffusivity in terms of loading X is given by (compare equation (2-44))

$$\widetilde{D}^{S} = \frac{D_0^{S}\frac{X}{c^{v}}\frac{\varrho_{par}}{MW}}{\left(\frac{\partial X}{\partial c^{v}}\right)_{T}}. \tag{A-11}$$

With $\dot{n}_{par} = \varepsilon_{par}\dot{n}^{mi}$ and with loading X, the mole balance (equation (2-46)) can be formulated related to particle volume in mol/m^3_{par}

$$\nabla \cdot \dot{n}_{par} = -\frac{\partial\left(\varepsilon_{par}c^{v} + \varrho_{par}X/MW\right)}{\partial t}. \tag{A-12}$$

With the divergence in spherical coordinates ($\nabla \cdot \dot{n}_{par} = \frac{1}{\xi^2}\frac{\partial}{\partial \xi}\left(\xi^2\dot{n}_{par,\xi}\right)+\ldots$) and reduction to the redial particle coordinate ξ due to symmetry, equation (A-12) is reformulated to

$$\frac{\partial\left(\varepsilon_{par}c^{v}(\xi) + \varrho_{par}X/MW\right)}{\partial t} = -\frac{1}{\xi^2}\frac{\partial}{\partial \xi}\left(\xi^2\dot{n}_{par}\right) = -\frac{\partial \dot{n}_{par}}{\partial \xi} - \frac{2}{\xi}\dot{n}_{par}. \tag{A-13}$$

In the linear region of the adsorption isotherm with a minor adsorbate concentration, and if Henry's law applies (with $\frac{dlnX}{dlnc^{v}} = 1$), transport in the adsorbed phase is negligible and transport in the adsorptive phase is the main transport phenomenon [91]. However, with increasing adsorbate concentration, surface diffusion is increasing significantly. Especially in microporous solids, with a large value of the surface area to pore volume, the ratio of adsorbed concentration to adsorptive concentration may be high, and thus, transport by surface diffusion becomes important [90]. The total, one-dimensional molar flux of adsorptive and adsorbate molecules at the pore wall at radial position ξ is thus given by

$$\dot{n}_{par}(\xi) = -\widetilde{D}^{mi}\frac{\partial X}{\partial \xi}. \tag{A-14}$$

With the total derivative

$$\frac{dc^{v}}{dt} = \left(\frac{\partial c^{v}}{\partial X}\right)_T \frac{dX}{dt}, \tag{A-15}$$

equation (A-13) can also be expressed in terms of change of loading, using equation (A-14)

$$\left(\frac{\varepsilon_{par}}{\left(\frac{\partial X}{\partial c^{v}}\right)_T} + \frac{\varrho_{par}}{MW}\right)\frac{\partial X}{\partial t} = -\frac{\partial}{\partial \xi}\left(-\widetilde{D}^{mi}\frac{\partial X}{\partial \xi}\right) - \frac{2}{\xi}\left(-\widetilde{D}^{mi}\frac{\partial X}{\partial \xi}\right). \tag{A-16}$$

The boundary conditions solving equation (A-16) are the symmetry of the loading profile in the centre of the particle and equilibrium loading at bulk conditions at the edge of the particle $\xi = R_{par}$

$$\left(\frac{\partial X}{\partial \xi}\right)_{\xi=0} = 0, \tag{A-17}$$

$$X|_{\xi=R_{par}} = X^{eq}(c^{v,bulk}, T). \tag{A-18}$$

So far, in the derivation of equation (A-16) only local thermodynamic equilibrium has been assumed. A further simplification in the derivation of the LDF approach is the assumption, that the intraparticle diffusion coefficient is independent of the radial position in the particle ($\widetilde{D}^{mi} \neq f(\xi)$), yielding

$$\frac{\partial X}{\partial t} = D^{eff,mi}\left(\frac{\partial^2 X}{\partial \xi^2} + \frac{2}{\xi}\frac{\partial X}{\partial \xi}\right), \tag{A-19}$$

with the effective intraparticle diffusion coefficient (or apparent diffusion coefficient [90])

$$D^{eff,mi} = \frac{\widetilde{D}^{mi}}{\frac{\varepsilon_{par}}{\left(\frac{\partial X}{\partial c^v}\right)_T} + \frac{\varrho_{par}}{MW}} = \frac{D^v \varepsilon_{par} + D_0^S \frac{X}{c^v}\frac{\varrho_{par}}{MW}}{\varepsilon_{par} + \frac{\varrho_{par}}{MW}\left(\frac{\partial X}{\partial c^v}\right)_T}. \tag{A-20}$$

Up to this point, simplifying the particle's mole balance has not yet yielded a dimensional reduction of the equation and thus any benefit concerning computational effort, which is the main advantage of the LDF approach. To achieve the model reduction, equation (A-19) is averaged over the particle radius, assuming a spherical particle, yielding a formulation for the rate of change of average loading

$$\frac{\partial \bar{X}}{\partial t} = \frac{3}{4R_{par}^3 \pi} D^{eff,mi} \int_0^{R_{par}} 4\pi \xi^2 \left(\frac{\partial^2 X}{\partial \xi^2} + \frac{2}{\xi}\frac{\partial X}{\partial \xi}\right) d\xi. \tag{A-21}$$

A further assumption needs to be made regarding the shape of the loading profile within the particle. Although the averaging of the loading is a strong simplification of the actual loading profile, the integral change in loading described with the LDF approach was found to be compatible for different profiles [98]. The most suitable results are obtained for a parabolic loading profile of the form

$$X(t, \xi) = a_0(t) + a_2(t)\xi^2, \tag{A-22}$$

with the linear term left out on account of spherical symmetry [97]. Applying the boundary condition in equation (A-18), the first term on the right-hand side yields

$$a_0(t) = X^{eq}(c^{v,bulk}, T) - a_2(t) R_{par}^2. \tag{A-23}$$

Inserting equation (A-23) in (A-22) results in a formulation of the spatial loading distribution in the particle

$$X(t,\xi) = X^{eq}(c^{v,bulk},T) + a_2(t)\left(\xi^2 - R_{par}^2\right). \tag{A-24}$$

Substituting equation (A-24) into (A-21) and integrating gives

$$\frac{\partial \bar{X}}{\partial t} = \frac{3}{R_{par}^3} D^{eff,mi} 6 a_2(t). \tag{A-25}$$

In a final step, $a_2(t)$ needs to be eliminated. For a spherical particle, the average loading is obtained by integrating the loading distribution over the radius of the particle

$$\bar{X} = \frac{3}{4R_{par}^3\pi}\int_0^{R_{par}} 4\pi\xi^2 X(t,\xi)\, d\xi = \frac{3}{R_{par}^3}\int_0^{R_{par}} \xi^2 X(t,\xi)\, d\xi. \tag{A-26}$$

Substituting equation (A-24) and rearranging yields

$$a_2(t) = \frac{5}{2R_{par}^2}(X^{eq}(c^{v,bulk},T) - \bar{X}). \tag{A-27}$$

The classic LDF approach for a spherical particle with a parabolic loading profile presented by Glueckauf [93] is finally obtained by substituting equation (A-27) into (A-25)

$$\frac{\partial \bar{X}}{\partial t} = \frac{15 D^{eff,mi}}{R_{par}^2}(X^{eq}(c^{v,bulk},T) - \bar{X}), \tag{A-28}$$

with the LDF-factor

$$k_{LDF} = \frac{15 D^{eff,mi}}{R_{par}^2}. \tag{A-29}$$

For the application of the LDF approach, appropriate formulations for the diffusion coefficient $D^{eff,mi}$ and thus D^v and D_0^S as well as the derivative of the adsorption isotherm need to be applied.

When using the DA adsorption isotherm from equation (2-24), the derivation according to the adsorptive concentration c^v yields

$$\left(\frac{\partial X^{eq}}{\partial c^v}\right)_T = C_1 \frac{\partial}{\partial c^v}\left(exp\left[-\left(\frac{C_2 ln\left(\frac{C_3}{C_6 c^v}\right)}{C_4}\right)^{C_5}\right]\right), \tag{A-30}$$

with the constants $C_1 = \varrho^{ad}(T) w_0$, $C_2 = RT/MW$, $C_3 = p^{sat}(T)$, $C_4 = E$, $C_5 = n$ and $C_6 = RT$. Applying the chain rule yields

$$\left(\frac{\partial X^{eq}}{\partial c^v}\right)_T = C_1 exp\left[-\left(\frac{C_2 ln\left(\frac{C_3}{C_6 c^v}\right)}{C_4}\right)^{C_5}\right] \frac{\partial}{\partial c^v}\left(-\left(\frac{C_2 ln\left(\frac{C_3}{C_6 c^v}\right)}{C_4}\right)^{C_5}\right). \tag{A-31}$$

With the power rule and the chain rule, we can write

$$\left(\frac{\partial X^{eq}}{\partial c^v}\right)_T = -\frac{C_1 C_2 C_5}{C_4} exp\left[-\left(\frac{C_2 ln\left(\frac{C_3}{C_6 c^v}\right)}{C_4}\right)^{C_5}\right] \left(\frac{C_2 ln\left(\frac{C_3}{C_6 c^v}\right)}{C_4}\right)^{C_5-1} \frac{\partial}{\partial c^v} ln\left(\frac{C_3}{C_6 c^v}\right). \tag{A-32}$$

Derivation of the ln expression gives

$$\left(\frac{\partial X^{eq}}{\partial c^v}\right)_T = \frac{C_1 C_2 C_5}{C_4 c^v} exp\left[-\left(\frac{C_2 ln\left(\frac{C_3}{C_6 c^v}\right)}{C_4}\right)^{C_5}\right] \left(\frac{C_2 ln\left(\frac{C_3}{C_6 c^v}\right)}{C_4}\right)^{C_5-1}, \tag{A-33}$$

and inserting the constants $C_1 - C_5$ finally yields

$$\left(\frac{\partial X^{eq}}{\partial c^v}\right)_T = \frac{\rho^{ad}(T) w_0 RTn}{E c^v MW} exp\left[-\left(\frac{RT ln\left(\frac{p^{sat}(T)}{RT c^v}\right)}{E\ MW}\right)^{n}\right] \left(\frac{RT ln\left(\frac{p^{sat}(T)}{RT c^v}\right)}{E\ MW}\right)^{n-1}. \tag{A-34}$$

Concerning the effective or apparent diffusion coefficient $D^{eff,mi}$, the following considerations are given based on the well-described explanations provided by Reyes et al. [90]. Determination of the diffusion coefficients is traditionally done by steady-state or unsteady-state experiments with microscopic or macroscopic methods. A separate measurement of D^v and $\widetilde{D}^S$ is complicated since an increase in adsorbate concentration is associated by a narrowing of the pores ($\varepsilon_{par} = f(X)$) and thus a decreasing cross section for the adsorptive transport. Due to the unsteady character of technical adsorption processes, a dynamic increase and decrease of adsorptive diffusion and surface diffusion takes place permanently, depending on temperature, pressure, surface heterogeneity, gas type, and gas surface interaction [158], which will not be discussed in detail here, but some thoughts reflected [90]. Concerning equation (A-6), the determination of a combined diffusion coefficient is possible applying steady-state flux measurements with a macroscopic gas concentration gradient as driving force (as applied in this work for consolidated beds). However, it is difficult to prepare a single particle sample of suitable thickness with only intraparticle transport that provides a suitable diffusion resistance measurable

as a gas concentration gradient across the sample (in consolidated beds of single particles, also interparticle void transport will occur). Alternatively, unsteady-state measurements based on equation (A-19) (but rather in a formulation in terms of gas concentration gradients, see [90]) are not limited by the prerequisite of a macroscopic measurable gradient across the sample. In such an experiment, the apparent diffusion coefficient $D^{eff,mi}$ rather than $\widetilde{D}^{mi}$ is directly obtained. Some limiting cases can be discussed, considering the apparent diffusion coefficient in equation (A-20). If adsorbate loading is negligible, surface diffusion is not contributing to the total transport, and consequently, adsorptive diffusion is the only transport mechanism and $D^{eff,mi}$ reduces to D^{v}. On the other hand, if surface diffusion is dominant ($\widetilde{D}^{S} \gg D^{v}$), $\left(\frac{\partial X}{\partial c^{v}}\right)_{T}$ is large compared to ε_{par} and if in addition, the values for $\frac{X}{c^{v}}$ and $\left(\frac{\partial X}{\partial c^{v}}\right)_{T}$ are in the linear, Henry's law region of the adsorption isotherm, $D^{eff,mi} \approx \widetilde{D}^{S}$, which is equivalent with a neglection of the Darken-factor. If the loading is even higher where the adsorption isotherm is nonlinear, $D^{eff,mi} \approx D_0^{S}\left(\frac{\partial lnc^{v}}{\partial lnX}\right)_{T}$, which is applied by many authors to model micropore transport. Finally, Reyes et al. [90] discuss a fourth case, in which the surface diffusion is small compared to gas transport, but the partial derivative of the adsorption isotherm $\left(\frac{\partial X}{\partial c^{v}}\right)_{T}$ is still significant, which allows no further simplification of equation (A-20).

The previous discussions reveal the difficulty but importance of the determination of sufficient diffusion coefficients in microporous adsorbents. With increasing computational resources and refined methods, diffusion coefficients in porous media are more and more obtained by molecular dynamic simulations. Pršlja et al. provide micropore diffusion coefficients for methanol at 298K in narrow slit graphite pores in dependence of two different pore sizes, which were recently obtained by using Monte Carlo, hybrid Monte Carlo, and Molecular Dynamics simulations [159]. MD simulations are helpful to understand the phenomenological adsorption-diffusion behaviour in microporous adsorbents. However, since the provided diffusion coefficients by Pršlja et al. are only valid for one temperature, they cannot be used throughout the temperature range of common adsorption processes.

A.2 Derivation of the Dusty-Gas-Model (DGM)

Already in 1866 (Clerk Maxwell) and 1871 (Josef Stefan), the essential foundations for the description of multicomponent transport processes were laid. Wesselingh and Krishna explain why the Stefan-Maxwell transport approach is superior to the very commonly used Fick diffusion

approach and why the latter is only approximately suitable for the evaluation of transport processes [83]. The main equation describing a diffusive, spatially one-dimensional, multicomponent transport (with neglection of external potentials e.g., gravitational, or electric potential), is given by

$$\frac{dpy_j}{dz} = RT \sum_{i=1}^{J} \frac{y_j \dot{n}_i^D - y_i \dot{n}_j^D}{\frac{D_{ij}}{\tau}}. \tag{A-35}$$

Herby, $\dot{n}_i^D$ and $\dot{n}_j^D$ are diffusive fluxes, y_i and y_j are molar fractions of species i and j, and D_{ij} is the binary diffusion coefficient. The term on the left-hand side describes the driving force for the transport with the partial pressure gradient ($p_j = py_j$) in the z direction. Here, z denotes the spatial coordinate e.g., of an adsorbent bed, composite, or of a primary particle. In this work, z is used as the spatial coordinate of the adsorbent composites, describing the outer dimension of the sample. With the regular diffusion path in a porous solid following the coordinate z', the tortuosity factor τ is defined

$$\tau = \frac{z'}{z}. \tag{A-36}$$

The Stefan-Maxwell term on the right side of equation (A-35) accounts for the sum of all pair interaction forces between molecules i and j through the binary diffusion coefficient D_{ij}. While in Stefan-Maxwell diffusion the interactions of the individual molecules among themselves are decisive, in Knudsen diffusion only the molecule-pore wall interactions are considered. With equation (2-40) and assuming ideal gas behaviour ($c = p/RT$), the one-dimensional Knudsen flux of species j can be formulated

$$\dot{n}_j^{Kn} = -\frac{D_j^{Kn}}{\tau RT} \frac{dpy_j}{dz}. \tag{A-37}$$

Formally, this equation can also be derived by applying the Stefan-Maxwell diffusion approach on a binary mixture containing a mobile gas species j and stationary "wall-dust" particles $i = w$. In a fixed, Eulerian specification of the flow field, the flux of dust-particles $\dot{n}_w^D$ is zero which yields

$$\frac{1}{RT} \frac{dpy_j}{dz} = -\frac{y_w \dot{n}_j^D}{\frac{D_{wj}}{\tau}}. \tag{A-38}$$

With $D_{wj}/y_w = D_j^{Kn}$ and $\dot{n}_j^D = \dot{n}_j^{Kn}$, equation (A-37) is obtained.

By combining the two transport approaches (equations (A-35) and (A-37)) and considering the dust-particles being the component $(J+1)$, the DGM for describing diffusive multicomponent mass transport in porous media is obtained

$$\frac{1}{RT}\frac{dpy_j}{dz} = -\frac{\dot{n}_j^D}{\frac{D_j^{Kn}}{\tau}} - \sum_{i=1}^{J}\frac{y_j\dot{n}_i^D - y_i\dot{n}_j^D}{\frac{D_{ij}}{\tau}}. \tag{A-39}$$

Considering equation (2-28) with the (one-dimensional) viscous flux from equation (2-31) and neglecting the surface diffusion term, the molecular transport of species j in porous media can be expressed as follows

$$\dot{n}_j^D = \dot{n}_j - \dot{n}y_j = \dot{n}_j + \frac{B_0}{\tau\eta}\frac{p_j}{RT}\frac{dp}{dz}. \tag{A-40}$$

In macro porous transport pores, the adsorption rate is negligible and thus the contribution of surface diffusion to the overall transport is negligible [158]. By inserting equation (A-40) into (A-39), the DTM considering diffusive and viscous flow is obtained

$$-\frac{dpy_j}{dz} = RT\left(\frac{\dot{n}_j}{\frac{D_j^{Kn}}{\tau}} + \sum_{i=1}^{J}\frac{y_i\dot{n}_j - y_j\dot{n}_i}{\frac{D_{ij}}{\tau}} + \frac{B_0}{\eta}\frac{py_j}{RTD_j^{Kn}}\frac{dp}{dz}\right). \tag{A-41}$$

The Stefan-Maxwell term can be disregarded for a pure-component adsorptive as regarded in the present work. Furthermore, by rewriting the partial quantities to absolute quantities and reformulation, equation (A-41) can be expressed in terms of the total molar flux as follows

$$\dot{n} = -\frac{1}{RT}\left(\frac{D^{Kn}}{\tau} + \frac{B_0 p}{\tau\eta}\right)\frac{dp}{dz}. \tag{A-42}$$

Note that $\dot{n}$ is the total molecular flux related to the cross-sectional area of the transport pores. It is convenient to correlate the total flux to the outer dimension of a porous sample, e.g., the cross-sectional area of a consolidated composite. With the volume fraction of the transport pores/ macropores ε^{ma} and in terms of mass flux

$$\dot{m} = \dot{m}^v\varepsilon^{ma} = \dot{n}MW\varepsilon^{ma}, \tag{A-43}$$

the DGM can be formulated related to the cross-sectional area of the consolidated composite

$$\dot{m} = -\frac{MW\varepsilon^{ma}}{RT}\left(\frac{D^{Kn}}{\tau} + \frac{B_0 p}{\tau\eta}\right)\frac{dp}{dz}. \tag{A-44}$$

Appendix B. Experimental Characterization of carbon-active adsorbent composites

Aiming to identify structure-property correlations of consolidated adsorbent composites containing adsorbent primary particles, heat additive, and binder, several composites were experimentally characterized for methanol adsorption capacity, mass transport, and heat transport. In addition, the experimental investigation aimed to parameterize the material models introduced in section 2.4. The samples examined in this work and the measurements carried out are outlined in Table B-1.

Table B-1: Overview of consolidated carbonaceous composites with varying types and amounts of binder and heat additive investigated in this work. In addition, the conducted experimental characterizations are stated.

Sample name	Adsorbent	Particle fraction /µm	binder /wt%	heat additive /wt%	Mass transport	Adsorption Isotherm	Thermal conductivity	Heat capacity
P_{42}	CDC	75-150	15 PTFE	-	-	yes	-	-
P_{47}	CDC	50-75	2 CMC	50 Ag	-	yes	-	-
P_{48}	CDC	50-75	2 CMC	10 Ag	-	yes	-	-
P_{49}	CDC	50-75	2 CMC	50 C	-	yes	-	-
P_{50}	CDC	50-75	15 PTFE	50 C	-	yes	-	-
P_{53}	CDC	50-75	15 PTFE	50 BN	-	yes	-	-
P_{55}	CDC	75-150	15 PTFE	50 Ag	-	yes	-	-
P_{56}	CDC	50-75	20 PTFE	-	yes	yes	-	-

P_{58}	CDC	50-75	5 CMC	-	-	yes	-	-
P_{59}	CDC	75-150	5 CMC	-	yes	yes	-	-
P_{60}	CDC	50-75	2 CMC	10 C	yes	-	-	-
P_{61}	CDC	50-75	2 CMC	50 BN	yes	yes	yes	-
P_{62}	CDC	75-150	2 CMC	10BN	-	-	yes	yes
P_{63}	CDC	75-150	2 CMC	-	-	yes	yes	-
P_{64}	CDC	50-75	2 CMC	-	yes	-	-	-
P_{65}	CDC	75-150	2 CMC	-	-	yes	-	yes
P_{66}	CDC	75-150	2 CMC	10 BN	yes	-	-	-
P_{67} (Exp_{CDC+BN})	CDC	75-150	2 CMC	10 BN	yes	-	yes	yes
P_{68} (Exp_{CDC})	CDC	50-75	2 CMC	-	yes	yes	yes	yes
P_{69}	CDC	50-75	2 CMC	10 BN	yes	yes	yes	-
$P_{80,21}$	AC	<80	10 CMC	-	-	yes	-	-
$P_{80,3}$	AC	<80	10 CMC	-	yes	-	-	-
$P_{80,4}$	AC	<80	10 CMC	-	yes	-	-	-

B.1 Void characterization with mercury intrusion

Mercury intrusion measurements were conducted for three different consolidated CDC composites with different compositions as exemplarily explained for a composite P_{68} (Exp_{CDC}) in section 4.2.2. Figure B-1 and Figure B-2 show additional results obtained for CDC samples with different compositions. Furthermore, the material parameters of the three samples are summarized in Table B-2.

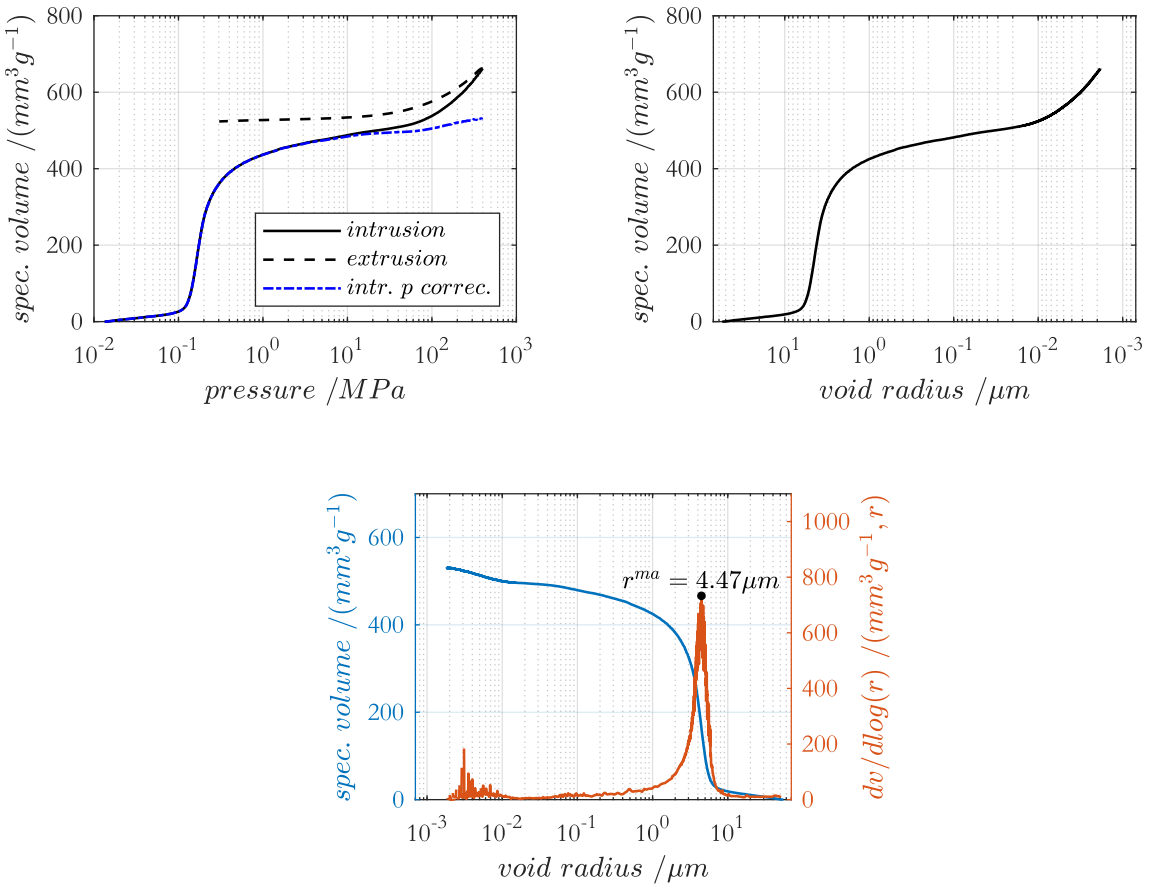

Figure B-1: Specific void volume of a consolidated CDC plate with a particle size of 75-150 µm, 2 wt% CMC binder, and 10 wt % BN heat additive as a function of pressure (top, left) and void radius (top, right). Differential pore volume (bottom).

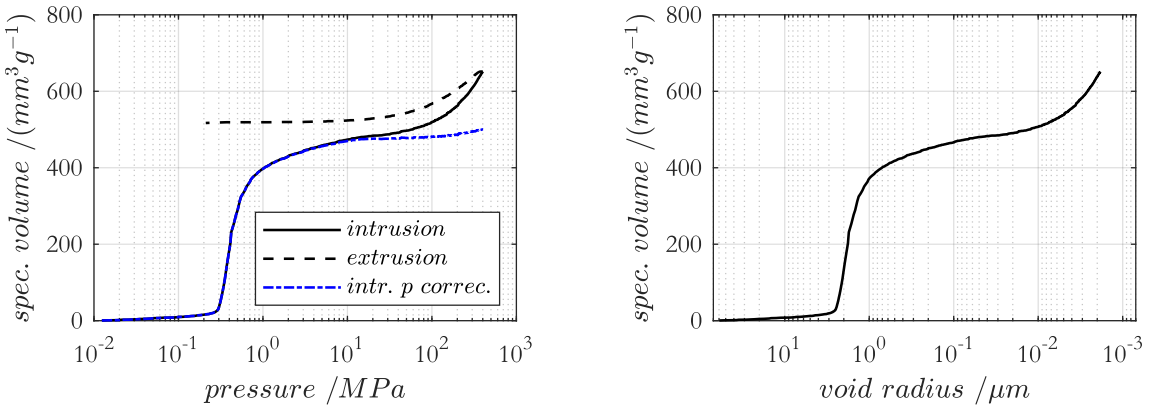

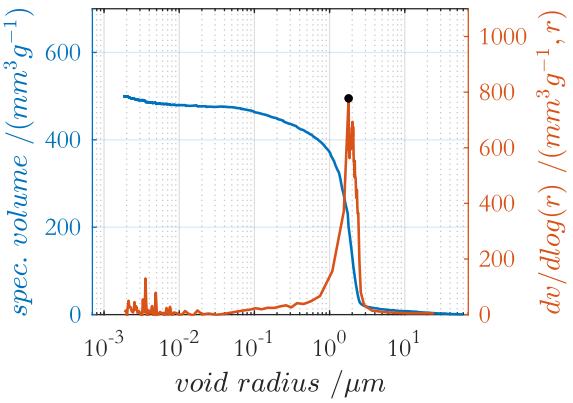

Figure B-2: Specific void volume of a consolidated CDC plate with a particle size of 50-75 µm and 2 wt% CMC binder as a function of pressure (top, left) and void radius (top, right). Differential pore volume (bottom).

Table B-2: Characteristic values of the investigated consolidated composites of CDC adsorbent with varying particle sizes, binder and additive obtained with mercury intrusion measurements, helium pycnometer measurements and N_2 physisorption.

	CDC 50-75 µm, 2 wt% CMC	CDC 75-150 µm, 2 wt% CMC	CDC 75-150 µm, 2 wt% CMC, 10 wt% BN
$r^{ma}/\mu m\ (Hg\ int.)$	1.79	5.18	4.47
$\varrho_{bulk}/(g\ cm_{com}^{-3})$ $(Hg\ int.@\ p \approx 0.01\ MPa)$	0.63	0.60	0.66
$\varrho_{skel}/(g\ cm_s^{-3})\ (He\ pyc.)$	-	2.27	2.17
$\varrho_{skel}/(g\ cm_s^{-3})\ (eq.\ (4\text{-}10))$	2.26	2.27	2.17
$\varepsilon_v = \varepsilon_{ma}/(m_v^3 m_{com}^{-3})\ (eq.(4\text{-}9))$	0.23	0.3	0.22
$\varepsilon_{p,com}/(m_p^3 m_{com}^{-3})\ (eq.(4\text{-}4))$	0.49	0.43	0.48
$\varepsilon_{p,par}/(m_p^3 m_{par}^{-3})\ (eq.(4\text{-}3))$	0.64	0.62	0.61
$\varrho_{app,par}/(g\ cm_{par}^{-3})$ $(Hg\ int.@\ infl.point, eq.(4\text{-}8))$	0.82	0.86	0.85

p_{infl}/MPa	0.7	0.46	0.25
$r_{v,infl}(@p_{infl})/\mu m$	1.05	1.58	2.98
$v_{int}(@p_{infl})/(mm^3 g^{-1})$	363	500	328

B.2 Mass transport through consolidated composites

B.2.1 Experimental results

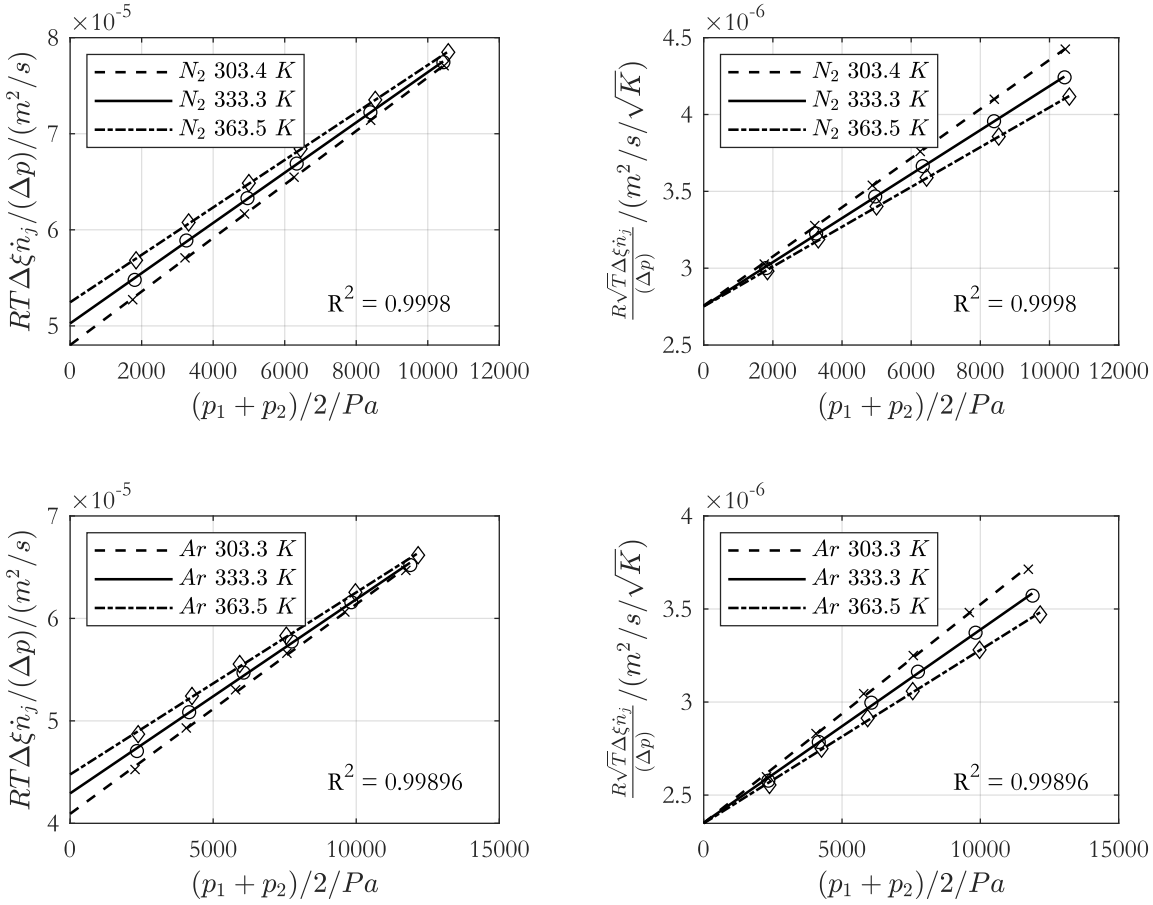

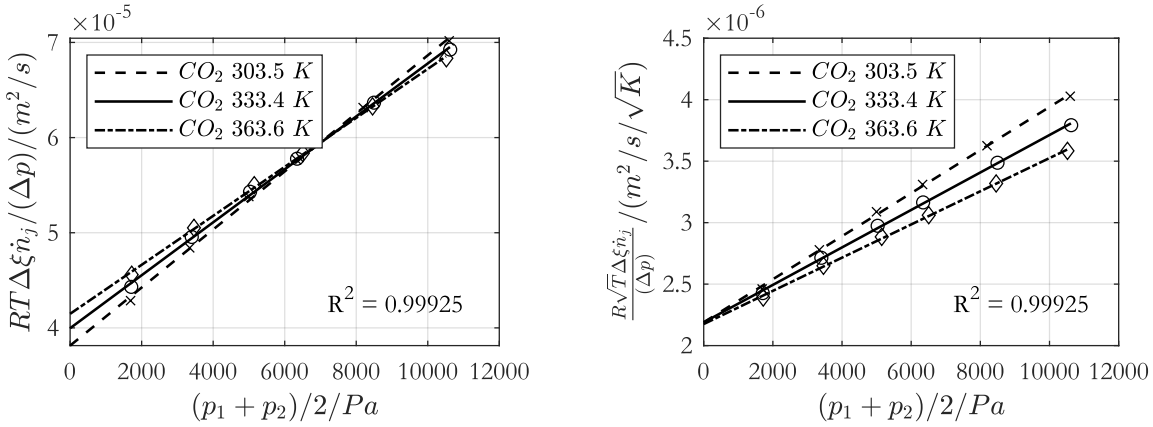

Figure B-3: Results of permeation experiment for samples EXP_{CDC} conducted with N2, Ar, and CO2 at three temperature levels. On the left: Evaluation with the classic DGM. On the right: with the temperature-independent ordinate.

Figure B-3 show experimental results of flow-through experiments obtained with sample P_{68} (Exp_{CDC}) with the non-/ weak-adsorbable gases Ar, N_2, CO_2.

B.2.2 Results of flow-through experiments

In the following table, the experimental results obtained with flow-through experiments are outlined for several samples.

Table B-3: Mass transport parameters and structural parameters of consolidated CDC-plates with varying amounts and type of binder and heat additive and particle size fraction.

Sample	Particle fraction /µm	Binder /wt%	Additive /wt%	$\frac{\varepsilon^{ma}}{\tau} d_{pore}$ $/(10^{-7} m)$	$\overline{B}_0^{eff}(CH_3OH)$ $/(10^{-14} m^2)$	$\overline{D}^{Kn,const}$ $/(10^{-6} m^2/s$ $/\sqrt{kg/mol/K})$
P_{56}	50-75	20 PTFE	-	3.96	7.79	3.37
P_{59}	75-150	5 CMC	-	4.72	13.19	4.04
P_{60}	50-75	2 CMC	10 C	2.53	3.75	2.16
P_{61}	50-75	2 CMC	50 BN	0.06	0.01	0.05
P_{64}	50-75	2 CMC	-	2.07	6.31	1.79
P_{66}	75-150	2 CMC	10 BN	3.65	9.94	3.13
P_{67}	75-150	2 CMC	10 BN	3.82	11.16	3.27

P_{68}	50-75	2 CMC	-	3.03	4.96	2.59
P_{69}	50-75	2 CMC	10 BN	1.78	2.67	1.52

B.2.3 Validation of independence of layer thickness

Theoretically, the effective diffusion coefficient describing the transport in a porous medium is independent of the layer thickness of the consolidated composite. The increasing transport resistance with greater thicknesses is due to the longer transport distances and thus to the increasing layer thickness per se. This behaviour was validated in a student research project [160] using two almost identical, consolidated commercial activated carbon composites (GAP_1 and GAP_2). Initially, both samples were investigated separately with He and N_2 in the permeation cell shown in Figure 4-5. In a third experiment, both samples were installed in series (GAP_{12}) in the cell, which can be seen in Figure B-4, and thus the layer thickness and transport resistance have been additively increased.

Figure B-4: Permeation cell with two commercial, identical consolidated activated carbon composites in series (GAP_1 and GAP_2).

The evaluation strategy presented in section 4.4 was applied. Figure B-5 shows the resulting (temperature-averaged) effective permeabilities for the three sample configurations versus the molar masses of He and N_2.

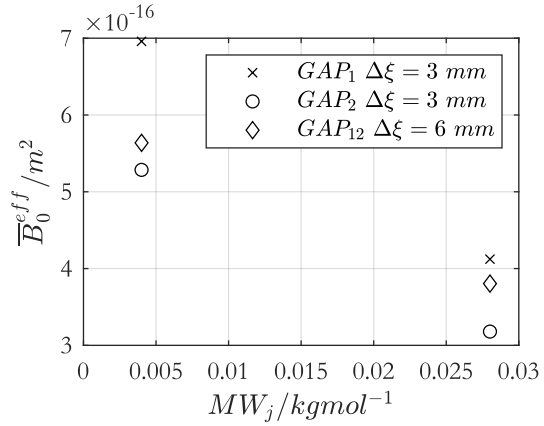

Figure B-5: Temperature-averaged effective permeabilities for GAP_1, GAP_2 and both samples in series GAP_{12} for experiments with He and N_2 as function of molar mass of the gas species and layer thickness of the sample.

$\overline{B}_0^{eff}$ of GAP_1 is approximately 23% higher for N_2 and 24% higher for He compared to GAP_2. Theoretically, both samples in series should result in an average permeability. With He, $\overline{B}_0^{eff}$ for GAP_{12} is slightly below average, for N_2 slightly above. But, in general, the independence of layer thickness could be proved with these investigations. The same conclusions could be drawn when evaluating the resulting Knudsen diffusivities as can be seen in Figure B-6. The trends are equivalent with a higher diffusion coefficient for GAP_1 than for GAP_2 and values in between for both samples in series GAP_{12}. To summarize, the numerical values are listed in Table B-4.

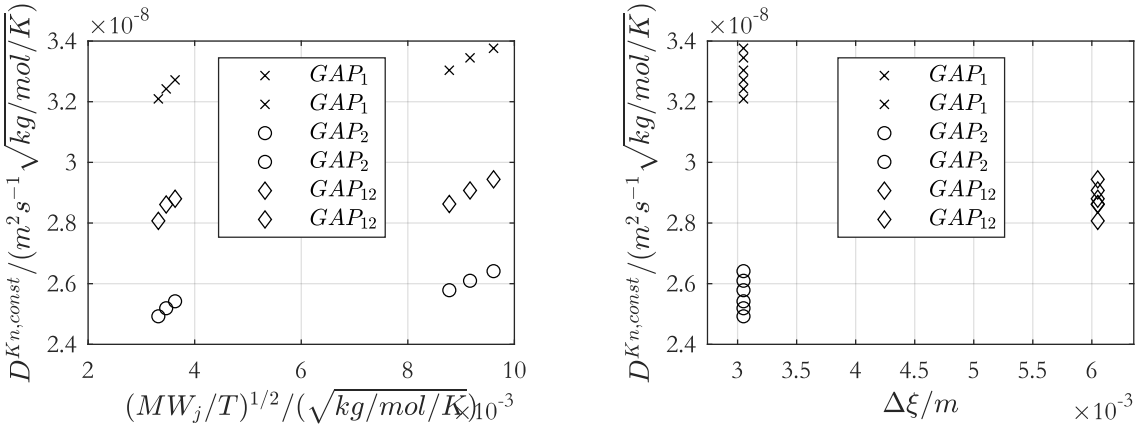

Figure B-6: Constant part of the Knudsen diffusion coefficient for GAP_1, GAP_2 and both samples in series GAP_{12} for experiments with He and N_2 as function of molar mass divided by temperature (left) and layer thickness of the sample (right).

Table B-4: Constant part of Knudsen-diffusion coefficients (averaged over molar mass and temperature) and temperature-averaged effective permeabilities for He and N_2.

	$\overline{D}^{Kn,const}/(m^2/s/\sqrt{kg/mol/K})$	$\overline{B}_0^{eff}(He)/m^2$	$\overline{B}_0^{eff}(N_2)/m^2$
GAP_1	$3.29\cdot10^{-8}$	$6.96\cdot10^{-16}$	$4.12\cdot10^{-16}$
GAP_2	$2.56\cdot10^{-8}$	$5.29\cdot10^{-16}$	$3.18\cdot10^{-16}$
GAP_{12}	$2.88\cdot10^{-8}$	$5.64\cdot10^{-16}$	$3.8\cdot10^{-16}$

B.3 Specific heat capacity and thermal conductivity of CDC- and AC-samples

In the following table, specific heat capacities, thermal diffusivities, structural parameters, and thermal conductivities are summarized for several CDC- and AC samples.

Table B-5: Summary of DSC and laser flash measurements for CDC- and AC samples. Effective thermal conductivities were obtained from equation (4-21) and linear fitting. The structural parameters are obtained from the Hg intrusion post-processing and are listed in Table 4-2.

	$c_p^s/(Jkg^{-1}K^{-1})$	$\overline{\alpha}/(mm^2s^{-1})$	ε^{ma}	ε^{mi}	$\varrho^{bulk}/(kg\,m^{-3})$	$\lambda^{\mathrm{eff}}(298-373K)/(Wm^{-1}K^{-1})$
P_{62}	$2.005T/K+268.9$	1.145	0.22	0.48	660	$0.00149T/K+0.226$
P_{65}	$1.809T/K+303.1$	–	0.3	0.43	600	–
P_{67}	$2.12T/K+199.9$	1.104	0.22	0.48	660	$0.00178T/K+0.066$
P_{68}	$1.625T/K+388.4$	1.0825	0.23	0.49	630	$0.00136T/K+0.18$
AC	$0.395T/K+722.4$	0.4143	0.3	0.3	513.3	$0.00035T/K+0.063$

B.4 Summary of material parameters and material parameters – composite composition correlations

For the development of effective material models, a complete and reliable dataset was required. The basis of the effective material models introduced in section 2.4 is a CDC-composite with particle fraction of 50-75 µm primary particles with 2 weight percent of CMC binder (P_{68}). These material parameters are correlated with composite composition to develop a sufficient material model to be used in the process simulations. Table B-6 summarizes the material parameters and the underlying measurement and evaluation technique as well as states the correlation between different material parameters for varying composite compositions.

Table B-6: Material parameters of a CDC-composite with particle fraction of 50-75 µm and 2 wt% CMC binder (P_{68}) and 75-150 µm, 2 wt% CMC binder and 10 wt% BN (P_{67}). Correlations for varying plate compositions are stated.

		P_{68} (Exp_{CDC})	P_{67} (Exp_{CDC+BN})	
adsorption isotherm	$w_0\ /(cm^3\, g_{comp}^{-1})$	0.603	0.543	Manometric adsorption equilibrium measurements and Dubinin-Astakhov fit
	$E/(Jg^{-1})$	212.5	212.5	
	$n/-$	2.32	2.32	
mass transport	$B_0^{eff}/(m^2)$	$4.96 \cdot 10^{-14}$	$11.16 \cdot 10^{-14}$	Diffusion cell and evaluation with Dusty-Gas-model
	$\mathrm{D}_{\mathrm{MeOH}}^{Kn,const}$ $/\left(m^2 K^{-1/2} s^{-1}\right)$	$2.6 \cdot 10^{-6}$	$3.27 \cdot 10^{-6}$	
thermal cond. & heat capacity	$\tilde{\lambda}^s/(Wm^{-1}K^{-1})$	$0.0017T/K + 0.229$	$0.00222T/K + 0.08$	Transient hot bridge and calculation
	$c_p^s/\left(Jkg_{comp}^{-1}K^{-1}\right)$	$1.625T/K + 388.4$	$2.12T/K + 199.9$	Differential scanning calorimetry
Parameters related to consolidated composites	$\varepsilon^{ma}/\left(m_{ma}^3 m_{comp}^{-3}\right)$	0.23	0.22	macro- or void-porosity, Hg-intrusion & $(eq.(4\text{-}9))$
	$d^{ma}/\mu m$	3.58	8.94	average void width composite, Hg-intrusion
	$\varrho^{bulk}/$ $(kg_{comp}m_{comp}^{-3})$	630	660	Bulk density, Hg-intrusion
primary particles	w_p/nm	0.97	1.02	average pore width primary particles, BET-method

related

$\varrho_{skel}/(kg^s m^{-3,s})$	2260	2170	Skeleton density, Hg-intrusion & ($eq.$ (4-10))
$\varepsilon^{mi} \equiv \varepsilon_{p,com} /(m_{mi}^3 m_{comp}^{-3})$	0.49	0.48	micro- or pore-porosity, Hg-intrusion & ($eq.$(4-4))
$\bar{d}_{par}/\mu m$	62.5	112.5	primary particle size

Appendix C. Experimental validation of the process model

An experimental small-scale adsorption chiller setup was introduced which was used to investigate adsorbent composites in the thermodynamic cycle. The transient results are utilized in a further step, to validate the distributed process model introduced in chapter 3. The experiments and validation simulations shown in this chapter are performed using the CDC composites characterized in chapter 4 with the material parameters summarized in Table B-6.

C.1 Gram-scale adsorption chiller – Experiments and model validation

To investigate the transient behaviour of gram-scale adsorbent composites in the adsorption cooling cycle, a laboratory adsorption chiller was designed and built. Due to the laboratory scale, rapid investigation of new adsorbents is possible without the necessity of using large amounts of active material, which is beneficial for experimental material design. Furthermore, transient, cyclic experiments can be used for the validation of the distributed process model.

In this section, experimental results obtained with CDC composites with 2 wt% CMC binder are presented and discussed. The macroscopical parameters of the investigated CDC composites are listed in Table C-1. Furthermore, the cyclic experiments are used to validate the process model taking the material parameters from Table B-6 into account.

Table C-1: Macroscopical parameters of CDC composites with 50-75 µm primary particles size and 2 wt% of CMC binder. The samples were investigated in the small-scale adsorption chiller and are used for validation of the process model.

$\sum A_{comp}/cm^2$	$\bar{s}_{comp}/mm$	$\sum V_{comp}\ /cm^3$	$\sum M_{cdc}/g$
18.5	2.7	5	2.788

C.1.1 Experimental setup – Laboratory-scale adsorption chiller

The laboratory-scale adsorption chiller for the experimental investigation of gram-scale adsorbent composites in the adsorption refrigeration cycle has been introduced in section 6.2.2. With this

setup, cyclic experiments with gram scale adsorbent composites under varying pressure and temperature conditions, as well as evaporation and condensation times, can be conducted, according to the refrigeration cycle introduced in section 1.1. For the validation of the one-dimensional process model, CDC composites are investigated. To ensure solely one-dimensional transport, the side surfaces of the composites are sealed as explained subsequently and placed on aluminium supports for the application in the small-scale chiller. The evaluation of the experiments follows the same procedure as discussed in section 6.2.

Sample preparation

Equivalent to the sample preparation outlined for the structured AC composites in section 6.2.2, the CDC composites are placed on aluminium supports using thermal adhesive tape. The sample shown in Figure C-1 is a CDC composite with 50-75 µm primary particles and 2 wt% of CMC binder. This sample is equivalently embedded in silicone (Elastosil E10) as the samples for the mass transfer measurements. In this case, the embedding is needed to guarantee a solely one-dimensional mass transfer by preventing adsorptive to enter the samples via the side surface. The experimental results obtained with these samples are used in section C.1.4 to validate the one-dimensional process model.

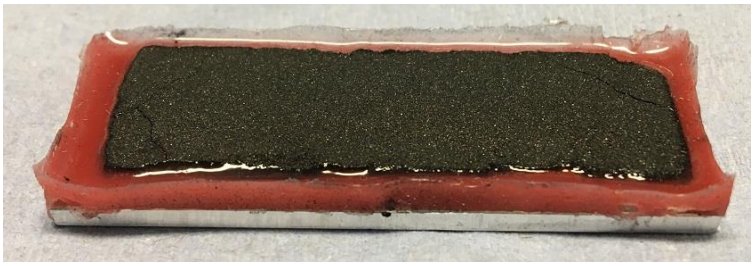

Figure C-1: CDC composite containing 2 wt% CMC binder (EXP_{CDC}) attached by means of thermal adhesive tape on a 2 mm thick aluminium support with a horizontal slit for the thermocouple.

C.1.2 Experimental results

Experimental results obtained with the small-scale adsorption chiller are presented in this section. The measurements were carried out with CDC composites with primary particles of size 50-75 µm and with 2 wt% of CMC binder as shown in Figure C-1. The macroscopical parameters of the samples are listed in Table C-1.

C.1.2.1 Transient experiments – cycles and cyclic steady state

In this section, results obtained with CDC composites with evaporation and condensation times of 400s are discussed. The temperatures in the thermostats were adjusted to guarantee temperatures of the heat transfer fluid of $T_e = 15°C, T_c = T_{ads} = 20°C, T_{des} = 90°C$.

To compare the performance of different composites, cycle times, and temperature levels, measurement results of the CSS are required. Figure C-2 on the left shows experimental results of the adsorber pressure and temperature of the adsorbent in a Clausius-Clapeyron diagram from initialization to CSS. Additionally, the saturation pressures of the evaporator and condenser are displayed. The integral adsorption and desorption kinetic are summarized in the mass flux exchanged between evaporator and adsorber as well as adsorber and condenser. The transient behaviour of the mass flux from initialization to CSS is shown in Figure C-2 on the right.

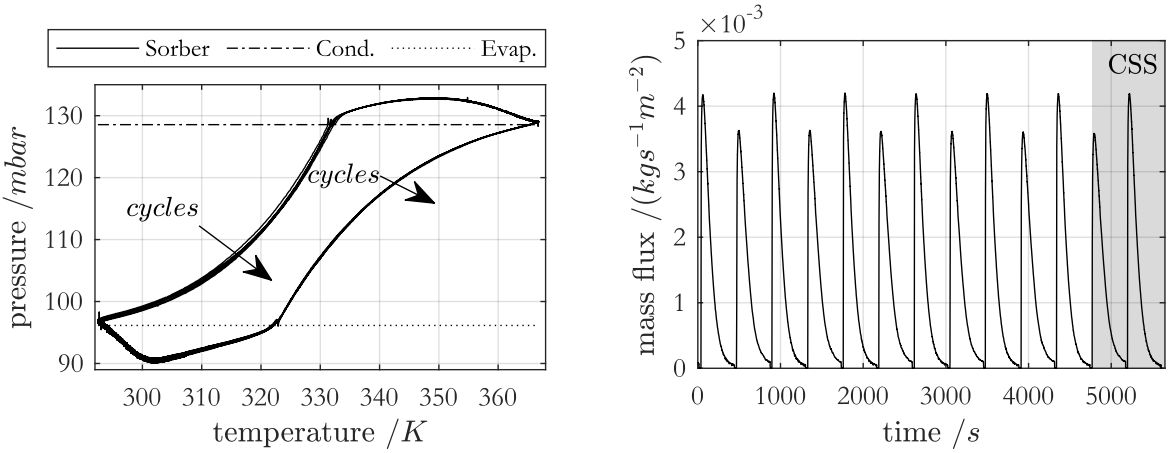

Figure C-2: Transient results from initialization to cyclic steady-state for experiments of CDC composites with $t_e = t_c = 400\,s$, $T_e = 15°C$, $T_c = T_{ads} = 20°C$, $T_{des} = 90°C$. Left: Clausius-Clapeyron diagram, right: mass flux between evaporator and adsorber as well as adsorber and condenser.

The number of cycles required to reach CSS mainly depends on the initial state of the adsorbent as well as the cycle time. With short cycle times, reaching CSS requires more cycles than for long cycle times. The results obtained in the last cycle are used to calculate the performance indicators as outlined in section 6.2.2.1. Figure C-3 shows the profiles in CSS in more detail. Additionally, error bars for the measured mass fluxes are added and the pressure profiles of evaporator, condenser, and adsorber are plotted.

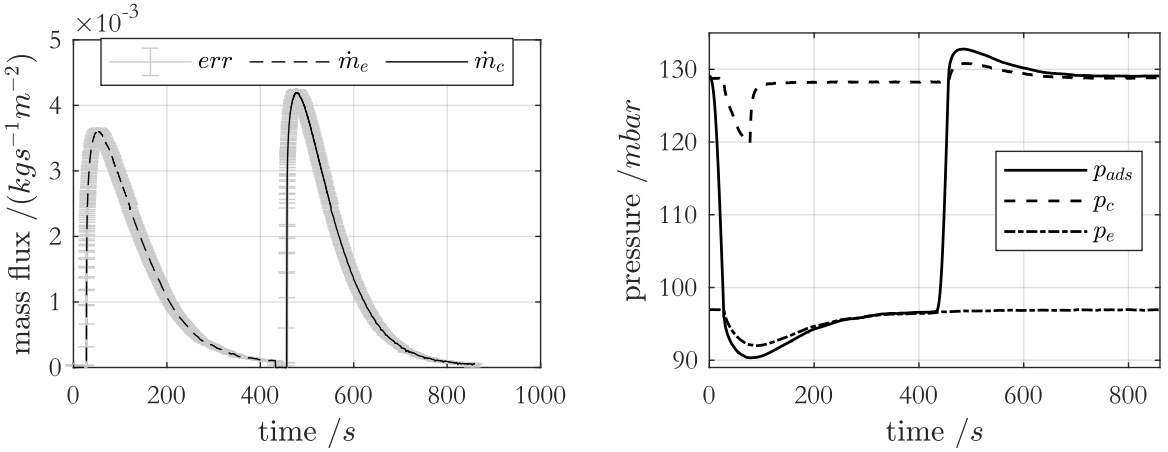

Figure C-3: Mass fluxes and pressure profiles in CSS obtained with the CDC composites for an experiment with $t_e = t_c = 400\ s, T_e = 15°C, T_c = T_{ads} = 20°C, T_{des} = 90°C$.

The cycle starts with the cooling of the adsorbent resulting in a pressure decrease due to the adsorption of methanol from the free gas phase. As soon as the evaporator pressure is reached, the two pneumatic valves connecting the evaporator and adsorber are opened, causing a sudden increase in mass flux. The flux induced by the adsorption reaches a maximum and decreases continuously until the adjusted evaporation time is reached. During the adsorption half cycle, the condenser is separated and thus not affecting the adsorption cycle. To prevent the accumulation of inert gas during multi-cycle experiments, the condenser gas phase is regenerated by shortly opening the control valve to the vacuum pump. The short pumping removes accumulated inert gas and ensures an initial and equilibrium condenser pressure for the next desorption half cycle. After the evaporation time, the two pneumatic valves are automatically closed, and the external fluid circuit is switched to the hot thermostat which induces the heating period. As soon as the pressure in the adsorber reaches condenser pressure, the two valves connecting these apparatuses open which start the condensation period for an adjusted time t_c and induces a sharp increase in the measured mass flux.

The maximal mass flux in desorption ($\dot{m}_c$) is slightly larger than in adsorption ($\dot{m}_e$). This indicates the faster kinetic due to better mass and heat transfer in the CDC composites at higher temperature and pressure levels. During the heating and cooling periods, the valves to the evaporator and condenser are closed. In the idealized cycle, these periods are isosteric. However, in the real cycle, these steps are non-isosteric. Since the laboratory plant is not optimized for the minimal hold-up in the adsorber gas phase and depending on the kinetics of the gram-scale adsorbents, the temperature levels as well as the adjusted evaporation and condensation times, the heating and cooling periods are comparably long. In an industrial application, the adsorber

would be constructed with as minimal hold-up as possible. By investigating different adsorbents with varying kinetical behaviour as well as different cycle times, the duration of the heating and cooling periods differ. Thus, to compare different experiments, the duration of the adsorption (t_{ads}) and desorption (t_{des}) phase with the corresponding adsorption from and desorption to the free gas phase as well as the corresponding mass fluxes are used for the evaluation.

C.1.2.2 Performance evaluation of CDC composites with varying cycle time

The single experiments from initialization to CSS were conducted for different temperature levels and cycle times. Here, results are discussed obtained for experiments conducted with moderate temperature levels of $T_e = 15°C$, $T_{ads,c} = 20°C$ and $T_{des} = 90°C$ and cycle times between $t_{cyc} = 200 - 2200\ s$. Figure C-4 (top) shows specific cooling powers and specific cooling energies related to the cross-sectional area as well as the mass of the CDC composites, respectively, vs. cycle time. Regardless of the reference, power density and efficiency density show the same qualitative profiles. For these composites, SCP is maximal at short cycle times of $t_{cyc} \approx 360\ s$. For longer cycle times, the adsorption equilibrium is more and more approached resulting in small mass fluxes and thus small cooling powers. For shorter cycle times, kinetical limitations are predominantly resulting in lower power densities. Unlike SCP, the energy density increases monotonically with cycle time, which is also the consequence of approaching adsorption equilibrium. At long cycle times, in equilibrium, q reaches the limiting value which is not determined in these experiments.

To compare different adsorbent composites, a representation of process power and efficiency within one graph is desirable. For the evaluation of the experiments, the COP cannot be used as efficiency criteria since the desorption energy is experimentally not accessible in the gram-scale setup. Alternatively, the energy density q (see equations (6-16) and (6-17)) can be used to represent the efficiency criteria. The Pareto-optimality is visualized in a double logarithmic representation in which SCP is plotted versus q. These types of plots are known as Ragone-plots and are commonly used in electrochemical engineering technology to get a quick assessment of the best performing region of an electrochemical device. In adsorption technology, such a visualization has been used by Ammann et al. [141]. The Pareto-optimality of power density and efficiency density is shown in Ragone-plots in Figure C-4 (bottom). In the double logarithmic representation, the cycle times, and the performance criteria ($SCP \cdot q$) are represented as straight lines. The maximal performance with respect to cross-sectional area of the CDC composites results to 705 $kJ^2/m^4/s$ and to 240 $kJ^2/kg_{comp}^2/s$ with respect to the composites mass.

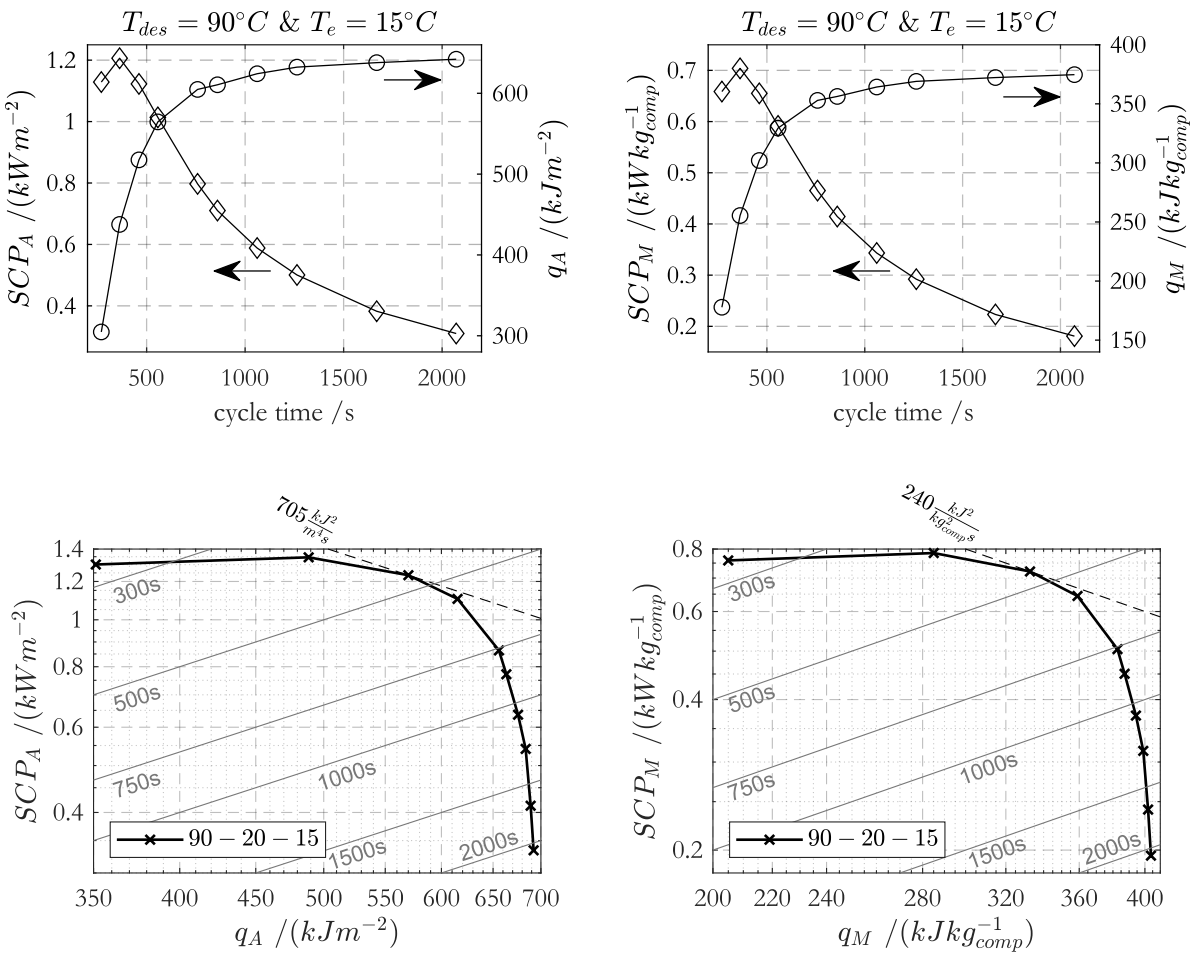

Figure C-4: (Top) Specific cooling powers and specific cooling energies related to the cross-sectional area and mass of the CDC composites, respectively, vs. cycle time. (Bottom) Ragone-plots indicating the Pareto-optimality of efficiency and specific powers. Additionally, the maximal performance related to cross-sectional area (left) and mass of CDC composites (right) are shown.

Due to the high adsorption rate in short cycles, the specific cooling power is maximal at short cycle times. However, in short cycles, only a small fraction of the adsorption capacity is utilized resulting in small efficiencies. This Pareto-optimality is common for many energy conversions processes. Depending on the application and the desired mode of operation, the process can therefore be operated in a power- or efficiency-oriented manner. Furthermore, the preceding discussion shows, that different variables of reference can be chosen for the evaluation of the process performance.

C.1.3 Model equations and measurement quantities for model validation

The transient experiments conducted in the gram-scale adsorption chiller are used to validate the process model presented in section 3.2.1 by considering the spatially distributed equations of the adsorbent composites given in section 3.2.3. The model of the CDC composites is parameterized using the material parameters listed in Table B-6. The model validation aims at the investigation of the physical plausibility of the process model. For clarity, the model equations are shortly reproduced in the following where explicit attention is paid to the validation quantities and the fitting parameters. Figure C-5 schematically shows the gram-scale adsorption chiller with the measurement quantities used for the model validation.

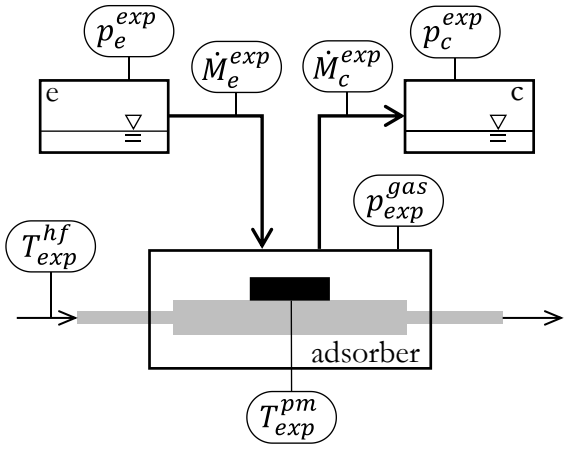

Figure C-5: Schematic representation of the gram-scale adsorption chiller with the measured quantities and measurement positions used for validation of the process model.

Besides mass flows ($\dot{M}_e^{exp}$ and $\dot{M}_c^{exp}$), the pressures in evaporator (p_e^{exp}) and adsorber (p_{exp}^{gas}) are used for validation of the process model. Furthermore, the inlet temperature of the adsorber heat transfer fluid (T_{exp}^{hf}) as well as the bottom side temperature of the adsorbent composites (T_{exp}^{pm}) are used in the validation procedure.

Adsorber

The adsorber is modelled with conservation equations for the four different phases shown in Figure 3-2: heat transfer fluid, passive mass, adsorbent composite, and free gas phase. For the model validation, the overall heat transfer resistance from heat transfer fluid to the aluminium support upper side is summarized in one heat transfer coefficient k^{hf}. Combining equations (3-7)-(3-9), the lumped-parameter energy balance for the adsorber heat exchanger is given by

$$m^{pm} c_p^{pm} \frac{\partial T^{pm}}{\partial t} = k^{hf} (T^{hf} - T^{pm}) - k^{pm} \left(T^{pm} - T|_{z=s_{cdc}} \right). \tag{C-1}$$

The heat transfer resistance between aluminium support and adsorbent composites bottom side is described with the heat transfer coefficient k^{pm}. T^{hf} is the process boundary temperature which is set to the Hex inlet temperature (T_{exp}^{hf}) and which corresponds to either the adsorption or desorption temperature level. Due to the fast switching of the pneumatic valves, almost constant temperature levels are established at the Hex inlet after few seconds. The temperature measured between aluminium support and composites bottom side T_{exp}^{pm} is the validation quantity for the simulated heat exchanger temperature T^{pm}. Furthermore, $T|_{z=s_{cdc}}$ represents the temperature at the lowest layer of the composites which is obtained from the distributed energy balance outlined below. To reproduce the tailing of the measured temperature profiles, the inertia of the Hex must be considered. For the aluminium hexagon Hex shown in Figure 6-14, these parameters are $m^{pm} \approx 21.06\ kg/m^2$ and $c_p^{pm} = 910\ J/kg/K$.

As outlined previously, the laboratory adsorber has not been optimized for minimal passive mass or gas phase hold up. Therefore, conservation equations of the adsorber gas phase are additionally required. The decisive parameter influencing the duration of the pre-heating and pre-cooling period and thus the switching times is the volume of the free gas phase V^{gas}. In terms of mass density and temperature, the free gas phase equations are given by (see equations (3-18) and (3-20))

$$V^{gas}\frac{\partial \varrho^{gas}}{\partial t} = \dot{M}_{e/c} - A_{comp}\dot{m}_0^v, \tag{C-2}$$

$$\left(\varrho^{gas}V^{gas}c_p^{gas} - \frac{\varrho^{gas}V^{gas}R}{MW}\right)\frac{\partial T^{gas}}{\partial t} = \dot{M}_e c_{p,e}(T_e - T^{gas}) - A_{comp}\dot{m}_0^v c_p^v(T - T^{gas}) + \frac{R}{MW}T^{gas}V^{gas}\frac{\partial \varrho^{gas}}{\partial t}. \tag{C-3}$$

The thermal radiation between the free gas phase and adsorbent composites $\dot{q}^{gas}$ is neglected. The adsorber gas-phase hold up (V^{gas}) was determined by equilibrium experiments in the gram-scale setup. With the valves between the adsorber and evaporator open, the adsorbent composites were initially equilibrated at a defined evaporator/ adsorber pressure p_1 and adsorption temperature T_1. Subsequently, the valves were closed and the temperature of the adsorber was increased to T_2 causing methanol to desorb into the free gas phase until an equilibrium pressure p_2 was reached. With the adsorption isotherm and with the mass of the adsorbent composites, the difference in equilibrium loading dX and the methanol mass desorbed was calculated. Neglecting the small amount of increased methanol mass in the interparticle voids, the volume of the free gas phase was calculated as follows, assuming ideal gas behaviour

$$V^{gas} = \frac{dX}{MW} M_{comp} \frac{R}{\frac{p_2}{T_2} - \frac{p_1}{T_1}}. \tag{C-4}$$

This type of equilibrium experiment was repeated several times revealing the volume of the free gas phase to $V^{gas} = 2.1\ l$.

In the adsorption cycle, once the pressure conditions are satisfied, the pneumatic vacuum valves open. For the model validation, the exchange flows $\dot{M}_{e/c}$ between evaporator and adsorber as well as adsorber and condenser are modelled with linear valve equations (see equation (3-19)) with $\beta_{e,c}$ being the fitting parameters describing the valve and MFM characteristics

$$\dot{M}_{e,c} = A_{comp} \beta_{e,c} \left(p_{e,c}^{sat} - p^{gas} \right). \tag{C-5}$$

The experimentally determined mass flows, as well as the pressures in evaporator and adsorber free gas phase, are used in the validation procedure.

The mass flux exchanged between the adsorbent and free gas phase is modelled with the effective diffusion coefficient formulated with the Dusty-Gas model. The transport equation is parameterized with permeation measurements (see section 4.4) and evaluated with the density gradient at the top adsorbent layer (see equation (4-12))

$$\dot{m}_0^v = -D^{eff} \frac{d\varrho^v}{d\zeta}\bigg|_{z=0}, \tag{C-6}$$

The adsorber model is completed using the distributed mass and energy conservation equations of the adsorbent composites as derived in section 3.2.3 (equations (3-55), (3-56), and (3-70)).

Evaporator & Condenser

The laboratory adsorption chiller is built without recirculation of refrigerant from the condenser to evaporator, and the liquid hold-ups are quite large that the change of mass during an experiment can be neglected. Therefore, no mass balances are used. The energy balances describing the change of energy in evaporator and condenser (equations (3-24) and (3-25)) are modified to represent the plant design. Kinetical resistance of the evaporation is neglected and thus the energy balance for the evaporator is given by

$$M_e c_{p,e}^l \frac{\partial T_e}{\partial t} = -\dot{M}_e \Delta_{evap} h(T_e) + \dot{Q}_e, \tag{C-7}$$

with the heat flow $\dot{Q}_e$ introduced to the evaporator from the external heat transfer medium circuit. The mass of refrigerant as well as the heat transfer coefficient of the heat flow are unknown and thus used as fitting parameters ($k_{1,e}$ and $k_{2,e}$) for the evaporator energy balance

$$\frac{\partial T_e}{\partial t} = \frac{1}{c_{p,e}^{l}} \frac{1}{\underbrace{M_e}_{k_{1,e}}} \left(k_{2,e} \left(T_e^{hf} - T_e \right) - \dot{M}_e \Delta_{evap} h \right). \tag{C-8}$$

In equivalence, the condenser energy balance in the unit Watt is given by

$$\frac{\partial T_c}{\partial t} = \frac{1}{c_{p,c}^{l}} \frac{1}{\underbrace{M_c}_{k_{1,c}}} \left(k_{2,c} \left(T_c^{hf} - T_c \right) - \dot{M}_c \left(\Delta_{evap} h + c_p^{gas} (T^{gas} - T_c) \right) \right), \tag{C-9}$$

with fitting parameters $k_{1,c}$ and $k_{2,c}$ and additionally taking the heat of condensation into account.

In summary, eight kinetical parameters are used for fitting the model behaviour to the experimental observations. For this, the dynamic profiles of the measured variables are used. The fitting parameters and measured quantities used for the model validation are summarized in Table C-2. At this point, it is noted that the comparatively large number of fitting parameters is motivated by the setup of the laboratory plant. For the process simulations carried out in this work, the process model is reduced in such a way that none of the fitting parameters appears in the model, and solely the kinetical behaviour of the adsorbent composites is investigated. The validation of the model is intended to show that the experimentally observed transient profiles are reproducible with the process model.

Table C-2: Fitting parameters and measurement quantities used for the validation of the process model.

Fitting parameters:	k^{hf}, k^{pm}, β_e, β_c, $k_{1,e}$, $k_{2,e}$, $k_{1,c}$, $k_{2,c}$
(Transient) measurement and validation quantities:	$\dot{m}_e^{exp}$, $\dot{m}_c^{exp}$, p_e^{exp}, p_{exp}^{gas}, T_{exp}^{pm}

Subsequently, the routine and procedure applied for the model validation are outlined.

C.1.4 Routine for model validation

For the validation of the process model a MATLAB [161] routine has been developed containing the following main parts: Loading of the experimental data, extract boundary conditions for

process simulations, initialize simulations with boundary conditions from experiments, define initial values for the fitting parameters, process simulation to CSS, comparison of experimental and simulation profiles in the least mean square sense, finish routine if termination criterion is achieved or else start new simulations with adjusted fitting parameters. These steps are summarized and visualized in the Flowchart in Figure C-6.

Initially, the experimental data set is chosen by defining the temperature levels and duration of evaporation (t_e) or condensation (t_c) period. After loading the experimental data in CSS to the MATLAB workspace, the data (F_{exp}) is interpolated to 1s steps (the recording rate of the data logger is 10 Hz). From the data set, the boundary conditions are extracted. Besides the temperature of the adsorber heat transfer fluid inlet (T_{exp}^{hf}), the pressures in evaporator (p_e^{exp}) and condenser (p_c^{exp}) are extracted. From these pressure values, the respective saturation temperatures in the evaporator and condenser are calculated, which serve as boundary temperatures for the process simulations. In the next step, the nonlinear least-square solver (lsqcurvefit with 'trust-region-reflective' algorithm) is initialized by defining an initial guess of the fitting parameters x_0 as well as lower and upper bounds. Furthermore, the experimental input data t with the observed output F_{exp} are passed to the least-square solver as well as a nonlinear function $fun(x,t)$ with solution $F_{sim}(x,t)$. In the least-square optimization, the coefficients x are found which best fit the results from $fun(x,t)$ to F_{exp} and thus solve the problem

$$\min_x \left|\left|F_{sim}(x,t) - F_{exp}\right|\right|_2^2 = \min_x \sum_i \left(F_{sim}(x,t_i) - F_{exp,i}\right)^2. \tag{C-10}$$

In other words, the parameter vector x is searched for which minimizes the deviation between the transient simulation and experimental data sets. In the next step, the four boundary temperature levels (e, c, ad, de), as well as the durations of evaporation and condensation steps, are passed to the sub-routine $fun(x,t)$ containing four DAE solver calls (ode15s) for the process simulation following the four partial steps of the adsorption refrigeration cycle (details of the simulation procedure are given in section D.1).

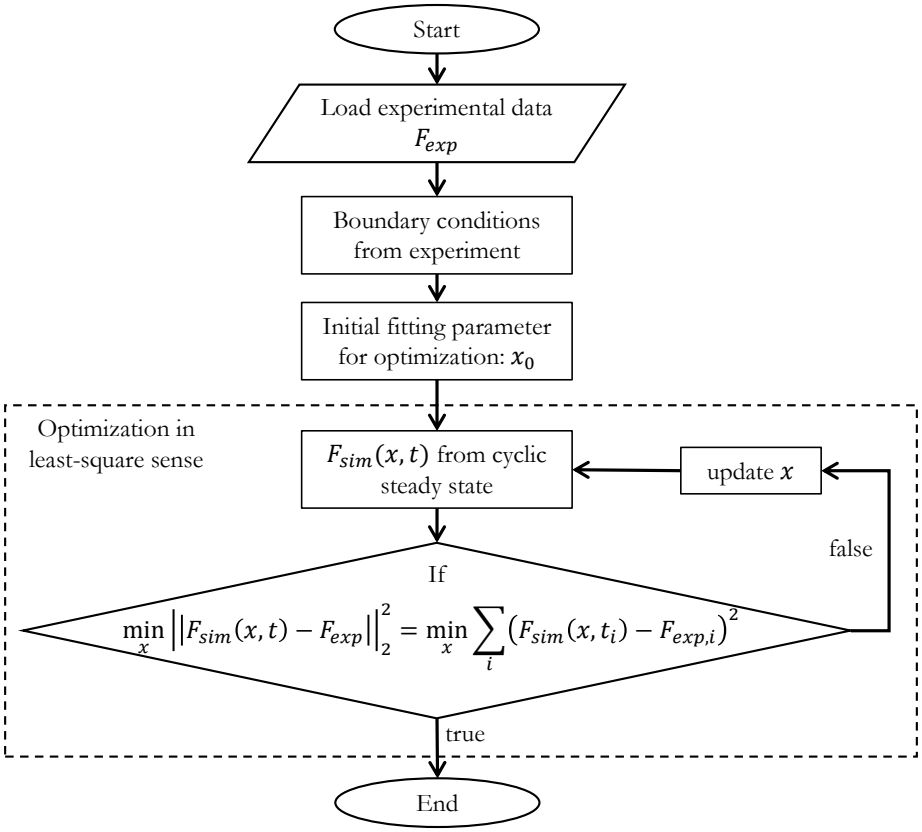

Figure C-6: Flowchart describing the routine used for validation of the process model with experimental date from the gram-scale adsorption chiller.

Beforehand, the DAE solver tolerance, as well as the termination criterion for CSS, are defined. The individual steps of the cycle are simulated following the experiments: evaporation and condensation duration are adjusted in the respective solver calls with the respective durations used in the experiment. In the pre-heating and pre-cooling phases, user-defined event functions are applied to terminate the ode15s-solver as soon as the respective pressure conditions are satisfied. Therefore, the duration of heating and cooling periods is not predefined but result from the simulations in dependence of the heat and mass transfer kinetics as well as the gas-phase hold-up. It follows, that comparison of the pre-heating and pre-cooling times of experiments and simulations are good measures of the quality of the simulation model. In CSS, the simulation terminates, and equidistantly spaced simulation results $F_{sim}(x,t)$ are obtained by interpolation of the result vector following the spacing of the measurement data, which are used in the least-square optimization following equation (C-10).

C.1.5 Results of the model validation

The validation of the process model is discussed with the CSS of two experiments and simulations with different dynamics conducted with evaporation and condensation times of $t_{e,c} = 200s$ and $t_{e,c} = 600s$, respectively. Figure C-7 shows transient profiles of the pressure in the adsorber, evaporator, and condenser as well as simulation results obtained with the dynamic model outlined in section C.1.3. Furthermore, temperature profiles of passive mass and the exchanged mass fluxes are plotted.

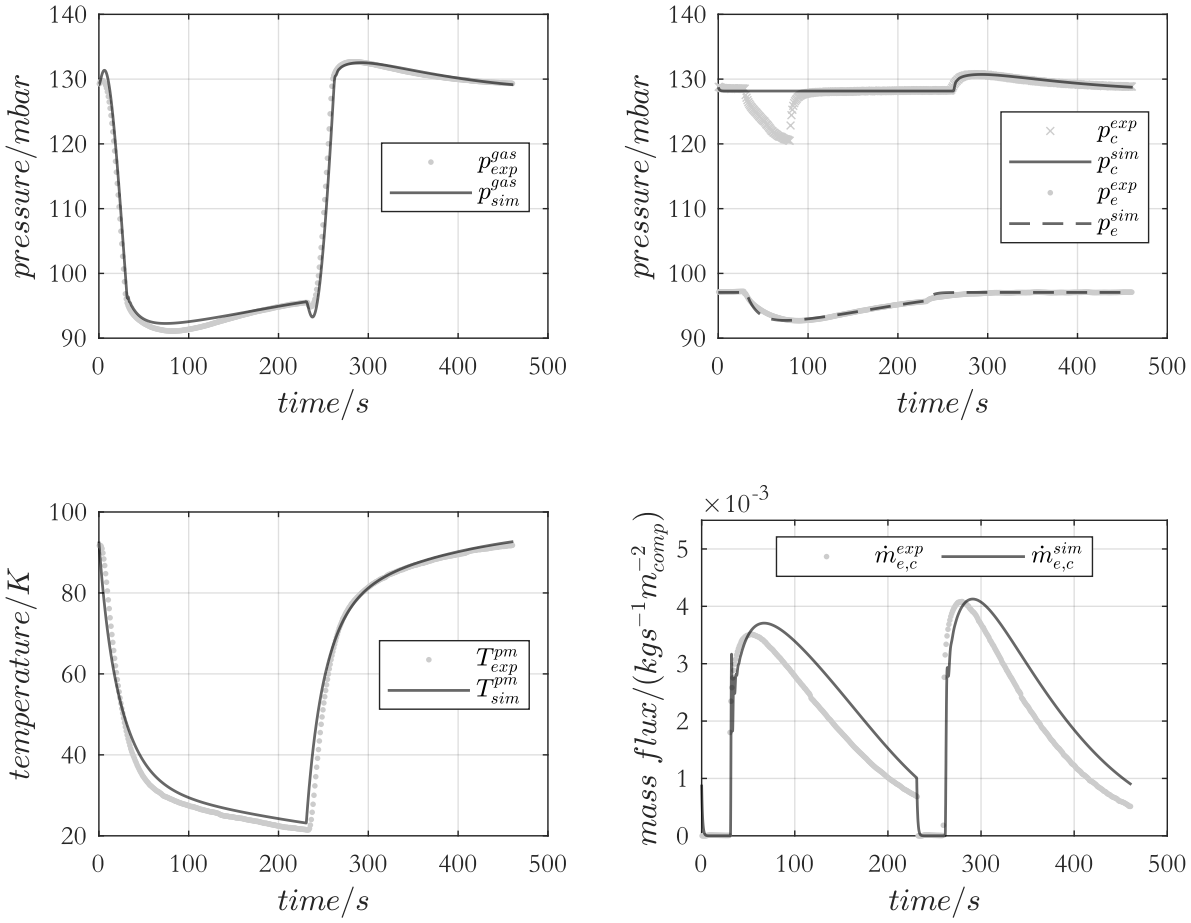

Figure C-7: Experimental and simulation results of the adsorption cooling process with $t_{e,c} = 200s$ and temperature boundaries of $T_e = 15°C, T_{c,ad} = 20°C, T_{de} = 85°C$.

The simulation results reproduce the experiments well. Even details such as the temporary pressure drop in the adsorber at the beginning of the heating period (at approx. 240 s) as well as the switching periods are simulated precisely. Especially the dynamic states, e.g., pressure and temperature profiles, can be reproduced well with the model. However, small deviations are

visible when comparing the experimental and simulated mass fluxes and thus the integral mass exchanged is slightly overestimated in simulations with short cycle times.

In addition, simulations and experiments at the same temperature levels with a cycle time of 600 s are compared. Figure C-8 shows dynamic states as well as the exchanged mass fluxes. In equivalence to the short cycle time, the experimental, transient states are reproduced quite well with the process simulations. However, again, the simulated mass fluxes are slightly deviating from the experiments. While the peak is slightly underestimated in the simulations, the mass flow in the middle range is slightly overestimated.

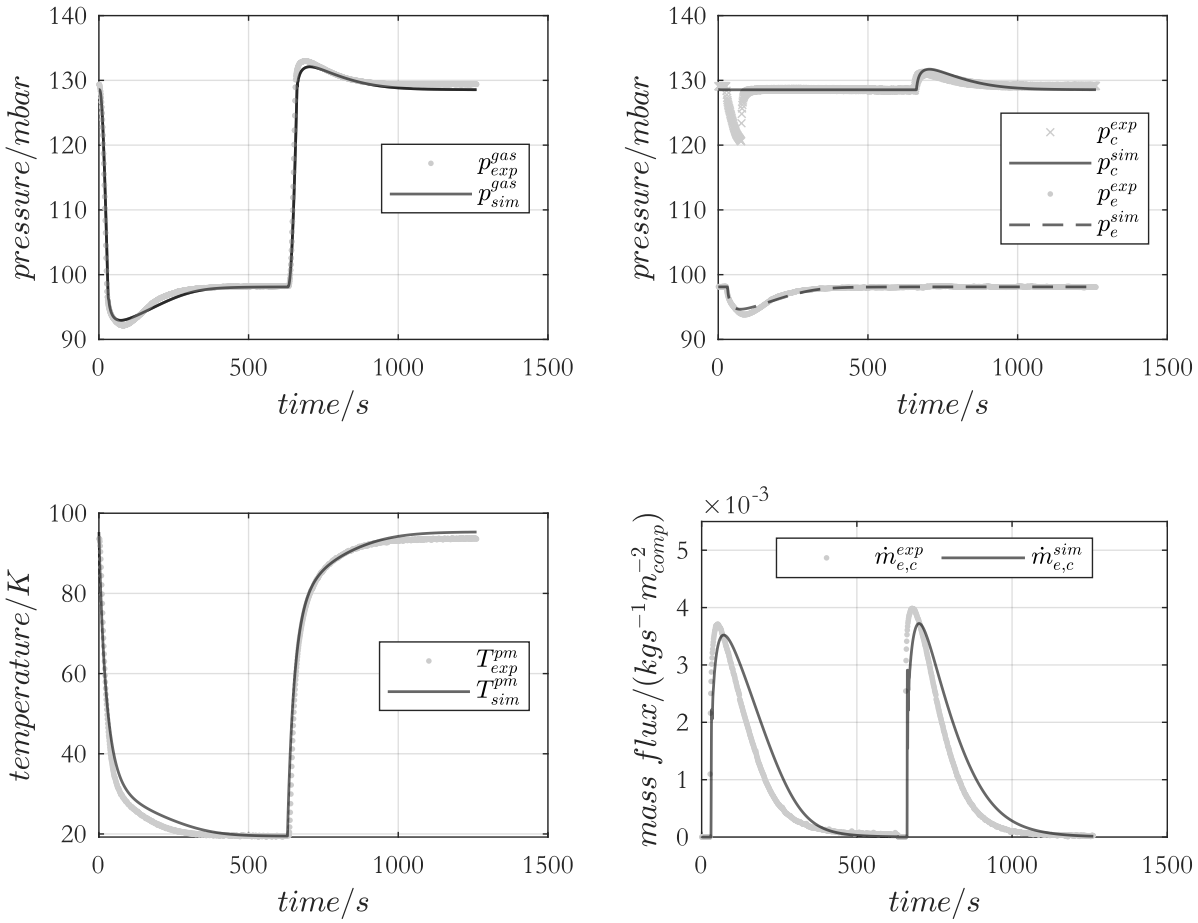

Figure C-8: Validation of process model with measurement results of an experiment with $t_{e,c} = 600s$ and temperature boundaries of $T_e = 15°C, T_{c,ad} = 20°C, T_{de} = 85°C$.

The previous discussion shows that the distributed parameter process model is mathematically capable to reproduce the dynamics of a real adsorption refrigeration cycle. To investigate the influence of the adsorbent composite on process performance and to conduct a combined

process and material design, the process model is reduced for the process simulations, solely taking the kinetic parameters of the adsorbent composites into account.

C.2 Summary

Besides the adsorbent composite related parameters, a validated process model is crucial for conducting representative process simulations.

A novel small-scale chiller has been used for the investigation of gram-scale adsorbent composites under transient process conditions with flexible temperature conditions. In this setup, the exchanged volume flow between evaporator/ adsorber and desorber/ condenser serves as the measurement quantity which is used in the post-processing step to calculate the adsorption and desorption rates. With this setup, carbide-derived carbon samples were investigated under process conditions. The transient experimental profiles were the base for the validation of the distributed process model derived in chapter 3 with the individually obtained material parameter characterized in chapter 4. The process model was extended for the sake of describing the experimental setup. Applying parameter fitting of simulation results to the transient experimental profiles, a good accuracy could be obtained. It was also shown that physical details can be represented by the process model, e.g., pressure undershoot at the beginning of the pre-heating phase and the duration of the isosteric phases.

Since the combined material and process development is the aim of this work, whereby the focus is on the resistances in the adsorbent composites, the process model is reduced for the process simulations in such a way that only the kinetic influences of the composites are considered. Thus, no specific component resistances (e.g., of the evaporator, the check valves, or the heat transfer between Hex and composites) are considered.

Appendix D.

D.1 Modelling scheme of adsorbent composites

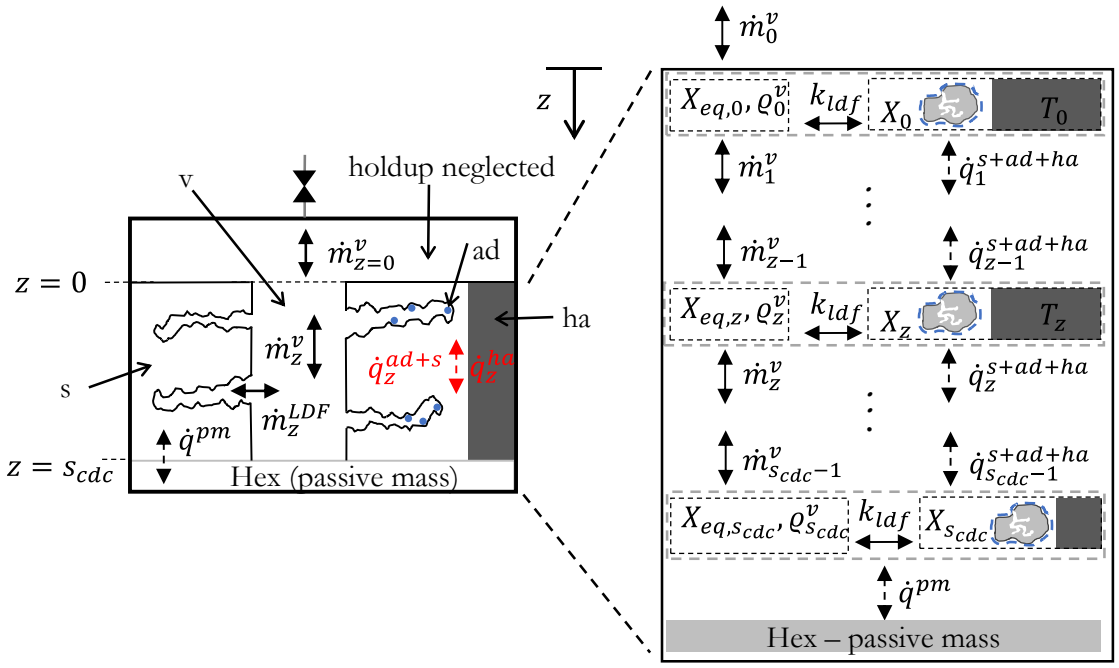

Figure D-1: Modelling domain of adsorbent composites containing adsorbent primary particles, interparticle voids, and heat conducting additive (left); discretization scheme of the adsorbent composites with exchanged mass and heat fluxes between adjacent elements (right).

D.2 Numeric, implementation strategy, and process boundary conditions

D.2.1 Discretization of spatial derivatives

Finite Volume method

For the numerical implementation, the partial differential model equations (PDEs) need to be discretized to obtain ordinary differential equations (ODEs). For that, the spatial first and second-order derivatives are approximated using the finite volume method [162]. In each volume

element, the states and variables are constant. The fluxes are formulated on the boundaries of adjacent volume elements.

For the spatial derivatives of the adsorbent composites, a staggered grid is applied as shown in Figure D-2 with two grids latterly shifted by half a volume element. One grid (•) denotes for the states and variables which are averaged in each volume element $\Delta V = A_{comp}\,\Delta z$, where A_{comp} is the composites cross sectional area. The other grid (x) applies to the fluxes on the volume element boundaries. By that, the incoming and outgoing fluxes are balanced for each volume element guaranteeing the conservation of mass and energy which is significant for cyclic processes. For the diffusive terms (second-order derivatives, e.g., $\frac{\partial \dot{q}}{\partial z}$), central differences are used. Exemplarily, central differences are applied for the heat fluxes in the composites on the grid (x) and their gradients on the grid (•) as follows

$$\dot{q}_z = -\lambda\,\frac{T_{z+1} - T_z}{\Delta z}, \tag{D-1}$$

$$\left.\frac{\partial \dot{q}}{\partial z}\right|_z = \frac{\dot{q}_z - \dot{q}_{z-1}}{\Delta z}. \tag{D-2}$$

At first glance, this notation is reminiscent of forward or backward differences. However, due to the latterly staggered grid, these formulations denote central differences.

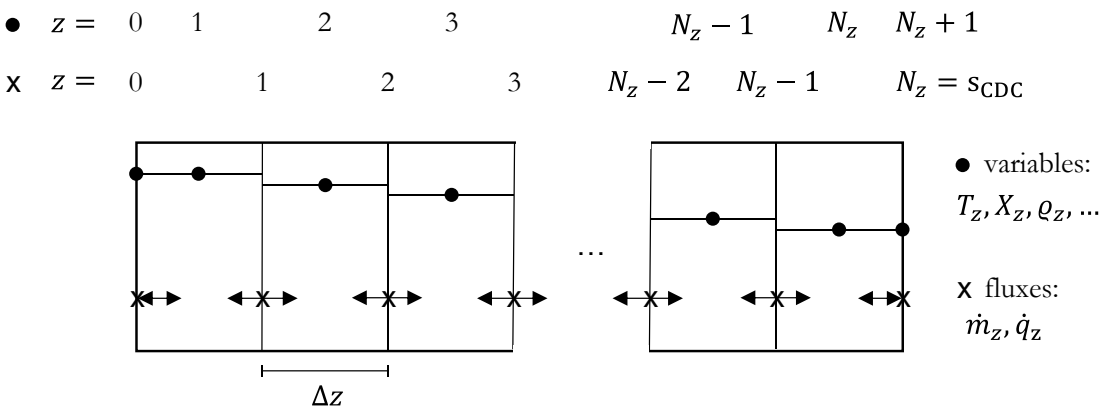

Figure D-2: A staggered grid of N_z finite volume elements with $\Delta V = A_{comp}\,\Delta z$. Fluxes are formulated on the boundaries of adjacent elements (x). Constant profiles are assumed for the variables within each element. Heat and mass fluxes can either be in the positive or negative coordinate direction. The states can either be "transported" to the right or the left depending on the flow direction.

The same procedure accounts for the discretization of the mass flux and spatial mass flux gradients.

An upwind scheme is applied for the convective terms (e.g., $u\frac{\partial \varphi}{\partial z}$) to account for the flux direction [163], which is generally written as follows

$$u\frac{\partial \varphi}{\partial z}\Big|_z = u^+\frac{\varphi_z - \varphi_{z-1}}{\Delta z} + u^-\frac{\varphi_{z+1} - \varphi_z}{\Delta z}. \tag{D-3}$$

For the convective enthalpy transport in the composites ($\dot{m}c_p\frac{\partial T}{\partial z}$), only incoming fluxes change the temperature of the respective volume element which is considered using two variables (α, β) accounting for the inflows. The convective enthalpy flux term is discretized as follows

$$\dot{m}c_p\frac{\partial T}{\partial z}\Big|_z = \alpha\dot{m}_{z-1}c_{p,z-1}\frac{T_{z-1} - T_z}{\Delta z} + \beta\dot{m}_z c_{p,z}\frac{T_{z+1} - T_z}{\Delta z}, \tag{D-4}$$

with $\alpha = 1$ if $\dot{m}_{z-1} > 0$ and $\beta = 1$ if $\dot{m}_z > 0$, else, $\alpha = \beta = 0$.

The convective terms accounting for the bed movement in the TMB setup are also discretized on an equidistant grid in y-coordinate direction using a finite volume upwind scheme to guarantee for numerical stability, e.g., for the first-order derivative of the temperature in the heat transfer fluid

$$\frac{\partial T^{hf}}{\partial y} = \frac{T_{j+1} - T_j}{\Delta y}. \tag{D-5}$$

For the convective terms in the TMB setup, no flow reversal needs to be taken into account, since the bed movement is solely in one direction.

D.2.2 Process simulations of 2-bed adsorption chillers - Numeric, implementation strategy, and simulation environment

Numeric

The spatial (first and second order) derivatives of the adsorbent structure (z-coordinate) are discretized with an equidistant grid using the finite volume method, with fluxes formulated at the boundaries of adjacent discretization elements to ensure mass and energy conservation (also known as staggered-grid as introduced previously).

By discretizing the spatial derivatives of the PDEs, a set of ODEs results related to time, and together with the algebraic equations a DAE-system is obtained of the form

$$\boldsymbol{B}(\boldsymbol{y},\boldsymbol{x},\boldsymbol{\lambda},t)\frac{d\boldsymbol{y}}{dt}=\boldsymbol{f}(\boldsymbol{y},\boldsymbol{x},\boldsymbol{\lambda},t), \tag{D-6}$$

$$0=\boldsymbol{g}(\boldsymbol{y},\boldsymbol{x},\boldsymbol{\lambda},t), \tag{D-7}$$

$$\boldsymbol{y}(t_0)=\boldsymbol{y_0}. \tag{D-8}$$

$\boldsymbol{y}$, $\boldsymbol{x}$, and $\boldsymbol{\lambda}$ are vectors of the dynamic variables, algebraic variables, and independent model parameters, respectively, t is the time, $\boldsymbol{f}$ and $\boldsymbol{g}$ are vectors containing the differential and algebraic equations, and $\boldsymbol{B}$ is the left-hand side matrix which is singular for a DAE system. The DAE system allows the calculation of the solution vector $\boldsymbol{y}$ in dependence of space, time (for the dynamic models), and of the model parameters $\boldsymbol{\lambda}$. An example of a DAE system is the distributed parameter model outlined in section 3.2.3. To obtain the solution vector, the DAE needs to be solved by time integration with a DAE integrator.

Process modelling and simulation tool

The initial value problem in equation (D-6) with consistent initial values $\boldsymbol{y_0}(t_0)$ is dynamically solved for the solution vector $\boldsymbol{y}$ by time integration using the MATLAB solver ode15s for numerically stiff problems. An absolute and relative solver accuracy of $1\cdot10^{-5}$ is used. For fast investigation of different parameter sets the code is parallelized using a MATLAB function. The different parameters are varied in nested *for* loops whereby the outer loop is used for varying the process cycle time with a *parfor* loop.

For the solution of the DAE-system, the right-hand side function is subsequently solved three times within one cycle with the ode15s solver. The solution vector obtained at the final execution time of the previous solver call serves as input for the next solver call. Initially, the pre-cooling period of the adsorber is simulated which is accompanied by a pressure decrease. An event function is used to terminate the solver as soon as the pressure in the top composite layer reaches evaporator pressure. The final execution time serves as starting time for the subsequent evaporation step. After reaching half of the cycle time $t_{cyc}/2$, the solver terminates, and the pre-heating and condensation steps follow in the third solver call. Opening the valve between the evaporator and the adsorber causes a sudden increase in mass flux. At this point, the Neumann boundary condition at the top layer energy conservation equation is changed to a Danckwerts boundary condition (see equations (3-76) and (3-77)). By that, the transient temperature profile experiences a step resulting in a stiff DAE system. Stiff differential equations are numerically

challenging, especially when applying implicit multi-step solvers. By using a pressure event-function for the pre-cooling step, the point in time of valve-opening is detected, the solver terminated, the boundary conditions are changed, and the solver starts again with consistent initial values. Thus, the discontinuity is detected, and the numerical stability is increased. In the last solver call, the pre-heating and desorption steps are simulated. For the pre-heating phase, no event-function is required since the opening of the valve between adsorber and condenser solely evokes a mass outflow and thus the boundary condition is not changed. Subsequently to the third solver call, the three result matrixes are appended resulting in the solution matrix containing the transient state and algebraic solution variables of cycle $\boldsymbol{i}$.

After every cycle $\boldsymbol{i}$, each entry of the final state solution vector $\boldsymbol{y_i}$ is compared with the final solution vector of the previous cycle $\boldsymbol{y_{i-1}}$ calculating the maximal deviation between two state variables. This value gives the maximal relative and absolute error serving for the determination of CSS

$$Err_{rel} = max\left(\frac{\left||\boldsymbol{y_i}| - |\boldsymbol{y_{i-1}}|\right|}{|\boldsymbol{y_i}|}\right) < 1 \cdot 10^{-3}, \tag{D-9}$$

$$Err_{abs} = max\left(\left||\boldsymbol{y_i}| - |\boldsymbol{y_{i-1}}|\right|\right) < 1 \cdot 10^{-6}. \tag{D-10}$$

If one of the criteria is reached, the simulation aborts, the results in CSS (of the last three solver calls) are saved to a result file and the simulation is finished.

Process boundary conditions and fixed parameters

To reduce the free parameter space, some process conditions and the temperature levels were held constant in the simulations which are listed in Table 3-1. In addition, the number of grid points and the initial material model parameters were fixed according to Table D-1. It is important to take the inert mass of the Hex into account to simulate the proper dynamic of the process. Throughout this thesis, a specific mass related to the cross-sectional area of the CDC composites is used to account for the passive mass.

Table D-1: Set of parameters kept constant in the simulations of the idealized two-bed adsorption refrigeration process (unless otherwise indicated).

grid points CDC-composites	$N_z = 120$
initial material model parameters	See Table B-6

D.2.3 Multi-bed process simulations - Numeric, implementation strategy, and simulation environment

Numeric

The mathematical models of the SMB and TMB adsorption cooling process introduced in chapter 7 have a similar mathematical structure containing algebraic equations, ordinary differential equations (ODEs), and partial differential equations (PDEs). The structure of the transient TMB model is similar to that of the SMB model, but the differential equations of the TMB approach include additional convection terms with u^{bed} to describe the transport in the moving bed.

The spatial (first and second order) derivatives of the adsorbent structure (z-coordinate) are discretized with an equidistant grid using the finite volume method, with fluxes formulated at the boundaries of adjacent discretization elements to ensure mass and energy conservation (staggered-grid, see Appendix D.2.1). This discretization method is the same as used for the adsorbent structures in the 2-bed process model. Furthermore, the spatial derivatives of the TMB in moving bed direction (y-coordinate) account for the convective flow of the AdHex and counterflow of heat transfer fluid. Due to the strictly convective transport in the moving bed direction, a first-order upwind scheme was used to guarantee numerical stability. However, due to the truncation error of the first order discretization, numerical dispersion occurs. Due to numerical dispersion, the solution of the TMB slightly underestimates the SMB solution. The method of characteristics was used in an example to prove that without numerical dispersion the TMB solution is the limit of the SMB solution for a high total number of adsorbers (see Appendix D.6).

As indicated in the introduction of chapter 7, the major advantage of the TMB model is its steady-state nature and the associated considerably lower cost of solving the model for the steady-state solution. The steady-state TMB model is obtained from the differential equations in section 7.1.2 by setting time derivatives to zero resulting in a DAE system with spatial derivatives of the state variables. By applying the discretization methods outlined in Appendix D.2.1 on the first and second-order spatial derivatives, the DAE is reduced to a large set of nonlinear algebraic equations (NLAEs) of the form

$$\boldsymbol{h}(\boldsymbol{y}, \boldsymbol{\lambda}) = 0, \tag{D-11}$$

with the state vector $\boldsymbol{y}(y, z)$ being a function of the positions in the adsorbent structure (z) and moving bed (y) and $\boldsymbol{h}$ the vector function containing the nonlinear algebraic equations. To obtain

the solution of the state vector, the NLAE system needs to be solved with an appropriate numerical solver. In a further step, the steady-state solution of the NLAE system $\boldsymbol{y_{ss} = y_0(\lambda_0)}$ serves as consistent initialization for the parameter continuation solver

$$\boldsymbol{h(y_0(\lambda_0), \lambda_0) = 0.} \tag{D-12}$$

By varying one entry λ of the parameter vector $\boldsymbol{\lambda}$, the current state of a model changes. The principle of parameter continuation is discussed in detail by Krasnyk in his thesis [164] and is briefly outlined in the following:

1. Specification of consistent initial values $\boldsymbol{h(y_{(0)}, \lambda_{(0)}) = 0.}$
2. Prediction of a new state $\boldsymbol{\tilde{y}_{(k+1)}}$ close to the solution branch $\boldsymbol{y(\lambda)}$ via a predictor step at $\boldsymbol{\lambda_{(k+1)} = \lambda_{(k)} + \Delta\lambda_{(k)}}$. The step size $\boldsymbol{\Delta\lambda_{(k)}}$ can either be fixed or increased according to a predefined rule. The index k represents the respective predictor step.
3. Corrector step of the predicted state $\boldsymbol{\tilde{y}_{(k+1)} \rightarrow y_{(k+1)}}$ to the solution branch $\boldsymbol{y(\lambda)}$.
4. Termination of the parameter continuation if the variation interval $\lambda \in [\lambda_{min}, \lambda_{max}]$ is completed or the maximal number of continuation steps is reached.

Important parameters of a continuation solver are the initial step size $\boldsymbol{\Delta\lambda_{(0)}}$, the maximal step size $\boldsymbol{\Delta\lambda_{max}}$ and the direction of the parameter continuation (to lower or higher values of λ). In regions of the solution branch with small gradient $\boldsymbol{dy/d\lambda}$, larger steps $\boldsymbol{\Delta\lambda_{(k)}}$ can be used.

Standard predictor methods are the *classical predictor* or the *tangent predictor* as shown in Figure D-3 for one state variable y.

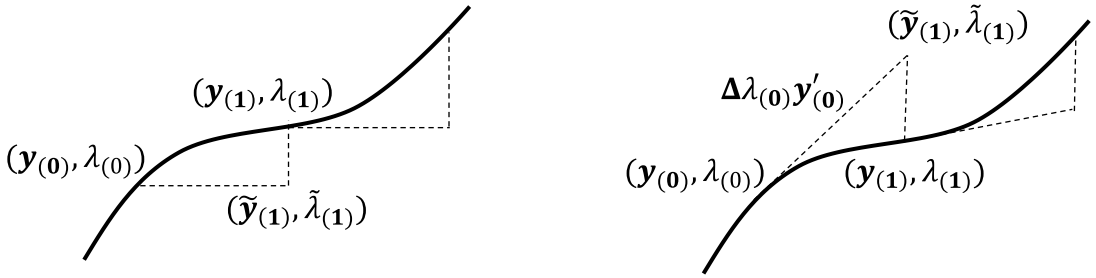

Figure D-3: Schema of classic (left) and tangent (right) predictor method to predict a new state vector $\boldsymbol{\tilde{y}_{(k+1)}}$ close to the solution branch [165].

The predicted states used in the classic predictor method are $\boldsymbol{\tilde{y}_{(k+1)} = y_{(k)}}$. For the tangent predictor method, the gradient $\boldsymbol{y'_{(k)}}$ at $(\boldsymbol{y_{(k)}, \lambda_{(k)}})$ is used and the predicted states are

$$\tilde{\boldsymbol{y}}_{(\boldsymbol{k+1})} = \boldsymbol{y}_{(\boldsymbol{k})} + \Delta\lambda_{(\boldsymbol{k})}\boldsymbol{y}'_{(\boldsymbol{k})}, \tag{D-13}$$

$$\boldsymbol{y}'_{(\boldsymbol{k})} = -\frac{\boldsymbol{h}'_{\lambda}\left(\boldsymbol{y}_{(\boldsymbol{k})},\lambda_{(k)}\right)}{\boldsymbol{h}'_{\boldsymbol{y}}\left(\boldsymbol{y}_{(\boldsymbol{k})},\lambda_{(k)}\right)} = -\frac{d\boldsymbol{y}}{d\lambda}. \tag{D-14}$$

$\boldsymbol{h}'_{\lambda}$ and $\boldsymbol{h}'_{\boldsymbol{y}}$ are derivatives of the non-linear algebraic equations according to the parameter $\boldsymbol{\lambda}$ or the state variables $\boldsymbol{y}$, respectively. The corrector step is solved iteratively with a Newton method with the predicted states as starting value. The index $\boldsymbol{i}$ counts the number of Newton iterations and the index $\boldsymbol{k}$ the number of predictor steps. The classical Newton method is of the form

$$\boldsymbol{y}^{\boldsymbol{i+1}}_{(\boldsymbol{k+1})} = \boldsymbol{y}^{\boldsymbol{i}}_{(\boldsymbol{k+1})} - \frac{\boldsymbol{h}\left(\boldsymbol{y}^{\boldsymbol{i}}_{(\boldsymbol{k+1})},\lambda_{(k+1)}\right)}{\boldsymbol{h}'_{\boldsymbol{y}}\left(\boldsymbol{y}^{\boldsymbol{i}}_{(\boldsymbol{k+1})},\lambda_{(k+1)}\right)}. \tag{D-15}$$

Process modelling and simulation tool

To solve the dynamic DAEs or steady-state NLAEs to obtain the solution vector of the state variables, the equations need to be implemented and solved with appropriate solvers. Profound discussions of the modelling and simulation environment used in this work for the multi-bed adsorption refrigeration processes as well as the implemented solvers are given in [164], [166].

The system of equations was implemented in the object-oriented modelling tool ProMoT using modelling definition language (MDL), from which the symbolic model information is translated into C++ simulation code. The simulation environment Diana is a platform for dynamic simulations and nonlinear analysis of DAEs or calculation of NLAEs, providing efficient solvers for dynamic simulations, parameter continuation, and optimization [167]. Dynamic solvers were utilized to solve the models dynamically (SMB model and transient TMB model) and steady-state solvers were used to solve the NLAE (steady-state TMB model). The scripting language Python is used to organize the simulation environment, e.g., organize the switching events in the SMB model.

In this work, for solving the DAEs (SMB and transient TMB model), the IDA solver by Sundials was applied, which uses a variable order, variable-coefficient Backward Differentiation Formula (BDF) integration method [168]. The nonlinear analysis and parameter continuation of the steady-state TMB model is done by a predictor-corrector method with a tangent predictor. A damped Newton method with a line search algorithm is implemented in the solver and has been used as a corrector method [164]. Parameter continuation of the residence time of the moving bed is used for the calculation of steady-state solution branches.

The python-based simulation environment was built in a way, that the desired model, parameter settings, and simulation strategy can be chosen in the main file. Depending on the selected settings, the appropriate ProMoT files are called and compiled to C++ simulation code using the *mdl2diana* command. Subsequently, the simulation code is solved dynamically for the cyclic steady-state solution, or by applying parameter continuation. The reporting interface is adjusted so that the desired model variables are saved to MATLAB files for post-processing.

Solution strategy of SMB and TMB simulations

The modelling tool ProMoT provides object-oriented modelling, allowing for aggregation of submodules to a parent composite model unit and inheritance of modelling units of other modules [166]. Specifically, once a module has been defined, its properties can be inherited by other modules, or the module can be multiplied. Thus, one single adsorber module based on the SMB model is defined and a multi-bed process with any number of beds can be created by multiplication. However, recalling the structural similarity of the two modelling approaches, and to develop a TMB model consistent with the SMB, the whole set of differential and algebraic equations was defined in one ProMoT module and the distributed equations were indexed for the adsorbent structure and the adsorber number (SMB)/ position in the moving bed (TMB). Since the only differences between the two model approaches are the convective terms with u^{bed} in the differential equations, a discrete switching variable is used to switch between the two models. In the case of an SMB simulation, the switching variable is set to 0 before compilation, in the case of a TMB simulation, it is set to 1. In addition to the ProMoT module containing the algebraic and differential equations of the adsorbers, modules for the evaporator, condenser as well as parameters of the appropriate modules are defined. The ProMoT modules containing the parameters are inherited to the appropriate submodule. Exemplarily, the "parameters_evaporator.mdl" module is inherited to the "evaporator.mdl" submodule, and so on.

To calculate multi-bed adsorption refrigeration processes, the coupling between adsorbers and evaporator as well as adsorbers and condenser according to the process setups in Figure 7-3 is needed. This is obtained by defining input and output variables. Exemplarily, the saturation pressure of the evaporator is calculated as a function of the evaporator temperature in the evaporator module and defined as output for the adsorber module. Here, the evaporator pressure is defined as the input variable used to evaluate the pressure condition which defines whether a mass flux is provided by the evaporator or not. The mass flux, however, once the pressure condition is fulfilled, is determined by the density gradient in the top layers of the adsorbent structure, and thus calculated in the adsorber module. Therefore, the mass fluxes of each

adsorber module are provided as output variables for the evaporator and summarized in the evaporator module to the integral adsorption flux used to calculate the cooling power.

After compilation of the model, it is appropriately solved depending on the predefined settings. For both model approaches, a consistent set of initial values is predefined which is called beforehand simulation. Furthermore, the reporting interface is adjusted depending on the variables to be saved.

First, the solution strategy of the dynamic SMB model is outlined. The large DAE system containing the model equations of all adsorber beds, evaporator module, and condenser module is dynamically solved for the residence time τ_{sw} of each adsorber at one position j. Thus, according to equation (7-13), the time set for the simulations depends on the predefined process cycle time t_{cyc} and total number of adsorber modules j_{max}. Once the solver has reached the predefined time and is finished, a subroutine is called increasing the position index j of each module of all dynamic states ($X_j(z), \varrho_j^v(z), T_j(z), T_j^{pm}$) by 1. The index of the states of the last module j_{max} is set to 0 according to the boundary conditions in equation (7-12). The position index of the heat transfer fluid velocity T_j^{hf} is not adjusted, the direction and velocity of its movement is rather defined by the predefined fluid velocity. By this, the movement of the adsorber modules in counterflow to the heat transfer fluid is achieved following Figure 7-1. After $(\tau_{sw} \cdot j_{max})$ solver calls, each adsorber module reaches its starting position completing one cycle. After every cycle i it is checked whether CSS has already been reached by comparing the state solution vector $\boldsymbol{y_i}$ with the solution vector of the previous cycle $\boldsymbol{y_{i-1}}$ in accordance with equations (D-9) and (D-10). If either the relative or absolute tolerance has been reached, the simulation breaks, the results in cyclic steady-state (of the last solver call with τ_{sw}) are saved to a Matlab file and the simulation is finished. Only the results of the last solver call are saved to reduce the file size. The solution is assembled and visualized in post-processing over an entire cycle.

The size of the DEA system linearly increases with the number of adsorber modules, and thus, the greater the amount of adsorbers, the higher the simulation effort. Additionally, the switching periods τ_{sw} decrease if more adsorber modules are simulated. Practically this means, that the dynamic solver is interrupted more often during a cycle with many adsorbers compared to a simulation with fewer adsorbers. Due to the implicit integration method with small step sizes at the beginning of each solver call, many short solver calls are numerically more expensive than

one solver call with a long cycle time. Thus, it can be summarized that the simulation time even increases over-proportionally with the number of adsorber beds.

The solution strategy of the TMB model involves similar approaches. After loading the set of consistent initial values, the spatially discretized, transient TMB-model is solved by time integration for the solution of the state vector $\boldsymbol{y}$ using the dynamic IDA solver. However, in contrast to the SMB simulations, the execution time of the solver is always set to the bed residence time τ^{bed} according to equation (7-21), independent of the number of discretization points of the moving bed. This continuity is one advantage of the TMB model compared to the SMB model, allowing an implicit solver to take larger steps using its step control. When the solver has successfully executed after τ^{bed}, the error considerations in equations (D-9) and (D-10) are applied, checking whether the cyclic steady state has been reached. If not, a new cycle is started. When cyclic steady-state is reached, the dynamic simulation breaks, and one last solver call with a steady-state solver is conducted solving the system of NLAEs of the steady-state TMB model (see equation (D-11)) with the solution from CSS as initial values

$$\boldsymbol{y_{(0)} = y_{ss} = y_{css}}. \tag{D-16}$$

Finally, the results of the steady-state solution are saved to a MATLAB file, and the simulation is finished.

This steady-state solution of the TMB model is further used initializing the parameter continuation solver to calculate solution branches for a variable bed residence time

$$\boldsymbol{h}\left(\boldsymbol{y_0}\left(\tau_0^{bed}\right), \tau_0^{bed}\right) = 0. \tag{D-17}$$

For initialization, a steady-state solution is calculated with a residence time of $\tau_0^{bed} = 300\ s$ and a variation interval of $\tau^{bed} \in [40\ s, 2000s]$ is chosen for the parameter continuation. Furthermore, the initial step size of the predictor step is chosen to be $\boldsymbol{\Delta\lambda_{(0)}} = 1 \cdot 10^{-5}$ and no limitation is set to the maximal step size. The initial direction of the continuation on the solution branch was chosen to be towards shorter residence times. For the corrector steps solved with a damped Newton method, a tolerance of $1 \cdot 10^{-6}$ has been used.

In the 2-bed process simulations used for the combined process and material design, the number of discretization elements of the adsorbent is of crucial importance to resolve steep gradients and to be able to simulate large layer thicknesses (see chapters 5 and 6). For the multi-bed process setups, however, a fine resolution of the bed coordinate (y) is also crucial. The fine, spatial resolution of the bed coordinate is even more important, especially when investigating the heat

recovery strategies in section 7.4. Contrary to the 2-bed setup simulated with MATLAB in the cause of structural adsorbent design, the optimal layer thicknesses in the multi-bed setups are much thinner resulting in flatter gradients. Based on these considerations and after conducting a grid study, the number of discretization points of the adsorbent structure (z-coordinate) was fixed to $N_z = 30$ grid points for the SMB and TMB models. In the TMB bed direction, $N_y = 100$ grid points are used spatially resolving the model. For the SMB simulations, the amount of adsorber modules is varied from 2 up to 100. With more grid points, either in y or z, accuracy increases. However, higher numbers of grid points increase computational effort. Therefore, a compromise between accuracy and computational effort was chosen.

Post-processing and visualization

Post-processing and visualization are done with MATLAB. In the case of an SMB simulation, the results of all adsorber modules ($j \in [1, j_{max}]$) are saved over a duration of the switching time τ_{sw} in a matrix of dimension (j_{max} x τ_{sw}), where the number of rows is equal to the number of execution steps of the dynamic solver, which are non-equidistant. The solution matrix is rearranged so that the solutions of all modules j are appended in one array. This array is equal to a solution array of one module j which has passed all positions during a whole cycle with cycle time t_{cyc}.

For comparison, the results of CSS of the transient SMB are visualized versus the normalized cycle time a module requires to pass through the whole cycle. The solutions of the steady-state TMB simulations are visualized versus the normalized length of the moving bed. The transient resolution of the SMB then equals the spatial resolution of the TMB. Results are discussed in depth in section 7.2.

Set of parameters used in the simulations of the multiple-bed setups

The 1+1-dimensional TMB model is used to evaluate the steady-state solution of adsorption cooling machines with varying adsorbent layer thickness and residence time of the moving bed. Parameters that were fixed in the TMB simulations are listed in Table D-2. Besides N_y, N_{ads} and N_{des}, the same values were used in the SMB simulations.

For the parameter continuation of the steady-state TMB model, the initial solution was calculated with the transient TMB DAE model to CSS with a residence time of $\tau^{bed} = 300\ s$, which is equivalent to a bed velocity of $u^{bed} = \frac{L^{bed}}{\tau^{bed}} = 0.025\ \frac{m}{s}$. Starting from the initial solution,

parameter continuations were carried out to calculate solution branches as a function of residence time in the range from $\tau^{bed} = 40\ s$ to $\tau^{bed} = 2000\ s$.

Table D-2: Set of parameters that were kept constant in the multi-bed simulations (unless otherwise indicated).

grid points CDC-plates	$N_z = 30$
grid points TMB (y)	$N_y = 100$
grid points adsorption zone	$N_{ads} = 50$
grid points desorption zone	$N_{des} = 50$
bed length	$L^{bed} = 10\ m$
Temperature levels	See Table D-1
Material model parameters	See Table B-6

D.3 Pseudocode for spatial porosity distribution in the triangular material model

In chapter 6, material design is performed for the application in adsorption refrigeration by the structuring of adsorbent composites. For that, triangular prism-shaped heat-conducting ribs and macroscopic mass transfer channels are used. For the digital material design, the local porosity distribution is correlated with the local material and transport parameters of the composites. The spatial porosity distribution is calculated with the short pseudocode outlined in the following.

$m^{ha} = \frac{0 - \varepsilon^{ha}_{bottom}}{s^{ha} - 0}$
$\varepsilon^{ha}(z) = \varepsilon^{ha}_{bottom} + z m^{ha}$
if $\varepsilon^{ha}(z) \geq 0$
  $\varepsilon^{ha}(z) = \varepsilon^{ha}(z)$

else
  $\varepsilon^{ha}(z) = 0$
end
if $z \leq s^c$ (no transport channels)
  $\varepsilon^{c}(z) = \left(1 - \varepsilon^{ha}(z)\right) \varepsilon^{ma}_{exp}$
else (transport channels)
  $m^{c} = \frac{\varepsilon^{c}_{top} - \varepsilon^{c}(z = s^c)}{1 - s^c}$
  $\varepsilon^{c}(z) = \varepsilon^{c}(z = s^c) + m^{c}(z - s^c)$
end
$\tilde{\varepsilon}^{s}(z) = 1 - \varepsilon^{ha}(z) - \varepsilon^{c}(z)$

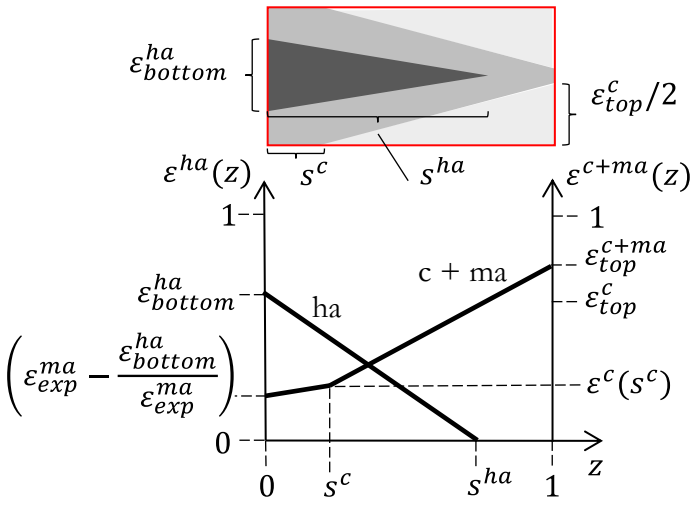

Figure D-4: Pseudocode to calculate the porosity distribution of structured composites (left) and examples of structured composite and the respective straight lines (right).

D.4 The thermodynamic potential of heat recovery in adsorption cooling

The idealized thermodynamic cycle of an adsorption heat pump as well as the performance evaluation criteria are discussed in sections 1.1 and 3.1. However, the thermodynamic maximal heat recovery potential in such heat transformation processes has not yet been addressed. For this, the thermodynamic model introduced in section 3.2.2 is evaluated and the results are discussed in depth in this section.

In adsorption refrigerators, the heat required to heat the sensible masses and regenerate the adsorbent is provided by an external source. The heat removed during the pre-cooling and evaporation step is transferred to an external sink. If the temperature levels of supply and removal overlap, heat transfer between different adsorbers can be used as a heat source in the desorption half cycle. To analyse the heat recovery potential (hrp) of adsorption refrigerators, the method presented by Schwamberger [119] and summarized in section 3.2.2 can be applied. This provides a methodical approach to pre-select and evaluate material pairs, adsorbent mass, temperature levels, and design concepts for adsorption heat pumps. However, since this is an equilibrium-based approach, the method only indicates the thermodynamic maximum efficiency

that can theoretically be achieved. In this work, the maximum efficiency is used for comparison with the performance of the multi-bed setup.

Applying the theory of Schwamberger and assuming for a driving temperature difference of $\Delta T = 0\,K$, the maximal amount of latent and sensible heat to be recovered has been calculated. As an example, the heat recovery potential for CDC composites with a thickness of $s_{cdc} = 3\,mm$ and with the material parameters outlined in Table B-6 is shown in Figure D-5.

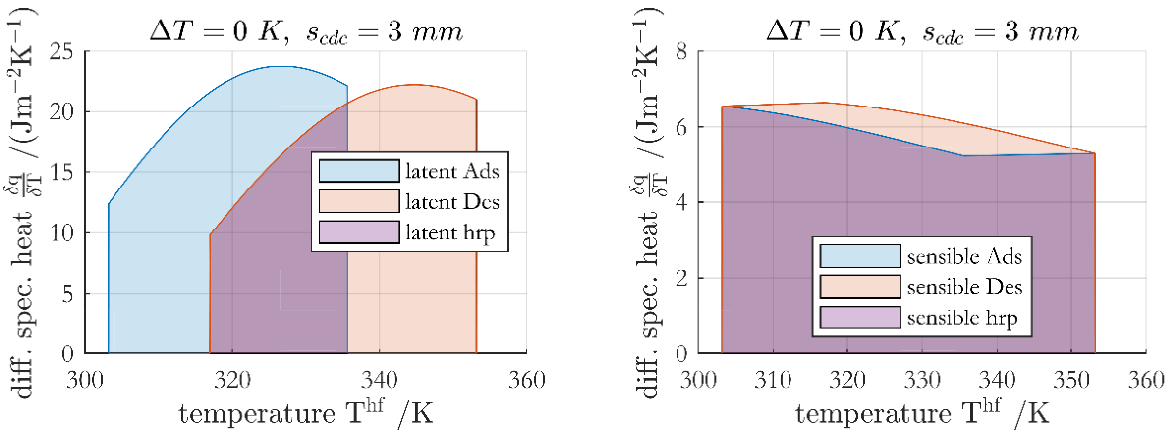

Figure D-5: Latent (left) and sensible (right) heat provided during the adsorption half cycle and required during the desorption half cycle, respectively, as a function of the heat transfer fluid temperature. The intersecting area represents the heat recovery potential (hrp).

In this example, with the specific mass of the Hex ($m^{pm} = 4\ kgm^{-2}$), a significant amount of the heat required in the desorption half-cycle must be supplied for phase change from adsorbate to adsorptive, whereas a large part of the heat provided during the adsorption half cycle is latent heat. This can be quantified using the Bowen ratio (Bow), which describes the ratio of sensible to latent heat. The Bowen ratio depends on a variety of parameters such as adsorber design (mass of adsorbent, heat exchanger, and heat transfer fluid), the adsorption pair, and the operating conditions (cycle time and temperature levels) [147]. Considering the example shown in Figure D-5, Bow is similar in the adsorption and desorption half cycles with $Bow^{ads} = 0.43$ and $Bow^{des} = 0.46$ respectively. However, due to the varying temperature levels at which the phase changes take place, only a fraction of the latent heat can be recovered. This can be quantified with the Bowen ratio of the heat recovery potential which results in $Bow^{hrp} = 0.96$. Thus, in this example, the heat recovery potential can be attributed to half of the latent heat and half of the sensible heat.

The integral heats provided in the thermodynamic analysis can further be used to calculate theoretical COPs with (COP_{hrp}^{theo}) and without heat recovery (COP^{theo}, see equation (3-1)). For the example shown in Figure D-5, the theoretical COP without heat recovery can be increased by a factor of 2.7 if the entire heat recovery potential is used.

$$COP^{theo}(s_{cdc} = 3\,mm) = \frac{q_e}{q_{heat} + q_{des}} = 0.64 \tag{D-18}$$

$$COP_{hrp}^{theo}(s_{cdc} = 3\,mm) = \frac{q_e}{q_{heat} + q_{des} - q_{hrp}} = \frac{COP^{theo}}{1 - r} = 1.64 \tag{D-19}$$

By summarizing latent and sensible heat, the heat recovery potential can be visualized as shown in Figure D-6 (left). By increasing the adsorbent thickness from $s_{cdc} = 3\,mm$ to $s_{cdc} = 10\,mm$, the profiles are qualitatively identical, only the scale differs. Due to the larger amount of adsorbent and, thus, the higher amount of latent heat, the Bowen ratio of the heat recovery potential decreases to a value of $Bow^{hrp} = 0.73$ for the $10\,mm$ composites.

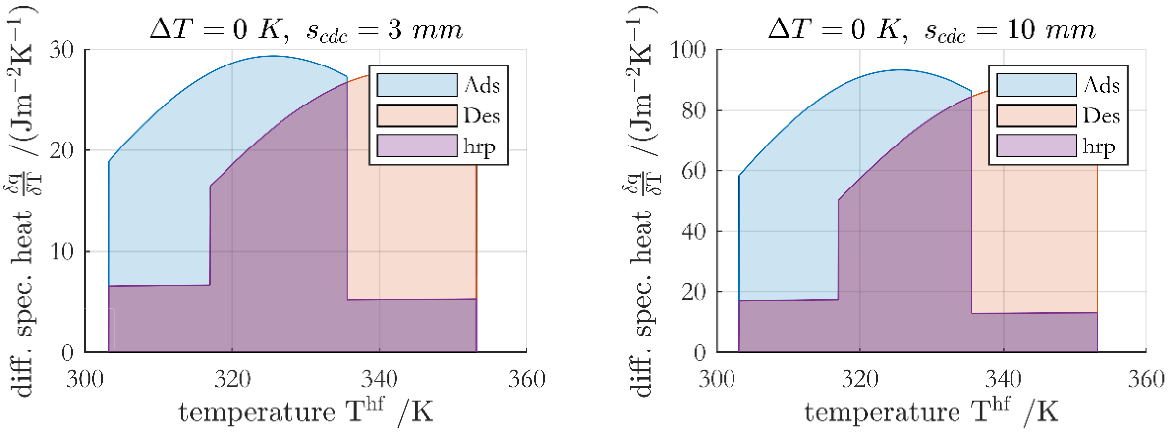

Figure D-6: Total heat required in the desorption half cycle, provided heat in the adsorption half cycle, and recoverable heat.

Interestingly, COP_{hrp}^{theo} does not change by a variation of the layer thickness, which is due to the fact, that an increase in COP^{theo} is accompanied by a decrease of r. In other words, the greater amount of energy released and recovered during the adsorption half cycle is to the same extent required in the desorption half cycle.

$$COP^{theo}(s_{cdc} = 10\,mm) = \frac{q_e}{q_{heat} + q_{des}} = 0.69 \tag{D-20}$$

$$COP_{hrp}^{theo}(s_{cdc} = 10\ mm) = \frac{COP^{theo}}{1 - r} = 1.64 \tag{D-21}$$

Hence, this thermodynamic analysis provides a method to calculate the maximal achievable efficiency for given adsorption isotherm, temperature boundaries, and adsorber design. Thus, it indicates the process's potential if only equilibrium plays a role. In real adsorption processes, however, kinetic effects are important in addition to equilibrium. In particular, the heat and mass transfer in the adsorbent structure is of crucial importance. With increasingly transport paths (layer thicknesses), the transport resistances have an increasing effect. The consideration of transport effects is therefore important for a correct estimation of process performance and efficiency, which requires a spatial resolution of the adsorbent structure.

D.5 Derivation of True-Moving-Bed model equations

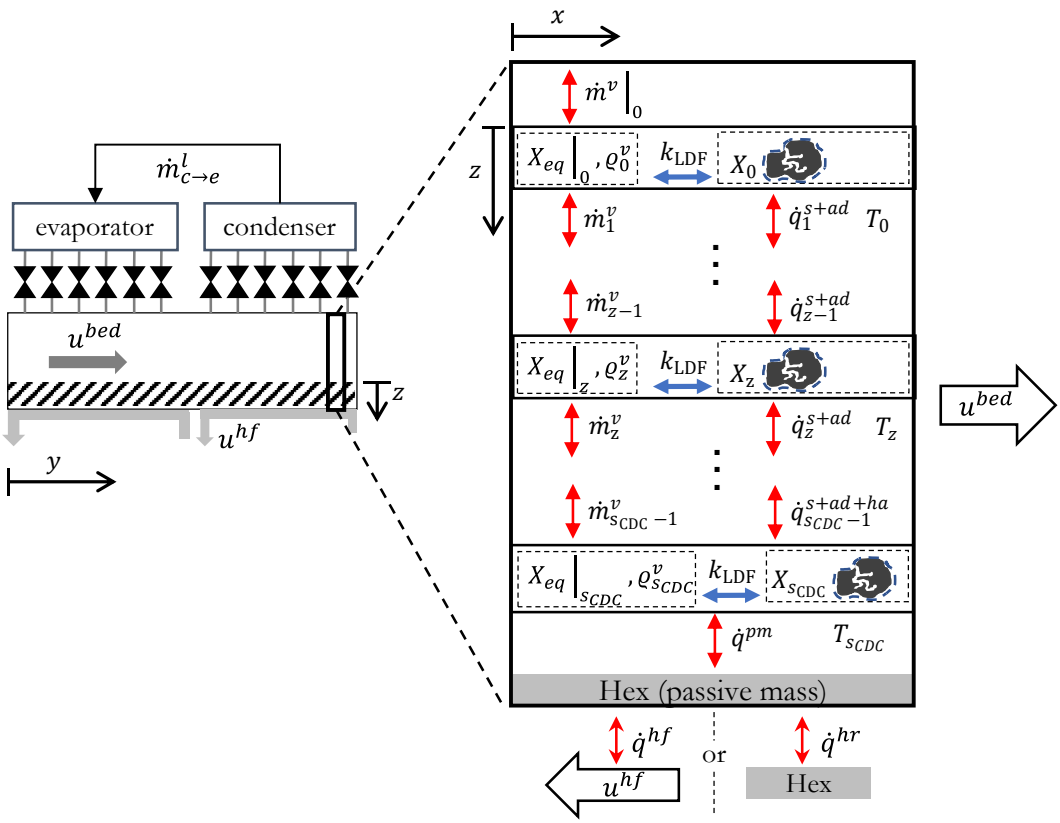

Figure D-7: Segment of the TMB with the spatial distribution of the adsorbent composites and the moving bed direction.

Figure D-7 shows a segment of the TMB containing the spatially resolved adsorbent composites (adsorptive, adsorbent, binder, and adsorbate) and the heat exchanger flat tube. The movement

of the TMB takes place with the velocity u^{bed} in counterflow to the heat transfer fluid, which moves with the velocity u^{hf}. In the heat recovery zone, the Hex of adsorption and desorption zone exchange the heat fluxes $\dot{q}^{hr}$.

In the derivation of the TMB model, the dimension is reduced by averaging over the width of the adsorbent bed (coordinate x) using the nomenclature shown in Figure D-8. Diffusive transport along the axial y-coordinate is not regarded since the aim is to approximate the (separated) SMB modules. Consequently, the derivation results in a one + one-dimensional model, taking mass- and heat-transfer over the adsorbent height and convective transport of the moving bed into account.

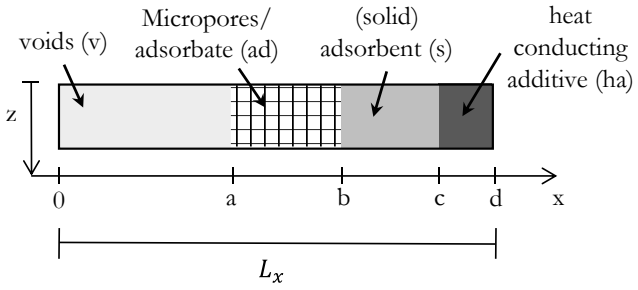

Figure D-8: Nomenclature for averaging over the x-coordinate in the TMB model approach.

D.5.1 Equation of continuity for adsorbent composites

- Transport in the moving-bed y-direction is convective with a constant velocity $v_y = u^{bed}$.
- In z-direction no mass transport in heat additive, adsorbent, and adsorbate phase.

$$\frac{\partial \varrho}{\partial t} + \underbrace{\nabla \cdot \varrho \vec{v}}_{\nabla \cdot \vec{\dot{m}}} = 0 \tag{D-22}$$

Adsorptive/ gas in void phase:

$$\int_0^a \frac{\partial \varrho^v}{\partial t} dx + \int_0^a \frac{\partial \dot{m}_z^v}{\partial z} dx + \int_0^a \frac{\partial \dot{m}_y^v}{\partial y} dx + \int_0^a \frac{\partial \dot{m}_x^v}{\partial x} dx = 0 \tag{D-23}$$

$$\frac{\partial \varrho^v}{\partial t} a + \frac{\partial \dot{m}_z^v}{\partial z} a + \frac{\partial \dot{m}_y^v}{\partial y} a + \dot{m}_{x=a}^v = 0 \tag{D-24}$$

With the adsorbent bed width L_x and $\varepsilon^{ma} = a/L_x \equiv V^{ma}/V_{comp}$

$$\varepsilon^{ma}\frac{\partial \varrho^{v}}{\partial t}+\frac{\partial \varepsilon^{ma}\dot{m}_{z}^{v}}{\partial z}+\varepsilon^{ma}\frac{\partial \dot{m}_{y}^{v}}{\partial y}+\frac{1}{L_x}\dot{m}_{x=a}^{v}=0 \tag{D-25}$$

Adsorbate in terms of adsorbate density per unit volume of micropores $\tilde{\varrho}^{ad}$:

$$\int_a^b\frac{\partial \tilde{\varrho}^{ad}}{\partial t}dx+\int_a^b\frac{\partial \dot{m}_{z}^{ad}}{\partial z}dx+\int_a^b\frac{\partial \dot{m}_{y}^{ad}}{\partial y}dx+\int_a^b\frac{\partial \dot{m}_{x}^{ad}}{\partial x}dx=0 \tag{D-26}$$

$$\frac{\partial \tilde{\varrho}^{ad}}{\partial t}(b-a)+\frac{\partial \dot{m}_{z}^{ad}}{\partial z}(b-a)+\frac{\partial \dot{m}_{y}^{ad}}{\partial y}(b-a)+\underbrace{\dot{m}_{x=b}^{ad}}_{0,bc}-\dot{m}_{x=a}^{ad}=0 \tag{D-27}$$

With $\varepsilon^{mi}=(b-a)/L_x\equiv V^{mi}/V_{comp}$

$$\varepsilon^{mi}\frac{\partial \tilde{\varrho}^{ad}}{\partial t}+\underbrace{\frac{\partial \varepsilon^{mi}\dot{m}_{z}^{ad}}{\partial z}}_{0,\ no\ transport\ in\ z}+\varepsilon^{mi}\frac{\partial \dot{m}_{y}^{ad}}{\partial y}=\frac{1}{L_x}\dot{m}_{x=a}^{ad} \tag{D-28}$$

In the direction of the moving bed (y), solely convective transport with constant velocity is regarded in analogy to the discrete movement of adsorber modules in the SMB approach. The mass flux in y is given by

$$\nabla\cdot\dot{m}=\nabla\cdot\varrho\vec{v} \tag{D-29}$$

Hence, the adsorbate material balance can be rewritten

$$\varepsilon^{mi}\frac{\partial \tilde{\varrho}^{ad}}{\partial t}+v_y\varepsilon^{mi}\frac{\partial \varrho_{y}^{ad}}{\partial y}=\frac{1}{L_x}\dot{m}_{x=a}^{ad}. \tag{D-30}$$

With the loading X and the bulk-density ϱ^{bulk}, we can write

$$\varepsilon^{mi}\tilde{\varrho}^{ad}=\varepsilon^{mi}\frac{M^{s}X}{V^{ad}}=\frac{M^{s}X}{V_{comp}}=X\varrho^{bulk}. \tag{D-31}$$

Hence, the adsorbate material balance follows to

$$\varrho^{bulk}\frac{\partial X}{\partial t}+\varrho^{bulk}v_y\frac{\partial X}{\partial y}=\frac{1}{L_x}\dot{m}_{x=a}^{ad}. \tag{D-32}$$

To describe the exchange mass flux between interparticle voids and pores in adsorbent particles $\dot{m}_{x=a}^{ad}$, an LDF-approach is used, with the difference between equilibrium loading and loading serving as driving force. By using the LDF-approach, the total transport resistance of the adsorbent particle is transferred into the boundary surface. With

$$\dot{m}_{x=a}^{ad}\frac{1}{L_x} = k_{LDF}(X^{eq}-X)\underbrace{\frac{M^s}{\Delta L^{bed}s_{cdc}}\frac{1}{L_x}}_{M^s/V^{abs}} = k_{LDF}(X^{eq}-X)\varrho^{bulk} \tag{D-33}$$

the adsorbate material balance is given by

$$\varrho^{bulk}\frac{\partial X}{\partial t} + \varrho^{bulk}v_y\frac{\partial X}{\partial y} = k_{LDF}(X^{eq}-X)\varrho^{bulk}. \tag{D-34}$$

Adsorptive + Adsorbate

With the boundary condition

$$\dot{m}_{x=a}^{ad} - \dot{m}_{x=a}^{v} = 0, \tag{D-35}$$

the final material balance of adsorptive in the voids results from equations (D-25) and (D-32)

$$\varepsilon^{ma}\frac{\partial \varrho^v}{\partial t} + \frac{\partial \varepsilon^{ma}\dot{m}_z^v}{\partial z} + \varepsilon^{ma}\frac{\partial \dot{m}_y^v}{\partial y} + \varrho^{bulk}\frac{\partial X}{\partial t} + \varrho^{bulk}v_y\frac{\partial X}{\partial y} = 0. \tag{D-36}$$

With equation (D-34) and $\dot{m}_y^v = \varrho^v v_y = \varrho^v u^{bed}$, it can be simplified

$$\varepsilon^{ma}\frac{\partial \varrho^v}{\partial t} + \frac{\partial \varepsilon^{ma}\dot{m}_z^v}{\partial z} + \varepsilon^{ma}u^{bed}\frac{\partial \varrho^v}{\partial y} + k_{LDF}(X^{eq}-X)\varrho^{bulk} = 0. \tag{D-37}$$

D.5.2 Equation of change for energy

$$\frac{\partial \varrho u}{\partial t} + \nabla\cdot(\varrho u\vec{v}) + \nabla\cdot\vec{q} + p\nabla\cdot\vec{v} = 0 \tag{D-38}$$

With $u = h - p/\varrho$ and mass flux vector $\vec{\dot{m}} = \varrho\vec{v}$,

$$\frac{\partial \varrho h}{\partial t} - \frac{\partial p}{\partial t} + \nabla\cdot\left(\vec{q} + \vec{\dot{m}}h\right) - \vec{v}\nabla p = 0. \tag{D-39}$$

Assumptions:

- Solely convective transport in the y-direction. No mass transport in adsorbent, adsorbate, and heat additive over the height of the composites.
- No heat conduction in y-direction since separated SMB-modules are regarded in the TMB-approach.

Heat additive:

$$\int_c^d \frac{\partial(\varrho h)^{ha}}{\partial t}dx + \int_c^d \frac{\partial \dot{q}_x^{ha}}{\partial x}dx + \int_c^d \frac{\partial \dot{q}_z^{ha}}{\partial z}dx + \int_c^d v_y\varrho^{ha}\frac{\partial h^{ha}}{\partial y}dx = 0 \tag{D-40}$$

$$\varrho^{ha}(d-c)\frac{\partial h^{ha}}{\partial t}+\underbrace{\dot{q}^{ha}_{x=d}}_{0}-\dot{q}^{\,ha}_{x=c}+\frac{\partial(d-c)\dot{q}^{\,ha}_{z}}{\partial z}+(d-c)v_y\varrho^{ha}\frac{\partial h^{ha}}{\partial y}=0 \tag{D-41}$$

With $\varepsilon^{ha}(z)=(d-c)/L_x\equiv V^{ha}/V_{comp}$, $dh=c_p dT$

$$\varepsilon^{ha}\varrho^{ha}c_p^{ha}\frac{\partial T^{ha}}{\partial t}+\frac{\partial\varepsilon^{ha}\dot{q}^{ha}_{z}}{\partial z}+v_y\varepsilon^{ha}\varrho^{ha}c_p^{ha}\frac{\partial T^{ha}}{\partial y}-\frac{\dot{q}^{ha}_{x=c}}{L_x}=0. \tag{D-42}$$

Solid adsorbent (corresponding to true adsorbent density):

$$\int_b^c\frac{\partial(\varrho h)^{s}}{\partial t}dx+\int_b^c\frac{\partial\dot{q}^{s}_{x}}{\partial x}dx+\int_b^c\frac{\partial\dot{q}^{\,s}_{z}}{\partial z}dx+\int_b^c v_y\varrho^{s}\frac{\partial h^{s}}{\partial y}dx=0 \tag{D-43}$$

$$\varrho^{s}(c-b)\frac{\partial h^{s}}{\partial t}+\dot{q}^{\,s}_{x=c}-\dot{q}^{\,s}_{x=b}+\frac{\partial(c-b)\dot{q}^{\,s}_{z}}{\partial z}+(c-b)v_y\varrho^{s}\frac{\partial h^{s}}{\partial y}=0 \tag{D-44}$$

With $\varepsilon^{s}(z)=(c-b)/L_x\equiv V^{s}/V_{comp}$, $dh=c_p dT$ and $\varepsilon^{s}\varrho^{s}\equiv\tilde{\varepsilon}^{s}\tilde{\varrho}^{s}=(c-a)/L_x\tilde{\varrho}^{s}$

$$\tilde{\varepsilon}^{s}\tilde{\varrho}^{s}c_p^{s}\frac{\partial T^{s}}{\partial t}+\frac{\partial\varepsilon^{s}\dot{q}^{\,s}_{z}}{\partial z}+v_y\tilde{\varepsilon}^{s}\tilde{\varrho}^{s}c_p^{s}\frac{\partial T^{s}}{\partial y}+\frac{\dot{q}^{\,s}_{x=c}-\dot{q}^{\,s}_{x=b}}{L_x}=0. \tag{D-45}$$

Instead of volume fraction times density of the solid adsorbent ($\varepsilon^{s}\varrho^{s}$), the apparent volume fraction times apparent density ($\tilde{\varepsilon}^{s}\tilde{\varrho}^{s}$) is used, which has the same value but is experimentally more easily accessible.

<u>Micropores / adsorbate phase:</u>

- Adsorbate is treated as an ideal fluid.
- Instead of the true adsorbate density, the apparent adsorbate density $\tilde{\varrho}^{ad}$ is balanced describing the adsorbate mass per unit volume of micropores. Thus, the adsorptive phase in the micropores is not explicitly modelled but rather a quasi-homogeneous micropore balance with a neglected hold-up in the gas phase.

$$\begin{aligned}&\int_a^b\frac{\partial(\tilde{\varrho}^{ad}h)^{ad}}{\partial t}dx-\int_a^b\frac{\partial p^{ad}}{\partial t}dx+\int_a^b\frac{\partial\dot{q}^{ad}_{x}}{\partial x}dx+\int_a^b\frac{\partial\tilde{q}^{ad}_{z}}{\partial z}dx+\int_a^b\frac{\partial v_x^{ad}(\tilde{\varrho}^{ad}h)^{ad}}{\partial x}dx+\\&\int_a^b v_y\frac{\partial(\tilde{\varrho}^{ad}h)^{ad}}{\partial y}dx-\int_a^b v_x^{ad}\frac{\partial p^{ad}}{\partial x}dx-\int_a^b v_y\frac{\partial p^{ad}}{\partial y}dx=0\end{aligned} \tag{D-46}$$

$$\begin{aligned}&(b-a)\frac{\partial(\tilde{\varrho}^{ad}h)^{ad}}{\partial t}-(b-a)\frac{\partial p^{ad}}{\partial t}+\frac{\partial(b-a)\tilde{q}^{ad}_{z}}{\partial z}+(b-a)v_y\frac{\partial(\tilde{\varrho}^{ad}h)^{ad}}{\partial y}-(b-\\&a)v_y\frac{\partial p^{ad}}{\partial y}+\dot{q}^{\,ad}_{x=b}-(v_x^{ad}\tilde{\varrho}^{ad}h)^{ad}_{x=a}+(v_x^{ad}p)^{ad}_{x=a}=0\end{aligned} \tag{D-47}$$

With $\varepsilon^{mi}(z)=(b-a)/L_x\equiv V^{ad}/V_{comp}$, for an ideal fluid $dh=c_p dT+1/\varrho dp$ and $\dot{m}_x^{ad}=v_x^{ad}\tilde{\varrho}^{ad}$

$$\varepsilon^{mi}\left(h^{ad}\frac{\partial\tilde{\varrho}^{ad}}{\partial t}+\tilde{\varrho}^{ad}c_p^{ad}\frac{\partial T^{ad}}{\partial t}\right)+\frac{\partial\varepsilon^{mi}\tilde{q}_z^{ad}}{\partial z}+\varepsilon^{mi}v_y\left(h^{ad}\frac{\partial\tilde{\varrho}^{ad}}{\partial y}+\tilde{\varrho}^{ad}c_p^{ad}\frac{\partial T^{ad}}{\partial y}\right)+\frac{\dot{q}_{x=b}^{\ ad}-(\dot{m}_x^{ad}h)_{x=a}^{ad}+(v_x^{ad}p)_{x=a}^{ad}}{L_x}=0. \tag{D-48}$$

With (mass) specific loading X and the spatial dependent bulk density ϱ^{bulk} describing the local mass of solid adsorbent to the sum of the local volumes of all phases

$$\varepsilon^{mi}(z)\tilde{\varrho}^{ad}=\varepsilon^{mi}(z)\frac{M^s(z)X}{V^{ad}}=\frac{M^s(z)X}{V_{comp}}=X\varrho^{bulk}(z). \tag{D-49}$$

Then, equation (D-48) follows to

$$\varrho^{bulk}h^{ad}\frac{\partial X}{\partial t}+\varrho^{bulk}c_p^{ad}X\frac{\partial T^{ad}}{\partial t}+\frac{\partial\varepsilon^{mi}\tilde{q}_z^{ad}}{\partial z}+v_y\varrho^{bulk}h^{ad}\frac{\partial X}{\partial y}+v_y\varrho^{bulk}Xc_p^{ad}\frac{\partial T^{ad}}{\partial y}+\frac{\dot{q}_{x=b}^{\ ad}-(\dot{m}_x^{ad}h)_{x=a}^{ad}+(v_x^{ad}p)_{x=a}^{ad}}{L_x}=0. \tag{D-50}$$

<u>Adsorptive:</u>

- Heat conduction is neglected in the adsorptive phase.
- Adsorptive is treated as an ideal gas.

$$\int_0^a\frac{\partial(\varrho h)^v}{\partial t}dx-\int_0^a\frac{\partial p^v}{\partial t}dx+\int_0^a\frac{\partial(\dot{m}_xh)^v}{\partial x}dx+\int_0^a\frac{\partial\left(\dot{m}_yh\right)^v}{\partial y}dx+\int_0^a\frac{\partial(\dot{m}_zh)^v}{\partial z}dx-\int_0^a v_x^v\frac{\partial p}{\partial x}dx-\int_0^a v_y\frac{\partial p}{\partial y}dx-\int_0^a v_z^v\frac{\partial p}{\partial z}dx=0 \tag{D-51}$$

$$a\frac{\partial(\varrho h)^g}{\partial t}-a\frac{\partial p^g}{\partial t}+a\frac{\partial\left(\dot{m}_yh\right)^g}{\partial y}+a\frac{\partial(\dot{m}_zh)^g}{\partial z}-av_y\frac{\partial p}{\partial y}-av_z^g\frac{\partial p}{\partial z}+(\dot{m}_{x=a}h)^g-v_x^gp_{x=a}=0 \tag{D-52}$$

With $\varepsilon^{ma}(z)=a/L_x, p^v=\varrho^vT^vR/MW$ and $dh=c_pdT$

$$\varepsilon^{ma}\varrho^vc_p^v\frac{\partial T^v}{\partial t}+\varepsilon^{ma}h^v\frac{\partial\varrho^v}{\partial t}-\varepsilon^{ma}\frac{R}{MW}\left(\varrho^v\frac{\partial T^v}{\partial t}+T^v\frac{\partial\varrho^v}{\partial t}\right)+\varepsilon^{ma}\dot{m}_y^vc_p^v\frac{\partial T^v}{\partial y}+\varepsilon^{ma}h^v\frac{\partial\dot{m}_y^v}{\partial y}+\varepsilon^{ma}\dot{m}_z^vc_p^v\frac{\partial T^v}{\partial z}+h^v\frac{\partial\varepsilon^{ma}\dot{m}_z^v}{\partial z}-\varepsilon^{ma}\frac{R}{MW}\left(v_y\varrho^v\frac{\partial T^v}{\partial y}+v_yT^v\frac{\partial\varrho^v}{\partial y}\right)-v_z^v\frac{\partial\varepsilon^{ma}p}{\partial z}+\frac{(\dot{m}_{x=a}h)^v}{L_x}-\frac{v_x^vp_{x=a}}{L_x}=0. \tag{D-53}$$

And simplified

$$\left(\varepsilon^{ma}\varrho^vc_p^v-\varepsilon^{ma}\frac{R}{MW}\varrho^v\right)\frac{\partial T^v}{\partial t}+\left(\varepsilon^{ma}h^v-\varepsilon^{ma}\frac{R}{MW}T^v\right)\frac{\partial\varrho^v}{\partial t}+\left(\varepsilon^{ma}\dot{m}_y^vc_p^v-\varepsilon^{ma}\frac{R}{MW}v_y\varrho^v\right)\frac{\partial T^v}{\partial y}+\varepsilon^{ma}h^v\frac{\partial\dot{m}_y^v}{\partial y}-\varepsilon^{ma}\frac{Rv_yT^v}{MW}\frac{\partial\varrho^v}{\partial y}+\varepsilon^{ma}\dot{m}_z^vc_p^v\frac{\partial T^v}{\partial z}+h^v\frac{\partial\varepsilon^{ma}\dot{m}_z^v}{\partial z}-v_z^v\frac{\partial\varepsilon^{ma}p}{\partial z}+\frac{(\dot{m}_x^vh)_{x=a}^v}{L_x}-\frac{(v_x^vp)_{x=a}^v}{L_x}=0. \tag{D-54}$$

Following, the individual energy equations are summed up to a quasi-homogeneous energy equation of the consolidated adsorbent composites in the TMB-approach. Hereby it is assumed, that the temperature variation over the height of the composites is much larger than on one level and thus each layer of the composite has a quasi-homogeneous temperature

$$T|_z \equiv T^v|_z = T^{ad}|_z = T^s|_z = T^{ha}|_z. \tag{D-55}$$

Quasi-homogeneous balance: Heat additive and solid adsorbent

With the heat transfer boundary condition at the interface of heat additive and solid adsorbent phase

$$\dot{q}^{\,s}_{x=c} - \dot{q}^{\,ha}_{x=c} = 0, \tag{D-56}$$

the quasi-homogeneous energy equation of adsorbent and heat additive results in

$$\begin{aligned}\left(\varepsilon^{ha}\varrho^{ha}c_p^{ha} + \tilde{\varepsilon}^s\tilde{\varrho}^s c_p^s\right)\frac{\partial T}{\partial t} + \frac{\partial(\varepsilon^{ha}+\varepsilon^s)\dot{q}_z^{ha+s}}{\partial z} + v_y\left(\varepsilon^{ha}\varrho^{ha}c_p^{ha} + \tilde{\varepsilon}^s\tilde{\varrho}^s c_p^s\right)\frac{\partial T}{\partial y} \\ - \frac{\dot{q}^{\,s}_{x=b}}{L_x} = 0.\end{aligned} \tag{D-57}$$

Quasi-homogeneous balance: Heat additive, solid adsorbent, and adsorbate

Heat transfer through the interface between solid adsorbent and adsorbate at point b (see Figure D-8) is described with the heat flux $\dot{q}_{x=b}$. Using the boundary condition

$$\dot{q}^{\,ad}_{x=b} - \dot{q}^{\,s}_{x=b} = 0, \tag{D-58}$$

equations (D-50) and (D-57) are summed up to the quasi-homogeneous energy balance of heat additive, solid adsorbent, and adsorbate

$$\begin{aligned}&\left(\varepsilon^{ha}\varrho^{ha}c_p^{ha} + \tilde{\varepsilon}^s\tilde{\varrho}^s c_p^s + \varrho^{bulk}c_p^{ad}X\right)\frac{\partial T}{\partial t} + \varrho^{bulk}h^{ad}\frac{\partial X}{\partial t} + \frac{\partial\left(\varepsilon^{ha}+\underbrace{\varepsilon^s+\varepsilon^{mi}}_{\tilde{\varepsilon}^s}\right)\dot{q}_z^{ha+s+ad}}{\partial z} + \\ &v_y^{ad}\varrho^{bulk}h^{ad}\frac{\partial X}{\partial y} + v_y\left(\varepsilon^{ha}\varrho^{ha}c_p^{ha} + \tilde{\varepsilon}^s\tilde{\varrho}^s c_p^s + \varrho^{bulk}Xc_p^{ad}\right)\frac{\partial T}{\partial y} - \\ &\frac{\left(\dot{m}_x^{ad}h\right)^{ad}_{x=a} - \left(v_x^{ad}p\right)^{ad}_{x=a}}{L_x} = 0.\end{aligned} \tag{D-59}$$

According to the closing condition $\sum_j \varepsilon^j = 1$

$$1 - \varepsilon^{ma} = \varepsilon^{ha} + \underbrace{\varepsilon^s + \varepsilon^{mi}}_{\tilde{\varepsilon}^s}. \tag{D-60}$$

Quasi-homogeneous balance: Heat additive, solid adsorbent, adsorbate, and interparticle void space

Finally, the adsorptive macropore energy equation is added to equation (D-59) using the boundary condition at the interface of interparticle macropores and micropores in the primary particles

$$(\dot{m}_x^v h)_{x=a}^v - (v_x^v p)_{x=a}^v - (\dot{m}_x^{ad} h)_{x=a}^{ad} + (v_x^{ad} p)_{x=a}^{ad} = 0. \tag{D-61}$$

Summation of equations (D-54) and (D-59) yields the energy balance of the adsorbent composites for the TMB-approach in units $Jm_{comp}^{-3}s^{-1}$

$$\begin{aligned}&\left(\varepsilon^{ha}\varrho^{ha}c_p^{ha} + \tilde{\varepsilon}^s\tilde{\varrho}^s c_p^s + \varrho^{bulk}c_p^{ad}X + \varepsilon^{ma}\left(\varrho^v c_p^v - \frac{R\varrho^v}{MW}\right)\right)\frac{\partial T}{\partial t} + \left(\varepsilon^{ma}h^v - \right.\\ &\left.\varepsilon^{ma}\frac{RT}{MW}\right)\frac{\partial \varrho^v}{\partial t} + \varrho^{bulk}h^{ad}\frac{\partial X}{\partial t} + \left(v_y\left(\varepsilon^{ha}\varrho^{ha}c_p^{ha} + \tilde{\varepsilon}^s\tilde{\varrho}^s c_p^s + \varrho^{bulk}Xc_p^{ad}\right) + \right.\\ &\left.\varepsilon^{ma}\left(\dot{m}_y^v c_p^v - \frac{Rv_y\varrho^v}{MW}\right)\right)\frac{\partial T}{\partial y} + \varepsilon^{ma}h^g\frac{\partial \dot{m}_y^v}{\partial y} - \varepsilon^{ma}\frac{Rv_yT}{MW}\frac{\partial \varrho^v}{\partial y} + \varrho^{bulk}v_y h^{ad}\frac{\partial X}{\partial y} + \\ &\frac{\partial(1-\varepsilon^{ma})\dot{q}_z^{ha+s+ad}}{\partial z} + \varepsilon^{ma}\dot{m}_z^v c_p^v\frac{\partial T}{\partial z} + h^v\frac{\partial \varepsilon^{ma}\dot{m}_z^v}{\partial z} - v_z^v\frac{\partial \varepsilon^{ma}p}{\partial z} = 0.\end{aligned} \tag{D-62}$$

This form is not yet applicable since the specific enthalpies h^{ad} and h^v are not known. Therefore, these terms are reformulated using the adsorption enthalpy $\Delta_{ads}h = h^{ad} - h^v$ and the continuity equation of the adsorptive void space in equation (D-25)

$$\begin{aligned}&\varepsilon^{ma}h^v\frac{\partial \varrho^v}{\partial t} + \varepsilon^{ma}h^v\frac{\partial \dot{m}_y^v}{\partial y} + \varrho^{bulk}h^{ad}\frac{\partial X}{\partial t} + \varrho^{bulk}v_y h^{ad}\frac{\partial X}{\partial y} = \\ &h^v\underbrace{\left(\varepsilon^{ma}\frac{\partial \varrho^v}{\partial t} + \varepsilon^{ma}\frac{\partial \dot{m}_y^v}{\partial y} + \varrho^{bulk}\frac{\partial X}{\partial t} + \varrho^{bulk}v_y\frac{\partial X}{\partial y}\right)}_{=-\frac{\partial \varepsilon^{ma}\dot{m}_z^v}{\partial z}} + \Delta_{ads}h\varrho^{bulk}\frac{\partial X}{\partial t} + \\ &\Delta_{ads}h\varrho^{bulk}v_y\frac{\partial X}{\partial y}.\end{aligned} \tag{D-63}$$

Inserting equation (D-63) in (D-62) results to

$$\begin{aligned}&\left(\varepsilon^{ha}\varrho^{ha}c_p^{ha} + \tilde{\varepsilon}^s\tilde{\varrho}^s c_p^s + \varrho^{bulk}c_p^{ad}X + \varepsilon^{ma}\left(\varrho^v c_p^v - \frac{R\varrho^v}{MW}\right)\right)\frac{\partial T}{\partial t} - \varepsilon^{ma}\frac{RT}{MW}\frac{\partial \varrho^v}{\partial t} + \\ &\Delta_{ads}h\varrho^{bulk}\frac{\partial X}{\partial t} + \Delta_{ads}h\varrho^{bulk}v_y\frac{\partial X}{\partial y} + \left(v_y\left(\varepsilon^{ha}\varrho^{ha}c_p^{ha} + \tilde{\varepsilon}^s\tilde{\varrho}^s c_p^s + \varrho^{bulk}Xc_p^{ad}\right) + \right.\\ &\left.\varepsilon^{ma}\left(\dot{m}_y^v c_p^v - \frac{Rv_y\varrho^v}{MW}\right)\right)\frac{\partial T}{\partial y} - \varepsilon^{ma}\frac{Rv_yT}{MW}\frac{\partial \varrho^v}{\partial y} + \frac{\partial(1-\varepsilon^{ma})\dot{q}_z^{ha+s+ad}}{\partial z} + \varepsilon^{ma}\dot{m}_z^v c_p^v\frac{\partial T}{\partial z} - \\ &v_z^v\frac{\partial \varepsilon^{ma}p}{\partial z} = 0.\end{aligned} \tag{D-64}$$

With the adsorbate continuity equation for the TMB-approach in equation (D-34), using the bed velocity $u^{bed} = v_y$ and $\dot{m}_y^v = u^{bed}\varrho^v$, finally the quasi-homogeneous energy equation for the TMB-approach results as it was applied in the process simulations

$$\begin{aligned}&\left(\varepsilon^{ha}\varrho^{ha}c_p^{ha} + \tilde{\varepsilon}^s\tilde{\varrho}^s c_p^s + \varrho^{bulk}c_p^{ad}X + \varepsilon^{ma}\left(\varrho^v c_p^v - \frac{R\varrho^v}{MW}\right)\right)\frac{\partial T}{\partial t} - \varepsilon^{ma}\frac{RT}{MW}\frac{\partial \varrho^v}{\partial t} + \end{aligned} \tag{D-65}$$

$$\Delta_{ads} h \varrho^{bulk} k_{LDF} (X^{eq} - X) + u^{bed} \Big(\varepsilon^{ha} \varrho^{ha} c_p^{ha} + \tilde{\varepsilon}^s \tilde{\varrho}^s c_p^s + \varrho^{bulk} X c_p^{ad} + \varepsilon^{ma} \left(\varrho^v c_p^v - \frac{R \varrho^v}{MW} \right) \Big) \frac{\partial T}{\partial y} - u^{bed} \varepsilon^{ma} \frac{RT}{MW} \frac{\partial \varrho^v}{\partial y} + \frac{\partial (1-\varepsilon^{ma}) \dot{q}_z^{ha+s+ad}}{\partial z} + \varepsilon^{ma} \dot{m}_z^v c_p^v \frac{\partial T}{\partial z} - v_z^v \frac{\partial \varepsilon^{ma} p}{\partial z} = 0.$$

It contains accumulation terms consisting of all the four individual phases, a source term accounting for adsorption or desorption enthalpy proportional to the rate of adsorption or desorption, a convective energy transport term in the moving-bed direction y, and energy transport terms over the height of the composites in direction z. It is composed of an effective heat conduction term describing the combined heat conduction in heat additive, solid adsorbent, and adsorbate phase as well as convective energy transport terms. The last term accounting for the spatial change in pressure is often neglectable.

Passive mass of flat tube:

$$\varrho^{pm} \frac{\partial h^{pm}}{\partial t} + \varrho^{pm} u^{bed} \frac{\partial h^{pm}}{\partial y} + \frac{\partial \dot{q}^{pm}}{\partial z} = 0 \tag{D-66}$$

Integration over the wall thickness of the flat tube s^{pm} gives

$$s^{pm} \left(\varrho^{pm} c_p^{pm} \frac{\partial T^{pm}}{\partial t} + \varrho^{pm} u^{bed} c_p^{pm} \frac{\partial T^{pm}}{\partial y} \right) + \dot{q}^{pm}_{z=s^{pm-cdc}} - \dot{q}^{pm}_{z=s^{hf-pm}} = 0. \tag{D-67}$$

With $\varrho^{pm} s^{pm} = m^{pm}$, $\dot{q}^{pm}_{z=s^{pm-cdc}} = \dot{q}^{pm}$ and $\dot{q}^{pm}_{z=s^{hf-pm}} = \dot{q}^{hf*}$

$$m^{pm} c_p^{pm} \frac{\partial T^{pm}}{\partial t} + u^{bed} m^{pm} c_p^{pm} \frac{\partial T^{pm}}{\partial y} + \dot{q}^{pm} - \dot{q}^{hf*} = 0. \tag{D-68}$$

The heat flux exchanged between heat transfer fluid and passive mass $\dot{q}^{hf*}$ is divided into the heat flux in the heat recovery zone $\dot{q}^{hr}$ and the heat flux exchanged in the other sections of the moving bed $\dot{q}^{hf}$

$$\dot{q}^{hf*} = \dot{q}^{hf} + \dot{q}^{hr}. \tag{D-69}$$

In the heat recovery zone, $\dot{q}^{hf} = 0$ at every position j and

$$\dot{q}_j^{hr} = k^{hr} \left(T^{pm}|_{\frac{L^{bed} - L^{hr}}{2} - j} - T_j^{pm} \right), \tag{D-70}$$

where k^{hr} is the heat transfer resistance between two adsorbers which is chosen largely to not limit the heat transfer in the heat recovery zone. In equivalence, $\dot{q}^{hr} = 0$ in the section without internal heat regeneration and $\dot{q}^{hf}$ as outlined in equation (3-7).

Heat transfer fluid:

$$\varrho^{hf}\frac{\partial h}{\partial t}+\varrho^{hf}u^{hf}\frac{\partial h}{\partial y}+\frac{\partial \dot{q}^{hf}}{\partial z}=0 \tag{D-71}$$

Integration over the flat tube fluid channel thickness s^{hf} gives

$$s^{hf}\left(\varrho^{hf}c_p^{hf}\frac{\partial T^{hf}}{\partial t}+\varrho^{hf}u^{hf}c_p^{hf}\frac{\partial T^{hf}}{\partial y}\right)+\dot{q}^{hf}_{z=s^{hf-pm}}=0. \tag{D-72}$$

With $\varrho^{hf}s^{hf}=m^{hf}$ and $\dot{q}^{\,hf}_{z=s^{hf-pm}}=\dot{q}^{hf}$

$$m^{hf}c_p^{hf}\frac{\partial T^{hf}}{\partial t}+u^{hf}m^{hf}c_p^{hf}\frac{\partial T^{hf}}{\partial y}+\dot{q}^{\,hf}=0. \tag{D-73}$$

$u^{hf}<0$ to ensure counterflow.

D.6 Method of Characteristics - transformed model equations

Due to the strictly convective transport in the moving bed direction, numerical dispersion occurs when using the method of lines or finite volume method for discretization. To show that the TMB solution is the limiting case of the SMB, the method of characteristics (MoC) [169] was used for a simple 0D-1D model, with a lumped-parameter model for the adsorbent composites. By applying MoC on the partial differential equations of the 0D-1D model, they can be transformed into a set of ordinary differential equations, their solution being calculated on the characteristics. In this way, the spatial fixed Eulerian point of view is transformed into a Lagrange point of view. The velocity of the characteristics is chosen equal to the convective velocity of the fixed moving bed in the y-direction u^{bed}. The transformation is carried out from the original coordinate system in (y,t) in a system described in $(r;\ s)$. Hereby, r is the transformed time and s is the index of the respective characteristic. The methodology of the transformation is exemplary shown for a classical convection-reaction equation

$$A(t,y)\frac{\partial u}{\partial t}+B(t,y)\frac{\partial u}{\partial y}=C(t,y,u). \tag{D-74}$$

Transformation on the new coordinate system with

$$y=y(r;s), \tag{D-75}$$

$$t = t(r; s), \tag{D-76}$$

$$u = u\big(y(r; s), t(r; s)\big). \tag{D-77}$$

Hereby, r is the progress on characteristic s. With the total derivative of u,

$$\frac{du}{dr} = \frac{\partial u}{\partial y}\frac{dy}{dr} + \frac{\partial u}{\partial t}\frac{dt}{dr} \tag{D-78}$$

one can identify the following set of ODEs

$$\frac{du}{dr} = C(t, y, u), \tag{D-79}$$

$$\frac{dt}{dr} = A(t, y), \tag{D-80}$$

$$\frac{dy}{dr} = B(t, y). \tag{D-81}$$

Equation (D-79) is the transformed ODE which can be transformed backward with Equations (D-80) and (D-81) into the original coordinate system.

Applying MoC on a 0D-1D-TMB model, one obtains the following set of ODEs

$$\big(Xm^s c_p^{ad} + m^s c_p^s\big)\frac{\partial \mathrm{T}(r; s)}{\partial r} = m^s \frac{\partial X(r; s)}{\partial r}\Big(\Delta_{ads}h + c_{p,e}^g(T^e - T)\Big) + \dot{q}^{pm}, \tag{D-82}$$

$$\frac{\partial X(r; s)}{\partial r} = k^{global}\big(X_{eq} - X\big), \tag{D-83}$$

$$m^{pm} c_p^{pm}\frac{\partial T^{pm}(r; s)}{\partial t} = \dot{q}^{pm} - \dot{q}^{hf}, \tag{D-84}$$

$$m^{hf} c_p^{hf}\frac{\partial T^{hf}(r; s)}{\partial t} = \underbrace{u^{\star,hf}}_{>0}\varrho^{hf} c_p^{hf}\big(T^{hf,in} - T^{hf}\big) + \dot{q}^{hf}. \tag{D-85}$$

The velocity of the heat transfer fluid in the transformed coordinate system is $u^{\star,hf} = u^{hf} - u^{bed}$. Note that k^{global} describes the integral kinetic transport effects in the adsorbent composite. The energy conservation equation (D-82) is valid for adsorption and needs to be adjusted for desorption.

Effect of numerical dispersion on the True Moving Bed limiting case

Dynamic simulations of the 1+1-dimensional SMB for the cyclic steady-state solution are very time demanding. To show that the TMB is the limit of the SMB with a large number of adsorbers, the adsorbent composites were modelled with a lumped parameter model resulting in a one-dimensional model in direction of the moving bed (TMB) or switching modules (SMB).

In theory, the SMB solution approaches the steady-state TMB solution with an increasing number of adsorber beds. Due to numerical dispersion, the TMB solution underestimates the SMB solution slightly when using a finite-difference upwind scheme discretizing the first-order derivatives. Using the method of characteristics, the TMB can be proven to be the limiting case. In the following, exemplarily this behaviour is shown for the mass flux $\dot{m}$ and the COP.

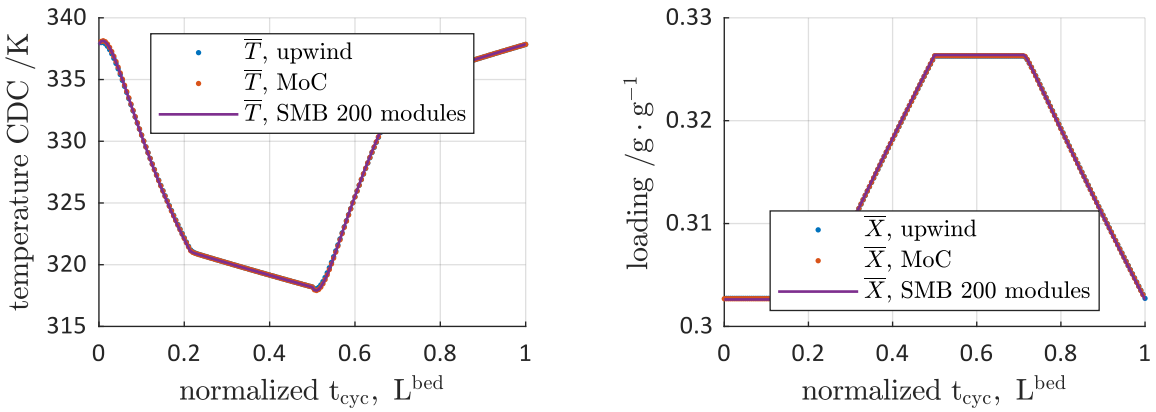

Figure D-9: Temperature and loading profiles resulting from the TMB and the SMB model, respectively. The TMB approach was once discretized with the finite-difference upwind scheme and once solved using the method of characteristics.

Figure D-9 shows the temperature and loading for TMB and an SMB simulation with 300 modules. The states of the TMB, which were discretized with an upwind scheme slightly differs from the solution with the method of characteristics. This behaviour can also be seen in the temperature profiles. Consequently, the maximal difference in loading from the beginning until the end of the adsorption cycle, is slightly smaller for the upwind discretized model resulting in less cooling energy and as a result, in a lower SCP and COP.

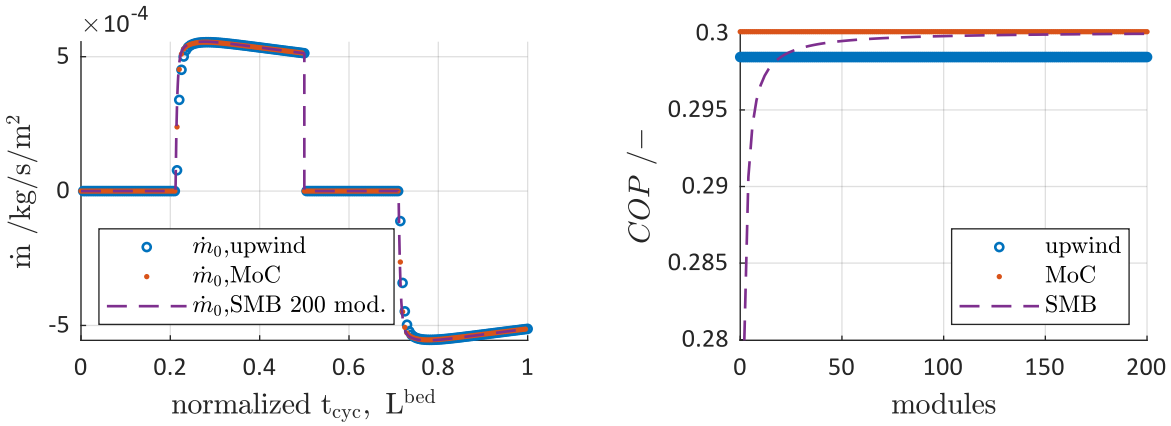

Figure D-10: Mass flux and COP resulting from the TMB and the SMB model, respectively. The TMB approach was once discretized with the finite-difference upwind scheme and once solved using the method of characteristics.

To adequately estimate steep fronts using the method of lines with convective transport, a fine grid is necessary, increasing the numerical costs. The steep fronts in the multi-bed approaches mainly appear when the switching conditions are reached and the valves between the adsorber bed and evaporator/condenser open. Figure D-10 (left) shows the exchange mass flux with steep fronts as a function of the normalized cycle time (SMB) or bed length (TMB with upwind or MoC). The behaviour of the SMB model can be sufficiently approximated with the TMB model, even though a small deviation exists (see COP in Figure D-10 on the right).

Since the deviation between MoC and upwind discretization is negligible and parameter continuation is difficult with the MoC model, the investigations in this work are performed using an upwind discretization scheme for the TMB model.